Thermal conductivity data acquisition using microfluidics and cheminformatics

Rosa América Moreno Jimenez

THÈSE PRÉSENTÉE
POUR OBTENIR LE GRADE DE

DOCTEUR DE L'UNIVERSITÉ DE BORDEAUX

ÉCOLE DOCTORALE DES SCIENCES CHIMIQUES

SPÉCIALITÉ Physico-chimie de la matière condensée

Par Rosa MORENO JIMENEZ

Acquisition de données de conductivité thermique par microfluidique et chémoinformatique

Thermal conductivity data acquisition using microfluidics and cheminformatics

Sous la direction de : Samuel MARRE et Benoît CRETON

Soutenue le 19 octobre 2023

Membres du jury :

Mme. AUBIN, Joelle	Directrice de recherche, CNRS-LGC	Rapporteur
M. HARTMAN, Ryan L.	Professeur, New York University	Rapporteur
Mme. ROTUREAU, Patricia	Ingénieure de recherche, INERIS	Examinateur
M. AYMONIER, Cyril	Directeur de recherche, CNRS-ICMCB	Président du jury
M.CRETON, Benoît	Ingénieur de recherche, IFPEN	Co-directeur de thèse
M. MARRE, Samuel	Directeur de recherche, CNRS-ICMCB	Directeur de thèse
Mme. MARLIERE Claire	Chef de laboratoire, L'Oréal	Invité

Acquisition de données de conductivité thermique par microfluidique et chémoinformatique

Résumé : Le changement climatique lié au réchauffement de la planète exige des mesures rapides pour réduire les émissions de gaz à effet de serre (GES), en particulier le dioxyde de carbone. Pour réduire les GES, les biocarburants issus de la biomasse riche en composés oxygénés représentent une alternative prometteuse comme source d'énergie. Plusieurs procédés sont utilisés pour convertir la biomasse source d'énergie incluant des conditions de hautes pressions et hautes températures, ce qui nécessite la connaissance des propriétés thermophysiques pour leur dimensionnement, en particulier la conductivité thermique (λ).

Les méthodes standard de mesure de λ impliquent l'utilisation de thermocouples et des appareils de mesure de flux de chaleur, mais ces méthodes peuvent être longues et sujettes à des erreurs lors de la manipulation des fluides. Pour surmonter ces difficultés, des technologies à plus petite échelle telles que les microsystèmes électromécaniques (MEMS) et la microfluidique ont été proposées. En combinant ces deux technologies, des dispositifs microfluidiques intégrant des MEMS ont été créés, connus sous le nom de "Lab On Chip". Cette approche offre plusieurs avantages, notamment une consommation réduite de réactifs, des temps de fonctionnement plus courts et des transferts de chaleur et de masse améliorés. Les derniers développements en matière de systèmes microfluidiques permettent maintenant d'élargir la gamme des conditions de fonctionnement de température et de pression. Cependant, les systèmes microfluidiques existants utilisés pour mesurer λ manquent d'inertie chimique et de propriétés thermomécaniques adéquates requises pour une application à diverses chimies et conditions. Par conséquent, la création d'un dispositif microfluidique capable de résister à des conditions difficiles reste cruciale.

Un dispositif microfluidique a été développé pour mesurer la conductivité thermique de liquides (λ_L) à différentes températures. Le dispositif a été testé avec des liquides aux propriétés connues, avant d'être utilisé pour générer de nouvelles données expérimentales.

Bien que la microfluidique soit utile pour générer de nouvelles données, il est essentiel de l'intégrer à d'autres approches comme la modélisation pour compléter les données expérimentales. Grâce à l'apprentissage automatique il est possible de développer des modèles prédictifs puissants à partir de données disponibles existantes. Néanmoins, les données disponibles actuellement sur la conductivité thermique des composés oxygénés, en particulier dans des conditions extrêmes, sont limitées et incohérentes entre différentes sources. Par conséquent, le besoin de générer de nouvelles données de conductivité thermique reste nécessaire.

Afin de faire des prédictions précises, il est important de disposer de données fiables et validées. Pour ce faire, une base de données a été créée qui comprend à la fois des données bibliographiques existantes et de nouvelles données expérimentales obtenues avec le dispositif microfluidique mis au point. Ces données ont été utilisées pour développer un modèle capable de prédire λ pour les liquides.

L'expériences et la modélisation se complètent. Ensemble, ils améliorent la compréhension du système étudié et la précision des prédictions.

Mots clés : Microfluidique, conductivité thermique, modélisation, capteur, biomasse

Thermal conductivity data acquisition using microfluidics and cheminformatics

Summary: Global warming-related climate change demands prompt actions to reduce greenhouse gas (GHG) emissions, particularly carbon dioxide. To reduce GHGs, biomass-based biofuels containing oxygenated compounds represent a promising alternative of energy source. To convert biomass into energy, several processes are operated at high pressure and high temperature conditions, which therefore required knowledge of thermophysical property data for their dimensioning, particularly thermal conductivity (λ).

Standard methods for measuring λ involve the use of thermocouples and heat flux measurement devices, but these methods can be time-consuming and prone to errors when handling fluids. To overcome these challenges, smaller-scale technologies such as microelectromechanical systems (MEMS) and microfluidics have been proposed. Combining these technologies, microfluidic devices incorporating MEMS have been created, known as "Lab On Chip." This approach offers several advantages, including reduced reagent consumption, shorter operating times, and improved heat and mass transfer. The latest developments in microfluidic systems now allow for expanded ranges of temperature and pressure operating conditions. However, existing microfluidic systems used for measuring λ lack chemical inertness and adequate thermomechanical properties required for diverse chemistries and conditions. Therefore, the creation of a microfluidic device capable of withstanding challenging conditions remains crucial.

A microfluidic device has been developed to measure the thermal conductivity of liquids at various temperatures. The device was tested with liquids of known properties before being used to generate new experimental data.

Although microfluidics offers a great way for producing new data, it's important to consider other approaches such as modeling to supplement experimental data. Through machine learning, powerful predictive models can be developed from existing available data. However, available data on the λ of oxygenated compounds, especially under extreme conditions, is limited and inconsistent across different sources. Consequently, the need to generate new thermal conductivity data remains essential.

In order to make accurate predictions, it is important to have reliable and validated data. To ensure this, a database has been created that includes both existing bibliographic data and new experimental data obtained using the developed microfluidic device. This data has been used to develop a model capable of predicting λ for liquids.

Experiments and modeling complement each other. Together, they improve the understanding of the system under study and the accuracy of predictions.

Keywords: microfluidics, thermal conductivity, modeling, sensor, biomass

Acknowledgement

First of all, I would like to thank Christophe PREUX to welcome me into the of Physico-chemistry of Interfaces and Complex Fluids Department (R171) at IFPEN in Rueil-Malmaison and Cyril AYMONIER for welcome the other half the time of my PhD into the ICMCB laboratory in Bordeaux.

I would like to express my gratitude to my supervisors from IFP Energies Nouvelles, Dr. Benoît CRETON and Dr. Claire MARLIERE, for the dedication and support they have given to this work, and for the direction and rigor they have given to me. Benoit, in particular, I want to thank you all for your invaluable guidance throughout the PhD.

I would also like to thank Dr. Samuel MARRE, my PhD director for all you taught me, your positivism, and your support.

My sincere gratitude goes to the members of the jury who have taken the time to review, examine and report my manuscript, Dr. Joelle AUBIN, Dr. Ryan L. HARTMAN, Dr. Patricia ROTUREAU and Dr. Cyril AYMONIER.

I would like particularly thank Lionel TEULE-GAY and Olivier NGUYEN, for their knowledge and support that were really helpful during the PhD. I sincerely appreciated your kindness and sense of humor, which were supportive during any challenging circumstances I might have had to deal with.

I would like to thank all my colleagues from ICMCB, the supercritical fluid team. They have provided an excellent working atmosphere; Emeline, Amandine, Rabie, Erwan, Fatma, Brian, Thomas, Antoine, Elen, Theo, Arnaud, Mathilda, Dorian, Neil, Maider, Enmmanuel, Insaf.

During these three years I also met other great colleagues and without them “la pause café” and the conviviality time would not have been the same; Elise, Alex C., Isa, Etienne, Lucas, Fouad, Louise and of course Brillon. During my Bordeaux journey I also got to meet more amazing people which I would like to thank them for being part of this rewarding experience; Adelita/Olivia, Vaïana, Massi, Antonio, Salva, Dani, Davidcito, Adriancito, Andres and so many other… I would like to thank you all for the hiking trips, beach trips, bar time, pétanque time, las noches de chicas and countless other wonderful moments that I will cherish.

I would also like to thank all my colleagues from IFPEN in the R171 department for the great working environment and experience, who welcomed me and with whom I spent good times. Christophe P, Sylvie, Eric, Marie, Christian, Anne S, Patricia, Brigitte, Anne-Claire, Aurelie.

I would also thank the other PhD students and colleagues; Laura and Alejandra (las chicas/ le bureau latino), who were essential to the success of this roller-coaster experience. Gracias chicas, por las aventuras y todos los pain au chocolat. Also, I would like to thanks, Claire M., Lamine, Mohamad, Camille, Peymann and all the interns that I could met during these years. Also, I would like to thank other great colleagues from IFPEN of which I could share some tacos, arepas, coffees, laughs and other great moments, Adrian, Adan, Luis, José, François.

Finally, I would like to thank my friends from Venezuela, France and all over the world, with whom I will always keep a unique bond despite the years and distance, and of course my family, my parents, my sisters and particularly to “mama” Luiscela, for all your love and support through the years.

Table of content

List of figures

Summary in French

L'utilisation de combustibles fossiles pour la production d'énergie suscite des préoccupations environnementales en raison de leur contribution aux émissions de gaz à effet de serre. Pour remédier à ces problèmes, l'utilisation de sources d'énergie renouvelables telles que la biomasse est envisagée comme alternative. Les biocarburants issus de la biomasse peuvent être utilisés dans les secteurs des transports tels que l'automobile et l'aviation. Différentes techniques peuvent être utilisées pour convertir la biomasse en biocarburants liquides, qui peuvent avoir des niveaux d'oxygène plus élevés que les carburants fossiles. Cette teneur en oxygène plus élevée est importante car elle permet une combustion plus complète et donc une réduction des émissions de polluants atmosphériques. Des données thermophysiques précises, en particulier la conductivité thermique (λ), sont essentielles pour optimiser le processus de conversion et concevoir des équipements efficaces, par exemple les échangeurs de chaleur. La détermination de la conductivité thermique implique des expériences couteuses en temps, pouvant prendre plusieurs heures à plusieurs jours et nécessiter de grandes quantités de produits, généralement de l'ordre d'une centaine de millilitres. Toutefois, grâce aux microsystèmes électromécaniques (MEMS) et à la microfluidique, il est désormais possible de réduire la taille des appareils électroniques et des installations expérimentales, ce qui a ouvert la voie à la réalisation de mesures à plus petite échelle. La combinaison de ces technologies a conduit à la création de dispositifs microfluidiques appelés "Lab On Chip" (LOC), capables de remplir des fonctions telles que la détection, la mesure, la manipulation et l'analyse de petites quantités de liquides.

La réduction d'échelle apportée par la microfluidique, tout comme MEMS, offre plusieurs avantages tels qu'une faible consommation de réactifs, un criblage rapide, un temps d'analyse plus court et une analyse i*n situ*. C'est pourquoi la microfluidique est largement utilisée pour déterminer les propriétés thermophysiques de fluides. Toutefois, les systèmes microfluidiques existants ne présentent pas l'inertie chimique et les propriétés thermomécaniques nécessaires pour mesurer λ dans des conditions extrêmes. La détermination des propriétés thermophysiques à des températures élevées (allant de 150° C jusqu'à 1000°C), en particulier λ, est cruciale pour les procédés impliqués dans la production de biocarburants. Cette connaissance permet d'optimiser les processus de conversion, d'améliorer les systèmes de transport et de stockage, et de concevoir des réacteurs et des catalyseurs efficaces. Cependant, les données de λ des composés oxygénés sont encore relativement manquantes et incohérentes entre elles. La microfluidique constitue une méthode idéale pour produire de nouvelles données de λ, en particulier dans des conditions inexplorées. L'environnement contrôlé ainsi que le criblage rapide et la faible consommation de réactifs rendent cet outil microfluidique très prometteur.

Les objectifs expérimentaux de ce travail de thèse sont donc de développer un dispositif microfluidique capable de mesurer λ à différentes températures, pour générer de nouvelles données expérimentales pour des composés oxygénés. Le premier objectif consiste à optimiser les techniques MEMS pour créer un capteur miniaturisé intégré dans un dispositif microfluidique résistant à la température. Cela permet de mesurer λ pour différentes conditions de température.

Avant de mener les expériences, un état de l'art a été réalisé pour explorer les matériaux et techniques utilisés dans la fabrication des puces microfluidique pouvant résister à des conditions de température élevée. Cela comprenait également l'exploration de technologies miniaturisées pour le contrôle et la détection de la température dans les systèmes microfluidiques. Ce dispositif microfluidique développé

utilise la technologie MEMS, comprenant l'intégration de microcapteurs afin de faire la mesure λ des liquides. La technologie microfluidique du silicium-borosilicate a été choisie pour élargir la gamme des conditions de fonctionnement par rapport à d'autres systèmes microfluidiques. Ce dispositif est avantageux car il est chimiquement inerte, peut fonctionner à des températures plus élevées que d'autres matériaux (e.g., le Polydiméthylsiloxane, verre…) communément utilisés en microfluidique et permet un accès optique pour le couplage avec d'autres caractérisations *in situ.* Il a été fabriqué selon une procédure en trois étapes : dépôt de capteurs sur un substrat en verre borosilicaté agissant comme isolant, gravure de microcanaux sur un substrat en silicium agissant comme conducteur et scellement des deux substrats par fusion. Le silicium a été choisi spécifiquement parce qu'il a une valeur de λ élevée, ce qui en fait un dissipateur thermique efficace et réduit les incertitudes dans les systèmes à l'échelle microscopique.

L'approche utilisant un seul élément résistif de mesure a été retenue pour assurer le chauffage et la détection de la température dans le dispositif microfluidique afin de mesurer λ. Afin de créer le microcapteur avec précision, plusieurs étapes ont été suivies pour assurer la meilleure reproductibilité possible. Une sélection rigoureuse des métaux a été effectuée, et l'utilisation de Platine (Pt) pour la conception du microcapteur a été l'option retenue, notamment en raison de sa résistance à l'oxydation et à la température. De même, plusieurs géométries du microcapteur ont été testées et la spirale est celle qui a été retenue, en raison de sa grande surface de contacte et de l'uniformité de la température qu'elle offre. Le microcapteur a été fabriqué en utilisant une photolithographie bicouche et en déposant un film métallique sur le substrat en verre borosilicaté à l'aide de la pulvérisation magnétron. La photolithographie bicouche est une méthode qui consiste à retirer la couche inférieure d'un matériau sensible à la lumière pour créer un motif spécifique. Cette technique est couramment utilisée pour déposer les métaux dans des structures de films discontinus avec une grande résolution. La résolution des géométries au cours du processus a été améliorée en tenant compte de facteurs tels que le temps de développement et la température de cuisson. Ensuite, le comportement des capteurs en termes de résistance à différentes températures a été étudié. Jusqu'à une certaine dimension de la spirale (2 mm de diamètre et 0,1 mm d'espacement), la résistance électrique du capteur a une réponse linéaire en fonction de la température (de 293K à 413K). Lorsque la taille de la spirale est réduite de moitié, un phénomène d'hystérèse est observé, quand la température augmente la résistance du capteur a une réponse linéaire (de 293K à 413K). En revanche, lorsque la température diminue (de 413K à 293K), le phénomène d'hystérèse se produit. Ceci peut s'expliquer par le fait que la réduction de la taille de la spirale et l'espacement plus étroit entre ses anneaux concentriques créent un environnement thermique plus confiné. Cette configuration restreint la dissipation de chaleur et amplifie les gradients thermiques à l'intérieur de la spirale, ce qui conduit à l'observation de ce phénomène.

Le deuxième élément de la puce microfluidique est composé par les microcanaux. Ces derniers ont été créés à l'aide de techniques de microfabrication, notamment la photolithographie. Cela implique de transférer un motif sur une plaquette de silicium à l'aide d'un masque, d'appliquer un revêtement photorésistant, d'exposer la lumière à travers le masque, de développer le motif et de faire la gravure de la plaque. Enfin, les substrats de silicium et de verre borosilicaté ont été assemblés par un processus de fusion, qui consiste à chauffer et à appliquer une pression pour créer des liaisons chimiques solides entre les deux substrats. Ce collage irréversible assure la résistance de la puce microfluidique à différentes conditions de température et pression.

Ensuite, le dispositif microfluidique a été intégré dans un système de mesure plus large (macroscopique), dans le but de tester, optimiser et valider l'approche microfluidique pour la mesure de la conductivité thermique. Le système comprend une interface fluidique telle que des tubes, des pompes et des composants électroniques conçus pour contrôler le débit de fluide dans un réacteur à petite échelle. Il comprend également des équipements pour la manipulation d'échantillons de petits volumes. Le processus de mise en place de la mesure de λ implique l'utilisation d'une alimentation pour appliquer un courant électrique. La chaleur générée par ce courant provoque un changement de la température du capteur, ce qui entraîne également à un changement de sa résistance, connu sous le nom d'effet Joule. Pour mesurer précisément le changement de résistance, un circuit connu sous le nom de pont de Wheatstone a été utilisé. Les données enregistrées sont ensuite traitées pour convertir la variation de résistance en un changement de température. Le transfert de chaleur entre le capteur et le fluide environnant peut être déterminé en mesurant le changement de température du capteur. Ces données peuvent être utilisées ensuite pour calculer la λ du fluide. Les incertitudes des instruments utilisés et la répétabilité des mesures ont ensuite été évaluées.

Pour quantifier λ pour différents liquides, la réponse du capteur a été calibrée en ajustant les comportements thermiques sur des mélanges binaires eau/éthanol. Les paramètres optimaux de puissance de chauffage, temps de chauffage et d'intervalle de temps ont été utilisés pour calibrer le capteur et ont ainsi été fixés respectivement à 60 mW, 60 secondes et une plage de temps de 28 à 44 secondes. Le dispositif microfluidique et ses réglages ont ensuite été testés sur deux fluides différents, le n-pentadécane et l'éthan-1,2-diol, pour des températures allant de 293,15 K à 333,15 K. Les erreurs obtenues pour le n-pentadécane et l'éthan-1,2-diol étaient respectivement de 8 % et 20 %. Il a été suggéré que l'erreur de 20 %, pour l'éthan-1,2-diol peut être due à sa viscosité plus élevée que celle des autres fluides. La viscosité de l'éthan-1,2-diol est environ dix fois plus élevée que celle de l'eau, de l'éthanol ou encore du n-pentadécane à 293,15 K. Cela indiquerait que la convection joue un rôle important dans le transfert de chaleur en microfluidique. Cependant, les mesures de λ restent précises pour la gamme de viscosités couvertes par les fluides utilisés pour l'étalonnage. Enfin, nous avons proposé de nouvelles valeurs expérimentales pour le 2,5-diméthylfurane, un sous-produit de la biomasse pour lequel il existe un manque d'informations sur les données de λ dans la littérature. Ce travail expérimental a été valorisé par une publication [1].

En raison de son haut débit et de ses mesures sensibles, la microfluidique est un bon candidat pour générer des données permettant d'entraîner les modèles et de bénéficier de leur pouvoir prédictif. La combinaison de la microfluidique et de la modélisation est essentielle pour créer une approche plus économe et automatisée, avec des résultats à haut débit pour des propriétés thermophysiques. De ce fait, le deuxième objectif du travail de thèse a été de développer des modèles prédictifs basés sur les données générées et collectées dans la littérature. Ces nouvelles données offrent la possibilité d'améliorer la précision des prédictions et d'aider à concevoir de futures expériences. L'intégration de l'apprentissage automatique permet la création de modèles prédictifs robustes qui apprennent à partir des données existantes. Toutefois, pour garantir la précision et la fiabilité de ces modèles, il est impératif de disposer de données expérimentales de référence.

Les méthodologies issues de la Chémoinformatique ont tout naturellement été appliquées pour la prédiction de la conductivité thermique d'hydrocarbures et de composés oxygénés en phase liquide.

Le principe de ces modèles appelées, Quantitative Structure Property Relationship (QSPR) visent à établir une relation entre la structure chimique d'un composé et la propriété thermophysique ciblée. Des descripteurs moléculaires sont employés pour représenter les informations structurelles des molécules sous forme de données numériques, simplifiant ainsi la complexité des structures moléculaires. Ainsi, des algorithmes d'apprentissage permettent de faire émerger des corrélations entre les descripteurs et la propriété ciblée. C'est ce type de modélisation qui a été choisie pour ce travail de thèse.

Le développement de ces modèles, nécessite de collecter des données expérimentales, et de les « nettoyer » soigneusement par un triage, la conversion d'unités, réajustements des modèles et la création des points de données d'importance égale. L'objectif est de compiler une base de données de valeurs expérimentales de référence fiables. Les données expérimentales utilisées dans cette étude ont été obtenues à partir de sources publiées et du dispositif microfluidique, qui a permis de générer des nouvelles données qui n'étaient pas disponibles auparavant. Les descripteurs de type FGCD (Functional Group Count Descriptors) ont été choisis pour leur simplicité et leur efficacité. Ensuite, un algorithme d'apprentissage, « Support Vector Machine » (SVM) a été appliqué à la base de données pour générer des modèles prédictifs. Dans ce cas, cet algorithme a la capacité de trouver des corrélations non linéaires entre les descripteurs des molécules et leurs valeurs de λ. L'ensemble du jeu de données a été divisé de manière aléatoire en n parties à peu près égales. Ces blocs ont ensuite été agglomérés et utilisés pour entrainer le modèle (Training) et pour le tester (Test). Ce processus, connu sous le nom de validation croisée, est répété plusieurs fois, différentes parties étant utilisées à chaque fois pour les Tests. Nous avons utilisé la stratégie du « compound out », ce qui signifie qu'une molécule n'appartient qu'à un seul bloc. Une attention particulière a été accordée aux molécules polyfonctionnelles, qui étaient très différentes des autres composés, donc elles ont été fixées et incluses dans le processus d'apprentissage. Le modèle Support Vector Regression (SVR) obtenu a montré une bonne capacité prédictive par rapport aux données de référence. Le coefficient de détermination (R^2) pour l'ensemble de la base de données a été calculée comme étant de 0,992, avec la racine de l'écart quadratique moyen (RMSE) ainsi que l'erreur absolue moyenne (MAE) de 0,0024 $W.m^{-1}.K^{-1}$ et 0,0018 $W.m^{-1}.K^{-1}$, respectivement.

Le modèle SVR a été utilisé pour compléter les données expérimentales de composés n'ayant qu'un à deux points expérimentaux disponibles. Les comparaisons ont montré une bonne concordance entre les valeurs prédites et les données expérimentales disponibles. Cela valide la capacité prédictive du modèle et son potentiel à prédire les conductivités thermiques à d'autres températures. La base de données nécessite de continuer à être alimentée car elle manque de données expérimentales et de conditions de température limitées pour certains types de composés oxygénés tels que les époxydes, les aldéhydes et les polyfonctionnels. Disposer de ces informations permettrait d'augmenter de le pouvoir prédictif du modèle pour ces familles chimiques. Ce travail de modélisation basé sur de l'apprentissage automatique a été valorisé par une publication [2].

En conclusion, l'objectif principal de cette thèse a été de développer un dispositif microfluidique permettant de mesurer la conductivité thermique à différentes températures. Cela a permis de recueillir de nouvelles données sur la conductivité thermique des composés oxygénés qui manquent actuellement dans la littérature. Nous avons pu montrer que le dispositif microfluidique qui utilise le silicium comme dissipateur thermique, est capable de mesurer avec précision la λ pour diverses

familles chimiques, notamment des composés oxygénés et des hydrocarbures. Les bénéfices de la microfluidique ont permis de la combiner avec la modélisation, pour développer des modèles prédictifs basés sur les données collectées et générées par la microfluidique. Nous avons montré que le modèle a une bonne capacité prédictive par rapport aux données de référence. L'ajout continu d'informations à la base de données est crucial, car certaines familles chimiques disposent de données manquantes.

Introduction

The use of biomass for controlling CO_2 emissions

In our society, energy plays a crucial role being essential to numerous sector of activities, including housing, transportation, business, and agriculture [3] . However, increasing energy consumption leads to several risks to our society and the environment. Indeed, the environmental impact is mainly related to the production of energy from fossil resources — coal, oil, and natural gas. Aside from local environmental hazards, fossil resources are the main contributors to the emission of greenhouse gases, among which carbon dioxide (CO_2) is the main actor.

Some strategies have been proposed for managing CO_2 emissions such as Carbon Capture, Utilization, and Storage (CCUS) [4]. In CCUS, CO_2 is captured and either stored underground or used for industrial processes like the synthesis of synthetic fuels or building materials [5,6]. Another strategy is the use of renewable energy. One such source is biomass, a renewable source of organic material derived from plants and animals. Biomass can be considered as a carbon-neutral energy since the amount of CO_2 captured during biomass production by plants is equivalent to the amount released during biomass burning for energy production [7,8].

The conversion of biomass into biofuels

Besides energy production by direct biomass burning, we can also produce biofuels which are easier to store and can be used alongside conventional energy production reactors. Biofuels derived from biomass transformation represent an alternative solution to fossil resources for automotive and aviation. This biomass transformation consists of converting organic matter into liquid fuels such as ethanol, biodiesel, and other synthetic biofuels. For this, there are several conversion techniques such as fermentation, gasification, pyrolysis, hydrotreatment, etc [9]. Molecules derived from biomass are already introduced into conventional fuels at varying levels of content. For instance, ethanol can be incorporated in gasoline up to 5 to 10% [10], biodiesel can be incorporated in diesel from 6 to 20% [11]. There are also many other molecules such as butanol, methanol or dimethyl ether that could be used as biofuels. However, their use is still marginal, and their content is very low in fossil fuels [12].

The level of oxygen content is one distinction between fossil fuels and biofuels. Fossil fuels such as gasoline and diesel are primarily composed of hydrocarbons and contain very small amount of oxygen (between 2 and 3% by weight) [13]. Biofuels such as biodiesel, bio-oil or ethanol, on the other hand, are made from organic material, and naturally contain higher level of oxygen than fossil fuels[14,15]. This higher oxygen content is important because it allows a more complete combustion and thus a reduction of the emissions of atmospheric pollutants [16]. The oxygen content of biofuels varies depending on their chemical composition and production method. Generally, vegetable oil-based biofuels are rich in functional groups such as esters. Biodiesels, which are produced from vegetable oils, contain about 11% oxygen by weight [17] and ethanol contains about 35% oxygen by weight [18]. However, research have been directed towards the use of other bio-derived oxygenated fuels such as: acids, aldehydes, and furans [19,20]. For instance, furans burn cleanly and emit fewer greenhouse gases and fine particles compared to fossil fuels because of its higher hydrogen-to-carbon ratio. Additionally, compared to current biofuels, they have the potential to produce more energy per unit of weight [21].

Importance of thermal conductivity in the industry

In the process of converting biomass to biofuels, it is important to access thermophysical data as support, such as density, viscosity, specific heat, thermal conductivity, and heat capacity. These properties are essential for designing the conversion processes. For instance, the performance of process operations involving heat transfers depends greatly on thermal conductivity [22]. Thermal conductivity, which is the measure of a material's ability to transfer heat, has been extensively studied. It was Joseph Fourier, a British physicist in the early 19th century, who pioneered the scientific investigation of thermal conductivity, marking a significant milestone in its study. Today, this property is very useful in industries for the design and manufacture of products and systems that require thermal control. For instance, thermal conductivity is used in the heat exchanger design, to determine the ideal operating temperatures for equipment, designing power plants and cogeneration plants, among other applications. Moreover, thermal conductivity is also important in many scientific fields such as geology [23], material physics [24], meteorology [25], etc.

Several experimental techniques have since been developed for measuring thermal conductivity and some of them will be discussed later in this manuscript. These methods involve the use of thermocouples and heat flow measuring devices. Such experiments, require hundreds milliliter of products and can take from a few hours to several days [26]. In the last decades, it has been suggested to use smaller scale technologies, combining MEMS (Micro Electromechanical Systems) and microfluidics to reduce the amount of time and product used.

Microfluidics for the determination of thermophysical properties

The development of MEMS began in the 1960s with the introduction of transistors, sensors, integrated circuits, and lithography technologies that allowed the production of miniature structures for mechanical, optical, medical, and electronic devices. In chemistry, the downscaling of experiments – Microfluidics – on the other hand, began in the 1980s with the development of micro-pump and valve systems, involving the manipulation of fluids at the microscopic scale. In the 1990s, these two technologies converged to create microfluidic devices incorporating MEMS, creating the concept of Lab On Chip (LOC) [27], to perform various functions such as detection, measurement, handling and analysis of materials of very small quantities of liquids. Microfluidics along with MEMs provides extraordinary capabilities thanks to its inherent advantages with its low reagent consumption, fast screening, low operating time, *in situ* analysis, heat improvement, mass transfers, etc. Since then, several studies on the use of this technology for determining thermophysical fluid properties (density, viscosity, thermal diffusion coefficient and thermal conductivity) have been conducted [28–32].

Research on microfluidic devices has advanced and the technology has improved, allowing for a wider range of operating conditions such as pressure and temperature [33]. This characteristic has opened the microfluidic fields of research to materials synthesis [34], chemistry in harsh conditions [35], geosciences [36,37], and particularly for determining the thermophysical properties of fluid systems under pressure capable reaching up to 500 bar and temperature up to 300°C [36,38,39]. However, only few works have investigated the measurement of thermal conductivity in liquids [30,40–42]. The existing microfluidic systems used for this purpose lack chemical inertness and their thermomechanical properties are not suitable for use of different fluid systems (oxygenated, hydrocarbons) and

conditions (temperature or pressure). Consequently, it is still essential to develop a microfluidic device capable of measuring thermal conductivity under harsh conditions.

Microfluidics is an ideal method for producing new thermal conductivity data subsequently used for developing predictive models. Since it provides a controlled environment and temperature for experiments, as well as fast screening and low product consumption. The combination of microfluidics and modeling would result in new thermal conductivity data generation, especially at unexplored products or conditions.

Experimentations and modeling to investigate thermal conductivity of oxygenated compound at high temperatures

The reactions and process involved in conversion of biomass often require high temperatures, making knowledge of the thermophysical properties of oxygenated compounds highly valuable. This knowledge serves to multiple purposes, including optimizing the conversion process, enhancing transport and storage systems, and designing efficient reactors and catalysts. For instance, in systems involving thermal conductivity information (*e.g.*, heat exchangers), the equipment design can be improved by predicting heat loads and anticipating variations with different variables. However, the data available on the thermal conductivity of oxygenated compounds remains limited and often varies depending on the source, particularly in extreme conditions.

Experimentations and modeling are two essential components of research, as they work in conjunction to validate and verify each other's results. Experiments provide empirical data to validate or refine the model, while models help to design future experiments, simplifying experimental steps that can be time consuming or expensive. Together, they enhance the accuracy of predictions and the comprehension of the system under investigation. In a broader context, artificial intelligence (AI) is revolutionizing our society by automating tasks, analyzing massive amounts of data, and enhancing decision-making processes. Machine learning (ML), a subset of AI, plays a crucial role in training models to learn from data, enabling predictions and optimizations. In chemistry, AI and ML are driving progress in drug discovery, material design, and chemical process optimization. However, for these models to be accurate and trustworthy, reference experimental data are required.

Aims and objectives

The main objective of this work is the development of a microfluidic device allowing to measure the thermal conductivity of liquids at different temperatures. The goal is to gather new data on the thermal conductivity of oxygenated compounds that is currently lacking in literature.

First, the challenge will stand in optimizing some MEMS techniques to develop a miniaturized *in situ* sensor that can produce a signal that can then be related to thermal conductivity, being integrated into a temperature-resistant microfluidic device. Thermal conductivity measurements at various temperatures conditions will be possible by establishing a measurement setup for readout device and signal processing. I have considered well-targeted liquids with well-known properties in the literature to validate the methodologies and tools developed. Following that, a small set of new experimental values have been generated, addressing the scarcity of thermal conductivity data at various temperature levels.

The second objective is to develop new models for predicting thermal conductivity of the liquids involved in the conversion of biomass found (oxygenated and hydrocarbons), across a broad range of temperatures. For the developed models to be accurate, it is essential to collect trustworthy and validated data. For this and as detailed later, a database has been created using existing validated experimental data on thermal conductivity from literature and new data produced in this work by microfluidics.

This manuscript is structured in four chapters. First, a chapter dedicated to bibliographic aspects, explaining the concepts of heat transfer, thermal conductivity, experimental and predictive methods for determining thermal conductivity in liquids, as well as microfluidic and modeling approaches that have been developed to assess this property. In the following chapter, I will detail the materials and methods for the conception of the microfluidics device allowing thermal conductivity measurement. The third chapter discusses the equipment and process used to measure the thermal conductivity of fluids, including validation and results from well-known fluids. Then, with the so obtained microfluidic device, the acquisition of new experimental thermal conductivity data of a biomass-derived product will be established at different temperature conditions up to 60°C. In the fourth chapter, I will detail the type of models used to predict thermal conductivity and the tools required for their implementation. This includes the principles of the methodology, the data analysis tools used to create and evaluate the models, and a discussion on the results obtained. Finally, the general conclusion will summarize the main results obtained, and the perspectives associated with this study.

Chapter I: Experimental and predictive techniques for thermal conductivity determination

This chapter discusses the importance of understanding the thermophysical properties of fluid systems, specifically thermal conductivity, in different industrial processes and model development. It provides a brief overview of heat and heat transfer mechanisms emphasizing on conduction, and the methods used to measure thermal conductivity. The chapter also highlights the role of microfluidics and MEMS as supplementary tools for determining this property, along with recent advancements in this field. Additionally, alternative approaches such as modeling are introduced, and the existing methods currently used for predicting thermal conductivity are discussed.

1.1. Introduction

When a system is heated, the increase in energy causes the particles in the system to move faster and collide more frequently with each other, increasing their kinetic energy. As a result, the system's temperature rises, which, depending on the specific system, can result in a number of changes. Depending on the intensity of the heat source, liquids may evaporate, gases may expand, and solids may melt or even vaporize. The amount of energy transferred, the system's thermal diffusivity, thermal effusivity, and the thermal conductivity of the materials involved are just a few of the variables that affect how much heat is transferred to the system and the resulting change in temperature.

Heat can be transferred by three main mechanisms: conduction, convection, and radiation. Conduction involves the transfer of energy from highly active molecules to fewer active ones, while convection is the movement of fluids that leads to the distribution of thermal energy. Radiation occurs when a hot object emits energy that can be transmitted through electromagnetic waves to another system. Convection and conduction are the two most prominent methods of heat transfer in liquids and gases.

The following sections provide an explanation of heat transfer mechanisms, specifically focusing on conduction. It discusses the concept of thermal conductivity and the different methods used to measure this property.

1.2. Heat transfer mechanisms

Heat transfer consists in the exchange of thermal energy, leading in a temperature difference or even accompanied by a phase transition within a system. Temperature is a physical parameter, reflecting the entropy of a system, as it determines its thermodynamic equilibrium. It gives a macroscopic view of the interactions between molecules: molecular agitation in liquids and gases.

The heat flow (Φ) as defined in equation (1- 1) stands in the amount of thermal energy/heat - caused by a temperature difference - transferred in a material per unit of time, t. Φ is expressed in Watts (W).

$$\Phi = \frac{Q}{\Delta t} \tag{1- 1}$$

where Q is the thermal energy in Joules.

The heat flux (φ), also referred to as heat flux density, corresponds to a flow of energy per unit of surface as presented in equation (1- 2) φ is expressed $W.m^{-2}$.

$$\varphi = \frac{\Phi}{A} \tag{1- 2}$$

where *A* is the area through which the heat transfer occurs.

The heat transfer can occur through heat conduction (conduction), heat flow (convection) or heat radiation (radiation), which are represented hereafter in Figure 1.

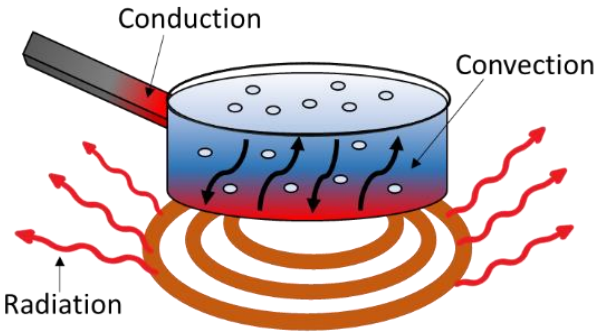

Figure 1: Illustration of different modes of heat transfer.

Heat transfer by thermal convection

Convection is the process in which heat transfer through its environment is due to fluid movement. Fluid displacement can be due to either natural or forced convection. In natural convection, the flow is induced by buoyancy forces in the fluid that arise from local density variations in lack with gravity. On the other hand, for forced convection the flow is caused by some mechanical or external solicitations such as a fan, pump, or atmospheric wind.

In the case of heat transfer from a solid surface to a fluid, Newton's cooling law states that heat transfer is proportional to the difference between the surface and fluid temperatures and the surface area. This is defined as [43]:

$$\Phi_h = hA(T_s - T_f) \tag{1-3}$$

Where Φ_h is the rate of heat transfer by convection in W, h is the convective heat transfer coefficient in $W.m^{-2}.K^{-1}$, A is the exposed surface area in m^2, T_s is the temperature of the solid at the surface, T_f is the temperature of the surrounding fluid.

Heat transfer by radiation

Thermal radiation consists of electromagnetic radiation generated by the thermal energy of particles (kinetic energy due to random movements) in matter having a temperature greater than absolute zero. Several types of electromagnetic radiations exist such as X-rays, gamma rays, IR, etc.

The power radiated by an object at a temperature T is given by Stefan-Boltzmann's law as follows in equation (1- 4) [43]:

$$\Phi_r = A\varepsilon\sigma T^4 \tag{1-4}$$

Where Φ_r is the rate of heat transfer by radiation in W, A is the surface area of the body in m^2, σ is the Stefan-Boltzmann constant and is equal to 5.6704×10^{-8} $W.m^{-2}.K^{-4}$ and ε is the surface emissivity (unitless). In the case of a blackbody (ideal physical object that absorbs all incident electromagnetic radiation regardless of frequency or angle of incidence), the emissivity $\varepsilon = 1$, otherwise $\varepsilon < 1$.

Heat transfer by conduction

Conduction was first described by Joseph Fourier in 1822 [44]. This theory is known today as Fourier's law of conduction. It states that when a temperature gradient exists within a system, the return to equilibrium results in a standardization of the temperature: the heat is propagated by contact within the material. This is expressed by the following equation:

$$\vec{\varphi}_k = -\lambda \overrightarrow{\nabla T} \tag{1- 5}$$

Where $\vec{\varphi}_k$ is the heat flux density in $W.m^{-2}$, λ is the thermal conductivity of the material (in $W.m^{-1}.K^{-1}$) and $\overrightarrow{\nabla T}$ is the temperature gradient through the conducting material [45].

Equation (1- 6) expressed the amount of heat conducted per unit of time in a certain direction of a homogeneous solid material. This amount is equal to the product of the conducting area perpendicular to the heat flow path along the x axis in equation (1- 6), and the thermal conductivity of the material.

$$\Phi_k = -\lambda A \frac{dT}{dx} \tag{1- 6}$$

Where Φ_k is the rate of heat transfer by conduction in W, λ is the thermal conductivity of solid material in $W.m^{-1}.K^{-1}$, A is the surface area of the material perpendicular to flow of heat in m^2, $\frac{dT}{dx}$ is the temperature gradient through the conducting material in $K.m^{-1}$ along the x coordinate.

Note, the minus sign is a consequence of the second law of thermodynamics, which states that heat must flow in the direction from higher to lower temperature.

Thermal conduction in solids is caused by the vibrating lattice of atoms or molecules. When heat is applied, the vibration becomes stronger and is passed on to the nearby atoms or molecules as kinetic energy. This energy spreads out from the heat source, leading to a temperature gradient across the solid material.

Thermal conduction in liquids is caused by the movement of free electrons and phonons (vibrations of atoms) within the medium. Liquids have more random and rapid movement of atoms or molecules compared to solids. Heat energy is transferred through collisions between molecules and the transfer of kinetic energy. However, heat transfer in liquids is less efficient than in solids due to the space between molecules.

In gases, thermal conduction occurs primarily through collisions between molecules, causing the heat to be transferred from one molecule to another nearby. However, since gas molecules are more spread out compared to solids and liquids, the conduction happens at a slower rate. Additionally, the thermal conductivity of gases is affected by temperature and pressure.

1.3. Thermal conductivity

To use the Fourier's law, the thermal conductivity of the material must be known. Thermal conductivity, (λ) which is referred to as a transport property, is expressed in $W.m^{-1}.K^{-1}$ and provides an indication of the rate at which energy is transferred by the diffusion process. It represents the ability of the matter (in solid, liquid or gas state) to conduct heat. This property is essential for the efficiency of a thermal system, and generally depends on the nature of the material (homogeneity, anisotropy) and changes with the temperature.

Thermal conductivity can be defined from the Fourier's law (equation (1- 7)) as the rate of heat transfer through a material per unit of surface and temperature gradient:

$$\lambda = -\frac{\Phi}{A.\nabla T} \tag{1- 7}$$

In the case of heat transfer along one direction: The distance of heat transfer is defined as Δx and ΔT is the temperature difference.

$$\lambda = \frac{\Phi \Delta x}{A \Delta T} \tag{1- 8}$$

The ability of a material to conduct heat depends on its physical structure at the atomic and molecular level, which is influenced by its state of matter. Figure 2 illustrates some orders of magnitudes of the thermal conductivity for different families of materials and various states of matter under normal temperature and pressure conditions.

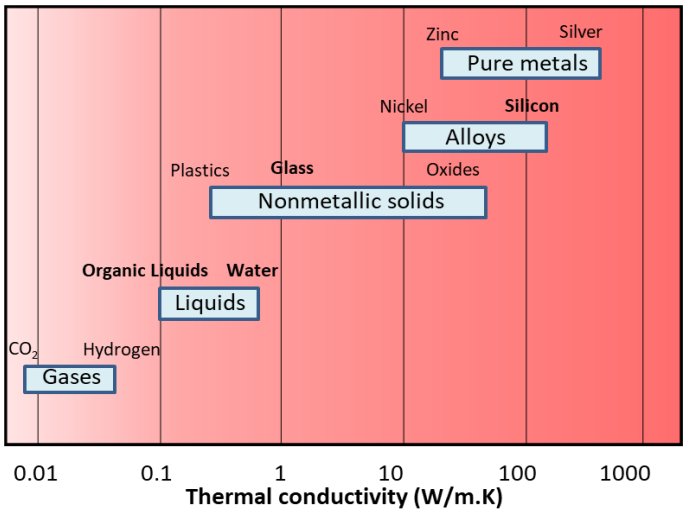

Figure 2: Some order of magnitude of the thermal conductivity of materials, adapted illustration from [46].

Solids have the highest thermal conductivity among the three states of matter due to the close arrangement of atoms and strong interatomic bonds. The thermal conductivity of metals, such as silicon (150-180 $W.m^{-1}.K^{-1}$ at room temperature) and aluminum (205 $W.m^{-1}.K^{-1}$ at room temperature), is especially high due to the presence of free electrons that can transfer energy quickly. This makes silicon and aluminum good heat conductor, which is why they are commonly used in electronic devices and other applications where thermal management is important. On the contrary, other solids such as

borosilicate glass has low thermal conductivity (1.2-1.5 $W.m^{-1}.K^{-1}$ at room temperature). This means that it is a poor conductor of heat, which makes it ideal for use in applications where thermal insulation is desired.

For fluids and gases, since the intermolecular spacing is much larger and the movement of the molecules are more random in the fluid state than in the solid state, thermal energy transfer is less effective. Therefore, the thermal conductivity of gases and liquids is generally smaller than solids.

Liquids have lower thermal conductivity compared to solids due to their less ordered molecular structure and weaker intermolecular forces. However, some liquids, such as metals in a liquid state, have high thermal conductivity due to the presence of free electrons. The thermal conductivity of liquids decreases with temperature.

Gases have the lowest thermal conductivity among the three states of matter due to their low density and lack of strong intermolecular forces. Moreover, gases are poor conductors of heat due to their high thermal resistivity. However, certain gases, such as argon and helium, have higher thermal conductivity due to their atomic structure and the presence of free electrons. The thermal conductivity of gases increases with pressure and temperature.

1.3.1. Effect of temperature on liquid's thermal conductivity (λ_L)

Values of the thermal conductivity are usually tabulated as a function of temperature for the saturated state of the liquid. Generally, thermal conductivity decreases as the molecular weight increases for liquids. Figure 3 shows some examples of thermal conductivity behavior of some fluids with temperature at saturation.

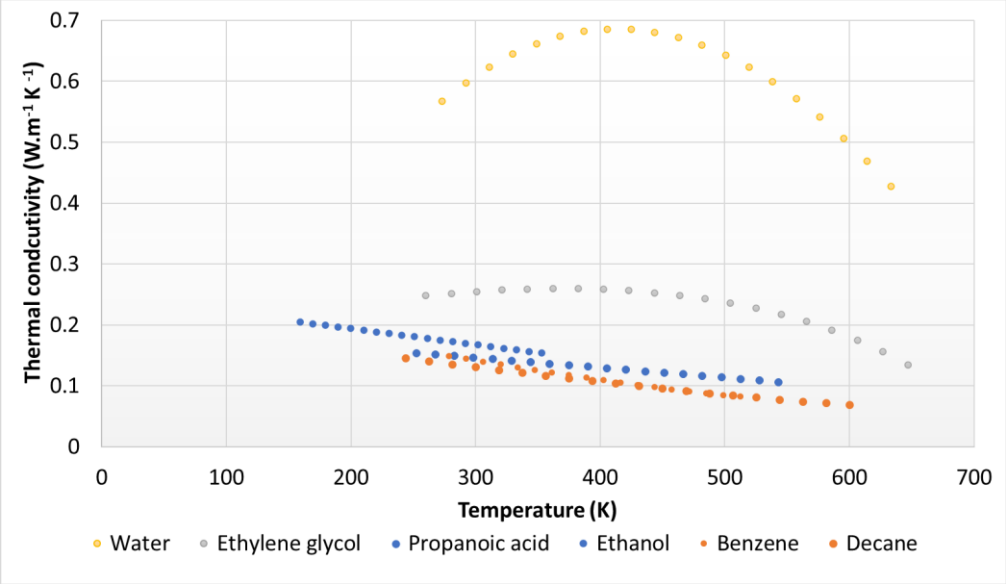

Figure 3 : Variation of thermal conductivity of some liquids with temperature at saturation.

The order of magnitude is approximately 0.1-0.2 $W.m^{-1}.K^{-1}$ for almost all liquids except for water which range is between 0.6 – 0.7 W $W.m^{-1}.K^{-1}$. As shown in Figure 3, associating liquids such as water and ethylene glycol have the most different thermal conductivity versus temperature behavior [47,48] due

to changes in the hydrogen bonding network with temperature. Indeed, at low temperatures, some of the energy being transferred is stored in hydrogen bonds as they form a network, leading to a lower thermal conductivity. As the temperature increases, less energy is captured by the hydrogen bonding network, leading to an increasing of thermal conductivity. This phenomenon competes with the typical decrease in thermal conductivity with temperature due to thermal expansion and results in a maximum in the thermal conductivity—temperature behavior of the fluid.

Otherwise, for organic liquids the thermal conductivity decreases with temperature due to the increase of molecule's movement, which obstructs transport of heat through liquid [49]. In addition, for nonpolar liquids the thermal conductivity decreases monotonically with increasing temperature due to the thermal expansion of the liquid [50].

Except for water, and some multihydroxy molecules, the thermal conductivities of most liquids decrease with temperature. Below or near the normal boiling point, the decrease is linear and often represented over small temperature ranges. The variation in thermal conductivity with temperature can be represented by:

$$\lambda_L = A - BT \tag{1- 9}$$

Where λ_L is the liquid thermal conductivity in W/m^{-1} K^{-1} and A and B are parameters that depend on the liquid and B generally ranges in between 1 to 3×10^{-4} W/(m.K^2) [51]. For a wider temperatures (higher than 150°C) [51,52], Reidel (1951) proposed the following relationship [51].

$$\lambda_L = B[3 + 20(1 - T_r)]^{2/3} \tag{1- 10}$$

Where T_r is the reduced temperature, which is defined as the ratio of the temperature of the sample over its critical temperature.

Although not suited for water, glycerol, glycols, hydrogen, or helium, Jamieson (1971) indicates that equation (1- 9) represented well the variation of λ_L with temperature for a wide range of compounds. While, few data for λ_L exist over the temperature range from near the melting point to near the critical point, for those that are available, Jamieson (1979) has found that neither (1- 9) nor (1- 10) is suitable, and he recommends:

$$\lambda_L = A(1 + B\tau^{\frac{1}{3}} + \tau^{\frac{2}{3}} + D\tau) \tag{1- 11}$$

Where A, B, C, and D are constants and $\tau = 1 - T_r$. For no associating liquids, $C = 1 - 3B$ and, $D = 3B$.

As liquids can be considered as incompressible in nature and at moderate pressures (5 to 6 MPa), the effect of pressure on the λ_L is usually neglected and it can be expressed only as a function of temperature, except near the critical point where the liquid behaves more like a dense gas than a liquid. Therefore, the effect of pressure is not considered in the remainder of this work.

1.4. Other relevant properties affecting heat transfer

Besides thermal conductivity, heat capacity, thermal diffusivity, and thermal effusivity are other important variables in heat transfer analysis. They affect how much heat is transferred and the resulting changes in temperature.

Heat capacity and specific heat

Heat capacity, usually denoted by a capital C (in $J.K^{-1}$), of a substance is the amount of heat ΔQ required to raise its temperature by ΔT and is defined as:

$$C = \frac{\Delta Q}{\Delta T} \qquad (1\text{-}12)$$

The heat capacity is therefore an extensive variable, meaning that it is dependent of the size/mass of the sample. In other words, a large quantity of matter will have proportionally a large heat capacity.

A more exact quantity is the specific heat (also called specific heat capacity), which is the amount of heat energy required to raise the temperature of a substance per unit of mass. Specific heat is therefore an intensive variable (independent of the size of the sample). The specific heat (denoted by Cp) of a substance is expressed in $J.kg^{-1}.K^{-1}$ and is defined as:

$$Cp = \frac{1}{m}\frac{\Delta Q}{\Delta T} \qquad (1\text{-}13)$$

Where ΔQ represents the amount of heat needed to uniformly raise the temperature of the sample by a small increment ΔT.

Thermal diffusivity

Thermal diffusivity noted β (in $m^2.s^{-1}$) a measure of how quickly heat diffuses through a material. It measures heat transfer rate of a material from the hot end to the cold end and is therefore related to the material's ability to conduct heat (thermal conductivity) and on its ability to accumulate heat (specific heat capacity):

$$\beta = \frac{\lambda}{\rho Cp} \qquad (1\text{-}14)$$

Where λ *is* thermal conductivity, ρ is the density in kg/m^3 and Cp is the specific heat capacity in $J.kg^{-1}.K^{-1}$.

Materials with large β value will respond quickly to changes in their thermal environment, while materials with small β value will respond more slowly, taking longer to reach a new equilibrium condition.

Thermal effusivity

Thermal effusivity reflects the capacity of a material to absorb heat from the surrounding environment. It is therefore the contribution of the thermal conductivity (λ) and the specific heat capacity (Cp). The greater the thermal conductivity, the greater the contribution of heat from the surrounding medium to the material. Thermal effusivity is expressed *in* $J/s^{1/2}.m^2.K$ as follows:

$$e = \sqrt{\lambda(\rho Cp)} \quad (1\text{-}15)$$

Materials with high thermal effusivity can quickly transfer heat between different components and surfaces, which is essential for maintaining optimal operating conditions.

1.5. Techniques for λ_L measurement

There are two basic techniques for measuring liquid's thermal conductivity (λ_L): steady-state and transient methods. The most distinctive feature between the two categories is the variation in time and temperature distribution. The steady-state method measures thermal properties when a thermal equilibrium is reached and maintained, in other words by establishing a temperature difference that does not change with time, while transient techniques are measured by monitoring temperature changes over time while the system reaches thermal equilibrium. The two strategies are detailed hereafter.

1.5.1. Steady state methods

These methods are based on the steady-state heat flow equation (Fourier's law of heat conduction equation), with the assumption that the system is at equilibrium. In practice, a heat flux is applied and transferred through the material having a surface A, following a perpendicular heat flow direction. Then, the temperature is measured at different points using one or more thermocouples. Knowing the distance between thermocouple and the heat source, thermal conductivity can be determined. The most common steady-state technique for liquids is the parallel plate method.

1.5.1.1. Parallel plate method

First relative measurements with the parallel-plate technique were performed by Christiansen [53] for gases, liquids, and solid bodies in 1881. The conventional schematic experimental setup for the steady state parallel plate is shown in Figure 4.The parallel-plate instrument was designed to fulfill as close as possible the ideal one-dimensional form of the Fourier law of heat conduction. To measure the heat transfer, a fluid sample is placed in a narrow gap between two circular copper plates with a fixed temperature difference. The top plate is heated to create a temperature gradient across the fluid, and the amount of heat transfer is measured once the temperature stabilizes. The O-rings and guard plates are used to minimize parasitic heat flows as much as possible [54]**,** a glass spacer is used to control the distance between the upper copper plate and the lower plate. Nonetheless, radiative heat is still present**.**

The thermal conductivity of the fluid between the plates is deduced from the linearized version of the Fourier law of heat conduction:

$$\lambda = \frac{\mathrm{d}}{A}\frac{P_g}{\Delta T} \quad (1\text{-}16)$$

Where P_g is the power generated (in W) in the upper plate to maintain a stationary temperature difference ΔT (in K) across the fluid layer, d the thickness (in m) between the upper and the lower plates, A the effective area of the upper plate (in m^2).

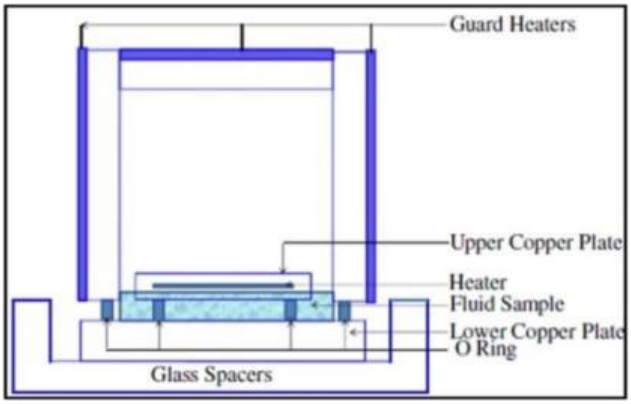

Figure 4 :Experimental set up of the parallel plate method (reproduced from ref [55]).

Further developments focused on uncertainties due to convective and radiative heat transfer, by reducing the layer thickness and the applied temperature gradient. In consequence, most parallel-plate instruments found in literature were exclusively designed for studying systems such as fluids at atmospheric [56,57] or high pressures [58] with uncertainties ranging from 1 to 5%. Rausch *et al*. [59] used a variant of this technique adding to the cell supplementary guard space systems to minimize parasitic heat flows due to convection, radiation (for instance fans), or heat leakages as well as the automated measurement and system controls allowing convenient and accurate measurements, which represent major improvements of the instrument. The challenge with these techniques lies in creating the cell with great care. The two plates must be placed exactly on a horizontal axis to reduce errors due to convection, and the space between them should be kept as small as possible. Also, using this method requires paying close attention to the radiation emissivity of the plates and other heat losses.

The steady-state methods require a constant temperature gradient in the sample under test, which results in longer measurements delays in comparison with transient methods. Furthermore, parasitic heat losses and thermal conduction through temperature sensor wires must be accounted for when calculating the thermal conductivity from steady-state measurements. The transient state techniques, on the other hand, are frequently faster and lasts only a few minutes or even seconds. The main benefit is the almost total elimination of radiation losses and natural convection, which makes experimental methods much simpler. Therefore, the use of transient techniques is suggested for this study.

1.5.2. Transient methods

Transient methods involve measuring the rate of temperature change in a material (liquid or solid) over time after a thermal perturbation is introduced. Thermal conductivity can be measured using a wire or sensor that is heated to a constant temperature and placed in contact with the material being tested, or by introducing a pulse of light or an electrical discharge. The ability to measure in a very short amount of time, while the heating process takes place, is a key component of these methods [60]. Several of the most known methods are briefly described below.

1.5.2.1. Transient hot-wire method (THW)

Nowadays the hot wire method is known as the reference method for measuring thermal conductivity of liquids and gases [61]. In 1962, THW was firstly suggested by Horrocks and McLaughlin [62], further it was improved by Kestin and Wakeham [63] and Nagasaka [64]. Currently THW is the mostly widely used method to measure accurate absolute values of thermal conductivities.

This method uses a platinum wire as both a heat source and a temperature sensor [65–67]. The platinum wire is immersed axially in a cylindrical container filled with the sample being tested, and an electrical pulse is sent through the wire, which heats up the sample. The higher the thermal conductivity of the sample, the less the wire's temperature will rise. Once the heat is entirely stored in the liquid the heat losses occur at the outer boundary of the wire and its temperature becomes constant. A derivation of Fourier's law and temperature data are used to determine thermal conductivity:

$$\Delta T(r,t) = \frac{q_w}{4\pi\lambda}\ln\left(\frac{4t\beta}{r^2 C}\right) \quad (1\text{-}17)$$

Where $\Delta T(r,t)$ represents the change in temperature (ΔT) as a function of radial distance (r) and time (t), q_w is the constant quantity of heat production per unit time and per unit length of the heating wire (in W.m^{-1}), λ is the thermal conductivity, β the thermal diffusivity, r is the radius of the wire and C=exp(γ) = with γ=0.57772 is the Eurler's constant.

Experimentally, thermal conductivity can be deduced by plotting temperature versus time (from the linear part of the curve): according to equation (1- 17) plotting the temperature difference $\Delta T(t)$ with respect to the natural logarithm of the measurement time ln(t) results in a slope $s = \frac{q_w}{4\pi\lambda}$ (1- 18) and the term $\left(\frac{r^2 C}{4\beta}\right) << 1$ as well as the wire's radius are negligible so they are not considered. Consequently, the thermal conductivity can be deduced as follows:

$$\lambda = \frac{q_w}{4\pi s} \quad (1\text{-}18)$$

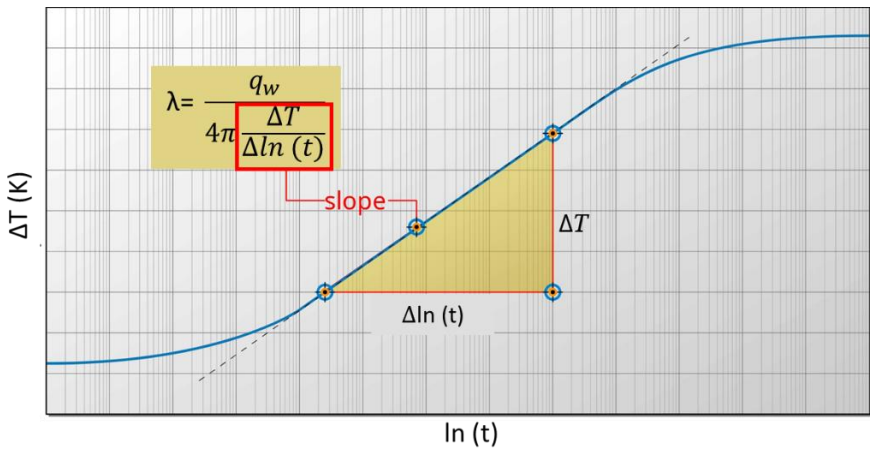

Figure 5: Example of temperature curve obtained with the hot wire method (reproduced from ref [68]).

Two components can be also used to generate the heat and to monitor temperature changes: a heater, which is made of a resistive metal wire or film, and thermocouples, which are used for temperature sensing [69,70]. Nevertheless, due to the low thermal conductivities of liquids in comparison with solids or metals, the thermocouple must be placed very close to the heating element, or the duration of the measurements must be sufficiently long, both of which are challenging to implement. Other extensions of this method were proposed later. Figure 6 shows the illustration of the hot wire method used as a) single resistive element and the variation of this method b) separating the heater and the sensor.

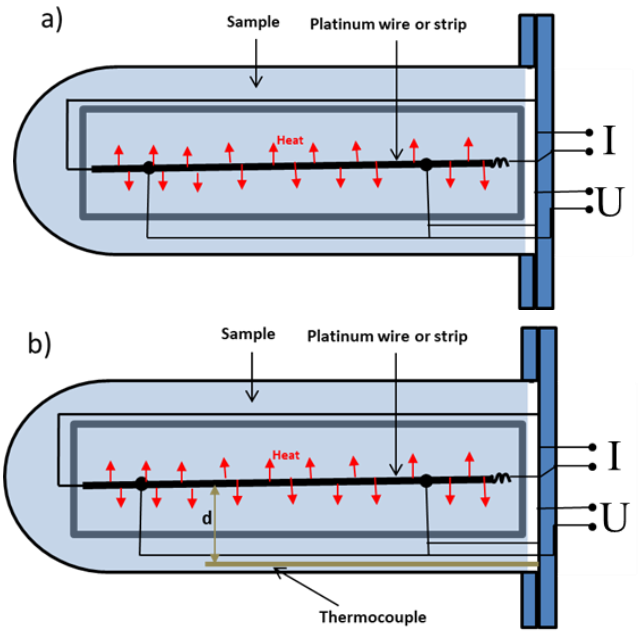

Figure 6: Schematic representation of a) the standard hot wire method and the b) parallel hot wire method adapted from ref [71].

1.5.2.2. Other methods based on the THW

Transient hot strip method (THS)

Instead of a wire, some authors proposed other geometries such as thin metallic sheet such as the transient hot strip (THS) method [65]. This alternative method uses the same principle that the THW method, but the advantages of this modification arise mainly from two factors: (1) due to the strip geometry, THS setup is easier to arrange than a THW setup as the strip is less fragile than a wire, being easier to manipulate. Also, (2) its greater surface/area and smaller thickness, leading to a lower density of heat flow and consequently a smaller thermal contact resistance to the sample.

Transient plane source (TPS) or hot disk method

Other proposals as double spirals with insulating materials have also been implemented such as transient plane source (TPS) method [65]. The original method and theory was developed in the 1980's by Gustafsson [72]. It is based on the THS technique for measuring thermal conductivity and diffusivity [73], which was developed for solids and liquids with low electrical conductivity. The TPS sensor or hot disk sensor is made of thin metal foil and its conducting pattern is a double spiral covered with two thin sheets of polyimide (Kapton), aluminum nitride, aluminum oxide, or mica, which act as a structural

support and electrical insulator. The hot disk is heated through an instantaneous electric pulse, which diffuses into the sample. The mean temperature of the sensor raises over time. The TPS method uses a geometry with higher surface contact than the hot strip or hot wire method, which are also more fragile, and temperature measurements can be performed with greater sensitivity and accuracy.

3ω method

Besides transient methods used to determine the thermal parameters, there are approaches based on harmonic (sinusoidal) excitation called the 3ω method [74]. The sensor acts both as a heat source and a temperature sensor. While the other techniques measure temperature in dependence of time, in the case of 3ω method, the metallic element of micrometer thickness is deposited on the surface of the material recording the amplitude and phase of the resistance depending on the frequency of the excitation.

The principle of this method consists in a heating element composed of a thin metallic layer (that plays the role of a resistance) in which an alternative electrical current is applied. Heat will be generated due to the Joule's effect and the power dissipated in the resistor (metallic layer) will have a frequency twice higher than the injected current. By measuring the voltage across of the resistance according to the Ohm law, the temperature oscillation amplitude can be deduced using the third harmonic voltage $V_{3\omega}$. However, the 3ω component will be overshadowed by the conventional ω component of a sinusoidal current. Therefore, to determine the 3ω component, a lock-in amplifier can be used. However, this technique requires supplementary instruments which can be costly, as well as complex installations for the measurement.

1.5.2.3. Measurement errors

When measuring thermal conductivity using transient and steady methods, heat losses caused by convection or radiation can lead to inaccuracies in the results [75]. Convection occurs when air flows around the sample, while radiation occurs when the sample is exposed to external heat sources or temperature differences. To minimize these losses, it is important to use a well-insulated setup, to reduce external heat transfer, and to maintain a controlled temperature conditions throughout the sample. Therefore, most measurements are conducted under vacuum with radiation shields to minimize heat losses from convection and radiation [76]. Besides the convection and radiation heat losses, another concern is the heat conduction through the thermocouple wires. It is therefore preferable to use thermocouples with small wire diameter (*e.g.* 0.25 mm [77]) and low thermal conductivity wires (*e.g.* chromel-constantan).

It can be difficult to measure thermal conductivity using large and additional equipment such as vacuums or modification of the experimental cell. However, the most effective way to deal with radiation heat loss is transient heating. Other alternatives, such as the use of smaller sensors and volumes are proposed. Thin films microsensors, created using microfabrication techniques, can effectively measure thermal conductivity [78,79]. Their low thermal resistance, due to their small thickness, allows for efficient heat transfer from the sensor to the sample. Additionally, they have less thermal mass than conventional sensors, requiring less heat energy to change their temperature, which lowers the system's overall thermal resistance [80]. They can be designed to take localized measurements, which minimizes errors and accurately captures thermal conductivity [80]. However, since convection and radiation occur when the sample is exposed to the environment, fluid

confinement can significantly reduce their effects. Overall, the combination of the fluid confinement and the use of miniaturized sensors can greatly reduce errors measurements. Some recent developments of such methods are described hereafter.

1.6. Miniaturization and integration of thermal conductivity of liquids (λ_L) measurement

The development of new, multifunctional systems with many integrated functions has been influenced by the advancement of contemporary technologies. Portable multiple-use devices are created by miniaturizing multifunctional systems (mechanical, fluidic, electromechanical, thermal, etc.). The technologies used to fabricate these miniaturized systems for heating and temperature sensing to determine thermal conductivity of liquids ($\lambda_{L.}$) are covered in more detail in the following section.

1.6.1. Micro-Electro-Mechanical Systems (MEMS)

The transistor, invented in 1947 by Bell Labs' John Bardeen and Walter Brattain, marked the beginning of a revolution in electrical engineering that has evolved to the current mainboard of a smartphone, which is full of what are now known as Micro-Electro-Mechanical Systems (MEMS). MEMS is a technology that uses semiconductor materials to fabricate mechanical components, sensors, actuators, and electronic elements, generally on silicon substrate [81] using microfabrication techniques. This technology has become significantly more diverse, being manufactured for chemical, biological, and biomedical applications [82,83].

These systems are capable of microscale sensing, control, and actuation operations that can be carried out individually or in bulk. Very small size (tens or hundreds of microns), low power consumption, low cost, ease of integration into systems, high resistance to vibration, and radiation, batch fabrication in large arrays, are some of the benefits of MEMS devices. MEMS is the term used most frequently in the United States, whereas "Micro-systems Technology" or "micro-machined devices" are used in some other countries. Nevertheless, the term is now frequently used to refer to a variety of miniature devices, typically 3D micro-structures, mostly fabricated from silicon and using techniques, which are often derived from the microelectronics industry. These include isotropic and anisotropic etching (“microengineering”), various thin film deposition methods, anodic bonding and the masking and doping techniques employed in integrated circuit manufacture. Today, silicon microsensors, “Laboratory-On-Chip (LOC)” and micro-TAS (micro-total analytical systems) devices are all referred to as MEMS.

Miniaturized structures, sensors, actuators, micro-structures and microelectronics are the functional components of MEMS (Figure 7), but the microsensors and microactuators are the most notable components. Microsensors and microactuators are categorized as transducers, which are devices converting a measured mechanical signal in electrical one. For instance, MEMS technology is used to manufacture different sensors for pressure, temperature, vibration, and chemical measurements.

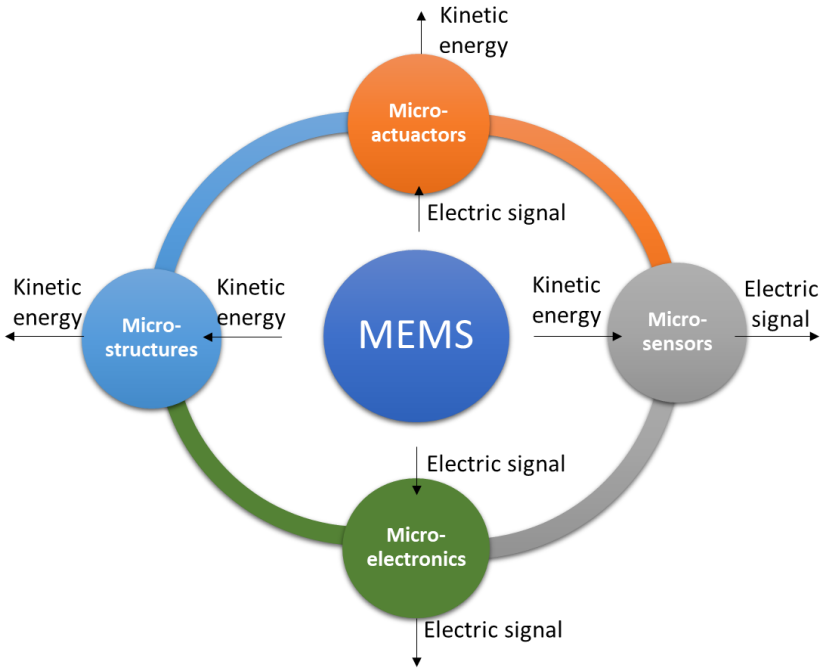

Figure 7: Main components of MEMS.

MEMS technology has enabled the physical size of calorimeters to be reduced when determining thermodynamic properties. Development and application of several MEMS calorimetric devices for liquid samples have been proposed. Chancellor *et al.* [84] and Olson *et al.* [85] presented micro-machined calorimeters that demonstrated measurement of enthalpy changes due to evaporation of water droplets. However, such devices require measurements in open environments without proper fluid confinement [84], which are sensitive to environmental disturbances and do not yield volume-specific information. Therefore, with the development of MEMS, a variety of applications evolved in chemical, biological, and biomedical research when fluid manipulation and confinement led to the separation of a new discipline – microfluidics.

1.6.2. Microfluidics

Microfluidics, considered as a subfield of MEMS, is the science of designing and manufacturing experimental devices that handle extremely small volumes of liquids (10^{-9} to 10^{-6} liters), by means of channels with dimensions ranging from tens to hundreds of micrometers. It is a field that is mainly driven by technological applications, the main vision being to develop entire bio/chemical laboratories on silicon or polymer microreactors.

Microfluidics has its origins in four distinct areas, namely microanalysis, biodefense, biology, and microelectronics. The oldest one is considered to be molecular analysis, which includes methods such as gas-phase chromatography (GPC) or capillary electrophoresis [86]. These techniques, developed from the 1950s and 60s, allow the separation of chemical compounds or biomolecules by flowing small amounts of a sample in narrow tubes or capillaries, reaching high sensitivity and resolution. The development of microfluidic systems was also motivated by the need to counter the threats posed by chemical and biological weapons after the cold war. The Defense Advanced Research Projects Agency (DARPA) supported programs in the 1990s to develop microfluidics systems for fast and *in situ*

detection. The third motivational force came from the field of molecular biology. The explosion of genomics in the 1980s and high-throughput DNA sequencing, required analytical methods with greater sensitivity and resolution than previously used in biology. One well-known example is the PCR (polymerase chain reaction) technique used to amplify a DNA sequence by means of heat was developed in the early 1980s by Kary Mullis [87]. Microelectronics made the fourth contribution to microfluidics. Initially, researchers tried to directly fit fabrication methods and materials from microelectronics to microfluidics; photolithography as well as silicon and glass were the first players on the microfluidics stage. Only later microfluidics split from microelectronics and semiconductors technology by using new specific microfabrication methods and materials microfluidics such as polymers [88].

Later, modern microfluidics grows into a Laboratory-On-Chip (LOC) concept because it integrates many functions and components such as valves, heaters, motors along with detection and sensory systems. Some examples can be mentioned; from fluid mixing, particle separation, DNA amplification, use of biosensors to additional electronics, and detection optics [89–91]. These devices integrate multiple fluidic functions on a chip, making operations easier to control and automate, while reducing the need for user intervention. They are cost-effective and disposable due to their size, materials, and simple assembly, allowing for the use of smaller reagent volumes, shorter reaction times, and parallel operations.

1.6.2.1. Microfluidics characteristics

Microfluidics studies the behavior of fluids in micro-volumes range, such as droplets or channels that are only a few micrometers in size. At this scale, hydrodynamics is somewhat different from the macroscopic world. For example, laminar flow is prevalent with respect to turbulent flow, as described by the Reynolds number, a ratio between inertial and viscous force components (equation (1- 19)).

$$Re = \frac{\rho v L}{\mu} \qquad (1\text{- }19)$$

Where ρ is the density, v the flow velocity, L the characteristic length and μ the viscosity. The smaller this number, the less the inertia affects the fluid behavior.

Another implication of the small sizes involves the surface tension, energy dissipation, and fluidic resistance start to dominate the system. One characteristic of microscale devices is the high Surface Area to Volume ratio (SAV). For instance, the small dimensions of microfluidic channels allow for a higher degree of heat transfer due to the increased surface area that can be in contact with the fluid. This results in a faster and more efficient exchange of heat between the fluid and the surrounding environment

Finally, the numbering-up approach, also known as an increase in the throughput of microreactors, is a typical scaling-up technique that involves the arrangement of several identical channels or microreactors in parallel. Higher flexibility in terms of selecting different experimental conditions or reproducibility between experiments results from an increase in the number of units. In comparison to macroscopic systems, wider operating conditions can be achieved by microreactors.

1.6.2.2. Microfluidics for harsh conditions

Microfluidic devices are fabricated from a range of materials including glass, polymer, metals, ceramics, silicon, quartz, applying techniques such as photolithography, laser ablation, micromachining, dry and wet chemical etching etc.

Much of the exploratory research in microfluidic systems has been carried out with a polymer — poly(dimethylsiloxane), or PDMS [92,93]. PDMS is an optically transparent, soft elastomer. It is a popular material for testing new concepts and for early-stage research engineering due to its ease of use and ability to support useful components such as pneumatic valves. However, microelectronic technologies have been indispensable for the development of microfluidics, and as the field has developed, glass, and silicon have become crucial materials for producing systems that need to withstand harsh chemicals and high temperatures. The silicon processing technology provided the fabrication techniques for different structures at micro and sub microscale such as microchannel, mixers, droplet generators, filters and valves. Silicon and glass both have very good stability and non-reactivity, which make them suitable to use with different materials.

Microfluidic systems etched into a glass plate and closed by a second glass plate (glass-to-glass microsystems) are manufactured by HF (hydrofluoric acid) etching or BOE (Buffer Oxide Etch, NH_4F-buffered HF solution) [94]. The individual parts are then bonded together by thermal bonding (fusion). Glass-to-glass microfluidic systems can work at pressures up to 400 bar at room temperatures under specific designs [95]. The main drawback is its low λ (on the order of 1 $W.m^{-1}.K^{-1}$). This may slow down rapid temperature changes and cause the microsystem to have thermal inhomogeneity. Optical access, ease of manufacture and commercial availability mean that glass-glass microsystems are widely used at room temperature for pressures below 50 bar.

Microfluidic systems etched into a silicon plate and closed with a borosilicate glass (silicon-borosilicate glass microfluidics Figure 8) plate *via* anodic bonding have many advantages. Silicon's high λ (148 $W.m^{-1}.K^{-1}$) allows for fast and efficient heat transfer in microfluidic systems, enabling precise temperature control of the fluid and the surrounding environment and even distribution of heat throughout the system. Additionally, silicon is a suitable material for microfluidic devices because it has good surface stability, is versatile for use with various solvents and chemicals, and has a low coefficient of thermal expansion [96]. This means it can be used without introducing thermal stresses that may cause deformations or mechanical failure, ensuring precise control over fluid flow and volume for accurate and reliable microfluidic devices. The mechanical strength of the bonding enables high pressure and temperature conditions to be reached [35] (300 bar and 400 °C, for example, always on specific designs). Borosilicate glasses transparency makes direct observation possible. As a result, silicon-borosilicate glass microsystems can be used in wide ranges of pressures and temperatures and are compatible with a wide range of chemicals.

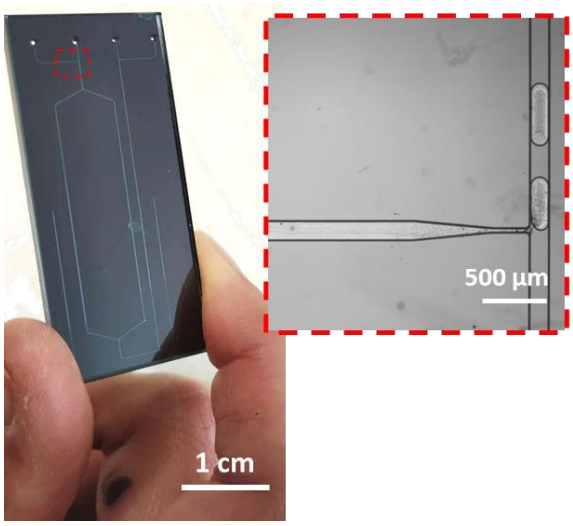

Figure 8: Image of a microfluidic device silicon-borosilicate with a zoom of a T-shape droplet generator (red frame).

To fabricate and etch fluidic geometries from glass or silicon, photolithography along with wet etching techniques are used. The flexibility in geometry enables multiple experiments to be done. For instance, in mixing [97,98], separation, droplets formation [99,100], confinement, localized measurements using sensors [101,102] etc. Being planar and on the same scale as semiconductor integrated circuits, microfluidic devices are ideal for integration with electronic or optical components such as sensors, actuators, and control logic. Significant progress has been made for sensing methods: chemical, electrical, flow, temperature, and pressure sensors. Numerous actuators, such as heating elements, and electrodes for electrokinetic flow, have also been demonstrated.

1.6.3. Existing temperature heating and sensing in microfluidics

Temperature is an environmental parameter that regulates most physical, chemical, and biological processes that can affect the results of experiments involving these processes. In microfluidic devices, the temperature of a liquid in a channel or chamber can vary over time and space, which can affect the outcomes of experiments. One crucial aspect of microfluidics is the ability to precisely control the temperature of the system. This is typically achieved using some form of heating element or temperature sensing element. In the following section, the existing types of temperature heating and sensing elements in microfluidics and their applications is detailed.

1.6.3.1. Heating elements

The development of LOC requires the integration of multiple functions within a compact platform that can produce high throughput data. One of these functionalities is the control of temperature, which can be done with high accuracy using either a temperature profile (homogeneous or gradient) or a temperature range. Multiple studies, involving heating/cooling or external methods such as the use of microscopic Peltier or pre-heated liquids [103,104], flowing through the microsystem have been used. These technologies allow for consistent temperature control throughout a microsystem, but they are not fully integrated, which could limit their usefulness in certain applications. Other technologies have been developed using Joule heating [105–109], microwaves [110–112], integrated wires, and lasers [40,113–115]; these can be used at high temperatures at localized spots in the microsystems.

For practical reasons, resistive heaters (Joule heating) are suitable for most of the applications as they are reliable and simple to implement in a broad set of well-established microfabrication processes [107]. An integrated heaters in a microsystem can produce temperature differences up to hundreds of Kelvins. Due to their small mass and optimized geometry to reduce thermal losses, most micro heaters have a fast response time (order of µs to ms) and low power consumption.

1.6.3.2. Temperature sensing

All the temperature measurement techniques can be divided into two groups based on the type of contact that exists between the thermometers and the liquid medium of interest: noninvasive and invasive thermometry.

Remote temperature measurement is possible thanks to non-invasive thermometry, which is provided by an infrared thermometer. However, because only surface temperature is measured rather than the internal temperature of the targeted medium, it does not always fulfil the requirements for response time and measurement accuracy.

Invasive thermometry is the most common type of temperature measurement, which involves placing thermometers inside the targeted medium. Various types of thermometers such as thermocouples (TC) and resistive temperature detectors (RTD) are used for this method. Thin film thermopiles are also invasive thermometer made up of smaller thin film thermocouple (TFCs), while diodes are another type of thermometer that generates large voltage signals but requires a power supply to heat up during measurement. Both types can be produced using standard micro-nano processing technology. However, the most accurate and cost-effective sensors are still TFTCs and RTDs due to their high sensitivity and accuracy. These two types of sensors are detailed below.

- **Thermocouples**

A thermocouple is a typical thermometer that produces temperature-dependent voltages. They are not frequently used in microfluidics and typically take the form of manually inserted commercial milli-thermocouples or smaller thin TFTCs. Thermocouples offer stable performances with a quick dynamic response time, high accuracy, and exceptional material flexibility.

A thermocouple is a sensor that converts thermal energy into electrical energy and is constructed by connecting wires of dissimilar metals together at a junction. The junction temperature change causes a stress that produces an electromotive force (EMF) and a small measurable voltage, known as the Seebeck effect [116,117]. The magnitude of the voltage depends on the temperature change and the properties of the two metals. A schematic representation of a thermocouple is proposed Figure 9 in which the right wire connection (known as the hot junction) experiences a temperature increase, and the temperature difference is displayed on the voltmeter (on the left). Since the generated EMF in the thermocouple circuit is very small (measured in millivolts), it must be measured with a very sensitive instrument, voltage balancing potentiometers and galvanometers are normally used [118].

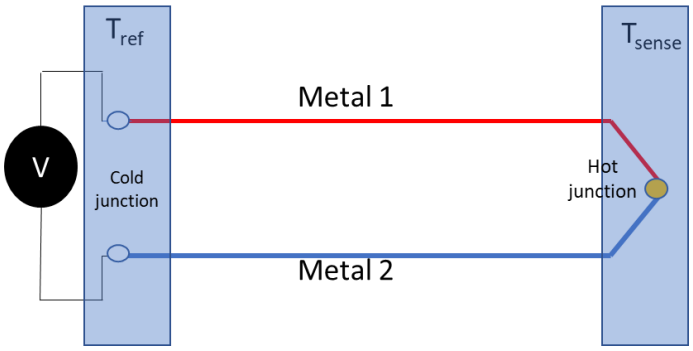

Figure 9: Schematic representation of a thermocouple.

The temperature range and the precision could therefore change depending on metals used for the thermocouple. The choice of a thermocouple usually depends on the temperature range measurement required by the application. Other considerations include temperature accuracy, durability, usage conditions, and expected lifetime.

Different metal combinations were investigated and classified into eight types of thermocouples: B, E, J, N, K, R, T, and S types [117]. Figure 10 displays the voltage responses range properties for some thermocouples.

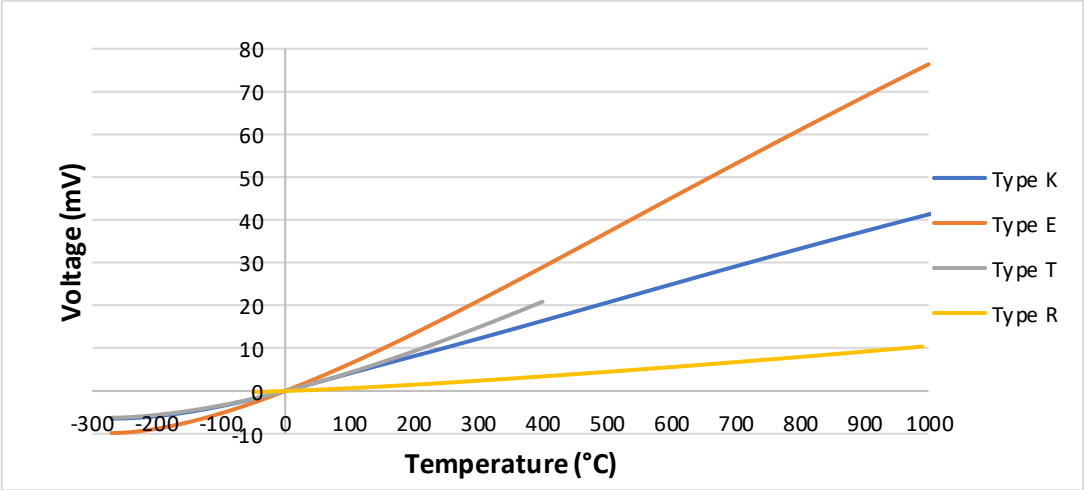

Figure 10: Voltage variation in function of temperature for different thermocouples.

Alloys are mixtures containing at least one majority metal. Some of the thermocouples mentioned earlier are made from the following alloys: chromel is made of approximately 90% nickel and 10% chromium, alumel is made of 95% nickel, 2% aluminum, 2% manganese, and 1% silicon, constantan is made of 55% copper and 45% nickel.

As shown in Figure 10, some of the couples reported in the literature for having interesting properties are the following: Type K (Chromel/Alumel), which has a reliable and precise for temperatures going up to 1000 °C, type E (Chromel/Constantan) temperature range from T < 0 and T > 1000°C. It generates the highest output voltage per degree compared to all other thermocouple types, type T, (Copper/Constantan) being stable at low temperatures from -180 to 300°C. More precise at lower

temperatures. Its temperature range is limited to 370°C and Type R (Pt/Pt-Rhodium 13%) recommended for high-temperature applications with a signal linearity from 0 to 1600°C.

Thermocouple drift within a few hours of use and are less accurate than RTDs [119]. Another disadvantage is the potential difference across the junction, which is very small (in the range of a few tens of $\mu V.°C^{-1}$) similar to the potential formed at parasitic junctions. As a result, parasitic junctions that are unintentionally formed in the circuit add to the potential difference and can cause errors in temperature measurement. Also, the response of thermocouple is not linear and can be described by complex polynomial equations [120] . This non-linearity can produce significant measurement errors when using a linear approximation of the Seebeck effect [120]. Their need of frequent recalibration, the parasitic junction measurement system necessary and their limited accuracy render this kind of sensor difficult to implement for wide range of applications [120].

- **Resistance Temperature Detector (RTD)**

RTDs sensors are based on its electrical resistances change with temperature variations. They are simple to fabricate and have a high thermal sensitivity. These sensors are deposited on a wafer or a glass surface *via* sputtering or a thin film evaporation process.

Resistance Temperature Detector (RTD) is usually made of pure metal, usually platinum, nickel or copper. As an electric current flows through the RTD, its energy is converted into heat *via* the Joule effect or resistive heating. The Joule's heating formula is given by:

$$\mathrm{Q} = \mathrm{I}^2 \times \mathrm{R} \times \mathrm{t} \tag{1- 20}$$

Where Q is the amount of heat generated in Joules, I is the electric current in Ampere, R is the resistance offered by the circuit to the electric current flow in Ohms, t is the time the current is allowed to flow in the circuit expressed in seconds.

Joule heating, which causes metal resistance to rise with temperature, is primarily caused by collisions between electrons and phonons. Common platinum, copper or nickel RTD sensor have a linear relationship between resistance and temperature and range operating temperature is known as Temperature Coefficient Resistance (TCR). TCR is defined as the change in sensor resistance per degree of temperature.

When analyzing the behavior of the heated sensor during a transient recording, resulting from the Joule effect, it is convenient to express the time dependent resistance R(t) with the following expression:

$$R(t) = R_0[1 + \alpha \Delta T(t)] \tag{1- 21}$$

Where R_0 is the initial resistance of the hot wire and $\Delta T\ (t)$ is the time-dependent temperature variation of the sensor and α is the TCR expressed in K^{-1}.

$$\alpha = \frac{1}{R_0}\frac{\Delta R}{\Delta T} \tag{1- 22}$$

In Table 1, TCR values for different materials are given. A higher TCR means that the resistance change is larger for the same temperature increase and can, therefore, be beneficial for temperature sensing. Pt is often the material of choice as it demonstrates the most stable and linear temperature dependance and the greatest repeatability and stability over long periods of time.

Table 1: temperature coefficient of resistance of pure metals [112].

Material	TCR (ppm/°C)
Aluminum	4200
Copper	4300
Gold	4000
Nickel	6800
Platinum	3927

Thin-film semiconductors or metals with a polycrystalline structure [121,122] are frequently used for microheaters and/or sensors. Due to their polycrystalline nature, thin films have some disadvantages, such as degradation caused by temperature. Their material properties are different from those in bulk form and are harder to model, making them dependent on the fabrication process. As a result, even if the material structure is the same, its properties can vary significantly depending on the process. Therefore, it is important to identify a heater that can be integrated with electronics and maintain its stable, well-defined properties when in thin film form and over a wide temperature range.

With the proper design, it is possible to use pure resistive metals produced through thin film deposition for both heating and sensing purposes, as reported in some examples in the literature [123,124]. As a result, only one single element could be used to detect and to generate temperature changes inside de microfluidic device.

There are important criteria to consider when resizing in a microliter scale or in microfluidics that are not considered when using conventional methods. For example, the geometry and the fragility of the hot wire method would generate complications when measuring λ_L [125,126]. Also, the geometry and the materials used for the conception of the sensor are important. Indeed, the thickness of the film deposited or even the property of the material for the conception have been shown to have an effect on the λ_L measurement [127,128]. Other criteria, external to the technique itself may be considered, such as the equipment cost or the implementation difficulty. Micro-sizes and microfluidics approaches to determine λ_L will be discussed in the following section.

1.6.4. Micro-sized approaches for thermal conductivity of liquids (λ_L) measurement

λ_L provides relevant information for many industrial processes, product development and design or quality control. As previously discussed, numerous strategies have been developed to measure the thermal properties of fluids, but in general, these macroscopic approaches involve milliliters to centiliters sample volumes creating additional cost and availability of a certain amount of sample. Therefore, the demand of micro/nanoscale thermal analysis is significantly increasing as it reduces samples consumption and can be employed in real-time process diagnostics [85,129]. In this regard, we will focus on the existing miniaturized methods to determine λ_L. They are divided into two categories: micro-sized λ_L measurement techniques, in which the sample is in an open environment

without confinement or manipulation of fluids and on the other hand, by microfluidics, where the fluid is confined and can be manipulated through micro-channels.

Some researchers have developed various micro-sized methods for the measurement of λ_L. Generally, a heat pulse is applied to the sample and the resulting temperature response is recorded. In some micro-size methods, a separated heating element and temperature sensors are used, which leads to a separated control and read-out devices [40,130]. Traditionally, miniature thermocouple is used for temperature sensing. In order to reduce heat losses, a more sophisticated method of localized heating with a laser can be used, combined with a thermocouple temperature sensor [40]. For instance, Choi *et al.* [40] proposed a novel method based on laser heating of a microthermocouple tip, and the real-time temperature response is detected by a thermocouple. The thermocouple used is a commercial product from OMEGA (E-type, CHROMEGA®/Constantan), 46 µm long and 25 µm diameter. The thermocouple is immersed in the sample and heated directly by the laser, which is localized on the thermocouple as shown in Figure 11. However, the non-uniformity of the thermocouple tip shape leads to an uncertainty up to 10% in determining the λ_L.

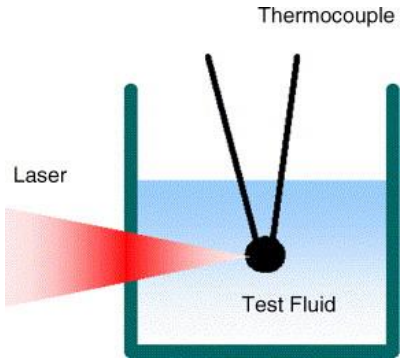

Figure 11: principle of the laser point heating thermometry (reproduced from ref. [40]).

Gustavosson *et al*. [131] demonstrated that it is possible to determine the thermal conductivity of conventional liquids and nanofluids in a microliter-sized sample. Here, the authors developed a device based on the hot strip method where a single liquid droplet is required to do the measurement. The schematic fabrication process is displayed in Figure 12 a). A PDMS block with a small hole was used to control the volume and the shape of the liquid droplet Figure 12 b). Photolithography was used to pattern the strip. Then, a Cr/Pt/Cr sandwich layer was deposited by electron beam evaporation with respective thickness of 5 nm, 50 nm and 5 nm. The upper chromium layer was used to ensure a better adhesion of the SiO_2 cover layer and the platinum electrodes. A Platinum strips of 2 mm long and 80 µm wide was fabricated. The Pt strip served both as heating and sensing elements, once the fluid was deposited, the temperature variation of the strip was recorded by applying a constant current and monitoring the resistivity changes with time. To record these changes, both current injection and voltage measurements were performed using a voltmeter (Agilent 34410A) and a function generator (Agilent 33220A) linked to a homemade current source. The THS methods uses the linear dependence of the increased temperature on the logarithm of time. λ_L was deduced from the strip resistivity rise as a function of time, allowing to deduce the slope between the curve *temperature versus logarithm of time* plot. The measurements have been performed successfully to determine λ_L samples of only 20 µL [132].

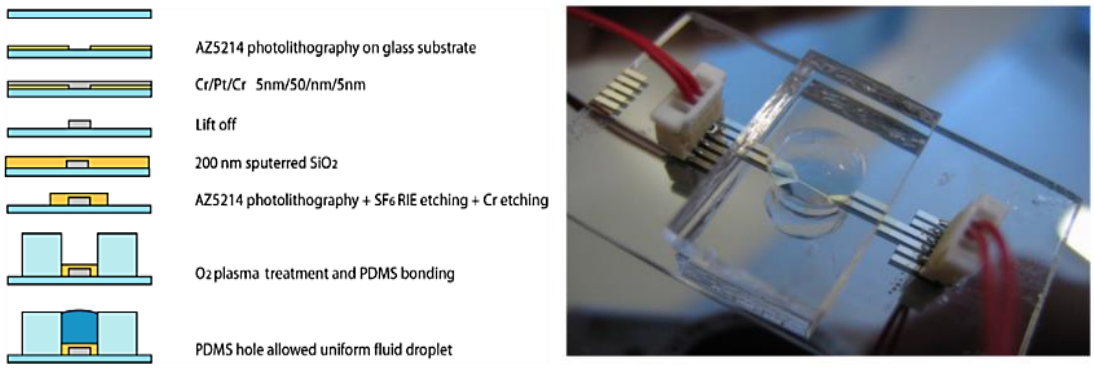

Figure 12: a) Schematic presentation of the THS devices fabrication process and b) Image of the THS device with a water droplet confined in the open hole (reproduced from ref. [132]).

In the same year, another micro-sized λ_L method was suggested. Labelled "3ω method", it is based on sinusoidal heating, with a simple sensor design such as the hot-strip sensor. This method has been employed by Choi and Kim [30]. The measuring device consists of a metallic strip and a dielectric thin film deposited on the surface of a borosilicate glass substrate. Using an e-beam evaporator, a 30 nm thick chromium film was deposited as an adhesion layer, followed by a 300-nm-thick gold film. The metals were then patterned, using photolithography to create a 20 µm wide and 1mm long strip. After that, a 200-nm-thick silicon nitride film was deposited on the substrate by plasma enhanced chemical vapor deposition (PECVD) to provide electrical insulation between the metallic strip and the surrounding liquid. Measurements were conducted by immersing the measuring device in a bath of the liquid sample.

Beside the conventional equipment to generate and detect the temperature changes in the strip, a supplementary equipment such as a lock in amplifier was used to amplify the signal to detect the 3 *ω component* of the signal, which is 1000 times smaller than the *ω* component. λ_L is determined by the slope between the curve of the *temperature versus ln ω* plot. This approach demonstrated that it is possible to determine λ_L using volumes as small as 1µl. In addition, a mathematical model was proposed to determine simultaneously heat capacity and λ_L. The results also showed important uncertainties (11%) of compounds with low λ_L (Figure 13 b). They assumed it was because the liquid was exposed to environmental disturbances, which resulted in small heat flows into the liquid, potentially causing heat losses due to heat transfer phenomena [30].

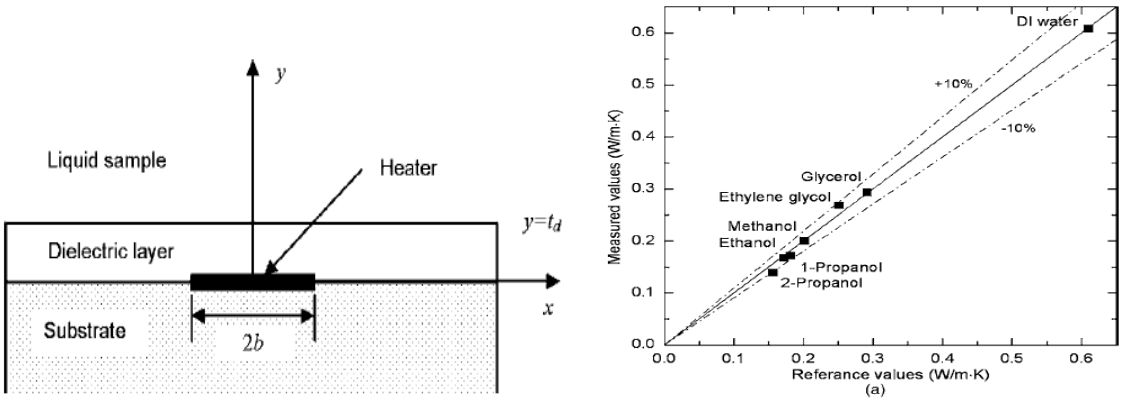

Figure 13: Schematic diagram of the 3 ω technique for measuring thermal conductivity of liquids and b) Experimental results of the thermal conductivity (reproduced from ref [30]).

Since 2007, there has been a shift in the methods used to measure thermal conductivity. Instead of depositing a small amount of liquid on a sensor, the use of microfluidics became more popular. Microfluidics allows for better control over flow rates and temperature gradients, resulting in more accurate measurements. In contrast, with micro volumes deposited on a surface, it can be challenging to control and maintain a stable temperature gradient throughout the sample.

1.6.4.1. Thermal conductivity of liquids (λ_L) measurement at different temperatures

While all previous studies described the measurement of λ microscale fluid volumes at room temperature, very few studies reported how this property varied with temperature [133] using micro volumes. λ_L is highly influenced by temperature; however, little research has been done so far at the micro scale.

Roy-Panzer *et al.* [134] investigated the application of 3ω method to the measurement of temperature-dependent λ of small volumes fluids. In this study, the measurement devices consist of metal heater patterned on a fused silica substrate using lift-off photolithography, obtained by depositing a 5 nm titanium adhesion layer that was 5 nm thick and a 60 nm thick platinum layer. They used 2 µl droplets for the conductivity measurement of deionized water (DI) and salt buffer solution, while a volume of 15 µl was used for a silicone oil at temperatures ranging from 24 °C to 80 °C. These respective volumes were chosen based on the rate of evaporation at elevated temperatures during the temperature-dependent measurement. To prevent evaporation of the DI water and salt buffer solutions, 20 µl of mineral oil is placed on top of the droplets. λ_L was deduced from a mathematical algorithm (least square method) applied on the curve of the *temperature versus ln ω* plot. They found an excellent agreement for each sample, with errors below 1% (Figure 14).

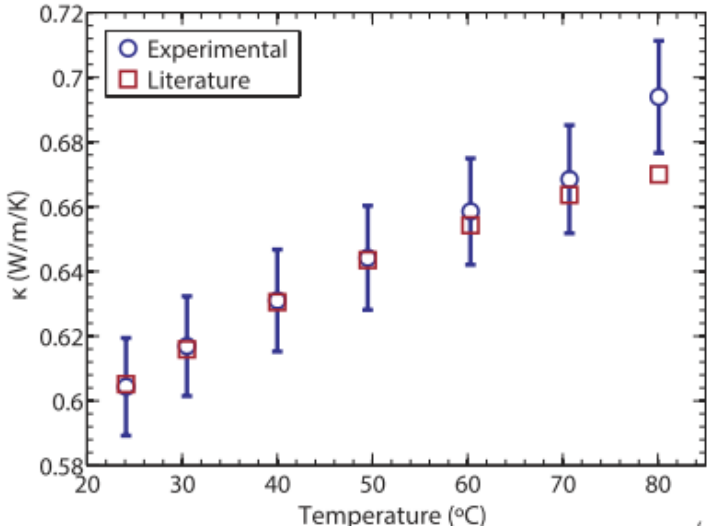

Figure 14: Temperature-dependent thermal conductivity DI water, with comparison to literature values (reproduced from ref. [134]).

1.6.5. Microfluidics approaches for thermal conductivity of liquids (λ_L) measurement

We have seen from the previous works that exposing the sample to the environment can lead to significant uncertainties and that it may also be impractical if the small volumes of liquid cannot be manipulated in a precise manner. Microfluidics can help to overcome these issues. Nevertheless, in both micro-sized methods and microfluidics there is also a significant challenge posed by the reduction of sample volume: the thermal penetration depth (or probing depth) [69,135]. It determines how far the heating energy travels from the sensor to the specimens, indicating how deeply the single element method records the thermal properties of the sample.

This limitation was not present in the sensor designs of Gustavosson *et al.* [131], whereby a temperature sensor was placed at a known fixed position from the source. Also Choi and Kim [30] did not consider the effects of the finite thickness and length of the heater.

In 2008, Choi *et al*. [41] proposed the same technique as that used in 2007 based on the 3ω method modified for use with liquids in microchannels, allowing for continuous flow, while limiting the liquid exposure to the environment. Not only this method measures simultaneously λ_L and heat capacity but also, considers the thermal penetration depth. As shown in Figure 15, the measuring device consists of a PDMS microchannel, and a gold/chrome (Au/Cr) thin-film strip deposited on a borosilicate glass substrate. The width and length of the metallic strip are 20 µm and 1 mm, respectively. To demonstrate the issue of penetration depth, a simulation of the thermal responses was carried out, showing the distribution of temperature oscillation in the measuring device.

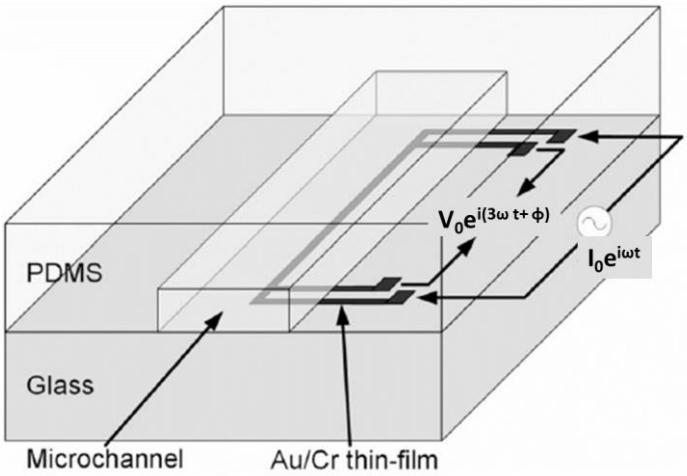

Figure 15: Schematic diagram of the sensor. The two current pads supply an AC of amplitude I_0 and frequency ω. Then the 3ω voltage is generated with amplitude V_0 and phase delay (reproduced from ref. [41]).

Figure 16 indicates that heat conduction through the boundaries of the microchannel modifies temperature. In other words, if the thermal wave penetrates the microchannel, the sensitivity is affected by the cell size and decreases with the thermal penetration depth. λ_L and heat capacity were deduced from a mathematical algorithm (least square method) applied on the curve of the *temperature versus ln ω* plot. The authors highly reduced the volume and uncertainties to reach 12 nanoliters and 5%, respectively. Yet, the required read out hardware for this method remains complex.

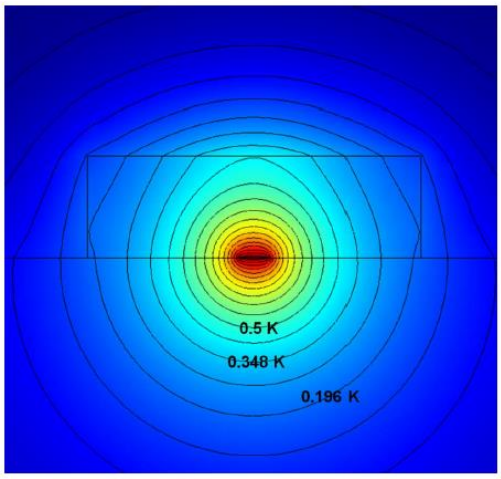

Figure 16: Distribution of the in-phase temperature oscillation in the microfluidic (reproduced from ref. [41]).

More recently, Ouderbrouckx *et al.* [42] a novel method based on the Transient Plane Source (TPS) principle, showing the possibility to eliminate uncertainties of probing depth. The authors used aluminum as a highly thermally conductive material that could act as heat sink to eliminate uncertainties encountered in micro-scale systems. In their work, they deliberately applied thermal pulses that exceeded the liquid's physical boundaries inside the microchannel, while staying within the limits of the aluminum top reference. As shown in Figure 17 (a) at the bottom, a polymethyl

methacrylate (PMMA) plate is used as a support for the flexible 40 µm thick polyimide substrate on which the sensor structure is present. The dimensions of the copper structure, shown in Figure 17 (b), is 5 mm X 1.3 mm. The height of the track is 15 µm while the width and spacing are both 60 µm. The total volume of the cylindrical fluid is 2.76 µl. The sensor is placed on the PMMA plate with the copper facing down to prevent electrical short circuits caused by fluids in the microchannel. A polyimide substrate is used as an electrical insulation layer between the metal structure and the fluid.

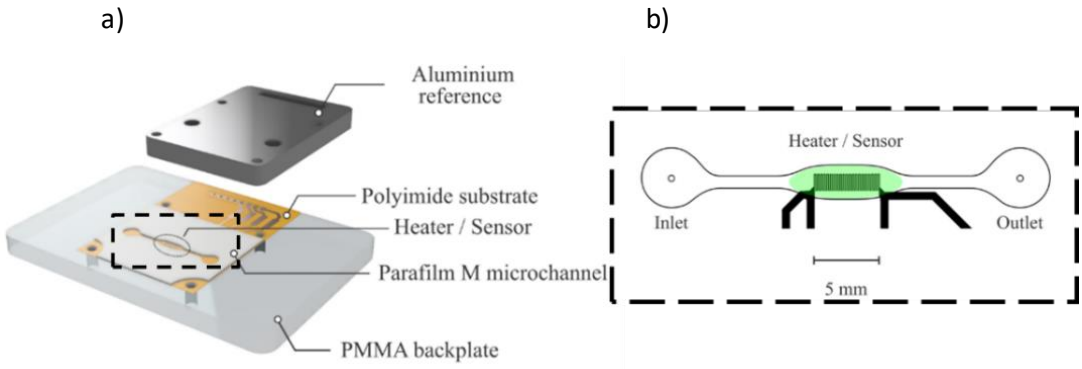

Figure 17: a) Illustration of the experimental sensor setup and schematic drawing of the microchannel and b) The elliptic cylindrical fluid column covering the sensor has a total volume of less than 3 µL (reproduced from ref. [42]).

The adapted method is called Transient Thermal Offset (TTO) as λ_L is derived from the offset at the end of the thermal transient curves Figure 18. Different water/ethanol mixtures from 0 to 100% ethanol were studied while a constant current was applied: In Figure 18 (a) voltage curves resulting from these thermal pulses are plotted on top of each other. Linear curve fits were performed on the voltage curves for the time interval of [2.4, 4.0] seconds $^{1/2}$. As the top reference material has a much higher thermal effusivity as compared to the substrate and the fluid, the heat dissipated by the sensor structure is absorbed, ensuring a constant temperature increase rates for all the measurements following transient pulse.

A calibration curve of defined water/ethanol mixtures is plotted on Figure 18 (b) using the percentage changes in offset versus the values of λ_L found in the literature, resulting of an exponential equation. From these calibration values, the offset measured values were then converted to λ. The result showed that experimental λ values were in agreement with values extracted from literature [136]. The maximum standard deviation was of 10% for a mixture of water/ethanol.

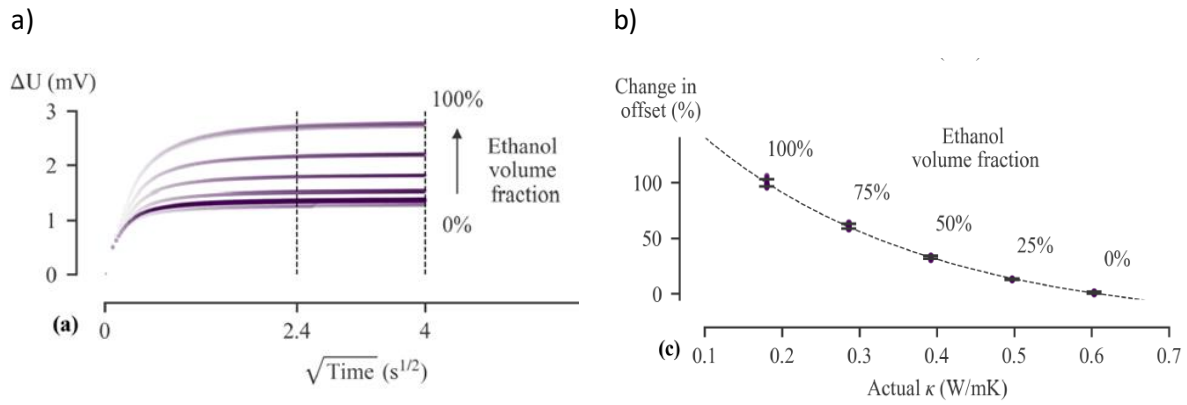

Figure 18: a) Thermal pulses applied while different water/ethanol mixtures were present in the microchannel. Linear curve fits were performed on the marked time interval. The raw data indicates that the various water/ethanol mixtures have an impact on the offset in the transient curves. b) Offset values are plotted as a function of the λ_L of the water/ethanol mixtures as found in literature. An exponential relation is observed (reproduced from ref. [42]).

All these previous works mentioned have shown the capabilities to measure thermal properties with very small amount of liquid (μl) with high accuracy. However, an important parameter has been emphasized by several authors [41,42] concerning the influence on uncertainty in measured results. It has been demonstrated that uncertainties can arise when working with small samples exposed to environmental disturbances. This can be avoided by using microfluidics, which involves both the study of fluid behavior in micro-channels and the use of microminiaturized devices that contain channels for fluid flow or confinement.

However, a parameter that impacts both systems is the thermal penetration depth. Indeed, if the heat flow exceeds the boundaries of the liquid sample, the environment or the surrounding materials can interfere with the measured result. In addition, another important parameter needs to be deeply studied: the compatibility with other functional groups and the temperature effect on λ_L. Only a few fluids have been experimentally measured in the cited works, and some of the considered microfabrication materials exhibit limited chemical compatibility and are only suitable for room temperature measurements.

1.7. Predictive models for thermal conductivity of liquids (λ_L)

While there are various experimental techniques to measure λ_L, it's often challenging to find literature data that cover for a synthesizable compound all the temperature and pressure conditions. In such cases, predictive or estimation methods for material properties become valuable. Predictive models are created and validated using existing theoretical aspects and experimental data, with varying levels of accuracy depending on the models and the types of substances involved. These models serve as a practical solution to supplement information for fluids when experiments are not possible for different reasons, i.e. too costly or time-consuming. For instance, the prediction of thermal properties such as λ_L is particularly useful in applications where optimizing system design and energy efficiency is crucial, (*e.g* in heat exchangers) [137,138].

This section introduces alternative modeling approaches that are used to determine thermal conductivity of liquids. Its purpose is to give readers a comprehensive understanding of the existing literature and methodologies in this field. This provides a context for the methodology used in the study and discusses previous research, methodologies, and limitations encountered during the development of a model. This highlights the relevance and novelty of the current research. By discussing existing models, we can provide explanations with respect to the selection of a particular model and highlight any improvements or modifications made to it. The existing models used to predict λ_L are detailed hereafter.

Different models are proposed in the literature to estimate λ_L, for instance Equations of State (EoS) [51,139,140] which are thermodynamic equations that relates state variables such as the pressure (P), temperature (T) and volume (V). These types of equations are used to describe the state of pure substances and mixtures in different states of matter at given conditions. The oil industry has used simple models known as the cubic EoS such as Van der Waals [141], Redlich-Kwong [142], Soave, and Peng-Robinson [143]. There have been several attempts to describe the thermodynamic behavior of fluids to predict λ_L at given conditions [140,144,145]. As a result, the oil industry has developed several forms of EoS to calculate reservoir fluid properties. However, these types of models have not often been applied to a wide range of polar substances, such as alcohols, ketones, organic acids, among others. Accurate prediction of EoS is still difficult due to the scarcity of experimental data on certain parameters required to compute the developed models. Considering the limitation of EoS models, some researchers have attempted to predict λ_L compounds using Machine Learning based methods [146–148]. This is the purpose of the following sections.

1.7.1. Cheminformatics and Quantity structure property relationship (QSPR)

Another alternative for modeling thermal conductivity is the use of Machine Learning (ML) based approaches. Machine Learning is a subfield of data science whose main objective is to create systems capable of automatic learning, *i.e.*, capable of finding complex patterns by themselves. Due to the advancement in computing power, ML has been applied in various scientific disciplines. One of them is chemistry, where researchers use ML models to predict the properties, reactions or activities of various molecules [149–152]. In this context of progress, Cheminformatics emerges as the combination of computational methods to transform data in chemistry into information, and information into knowledge to make better and faster decisions in the field of drug identification and optimization. This is how it was defined for the first time by Frank K. Brown in 1998 [153]. Cheminformatics represents an interdisciplinary field that merges chemistry and computer science to analyze and interpret chemical data. It involves the use of computational techniques and tools to efficiently organize, retrieve, and analyze large amounts of chemical information. Notably, cheminformatics extends its significance beyond chemistry to encompass other fields as biology, biochemistry, and other scientific domains [154,155].

Some of the areas of cheminformatics include molecular modeling and simulation, chemical database management, chemical data mining, chemical information retrieval, chemical structure representation and analysis, etc. One of the prominent areas of Cheminformatics is Quantitative Structure–Property Relationships (QSPR) that aims to establish a relationship between the chemical structure of a compound and a specific endpoint, such as a physicochemical property. We also include Quantitative Structure Activity Relationships (QSAR), which relates the molecule structure to the activity, is also

included in the term QSPR. QSPR models are developed using theoretical or experimental data for chemicals with known structures, employing Machine Learning and statistical techniques. Over the past centuries, QSPRs have found widespread applications, and the subsequent paragraph provide an historical overview of these models.

More than a century ago, Crum-Brown and Fraser expressed the idea that the physiological action of a substance was a function of its chemical composition and constitution [156]. A few decades later, in 1893, Richet showed for a set of organic molecules that the cytotoxicity was inversely related with water solubility [157]. Meyer suggested in 1899 that the narcotic action of a group of organic compounds is related with solubility into olive oil [158]. Ferguson introduced in 1939 a thermodynamic generalization to the correlation of depressant action with the relative saturation of volatile compounds in the vehicle in which they were administered [159]. Hammett in 1935 introduced a method to account for substituent effects on reaction mechanism [160]. Taking Hammetts model into account Taft proposed in 1956 an approach for separating polar, steric, and resonance effects of substituents in aliphatic compounds [161]. Then, the classical approach to QSAR/QSPR was led by the pioneering works of Hansch and Fujita (1964) in the development of linear Hansch equation [162]. Hansch and Fujita opened a new field of research widely used for the prediction of biological activities and physicochemical properties for rational drug design. The methodology has evolved over the years from a simple regression model with few variables to the analysis of large amounts of data through different statistical and machine learning techniques [163] applicable to a wide range of chemical, biological, and pharmacological related problems.

QSPR models have been applied to establish relationships between different molecules structures and a property, including those related to organic liquids. Some examples of properties that have been estimated using QSPR are: melting, boiling or flash points [164–167], transport properties such as viscosities [168,169], surface tension [170], thermal conductivity [171,172] and even toxicological properties of compounds [173].

There are existing reviews that provide detailed information about the advancements and uses of QSPR models, as well as recommendations for developing these models [150,174]. The process described in these reviews comprises several key steps, including 1) the collection of reliable data in the largest possible number resulting in a database, 2) The process involves representing molecules using character strings and calculating descriptors. These descriptors provide a numerical representation of the molecular structures of compounds and are stored in a database 3) the use of data analysis tools to select appropriate descriptors and set up the model, 4) the model is then tested for correlation and reliability through internal, or external validations which require additional experimental data to determine the predictive power of the model. All these main steps are detailed hereafter.

1.7.1.1. Database importance

The database provides a collection of molecular structures and their associated properties, which serves as the foundation for model development. By using a comprehensive database, scientists can extract relevant information, identify trends, and establish correlations between structural features and properties of interest. Furthermore, the database can be continuously expanded and updated with new experimental data, thereby enhancing the reliability and generalizability of the QSPR models.

Creating a database can be difficult because data needs to be extracted from different sources with different formats and structures. It can be challenging to merge this data together due to differences in file types (such as CSV, Excel), data structures, measurement units, and classification. Therefore, meticulous alignment and organization are necessary to establish a unified structure for the data. Ensuring data consistency and reliability is also a challenge, as there may be inconsistencies or errors in the data that need to be resolved such as duplicates or conflicting information. Additionally, accessing certain databases or literature sources may be restricted. Collecting data is a time-consuming process and can take up a significant amount of time and effort when developing predictive models. Figure 19 shows that approximately 60% of the time during model development is dedicated to curating databases.

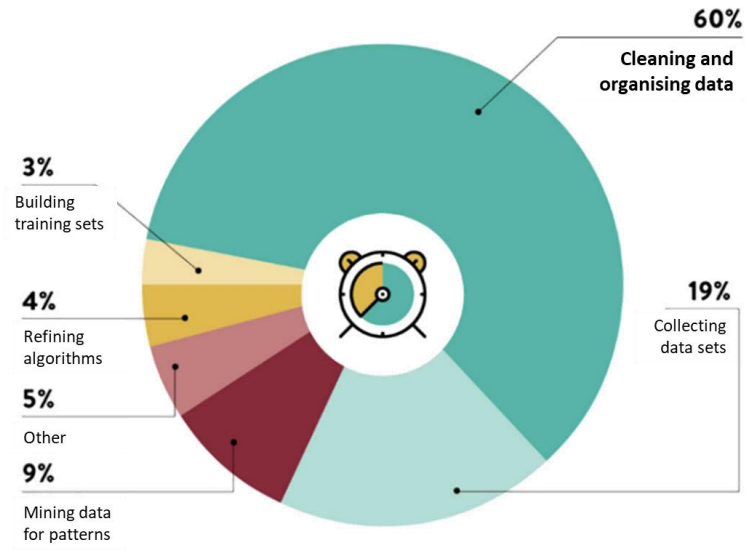

Figure 19: Time spent by data scientists on various activities extracted from reference [175].

To ensure the reliability of collected data and maintain a robust database, external sources of validation have been created. One notable example is the Design Institute for Physical Properties (DIPPR) [176] was created by the American Institute of Chemical Engineers in 1980 to provide reliable and consistent thermophysical property data for industrial purposes. This database is globally recognized and includes carefully evaluated data for accuracy, thermodynamic consistency, and reliability within the different chemical families.

1.7.1.2. Computational representation of molecules

Historically, chemists used simplified models to represent the structure of molecules. Molecules depending on the complexity can be represented in different ways. For instance, one common representation is the molecular formula, which uses chemical symbols and numbers to indicate the types and numbers of atoms in a molecule. There are also more advanced, like 3D representations, which show both the arrangement of atoms and how they are connected.

A computational representation of a molecule is a way of encoding the complex structural and/or chemical information of a molecule in a format that can be processed by computers, facilitating the handling of data. Two common types of computational representations of molecules are detailed hereafter.

Simplified Molecular Input Line Entry System (SMILES)

One format for encoding molecules consists in using "Text-based character strings". These files, also known as line notation, use a single line of characters to represent a molecule. Some of these include International Chemical Identifier (InChI), SMILES Arbitrary Target Specification (SMARTS). Currently, the most known and used is the SMILES (Simplified Molecular Input Line Entry Specification), created at the end of the 1980s by David Weininger [177]. SMILES is designed to make chemical structures easily readable and has greatly advanced the field of cheminformatics. It has also contributed to the development of more efficient ways to store and search for large amounts of data.

The SMILES code uses symbols from the periodic table to represent atoms and indicates double bonds with an equal sign (=). It assumes that the necessary number of hydrogen atoms is present to complete each atom's octet. Including hydrogen atoms in the SMILES code would make it longer and less efficient. More details about the encoding of SMILES can be found in ref. [178].

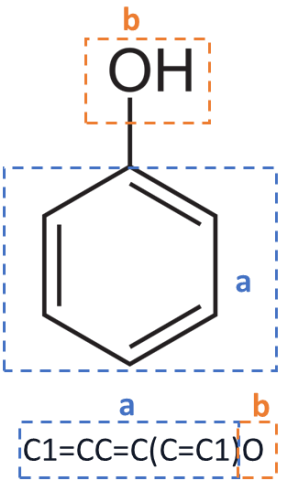

Figure 20: Structure of phenol and its respective Canonical SMILES.

Figure 20 shows a 2D representation of the phenol molecule and provides its SMILES code below.

Molecular descriptors

Another way to represent the structure of a molecule is using Molecular descriptors (MDs) which are numerical or binary values that quantitatively describe various properties or characteristics of a molecule. In QSPR modeling, the generation of descriptors is essential to simplify the complexity of molecular structures by converting them into numerical representations. This transformation is crucial for establishing precise quantitative relationship between the chemical structure and the property. The general form of QSPR models can be expressed as follows:

$$\text{Property} = \text{f}(\text{Descriptor}) \tag{1- 23}$$

MDs can be categorized into two types: experimental or theoretical. Experimental descriptors are properties obtained through specific experimental procedures such as molar refractivity, polarizability. While theoretical descriptors are obtained through algorithms applied to molecular representations. These includes physical attributes (*e.g.*, molecular weight), chemical features (*e.g.*, polarity,

electronegativity), or structural details (*e.g.*, the number of rings, hydrogen bond donors/acceptors). These descriptors can be classified based on the level of representation of the chemical structure, which is illustrated in Figure 21. The classification was defined based on the following reference [179].

0D descriptors are based on chemical formulas, which are the simplest representation of molecules. They do not require information on molecular structure and atom connectivity, do not require molecular structure optimization and are independent of any conformational issues. They are atom, bond counts and molecular weight. In general, they have a low information content and exhibit very high degeneracy, i.e., they have the same value for several molecules (*e.g.* isomers). However, they can play an important role in simulating various physicochemical properties or participating in more complex models.

1D descriptors is a list of structural fragments called fingerprints. Fingerprints are used to encode the structure of a molecule using binary digits. These digits represent the presence or absence of specific substructures in the molecule. Comparing fingerprints can help find matches with a particular substructure. Among then we can mention functional groups and atom-centered fragments, e.g., primary carbons, secondary carbons.

2D descriptors include topological or structural parameters. The representation of a molecular structure depends on its topology, which indicates the positions of individual atoms and the connections between them. These molecular descriptors are computed from the graphical representation of the molecule.

3D descriptors include geometric parameters which require a spatial reference frame. Among the most well-known are: WHIM [180], GETAWAY [181]. Their main drawbacks are that they often require a lot of computational power, rely on the specific method used to optimize the molecular structure, and cannot accurately represent the different shapes of very flexible molecules. [150,182].

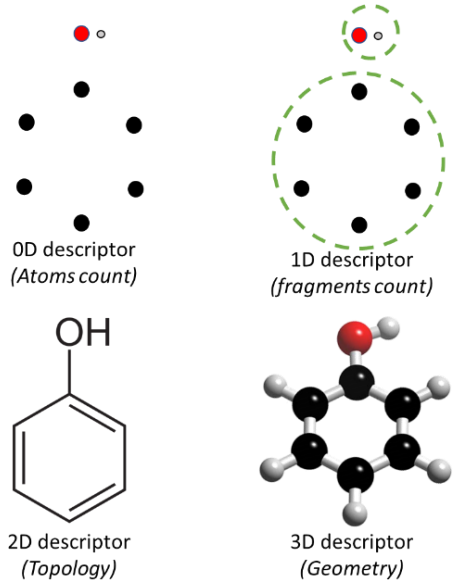

Figure 21 : Representation of the 4 classes of molecular descriptors for phenol.

It is important to note that the choice of descriptor dimensionality depends on the specific properties or activities being predicted, the available computational resources, and the type of molecules being studied. A combination of different dimensionality descriptors can also be used to capture multiple aspects of a compound's structure.

0D and 1D descriptors have been used on several occasions due to their efficiency and simplicity. These descriptors are used in group contributions methods (GCM) [49,183], where the molecule is broken down into groups (functional groups or fragments or building blocks or descriptors) and the property of the compound is calculated by adding up the contributions of the chemical groups that constitute the molecule. The classical group contribution method decomposes each chemical compound into First,[184], Second,[185] or Third [186] order functional groups based on its molecular structure. The first order describes the simple functional groups in molecules, whereas the second and third orders allow a much more detailed description of the structure of molecule (surrounding of functional groups).

Additionally, 2D and 3D descriptors have been also used on several occasions to predict physicochemical properties. For instance, 2D and 3D descriptors related to molecular size, shape, and intermolecular forces can be used to predict properties such as the boiling point of a compound [187,188]. These descriptors provide insights into the strength of intermolecular interactions and can be useful in various applications, including material science and drug formulate. However, they often require longer computation time and several studies have demonstrated that models perform significantly better when using functional groups as features instead of more complex molecular descriptors [165,189–191]. The type of information that is provided by the descriptors mentioned is summarized in Figure 22.

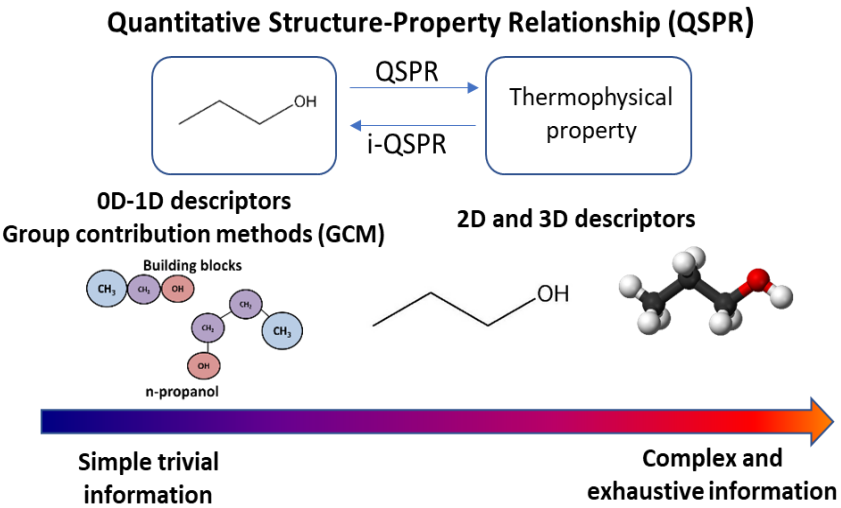

Figure 22: QSPR modeling involving the use of molecular descriptors to provide information about the molecule structure.

1.7.1.3. Feature selection and model development using ML-based methods

Feature selection is an important step in developing QSPR models for predicting the properties of molecules. It involves identifying the most relevant descriptors or features that capture the essential

properties of a chemical compound. This helps to reduce the dimensionality of the dataset and eliminate redundant or irrelevant features that may negatively impact model performance.

Various statistical or ML algorithms can be used for feature selection. These techniques help in identifying the most informative features and are classified as unsupervised methods. These algorithms do not require labeled data, meaning they do not need known outcomes or labels during training. Instead, they are used to identify patterns or clusters within the data. Some examples include correlation analysis and principal component analysis (PCA).

Once feature selection is complete, the next stage is model development. Another class of ML algorithms, known as supervised methods, are employed during this process, which use labeled data to train the model in predicting the target property. These methods can be broadly classified into "linear" and "nonlinear" models based on the outputted relationship between the input features and the output variable. "Linear" models assume a linear relationship between the input features and the output variable. They are simple and easy to interpret but may not be able to capture complex relationships. Examples of linear models include multiple linear regression (MLR) [192]. On the other hand, nonlinear models are more flexible and powerful, but they may be more difficult to interpret and require more data and computational resources to train. Examples of nonlinear algorithms include Artificial Neural Networks (ANN) [193] and Support Vector Machines (SVM) [194]. The two ML methods that were employed during the thesis are: Principal Component Analyses and Support Vector machines. This latter is briefly described below.

The SVM aims to find a hyperplane in a high-dimensional space, maximizing the margin between data points of different classes or predicting continuous values. This is possible by finding an optimal hyperplane iteratively, which is used to minimize an error. On the basis of which side of the gap they are on, new examples that are subsequently mapped into that same space can be categorized.

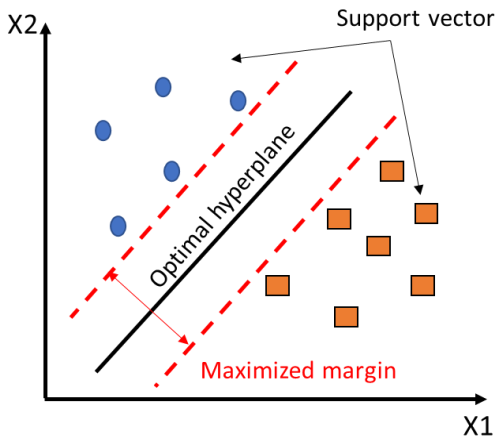

Figure 23: SVM algorithm representation adapted from ref. [195].

ML algorithms are reliable within a designated zone of the feature space, which is a reduced-dimensional representation created by selecting specific descriptors to describe the molecule structure. The applicability domain (AD) is crucial in this context, as it defines the range of features and chemical space where the model's predictions remain reliable. AD is determined based on the similarity of new compounds to those in the Training dataset, ensuring that predictions outside this

domain may be less accurate or completely unreliable. Therefore, including a diverse range of compounds and property values in a database is essential, as it enables the model to capture a broader representation of patterns and trends, considering the different characteristics and variations in the data.

1.7.1.4. Model validation

Model validation refers to the process of ensuring that a developed model accurately represents the relationship between the chemical structure and the property being predicted. This is known as predictive power. It involves assessing the performance of the model using various statistical measures, testing its ability to make accurate predictions for new compounds, and ensuring its applicability for real-world applications.

Validation typically involves two key steps: data splitting and statistical analysis. Firstly, the dataset is divided into two subsets: Training set *(e.g.* 70% of the database) and a Test set *(e.g.* 30% of the database). QSPR models are then constructed based on the Training set, and their predictive performance is subsequently assessed using the Test set. This evaluation on an independent dataset constitutes an external validation of the model's generalization ability.

Moreover, the Training set can be further divided into multiple subsets or folds. In a process known as k-fold cross-validation, the model undergoes training and evaluation multiple times. During each iteration, a different fold or subset is reserved for Test, while the remaining folds are employed for Training. This provides a more robust assessment of the model's performance and reduces the risk of overfitting. The final step of model validation, external validation is employed to assess the model's performance on a separate Test set called "Validation set". This set is distinct from both the Training set and the Test set, which was not used during model training or hyperparameter tuning and consists of completely new data that the model has not been exposed to. The purpose is to evaluate how well the model performs on this unseen and independent data.

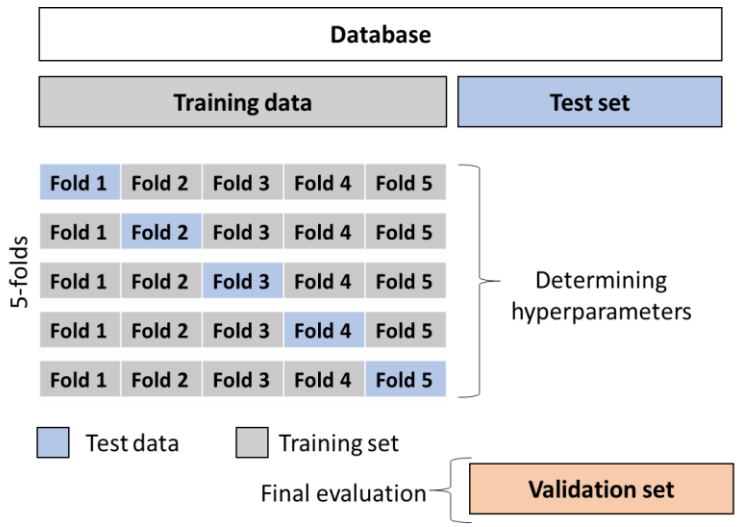

Figure 24: Illustration of the k-fold cross-validation.

Numerous indices have been developed to assess the accuracy of a QSPR model [196,197]. One of the widely used is the coefficient of determination (R^2) which estimates the proportion of the variation of

Y explained by the regression (the explained variance of the model). R^2 values range from 0 to 1, poor to accurate prediction, following the formula:

$$R^2 = 1 - \sum_{i=1}^{N} \frac{(y_i - \hat{y}_i)^2}{(y_i - \bar{y}_i)^2} = 1 - \frac{SSR}{SST} \quad (1\text{-}24)$$

Where a data set has reference values marked y_i, associated with a predicted value $\hat{y}_i$, and with $\bar{y}_i$ the observed mean data. Therefore, SSR is the sum of squares of regression, and SST is the total sum of squares.

The root-mean square error (RMSE), and Average Absolute Relative Difference (AARD) can be used as an additional information to quantify accuracy of a QSPR model. These metrics are defined as follows:

$$\mathrm{RMSE} = \sqrt{\sum_{i=1}^{N} \frac{(y_i - \hat{y}_i)^2}{\mathrm{N}}} \quad (1\text{-}25)$$

$$\mathrm{AARD}\,(\%) = 100 \times \sum_{i=1}^{N} \left| \frac{(y_i - \hat{y}_i)}{y_i} \right| / N \quad (1\text{-}26)$$

The lower the RMSE and AARD, the better a given model accurately predicts. However, the range of the dataset is important in determining whether a given RMSE or AARD are considered acceptable for a good predictive model, and it can only be compared between models whose errors are measured in the same units.

The main steps for the development of QSPR models are summarized in Figure 25.

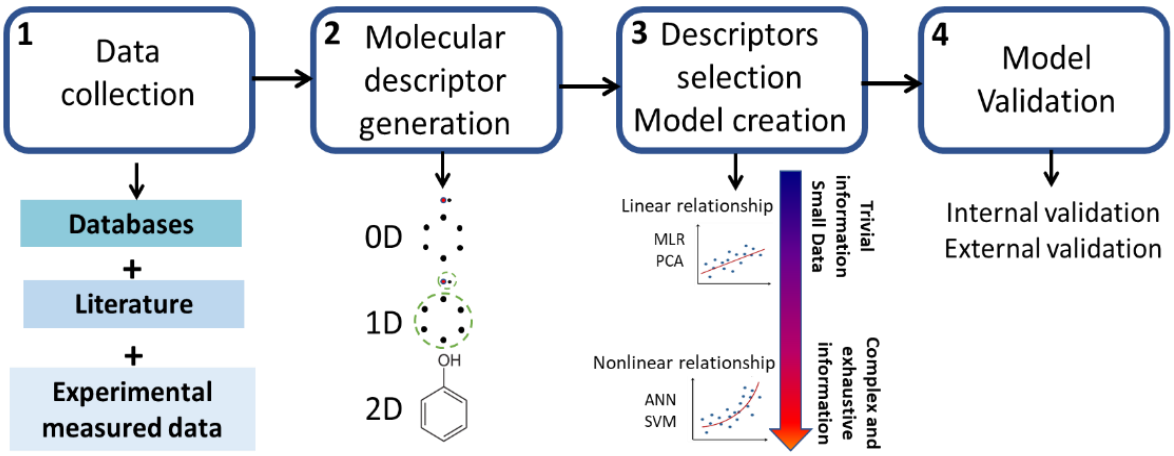

Figure 25: Main steps involved in QSPR modeling.

1.7.2. Existing QSPR models used to predict λ_L for oxygenated and hydrocarbons

Predicting the thermal conductivity of substances such as oxygenated compounds and hydrocarbons encountered in biomass conversion is important for several reasons. This prediction can improve

combustion systems, simulate conversion processes, select suitable feedstocks, and ultimately enhance the efficiency and cost-effectiveness of conversion systems. These predictive models leverage various techniques, including ML.

As previously discussed, numerous strategies have been developed to predict thermophysical properties using ML based models such as QSPR. More specifically, some models have been already developed to predict the thermal conductivity of substances such as oxygenated compounds at room temperature. The following works are discussed and a summary table (Table 2) is provided with the main information such as chemical family groups targeted, the temperature range, number of descriptors, number of compounds, and results of R^2 for Training and Test sets, in each QSPR study. These works are detailed hereafter.

In the work by Kauffman *et al.* [198], the data set consists of the thermal conductivity of 185 common organic solvents at room temperature extracted from reference [199] from which four outliers (glycerol, formamide, 2,2'-Thiodiethanol, formic acid) were removed to improve the results. They used two ML algorithms: An MLR and a convolutional neural network (CNN) [200]. The database was split into a Training set (145 compounds), Validation set (18 compounds, and Test set (19 compounds), and a nine-descriptor model was selected as the best detailed in Appendix A. Table 2 summarizes the results of the Training and Test data and the two models.

Khajeh *et al.* [172] developed a dataset consisting of the thermal conductivity of 116 alcohols at room temperature taken from reference [201]. The dataset was divided into a Training (93 compounds) and a Test set (23 compounds). They investigated linear and nonlinear relationships between molecular descriptors and λ_L, using GFA and Adaptive neuro-fuzzy inference system (ANFIS) using 5 descriptors: autocorrelations descriptors (ATS2m and GATS1m), one molecular property 2D descriptor (Hy) and two 3D descriptors (G1s and HATS2P) which are detailed in Appendix A, and led to the equation (1-27). The results from the equation () applied on the Training and the Test set are detailed in Table 2, respectively.

$$\lambda_L = -0.0183\ (ATS2m) + 0.0486(GATS1m) + 0.0270(G1s) - 0.0732(HATS2P) + 0.0119(Hy) + 0.1571 \quad (1\text{-}27)$$

Shi *et al.* [202] built a QSPR model to predict λ_L of organic compounds based on SVM. The data used was extracted from reference [203]. The dataset is composed of 147 compounds containing hydrocarbons, halogen, ethers, alcohols, esters, aldehydes, ketones, amines, and amino compounds, randomly divided into two subsets, the Training set (80%) and the Test set (20%). Five descriptors were selected: 2 electrostatic descriptors ($X_1\ and\ X_3$), 2 constitutional descriptors ($X_4\ and X_5$) and 1 quantum-chemical descriptor (X_2**)** detailed in Appendix A and leading to equation (1- 28). Table 2 shows the R^2 results for both the Training and Test sets.

$$\lambda_L = 4.499 + 1.587(X_1) - 0.9941(X_2) + 13.87(X_3) + 0.5519(X_4) - 0.00559(X_5) \quad (1\text{-}28)$$

Even if these QSPR models have been developed to predict thermal conductivity, these models are limited to data of thermal conductivity at room temperature only. Some other authors have proposed the use of QSPR model considered the effect of temperature on λ_L. These works are detailed hereafter.

Latini *et al*. [204] and Pierantozzi *et al*. [205] proposed the use of ANN models. Latini *et al.* [204] used ANN with one hidden layer and 37 neurons, to modeling λ_L of 23 n-alkanes, 14 ketones, and 18 silanes for different temperatures at atmospheric pressure. The model reproduced the data with an AAD for n-alkanes, ketones, and silanes of 1.8%, 1.8% and 3.5% respectively. Similarly, Pierantozzi *et al.* [205] proposed an ANN with one hidden layer with 43 neurons to determine λ_L of 26 alcohols with different temperatures from their melting point to boiling point. the model exhibits slight deviations between the experimental and calculated values with AAD less than 0.0016%. For both ANN models from Latini *et al*. and Pierantozzi *et al.* few datapoints and compounds were considered. To perform in an optimal way an ANN model it is necessary to have a considerable amount of datapoints, otherwise with datapoints size, the network would easily memorize and therefore overfit the model which can be seen in their results showing very low errors and a R^2 very close to 1.

Lu *et al.* [147] developed a QSPR model for predicting λ_L of diverse liquid oxygen-containing organic compounds. At first, 992 λ_L data of liquid aliphatic alcohols, ethers, aldehydes, ketones, acids, and esters at different temperatures were collected from reference [206]. A total of 112 compounds at different temperatures were collected. In addition, 72 experimental λ_L data for 15 compounds were measured in their laboratory and used as the Test set. GFA was used to screen molecular descriptors and provide several MLR models. 6 descriptors were used: $\mathrm{SM2}_{\mathrm{B(s)}}$ spectral moment of order 2 from the Burden matrix weighted by I-state, $SIC0$ structural information content index (neighborhood symmetry of 0- order), $IC1$ information content index (neighborhood symmetry of 1-order), T is the temperature, Eta_F functionality index, and $MATS2m$ is Moran autocorrelation of lag 2 weighted by mass and detailed in Appendix A. For the Training, and Test sets R^2 values are reported on Table 2. Despite the results obtained, there was an unequal distribution of data points for each compound in the Training set. This implies that compounds with more data points have a greater impact on the predictions of the model. Also, some compounds from the Training set were used in the Test set which cannot confirm a reliable and accurate model. The same problematic is shown in one of their previous article [148].

$$\lambda_L = -0.0793 + 0.0711 \times \mathrm{SM2}_{\mathrm{B(s)}} + 0.296 \times SIC0 - 0.0511 \times IC1 - 0.0002 \times T - 0.0127 \times Eta_F - 0.0587 \times MATS2m \quad (1\text{-}29)$$

The works proposed considered this time the effect of temperature on thermal conductivity, however some drawbacks can be mentioned. This model approximates the temperature dependency of thermal conductivity as a constant identical value for all compounds, which experimental data do not seem to show. Furthermore, the studies mentioned only restricted the application of predicting thermal conductivity to oxygenated compounds. There is still a need of developing models using both hydrocarbons and oxygenated compounds.

Table 2: Summarized results for each QSPR work for determining λ_L.

Model Linear /no linear	Authors	Compounds	λ_L (W/m.K)/ T° range (K)	Descriptors	N° of data points	N° of compounds	R^2 Training set	R^2 Test set
MLR/ CNN	Kauffman *et al.* [198]	Organic solvents	0.11-0.20/room temperature	9	182	182	0.88/ 0.96	0.96/0.97
GFA /ANFIS	Khajeh and Modares [172]	Alcohols	0.10-0.20/room temperature	5	116	116	0.98/0.99	0.95 /0.96
HM /SVM	Shi *et al.* [202]	Organic compounds	0.09-0.29/ room temperature	5	147	147	0.93/0.92	0.96/0.97
ANN	Latini *et al.* [204]	Organic compounds	Not documented	3	1057	55	0.99	1
ANN	Pierantozzi et al. [205]	Alcohols	0.10-0.24/ not documented	3	520	26	1	1
MLR/-	Lu *et al.* [148]	Alcohols	0.13-0.16/300-380 K	4	139	93	0.98	0.97
GFA-MLR/-	Lu *et al.* [147]	Aliphatic oxygenated	0.10-0.24/180-500K	6	1064	127	0.91	0.89

1.7.3. Estimation methods based on GCM to predict λ_L of oxygenated compounds

In this section, methods known as GCM to predict to predict λ_L are reviewed and Table 3 summarizes some existing models. The works of Nagvekar and Daubert [183], Sastri and Rao [49], and Rodenbush *et al.* [207] have contributed to the development and understanding of the group contribution methods for determining thermal conductivity. Nagvekar and Daubert [183], proposed a group contribution method for estimating the thermal conductivity of organic compounds. They

developed a database of group contributions based on experimental data and applied these contributions to calculate the thermal conductivity of various organic compounds. Their work provided a foundation for subsequent studies in this field.

Sastri and Rao [49], extended the group contribution method established by Nagvekar and Daubert for the estimation of thermal conductivity of liquid organic mixtures. They incorporated additional group contributions for various binary interactions between functional groups to improve the accuracy of predictions for mixture properties. The method was validated using experimental data for a range of liquid organic mixtures.

Rodenbush *et al.* [207] further extended the group contribution method to predict the thermal conductivity of pure liquid hydrocarbons. They introduced additional group contributions specific to hydrocarbon compounds and considered the effect of molecular size and branching on thermal conductivity. The method was validated using experimental data for various liquid hydrocarbons.

Since then, several models have been created and the methods suggested by these models have been compared to their work. For instance, the recent work of Cordona *et al.* [191], considered a group contribution model with five adjustable parameters that have been generalized using the acentric factor, RT_c/P_c relation, where R is the gas constant (R = 8.314472 J/(mol.K)) and T_c correspond to the critical temperature and P_c the critical pressure, and a contribution of each group in the substance through a tendency graphical analysis. The model was applied to 351 substances distributed into 160 Training, 96 for Testing, and 95 for predictive capabilities. It included 24 organic families and 56 functional groups. The average absolute deviations had a minimum and maximum values below 6.51% and 30.43%.

Table 3: Main equations for λ_L using GCMs (taken from reference [209]).

Author	Year	Estimation method	No of data	Deviation
Nagvekar and Daubert [183]	1987	$\lambda_L = A + B(1-Tr)^{2/3}$ Parameters are determined by GCMs. The method is applicable for a reduced temperature range 0.3 <Tr< 0.9	2089	AARD: 5.9%
Sastri and Rao [49]	1999	$\lambda_L = \lambda_{Lb}\, 0.16^{\left[1-\left(\frac{[1-T_r]}{[1-T_{br}]}\right)^{0.2}\right]}$ $= \sum_k N_k \Delta\lambda_{bk} + \sum \Delta\lambda_{corr}$ The method employs the GCM to estimate the λ_L at T_b	934	AARD Below T_b: 5.6% Above T_b: 8.3%
Rodenbush *et al.* [207]	1999	$\lambda_L = DT^{-2/3}$ Based on the additivity of bond property, the parameter D is obtained by the GCM	1487	AARD: 2.5%
Cardona *et al.* [191]	2023	$\lambda_L = \lambda_c \cdot \rho_c \cdot exp\left[\delta_L \frac{(\Delta H_L^{id} - \Delta H_c^{id}}{RT}\right] + \sigma_c \cdot (Z_L - Z_c$	6400	AARD: 6.51% to 30.43%

Table 4 presents data on the classification and AARD% of various oxygenated families, sourced from Rodenbush *et al.*, Nagvekar, and Daubert. The data sets for each family contain no more than 100 compounds. It is worth mentioning that there is less information available on the thermal conductivity of ethers and aldehydes compared to other chemical families. Similarly, there is limited data on the influence of temperature on thermal conductivity.

Table 4: Results of λ_L prediction using GCM method.

	Rodenbush *et al.* [207]			**Nagvekar and Daubert** [183]		
Classes	**No. of data points**	**No. of compounds**	**AARD/%**	**No. of data**	**No. of compounds**	**AARD/%**
Alcohols	267	21	2.7	634	23	6.3
Acids	68	17	3.2	787	20	6.5
Esters	92	29	2.8	243	29	9.7
Ketones	48	11	3.2	68	9	6.3
Ethers	18	5	3.1	75	10	7.3
Aldehydes	28	8	2.1	43	9	8.3

QSPR modeling presents a range of methods for predicting the thermal conductivity of liquids. These methods encompass the Group Contribution Method. In this methodology, the structural information of a molecule is represented numerically using molecular descriptors. These descriptors help to build the relationship between the chemical composition of molecules and their thermal conductivity property. The descriptors can be categorized based the level of representation of the chemical structure, ranging from simpler and more generalized (0D or 1D descriptors) to more complex and detailed (2D and 3D descriptors).

The advantage of group contribution methods lies in their simplicity and ability to incorporate expert knowledge. Group contribution models are well-established and widely applicable. On the other hand, more complex descriptors capture diverse molecular attributes, such as shape, and electronic properties. While these descriptors can offer more precise predictions for complex molecules, they require greater computational power and extensive Training data sets.

1.8. Conclusion

Microfluidics is a multidisciplinary field of science and technology dedicated to the manipulation and control of very small amounts of fluids at the microliter scale. It is of great interest to industrial groups and research labs, due to the faster screening using smaller volumes. Moreover, microfluidics offers advantages in minimizing the impact of heat transfer effects, such as convective heat transfer, which can introduce experimental errors. This makes it an attractive alternative to traditional methods for measuring thermal conductivity.

The two conventional methods for measuring thermal conductivity were adapted to micro-sized samples or microfluidics, requiring either a separate heater and temperature sensing or the use of a

single metallic element whose electrical resistance changes with temperature. Different approaches have been discussed in terms of complexity, accuracy, ease of integration, cost, etc.

In this chapter, we showed those microfluidic tools along with MEMS technologies that have been developed for characterizing thermophysical properties of fluids. The previous works have shown the capabilities to measure thermal conductivity with very small amount of liquid (μl) with high accuracy. However, an important parameter has been emphasized by several authors [41,210] concerning the influence on uncertainty in measured results. It has been demonstrated that uncertainties can arise when working with small samples exposed to environmental disturbances. This can be avoided by using microfluidics, which involves the use of microminiaturized devices that contain channels for fluid flow or confinement.

However, a parameter that impacts both systems is the thermal penetration depth. Indeed, if the heat flow exceeds the boundaries of the liquid sample, the environment or the surrounding materials can interfere with the measured result. Some works have proposed different solutions for this issue, allowing a more accurate measurement of the thermal property.

There are still some issues that require in-depth research, for instance, only a few fluids have been experimentally measured in the cited works, and some of the considered microfabrication materials exhibit limited chemical compatibility and are only suitable for room temperature measurements.

Modeling and experimentation are two essential components of research. The use of predictive models simplifies the experimental steps that can be dangerous, time consuming or costly. Various papers showed different types of models that are used to predict thermal conductivity values, and from the literature survey we mainly focused on Quantitative Structure Property Relationship (QSPR) to predict liquid's thermal conductivity (λ_L). However, one persistent challenge in QSPR modeling for predicting λ_L at different temperatures is the lack of reliable experimental data, particularly for oxygenated compounds. While the literature mentions a total of approximately 180 oxygenated compounds, fewer of them have associated information regarding their thermal conductivity at different temperatures. Among the works referenced, where temperature was considered [147,148], only about 90 oxygenated compounds have enough (three or more) experimental available data to observe thermal conductivity *vs* temperature trend or behavior.

Experimental measurement of thermal conductivity for a wide range of liquids is time-consuming and costly, leading to limited data availability. This scarcity makes it challenging to create accurate predictive models, as large and diverse datasets are necessary for proper Training. Therefore, addressing the lack of data is crucial for improving the reliability and usefulness of these models.

Because of its high-throughput and sensitive measurements, microfluidics is a good candidate for both generating data to train models and benefiting from their predictive power. The combination of microfluidic and modeling is then necessary to implement a low-cost, automated method of measuring/predicting thermophysical properties with high-throughput results.

The remainder of the manuscript will detail the methodology used to fabricate and to validate the strategy for determining thermal conductivity using our microfluidic device. The results for using

different liquids will be discussed. Also, the methodology and the results to develop new QSPR models will be detailed.

Chapter II: Development of a microfluidic device to measure thermal conductivity for temperature operating conditions

This chapter presents the development of a microfluidic device for measuring thermal conductivity at different temperatures conditions. The technology chosen for this thesis work, out of the ones mentioned in the previous chapter, is silicon-borosilicate microsystem, which can operate at high temperatures and pressures technology. The microsystems developed by Murphy *et al*. [211] and Marre *et al*. [33] have the thermo-mechanical properties to operate effectively up to 400 bar and 400°C. The conditions considered in this work is largely covered by these ranges. In addition, Pyrex® offers optical access enabling coupling with *in-situ* characterization techniques such as Raman microscopy.

2.1. Introduction

As mentioned in chapter I, in comparison to conventional experiments, microfluidics devices can be used to lower the risks related to the operating environment, reagent consumption, and experimentation time.

In this perspective, the experimental setup developed at IFPEN allows to work at pressures up to 100 bar and initially allowed to heat the microsystem up to 100 °C. The bench integrates pressure management downstream of the microsystem, enabling precise control of the global pressure. A new holder [212] was developed to explore higher temperatures, with precise heating and temperature control. This new holder allowed to reach temperatures close to 350 °C. Gavoille [212] investigated fluids behavior and demonstrated that phase diagrams can be drawn using such a bench. Although, quantitative measurements have not yet been made with this new holder.

The microfluidic device plays a central role in the process of measuring a specific. We have seen in the first chapter that several thermophysical properties have been measured in microfluidics (surface tension, viscosity, density, specific heat capacity, thermal conductivity). Typically, one microfluidic device, is generally dedicated to the measurement of one property, as these devices are composed of multiple components. These include microchannels or chambers for sample handling, elements for controlling temperature, sensors for measuring temperature or other relevant factors, and a detection system for analyzing material responses. For instance, some microfluidic devices have been fabricated for the thermal conductivity measurement of liquids. These devices rely on a microheater, and temperature sensors integrated on a chip made of a certain material (PDMS, PMMA…) to measure the temperature rise caused by a flowing liquid. However, some of the considered materials used so far, exhibit limited chemical compatibility and are only suitable for room temperature measurements.

In this regard, a new microfluidic device has been specifically designed for integrating MEMS technologies such as microsensors for the measurements liquid's thermal conductivity. This chapter describes the development a microfluidic device to measure thermal conductivity values for different temperature conditions. The silicon-borosilicate microfluidic technology was chosen for this work as it allows extending the range of operating conditions compared to conventional microfluidics materials.

The microfluidic device is designed to address a particular problem, considering factors such as the geometric constraints related to the fluidic interfacing of the microfluidic device (maximum external dimensions of 1.5 cm x 4.5 cm), the characterization instrumentation to be used, the mechanical strength required (temperature). To achieve the final microfluidic device, particular designs, dimensions and materials were chosen based on these characteristics.

The microfluidic device including sensors deposited on Borofloat 33 integrated into microchannel in silicon was fabricated following a three-step procedure: First, microchannels were etched on a silicon substrate using photolithography and wet etching techniques; then, the sensors were created on the borosilicate glass substrate surface by selectively depositing a structured metallic film patterned according to the microchannels features; finally, the silicon and borosilicate glass substrates were sealed using a fusion bonding process resulting in the final microfluidic device. Indeed, when the bonding between silicon and Borofloat 33 is adequately done, it allows working at high temperatures and under pressures. This three-step procedure is detailed in the subsequent sections.

The microfluidic device includes two different approaches for heating and temperature monitoring, which enable the measurement of thermal conductivity using two approaches, which are shown in Figure 26 : a) A single resistive element was tested as both sensing and heating element, using two different geometries, meander and spiral (one element approach). b) The use of separate elements - the sensor and the heating element. This approach uses a heater (spiral in green frame), and a thermocouple (the cross in green frame). The choice with respect to the design of the microfluidic device, the dimensions, geometries, and materials selected for the sensor and the microchannels are detailed hereafter.

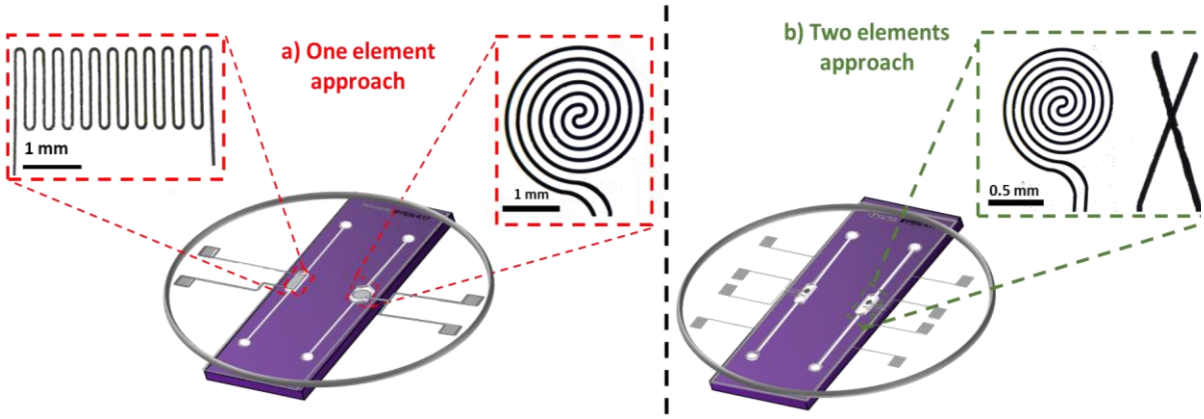

Figure 26: Illustration of the two microfluidic devices methodologies implemented, a) the one element methodology (with the use of a metallic spiral used as sensing and heating element) and b) the two-element methodology (with the use of a thermocouple and a heating element).

2.2. Preliminary tests conducted on the fabrication of sensors and heaters.

Sensors structures are design and used as MEMS technology (microsystems that operate using electrical and mechanical principles) during the process of the microfluidic device fabrication. Microsensors are designed to detect or measure physical properties. The temperature microsensors considered in this work are divided into two types: resistive temperature sensors (made of one metal) and thermocouples (pair of metals), which are placed on the borosilicate substrate.

Multiple steps are needed to fabricate both methodologies: metal deposition technique, choice of the material, the geometry of the sensor/heaters, and the processes to achieve the fabrication; bi-layer photolithography, lift-off process. These are detailed in the next sections.

2.2.1. Metal deposition (Magnetron Sputtering)

Magnetron Sputtering is one type of Physical Vapor Deposition processes (PVD), which is an under vacuum method that can deposit thin films on the selected substrate. It provides advantages such as deposition rate, uniformity, low levels of impurities, thickness control, adhesion etc. This technique is used for highly automated high-volume production, particularly for thin films in short deposition times.

The source material (target) is placed in front of a substrate (Borofloat 33) in a vacuum chamber filled with sputtering gas, argon. Two pumps are used, the first one (primary vacuum) produces a pressure down to 10^{-1} mbar, the second one (high vacuum) reaches 10^{-7} mbar pressure. As shown in Figure 27, by applying a high potential difference between the source and substrate, a plasma is generated by the sputtering gas ionization and bombards the source material, which ejects metallic atoms. To create and direct these ions and maintain the plasma, the target is connected to a cathode at a negative potential and the substrate holder to an anode connected to the ejected atoms get deposited on the substrate. Magnetron sputtering deposition uses magnets behind the negative cathode to trap electrons, enabling faster deposition rates. The deposition thickness varies from angstrom to few micrometers.

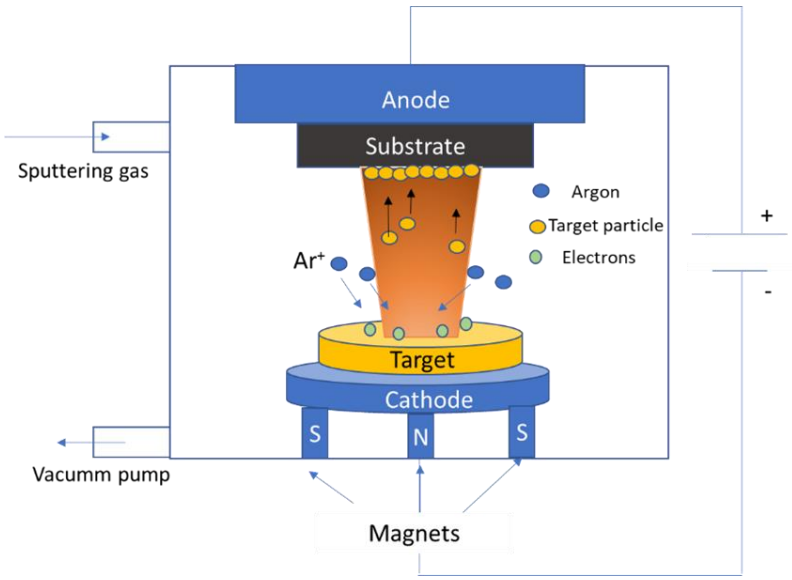

Figure 27 : Metal deposition (Magnetron Sputtering) principle.

For an insulation layer deposit which can be used as electrical insulator such as SiO_2 layer, it is necessary to consider the accumulation of electrons on the surface of the target. The sputtering gun is equipped with a radiofrequency (RF) power supply to solve this problem. This latter alternates the electrical potential of the target at 13.56 MHz, which, over time, can lead to arcing and damage the target. Additionally, it helps in preventing droplets from escaping, which could result in quality control issues for the film.

2.2.2. Choice of the material for thin film deposition

The first step in manufacturing a sensor or heating element is the selection of the appropriated material that can perform proper temperature detection, and that has a high-temperature and chemical resistance. Indeed, bonding protocols that involve joining the silicon part (microchannels)

with the borosilicate glass (Borofloat 33) (sensors) can be carried out at temperatures ranging from 400°C to 800°C, requiring the use of metals that can withstand such high temperatures.

Metals are essential in many heating and sensing applications due to their excellent thermal and electrical properties. In general, heating and sensing elements are selected based on the operating temperature range of the respective application and should have good uniformity over the active surface. Additionally, the material chosen for manufacturing microsensors should be easy to process and have sufficient width and thickness to control the heat generated. The commonly used metals for both microheaters and resistive sensors are Platinum (Pt), Gold (Au), Silver (Ag), Titanium (Ti), and Tungsten (W). One the other hand, some examples of metals used for thermocouple can be mentioned such Type K chromel/alumel, Type T copper/constantan, Type E chromel/constantan.

As shown in Figure 28, for the one element approach, Pt was selected as best and as default because of its chemical inertness, it does not oxidize with air at any temperature, and its resistance changes linearly with temperature [213,214]. However, noble metals with low reactivity such as Pt show poor adhesion to semiconductor and dielectric substrates such as Borofloat 33 [215,216]. This is because Pt is inert and cannot effectively bond with oxide surfaces. Therefore, a thin Chromium (Cr) with a thickness in the nanometer range is inserted as an adhesion layer between the Pt film and the substrate. Cr has good adhesion on glass and possesses a high temperature coefficient of resistance of about 4×10^{-3} K^{-1}, which guarantees a good sensitivity for resistance temperature sensor devices. On the other hand, in air or in an O_2, Cr is oxidized. Therefore, it is important to be cautious about the amount of Cr used as an adhesion layer. The bottom Cr layer on the glass should be kept at a minimum thickness to avoid thermomechanical mismatch [217]. However, if the amount of Cr is too small, the platinum (Pt) may detach from the Pyrex surface. Therefore, various thicknesses were tested to determine the impact on temperature exposure and the quality of adhesion.

As shown in Figure 28, for the two-elements approach, Pt is selected as heater, which can withstand high temperatures without issues. Recent advances in temperature control have led to the successful integration of MEMS platinum microheaters into systems [218–220]. Regarding the sensor, four metals were tested: alumel, chromel, constantan and cooper. In fact, as it was shown Figure 10 from chapter I section Temperature sensing 1.6.3.2, certain combinations of pairs of metals, like chromel/constantan (Type E) or type copper/constantan (type T) generate interesting properties such as producing the highest output voltage (Electromotive force or EMF) per degree compared to all other thermocouple combinations, which would be a suitable choice for temperature detection up to 200 °C. The thermal and chemical resistances protocol applied to the initial metals selected as well as their results are detailed hereafter.

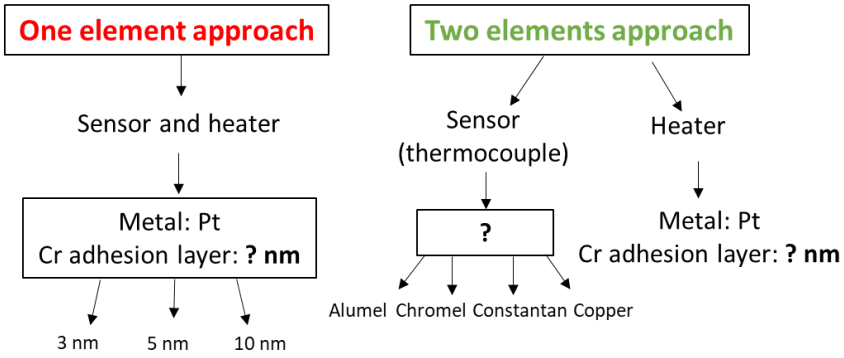

Figure 28: Schematic materials used for the one element and two element approaches.

2.2.2.1. Thermal and chemical resistance protocol

Thin films must have the ability to experience extreme temperatures and exposure to chemicals, as they are subjected to harsh environmental conditions during the measurement of a liquid's thermal conductivity.

For instance, these films may be exposed to high temperatures during operations or manufacturing processes of microfluidic devices, and it is crucial for them to remain intact and functional under such conditions. Any degradation or instability could lead to failure, loss of performance, or even damage to the entire system or device.

Moreover, thin films are often exposed to various chemicals, either during the microfluidic device fabrication or during their intended applications. Chemicals can include solvents, acids, bases, that might cause corrosion, chemical reactions, or erosion of the film material. It is crucial for the thin films to be stable against these chemicals to ensure longevity and reliability of the thin films. Any degradation or changes in their chemical composition can negatively impact their functionality and effectiveness.

To understand the effects of high temperatures on thin film metal samples, experiments were conducted. The samples were exposed to a temperature of 450 °C under air conditions for an extended period, this condition was chosen based on the initial operating conditions required to permanently seal silicon and glass in order to create a microfluidic device. The objective was to find out if the exposure had any impact on the properties of the sample, such as oxidation, corrosion.

Afterwards, a joint experiment was conducted to test the thin film metal samples under both thermal and chemical stress. The experiment involved exposing the samples to cyclic temperature conditions (200 °C) and a chemical solution at the same time under pressure. The purpose was to assess if the combination of thermal and chemical stress had any combined impact on the resistance properties of the samples.

The experiments involved testing ten different metals and alloys. Two duplicate substrates of chromel, alumel, copper and constantan were used, to represent the strategy of the two-element approach. Additionally, three substrates of platinum with varying thicknesses of a Cr adhesion layer (3, 5, and 10 nm) were used to represent the one-element approach. In all cases, 200 nm of metal

were deposited on a Borofloat 33 substrate (dimension 1 x 2 cm) and the stability protocol is detailed bellow:

Temperature resistance protocol

To successfully seal a microfluidic device, it is s first necessary to subject the samples to the bonding protocol conditions, which called for temperatures as high as 450°C for one hour. Thus, all samples were placed in an oven, the temperature rise is programmed for 1 hour until 450°C; then a temperature plateau is maintained for 1 hour. Finally, the temperature is decrease programmed for 1 hour (Figure 29). A X-ray diffraction (XRD) analysis was then performed to verify the integrity of the deposit.

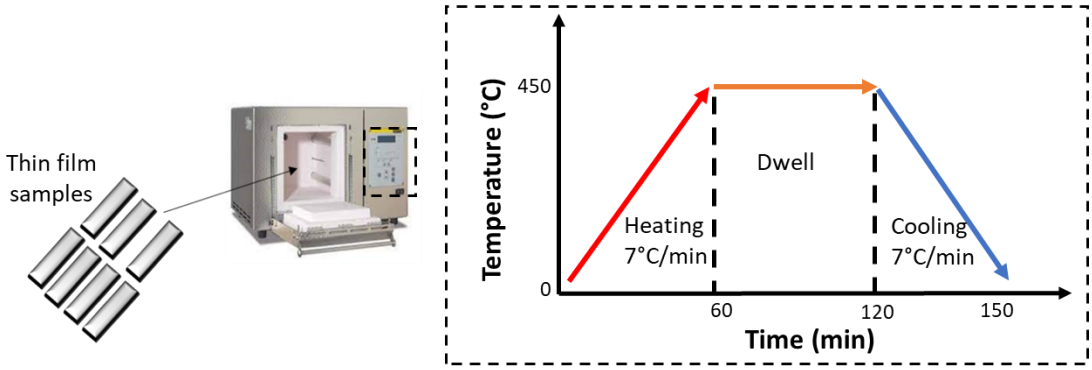

Figure 29 :Temperature bonding protocol.

Chemical resistance protocol

Chemical resistance tests, with the different substrates in contact with two different oxygenated compounds were then carried out. These tests aim at observing whether the sensor surface degrades under conditions close to those initially desired for measuring thermal conductivity (in temperature and in contact with an oxygenated compound), which would also provide an indication of the sensor's expected lifetime.

During this study, ethanol and 2,5-dimethylfuran (DMF) were chosen as compounds to test the resistance of the thin metallic films. Ethanol is a commonly used compound with well-known thermal conductivity properties being not harmful an easily accessible, while DMF is a combustible compound with less information regarding its thermal conductivity, containing other kind of functional groups (esters and furans) which could react with certain materials.

Each sample is placed separately in a high-pressure test tube, filled with ethanol or DMF. The safety data for each substance can be found in Appendix C. Then the tube is placed in the oven. Temperature rise is programmed for 30 minutes until 200 °C (increase of ≈ 7 °C per minute); then a temperature plateau is maintained for 3 hours, which represents a time compromise to expose the sensor for a reasonable time to test the performance under these conditions. Finally, the decreasing temperature is programmed for 30 minutes (decrease of ≈ 7 °C per minute) until reaching 25 °C. This protocol is repeated three times (Figure 30). Before and after exposing the samples to temperature, their resistance was measured using the 4-wire principle. This method was selected to investigate the impact of surface degradation or adhesion layer thickness on electron transfer. It is a method used

to measure resistances accurately in electrical measurement systems. It uses four separate wires - two for carrying the current and two for measuring the voltage drop. This eliminates any errors caused by resistance in the connecting wires, resulting in highly accurate measurements, especially when the resistance being measured is small compared to the total resistance of the circuit. More details about this technique can be found in Appendix B. This measurement only provides qualitative information about the conduction of the metal surface. The obtained values have been normalized from 0 to 1, with 0 referring to complete damaged or removed thin metallic film from the surface and 1 to a no damaged surface so there will be a conduction.

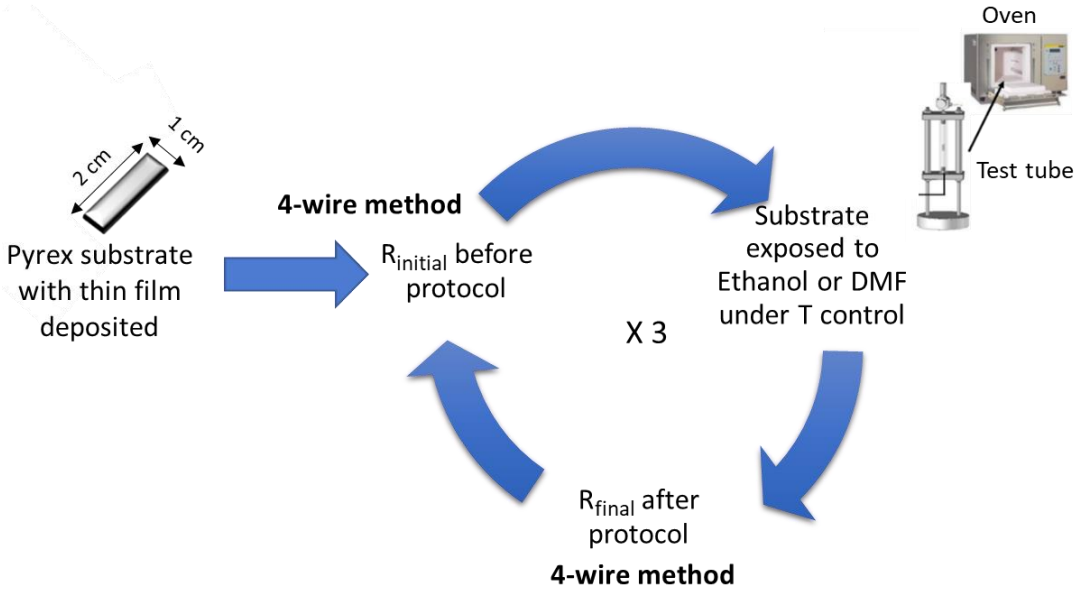

Figure 30: Cycle used for the aging metallic test under pressure and temperature.

2.2.2.2. Thermal and chemical resistance results.

Temperature stability is important for both RTD (single metal) and thermocouples (pair of metals). If the temperature is not stable, the temperature reading may be distorted and give an inaccurate reading. Likewise, compatibility with chemical compounds is important, as chemical compounds can damage the materials, resulting in loss of accuracy or total failure. The use of thin-film thermocouples with Pt with the Cr adhesion layer requires careful consideration of chemical compatibility because the small layers of electrode materials can be easily affected by chemicals, leading to unstable temperature reading or complete loss of their function.

Thus, a comprehensive understanding with respect to chemical compatibility is necessary to ensure accurate temperature measurement and long sensor life. Parallel measurements were stablished to test thermal and chemical resistance of the different metals.

Temperature resistance

Sensors can experience accuracy issues if they suffer from oxidation, which can happen when they are exposed to high-temperature gases or air [221–224]. When oxidation occurs, an oxide film can be form on the thermocouple, compromising its durability and being less reliable over time. It is therefore important to prevent oxidation by using oxidation-resistant materials and reducing the exposure of thermocouples to oxidizing environments.

Apart from noble metals such as Pt, among other ones suitable for the thermocouples the most resistant to oxidation are alloys of nickel: chromel, alumel and constantan. These thermocouples are used for wide ranges of applications for the temperatures from -200 °C to 1100 °C [224]. However, when used in thin films, these alloys can be more sensitive to temperature variations and oxidation, which can influence their thermal behavior. Indeed, when the layer is thin, the diffusion zone of the atoms is smaller, which can lead to faster oxidation and lower thermal resistance [225]. In this regard, temperature stability needs to be tested because temperatures of up to 450°C are required for sealing the microchannel and the sensor.

As mentioned, the test consisted in exposing all samples at 450°C for 1 hour in the oven. Each Borofloat 33 substrate contains a metal deposition of 200 nm, Figure 31 a) illustrates the samples before the temperature resistance test, while Figure 31 b) shows the metals after the temperature resistance test.

The color changed for most of the sample, after exposing them to high temperature, meaning that the oxidation could take place for some sample. Before the exposure, a measurement with the 4-wire method was carried out to verify the conduction of each metal. After the exposure, the measurement was done again and this time, except for Platinum, no resistance was detected for the rest of the samples.

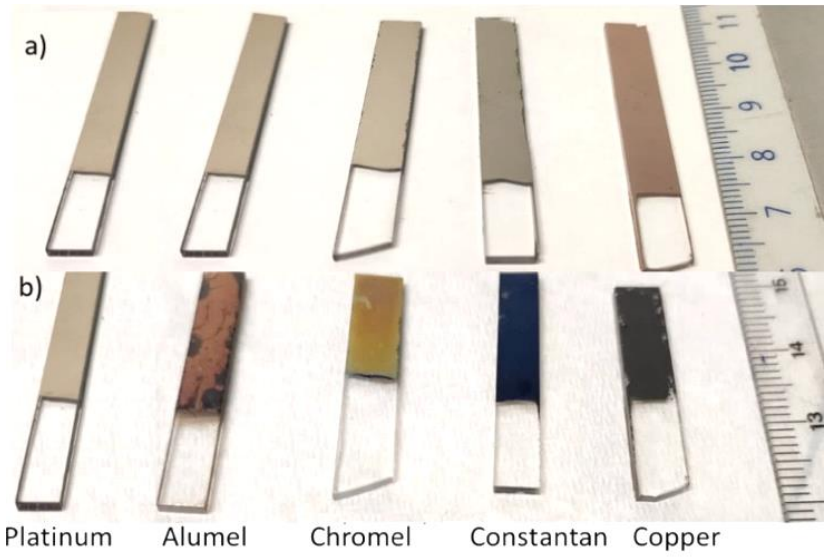

Figure 31: Metal deposition samples before (a) and after (b) bonding simulation protocol.

The study also found that the resistance of Pt did not vary depending on the thickness of adhesion layer used.

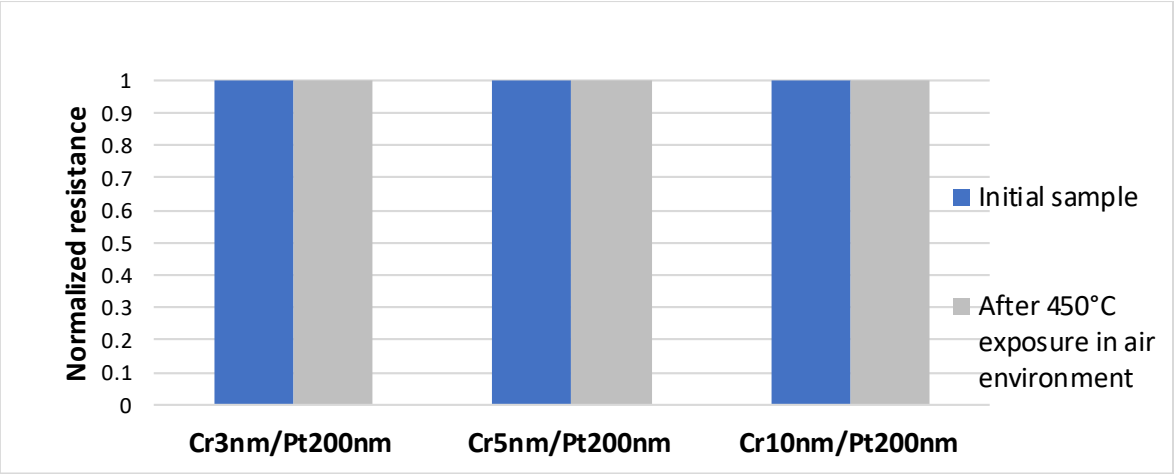

Figure 32: Resistance comparison before (initial) and after 450 °C temperature exposure.

No change is observed for Pt before and after the temperature exposure, being the only metal that resisted to high temperatures. For all the remaining metals, an XRD analysis was performed on the samples to confirm the oxidation hypothesis.

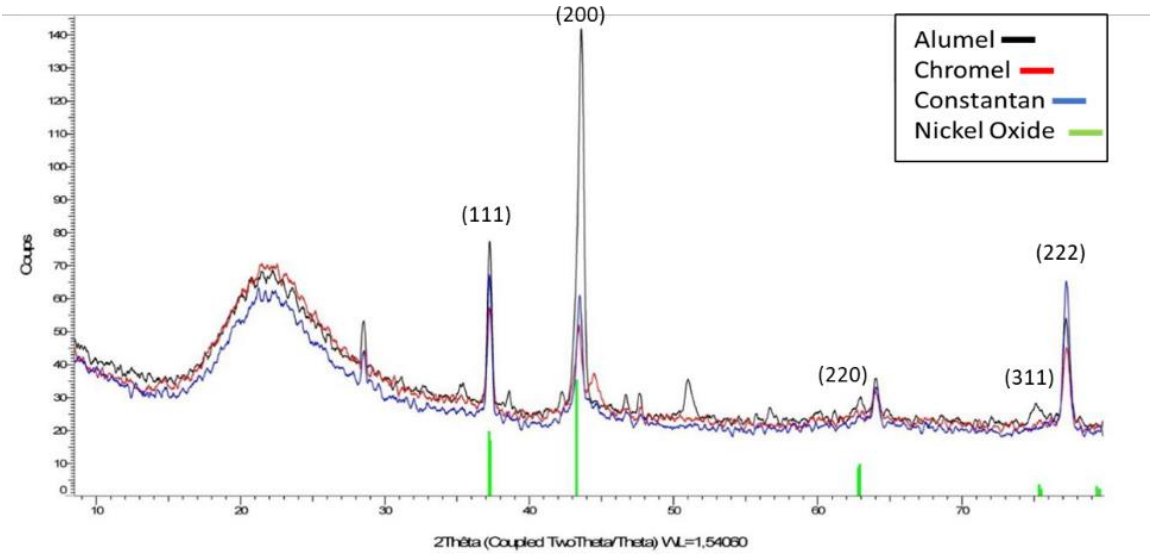

Figure 33: XRD spectra of Alumel, Chromel and Constantan thin films after exposure to high temperatures. Green peaks represent the Nickel Oxide phase.

The XRD spectra in Figure 33 shows the alumel, chromel and constantan after exposure. All these samples contain at least 50 % of Ni, Nickel oxide is also present in all samples. It shows peaks having orientations in the (1 1 1), (2 0 0), (2 2 0), (3 1 1) and (2 2 2) planes, corresponding to the diffraction peaks indexed to the cubic phase of NiO which confirms the metals oxidation.

Chemical resistance

In parallel, samples with the same metals were subjected to tests in ethanol and DMF to determine their chemical resistance levels, following the protocol in Section 2.2.2.1. Each fluid underwent a total of three cycles. A resistance measurement was made between each cycle. The resistance of each sample was adjusted to a scale of 0 to 1, where 0 indicates a lack of detectable resistance and 1

indicates no change from the initial value. This can be seen visually as a deterioration or oxidation of the metal layer. The resistance of oxygenated compounds was tested on metals such as alumel, chromel, constantan, copper, and platinum. The results for each metal are provided, and photos of metal deposition samples before and after the chemical exposure can be found in Appendix D.

In Figure 34, for resistance to ethanol at 200 °C, a major degradation can be seen with constantan and copper. Other materials, alumel and chromel seem to resist well to the fluid at 200°C.

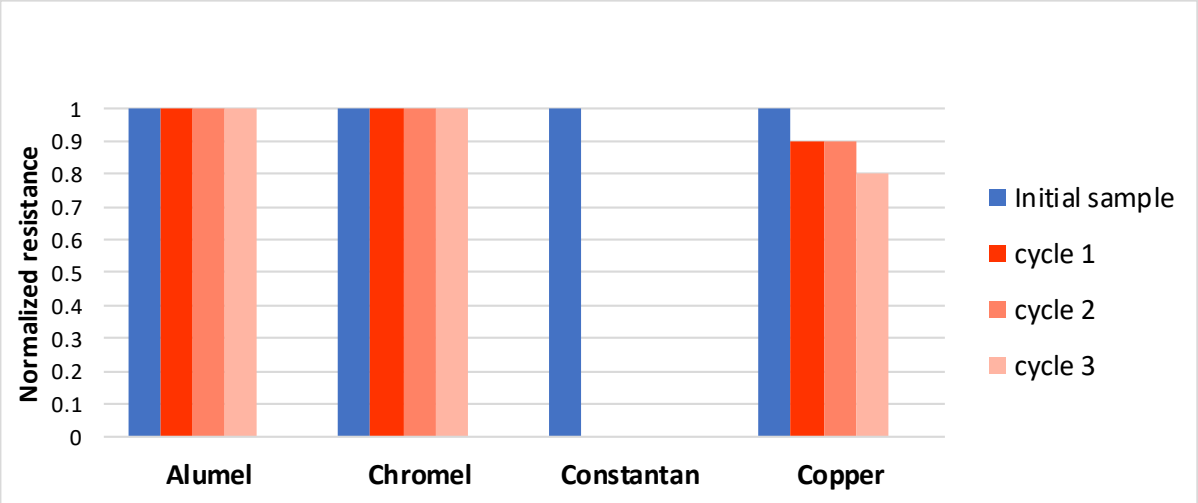

Figure 34 :Results before (initial) and after each cycle of experimental protocol using ethanol for alumel, chromel, constantan and copper.

Concerning the results with DMF at 200 °C in Figure 35, a degradation can be seen almost instantly with constantan and copper. Alumel and chromel seem to resist well to this fluid at 200 °C.

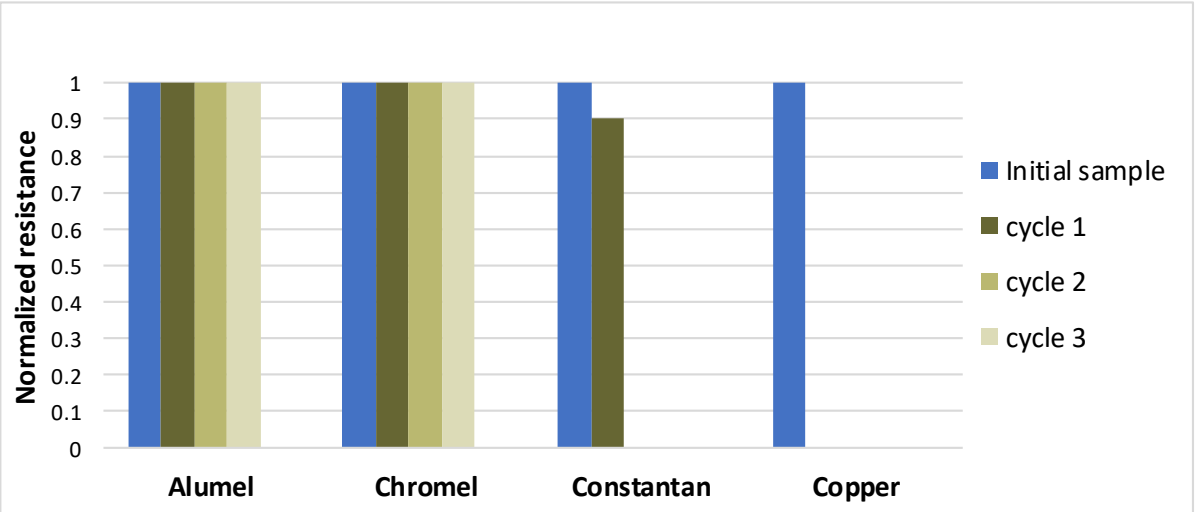

Figure 35: Results before (initial) and after each cycle of experimental protocol using DMF for alumel, chromel, constantan and copper.

Regarding Pt, the results using different adhesion layers, exposed to ethanol and DMF are shown below (Figure 36 and Figure 37).

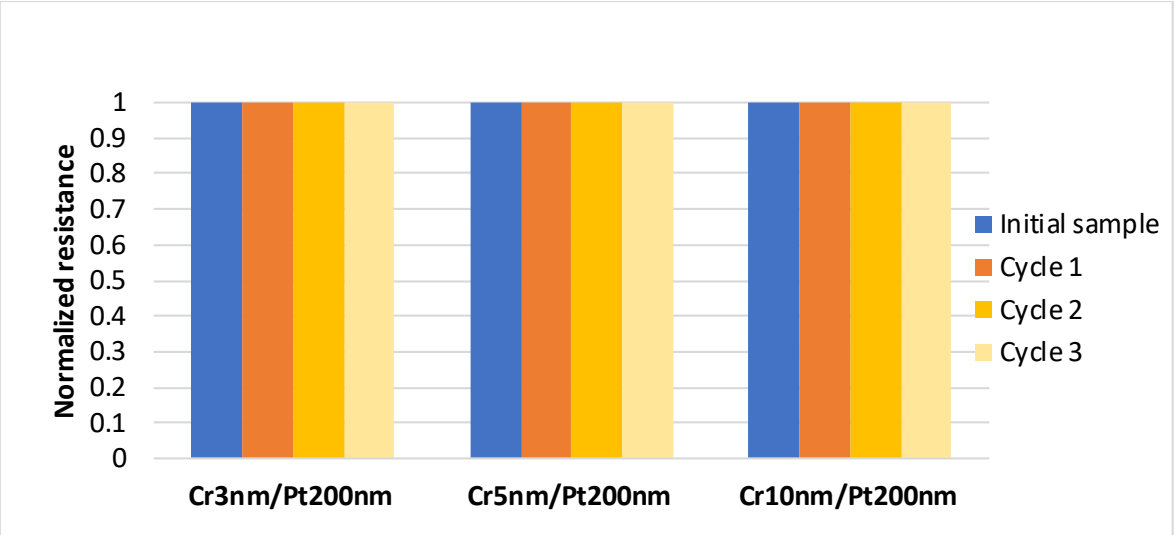

Figure 36: Results before (initial) and after each cycle of experimental protocol using ethanol for the different samples of Pt with three different adhesion layers of Cr.

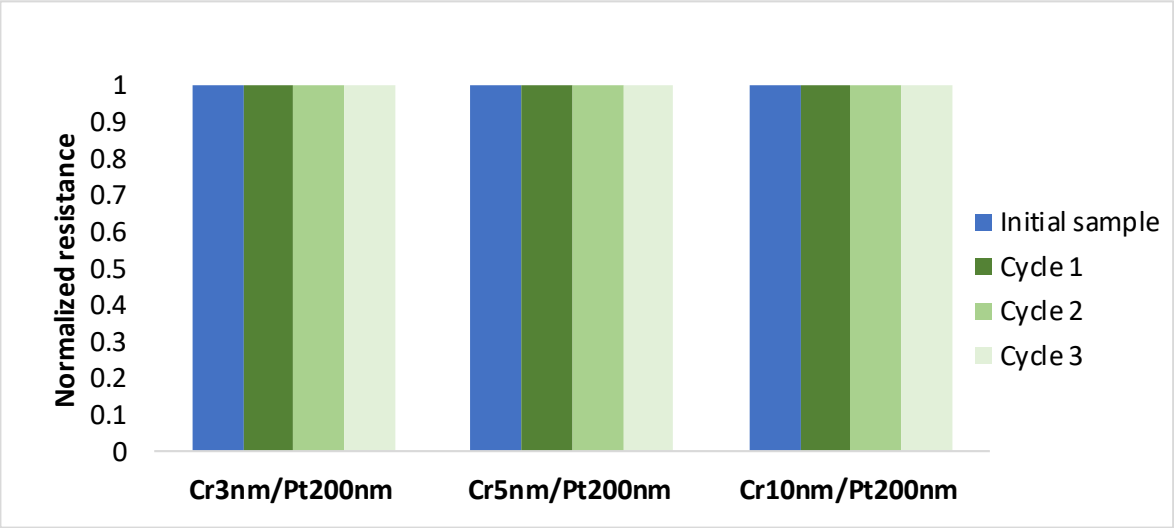

Figure 37: Results before (initial) and after each cycle of experimental protocol using DMF.

No change is observed for Pt before and after the cycles applied using ethanol (Figure 36) or DMF (Figure 37). This suggests that Pt can be also used as reliable sensor without being damaged by high temperatures or chemicals that cause instability. The fact that the values remain the same regardless of the thickness of the adhesion layer indicates that the adhesion layer does not impact the signal.

Since none of the metals selected for the thermocouple fabrication gave satisfactory results, we proposed to use Pt and an alloy Pt + 13wt% Rhodium as an alternative to keep studying both approaches (one and two-elements approach). Platinum rhodium (Pt-Rh) is known to withstand high temperatures and fluids conditions and has comparable properties as Pt [226]. Therefore, this pair corresponds to a type R thermocouple which is mainly used for high temperatures (above 600 °C) being less sensitive to lower temperatures.

2.2.3. Choice of sensor geometry

The design and material of the microheater and/or sensor play a critical role in enabling low power consumption, low thermal mass, effective temperature uniformity across the device, and enhanced thermal insulation from the surroundings. The resistance of the heater/sensor is extremely dependent on its physical dimensions. In general, ideal microsensors should have the following characteristics: sufficient durability during assembling, minimal size to reduce the influence on the cell performance, low cost, and easiest fabrication. The microheater/sensor design can vary depending on the application, from simple wire or line patterns to complex wing-shaped patterns to provide uniform thermal distribution and it is designed to have two contact pads. These pads allow the passing of electrical current through the metallic design and at the same time to measure the resistance (RTD sensor type) or voltage (thermocouple sensor type) across it. The sensor designs are made beforehand using the AutoCAD software and then printed.

Multiple research works have proposed the design of a simple metallic line. Nonetheless, the most current geometries used are meander and spiral structures, mainly because of their higher surface contact [227]. However, meanders have shown issues on several occasions regarding their temperature uniformity [228,229].

Various designs and geometries were investigated and fabricated, illustrated in Figure 38: spirals with different types of dimensions (b) long meander and small triple meanders.

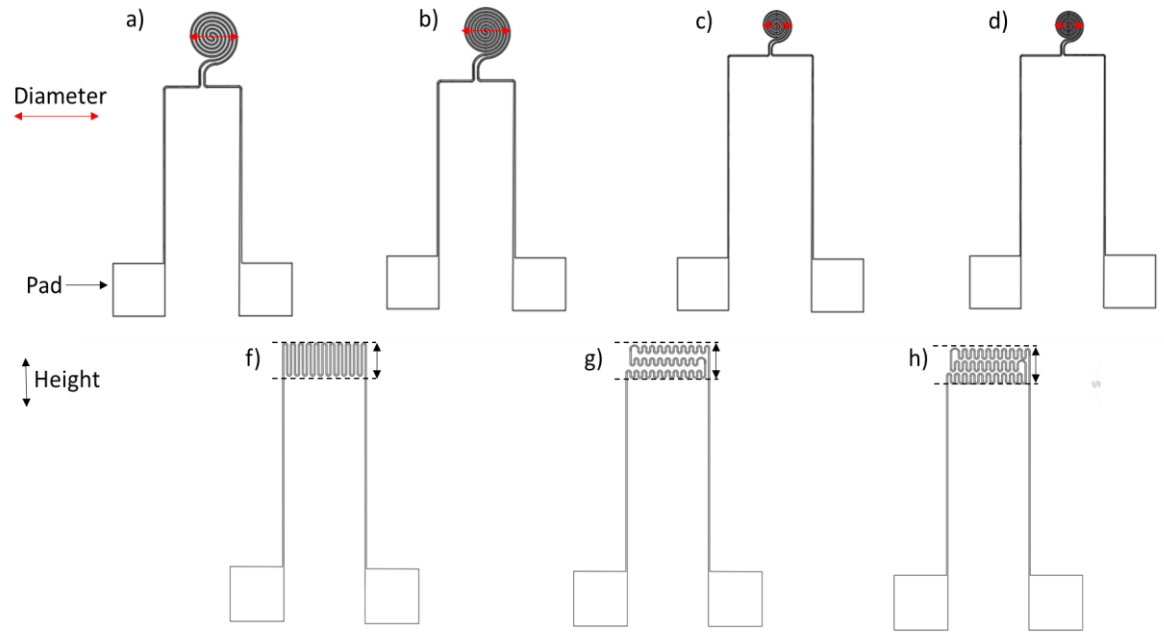

Figure 38: Schemes of the different designs and geometries investigated for the one element approach designed by AUTOCAD. a) 2 mm diameter spiral with 0.1 mm of spacing (6 concentric rings), b) 2 mm diameter spiral with 0.075 mm of spacing (7 concentric rings, c) long meander with 11 round arcs, d) triple medium meanders with 29 round arcs, e) triple small meanders with 29 round arcs.

Table 5 : Detailed dimensions of the designed spirals sensors.

Dimensions	Spiral (a)	Spiral (b)	Spiral (c)	Spiral (d)
Diameter (mm)	2	2	1	1
Width (mm)	0.05	0.05	0.03	0.03
Spacing (mm)	0.1	0.075	0.06	0.045
Total length (mm)	40	44	24	26.5
Total surface (mm^2)	2.00	2.20	0.72	0.80

Various dimensions were chosen to study how the surface area of the sensor and the reduction of dimensions affect the detected signal. For instance, in Table 5 sensor a) and b) were chosen as maximum dimension for spirals to keep a reasonable microchannel size. Both sensors, have the same external diameter but different total surface areas. Indeed, the spacing between the metallized the rings of the spiral a) is 0.1 mm (with a total of 6 concentric rings) and b) 0.075 mm (with a total of 7 concentric rings). Spiral c) and d) are miniaturized versions of the two sensors mentioned, which would enable a reduction in the size of the microchannels and therefore be able to withstand harsh conditions in terms of pressure. However, the detected signal might be less sensitive when using smaller dimensions.

Table 6: Detailed dimensions of the designed meanders sensors.

Dimensions	Meander (f)	Meander (g)	Meander (h)
Length (mm)	3.2	3.2	3.2
Height (mm)	1.22	1.22	1.22
Width (mm)	0.05	0.05	0.05
Spacing (mm)	0.1	0.1	0.1
Total length (mm)	55	43	55
Total surface (mm^2)	2.75	2.15	2.75

As observed in Table 6, meanders f) and h) have the same external size and surface area, but different pattern. We are interested in finding out whether this pattern difference alters the temperature and creates different signal responses. Additionally, we have also tested different total surface area, which is the case for meander g).

For the two-element approach spiral-shaped heater was used with a 1.5 diameter with 6 concentric rings, each having a width and spacing of 25 µm and 50 µm, respectively. The spiral is being used solely for heating purposes. Thus, we have selected a suitable size to ensure a uniform distribution of temperature. In the case of the thermocouple, we opted for an overlapping of both materials (metal 1 and metal 2) to generate the Seebeck effect. Several designs were tested, but the design shown in Figure 39 was retained as it was more convenient to develop during the microfabrication process. Besides, the smaller junction area could benefit the sensor's performance; however, it may

raise durability issues. Thus, junction size of 50 µm x 50 µm is chosen. Both thermocouple and heater designs are illustrated in Figure 39.

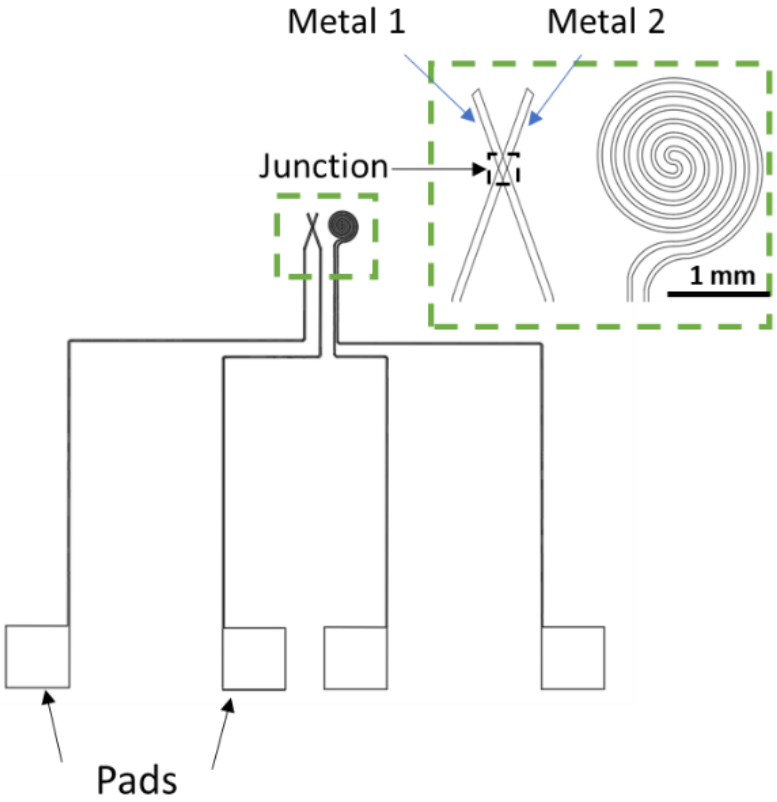

Figure 39: Thermocouple and spiral designs by AUTOCAD. Zoom of the thermocouple and spiral (green frame) and visualization of the junction in black dotted frame.

The advantage of the one element configuration is that implementing the same material and fabrication technique will simplify the fabrication process, structure, and cost. On the other hand, with the use of a separate sensor and heater, the instrumental detection and the signal treatment are easier to implement. The next section will provide more information on the bi-layer photolithography microfabrication method, which allows for the integration of metallic sensor design on a Pyrex substrate. This method involves using photolithography to pattern layers of thin film metals.

2.2.4. Bi-layer photolithography

Once the metal and sensor design are defined, the microfabrication begins. Microfabrication is carried out in a cleanroom to maintain a controlled environment that is free from dust, particles, and other contaminants that can impact the quality and consistency of the microfabrication process.

To fabricate our microsensor, we use a bi-layer photolithographic process, which involves depositing a thin metal film over a patterned photoresist resin. This process uses a non-photosensitive polymer layer and another photosensitive layer to transfer a design onto a substrate using a mask and UV exposure. This technique is widely used in the production of integrated circuits, as it allows for the precise formation of complex patterns with high resolution and accuracy. The different steps are detailed hereafter.

The sensor device consists of the selected geometries and square contact pads deposited on a borosilicate glass substrate (Borofloat 33, Schott). The metal film is deposited on the borosilicate substrate using a bi-layer photolithography process using two resin layers: a non-photosensitive resin (Lift-Off Resists, LOR) layer and a photoresist resin layer. The LOR is used as a sacrificial layer for the deposition. This technique allows accessing high resolution and high aspect ratio structures [230].

The process starts with the use of a borosilicate glass substrate spin-coated with LOR resin from Micro Chem Corp, at 750 rpm for 45 s, allowing the layer to spread out to a thickness of 0.7 µm. For clean lift-off processing, it is suggested that the LOR film should be thicker than the metal deposition thickness, typically 1.1 to 1.3 times [231]. The substrate is placed on a hot plate, and the resin undergoes a baking step for 3 min at 150°C. Then, a positive photoresist resin (S1818 - Shipley) is spin-coated at 1200 rpm for 30 s on the same substrate, resulting in a photoresist resin layer of 4 µm thickness on the silicon surface. The substrate is then placed on a hot plate, and the photoresist resin undergoes a pre-baking step for 4 min at 115 °C. The substrate is then exposed through the photomask to ultraviolet (UV) using a LED UV-masking insulator (UV-KUB2, KLOE) at 40 mW/cm^2 (λ = 365 nm) for 45 s. The exposed photoresist resin is then developed using a MF319 developer (Shipley) for 40 s. The substrate is rinsed with water, and the wafer is finally post-baked for a final 6 min at 115°C to ensure its strength after the development stage. At this stage, the pattern is developed in the two layers (the LOR and the photosensitive resin). The cross-section illustration after the UV exposure and development is presented in Figure 40. An undercut between the polymer LOR and the resin is formed, which ensures the high resolution of the spiral geometry [232]. Figure 40 illustrates the steps followed during the bi-layer photolithography process.

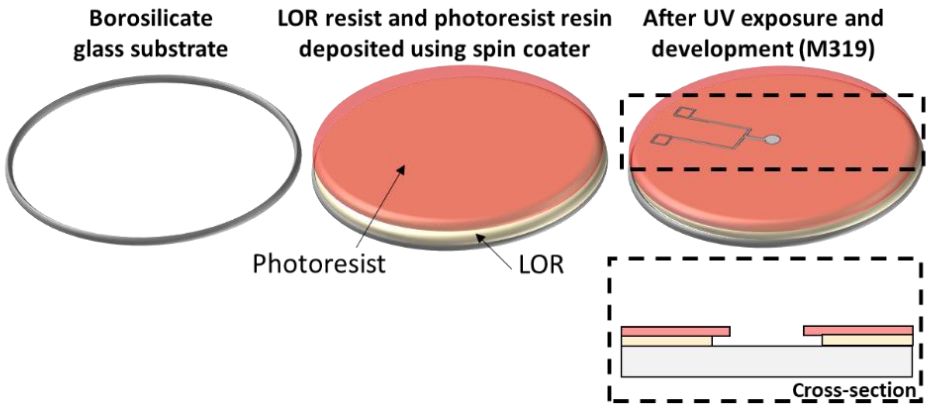

Figure 40:Illustration of the bi-layer photolithography steps used for sensor fabrication.

Once the photoresist resin is fully developed and the photoresist resin stops dissolving, the developer continues to dissolve away the LOR layer in the borders of the open areas. Undercut width increases with the standard photoresist resin development time (as shown in Figure 41 a)), and/or when decreasing the bake temperature (as shown in Figure 41 b)), and vice versa if the development time decreases and the bake temperature rises. These parameters are adjusted to suit the deposition requirement.

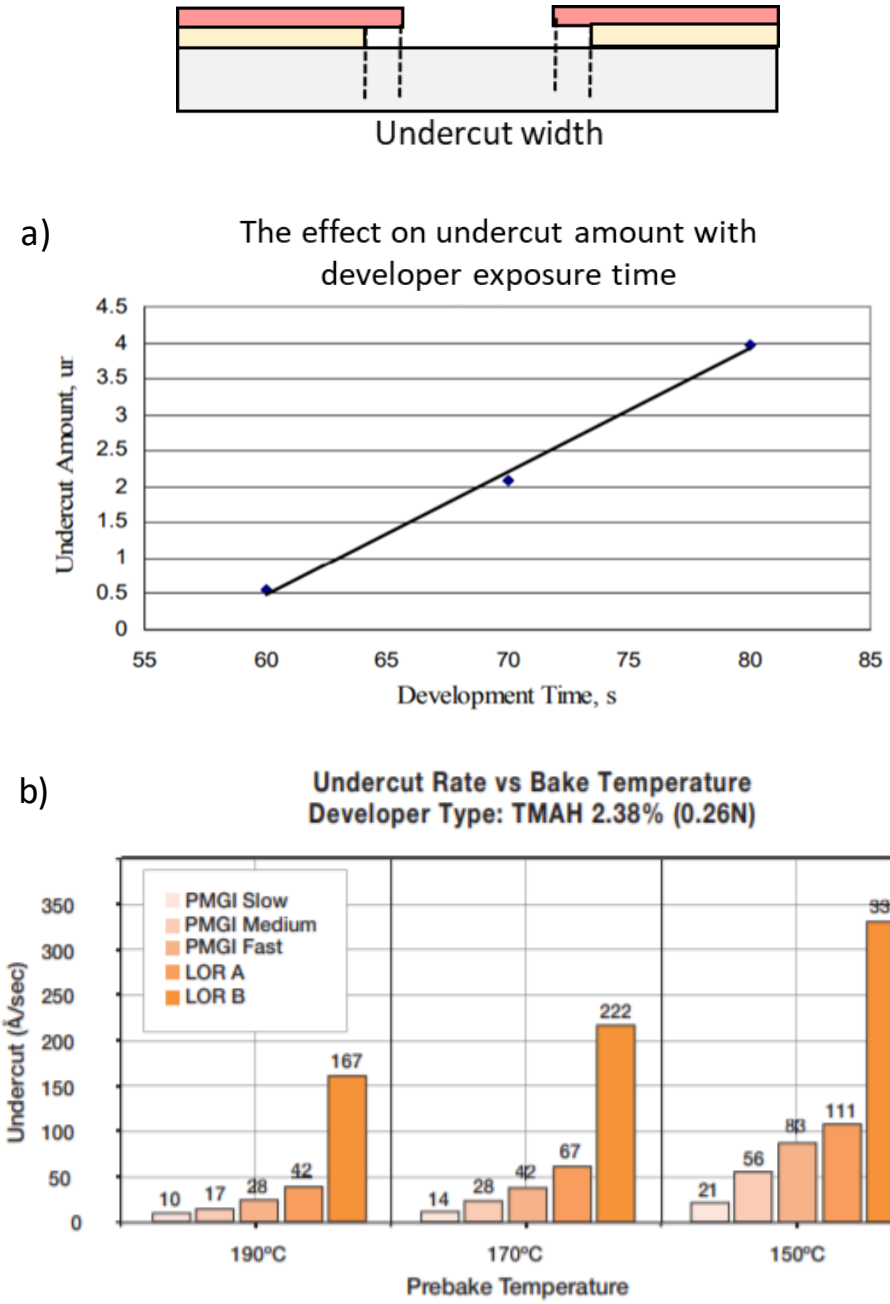

Figure 41: Effect on undercut while modifying develop time and bake temperature [233].

During the bi-layer photolithography process, LOR type B was employed. The difference between Type A and Type B LOR is their solubility properties. Type A is soluble in alkaline developers, while Type B is soluble in organic solvents, allowing for an efficient lift-off.

Thin film metal deposition and removal of the exceeding metallized section

After the bi-layer photolithography, the metal deposition of thin films is performed using magnetron sputtering using a Plassys MP450 system. Due to the lack of adhesion of the Pt on glass, we first deposited a Cr film adhesion layer of 5 nm, on the top of which a 200 ± 20 nm thick Pt film, is deposited to elaborate resistive elements in the ≈ 10^2 Ω range. The parameters used to perform the deposition are the following: Argon as discharged gas with a pressure of 1 Pascal and 30W RF Power

(13.56Mhz) with a deposition time of 40 min, the distance between the target and the substrate is fixed at 80 mm. After de deposition, the substrate is placed in a beaker and the photoresist resin is dissolved using a commercially available remover, N-Methyl-2-pyrrolidone (NMP) based solvent stripper designed for efficient photoresist resin removal (along with the undesirable metallic deposited surface). These steps are illustrated in Figure 42.

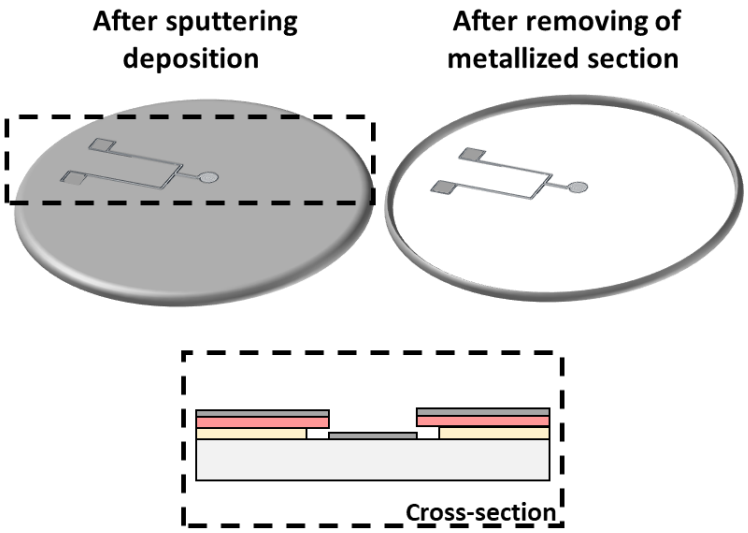

Figure 42: Illustration after metal deposition step and final sensor.

2.2.4.1. Optimization parameters for the bi-layer photolithography

The process of bi-layer photolithography needs to be improved and adjusted depending on the shape and size of the metal deposition, as well as the chemical products used during the process (polymer, resin…).

Bi-layer photolithography involves removing the bottom layer of photoresist resin to create a lift-off profile, which is mainly used for patterning metals in a discontinuous film deposition. The undercut created by this process enables the removal of metal deposit on the resin without affecting the deposit on the Pyrex®. Controlling the amount of undercut is crucial as it affects the final pattern's resolution and shape. To control the undercut, the etching conditions such as the developer chemistry, concentration, temperature, and time exposure must be carefully chosen. Thus, to have an optimal bi-layer photolithography process numerous tries were carried out. The examples of undercut morphologies in the bi-layer photolithography affecting the final pattern are:

- If the undercut is too small, it can lead to incomplete removal of the upper layer, resulting in poor pattern fidelity and compromised device performance. This can occur if the development time or the concentration of the developer solution is too low [233].
- If the undercut is too long, it can affect the resolution and edge sharpness of the pattern. With long undercut, the pattern will lose its fine details and become distorted, which happens when the development time is too long. This can result in poor quality and reduced precision in the final product [232].

Figure 43 provides two specific experimental examples from the thesis work that demonstrate the effects of having undercuts that are either too short or too long. The first example 1) shows visible

geometries on the resin but a poor execution of lift-off (too short undercut), while the second example 2) involves overdeveloping with poorly defined geometries in the resin (too long undercut). These undercuts are controlled by the development time in the photolithography process.

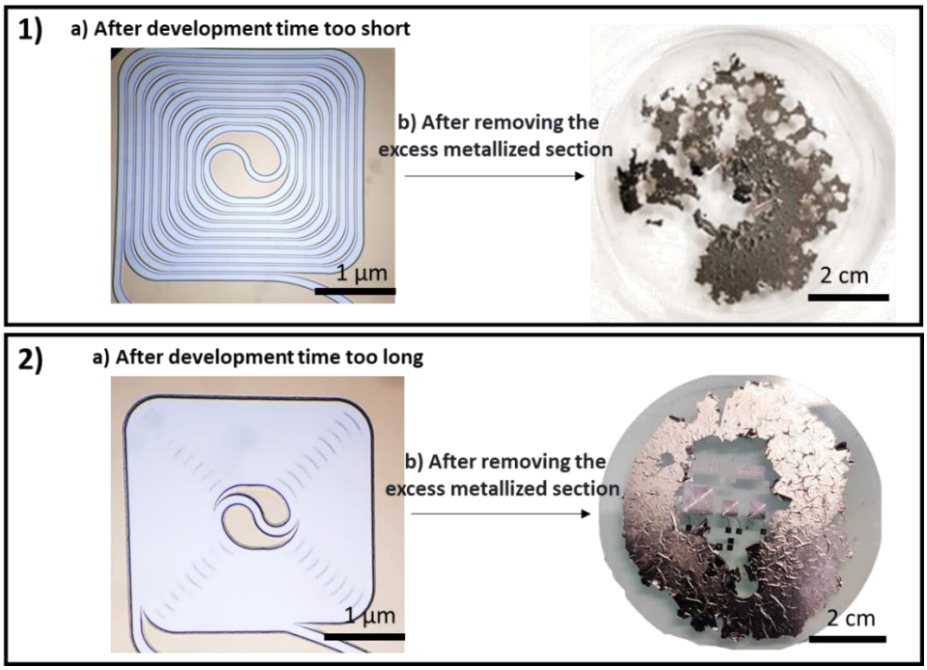

Figure 43: Two examples of 1) a) too short development time (< 20 seconds) with well design patterns followed by b) removal of the exceeding metallized section causing the pattern to spread out completely. 2) a) too long development time (> 60 seconds) loss of resolution followed by b) removal of the exceeding metallized section without the spread out of the pattern.

To control the undercut using the LOR polymer, the development time and the bake temperature are the two main parameters to be considered. For instance, the accuracy of the lift-off is strongly affected by modifying the width of the undercut. The strategy to obtain an optimal lift-off was to modify the development time and bake temperature to obtain a higher undercut with respect to the initial conditions. The initial and optimized conditions are shown in Table 7.

Table 7: Initial and optimized conditions modified during the bi-layer photolithography process.

Initial conditions		**Optimized conditions**	
Development time (s)	30	**Development time (s)**	45
Bake temperature (°C)	170	**Bake temperature (°C)**	150

Modifying only the development time to increase undercut should be done carefully as too much time can lead to overdevelopment. As a complement to avoid overdevelopment, adjusting the baking temperature was employed to enhance undercut.

- **Optimized parameters**

The following figures show some examples of final the microsensor type RTD and thermocouple (Figure 44).

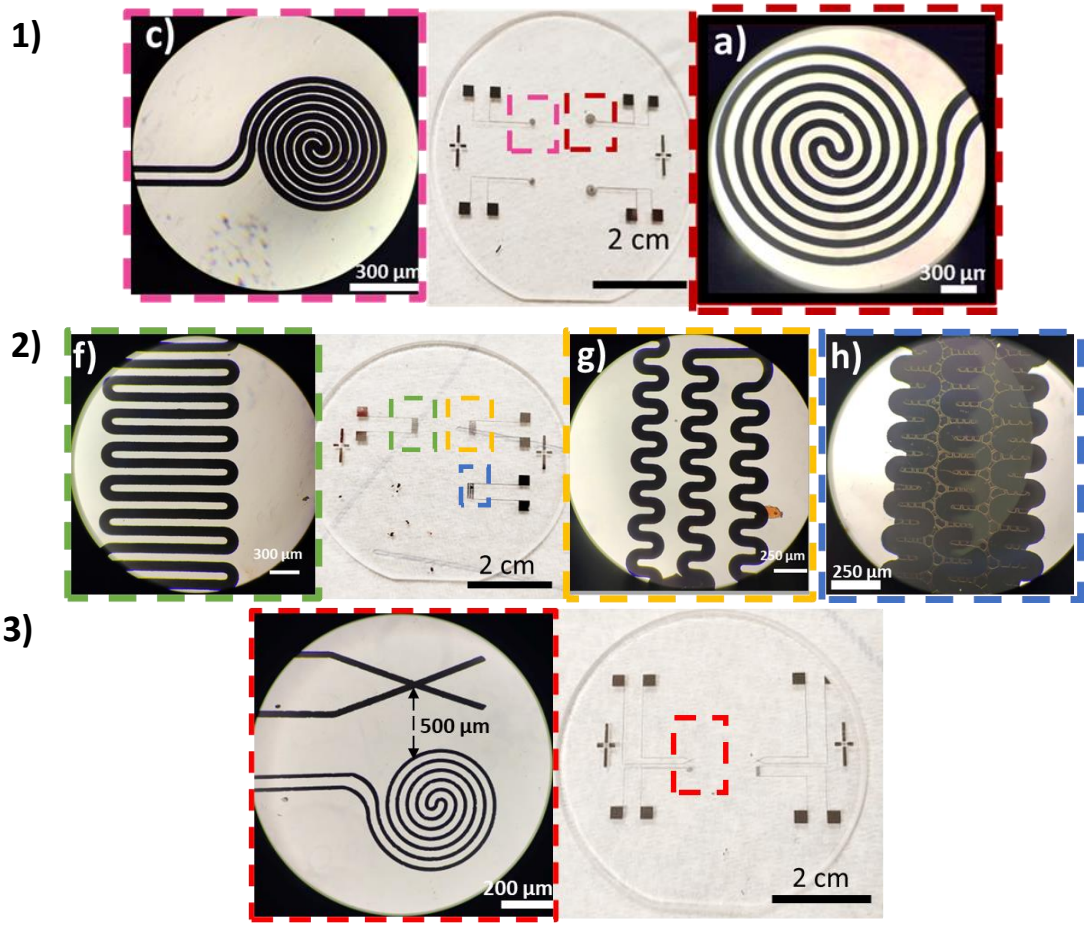

Figure 44: Lift-off of the spiral RTD type microsensor deposited 1) spirals 2) meanders and 3) the thermocouple type microsensor along or spiral geometry (up) used as heater, deposited on a Pyrex substrate.

This demonstrates that the lift-off is proven to be highly effective in patterning various complex shapes and small dimensions when the ideal settings are used. However, as observed in Figure 44, it was not possible to remove the excess metallization from sensors h, as well as for sensor d. The gap between the concentric rings and meanders was too small (less than 0.040 mm of spacing) for the commercial remover to effectively remove the exceeding metal. Removing the metallized part required significantly more time compared to the commercial remover (an additional 30 minutes in the remover). Extending the time in the remover resulted in the removal of the pattern on the sensor. Despite multiple attempts, the removal was not successful with these designs.

Additionally, as shown in Figure 44 example 3), for the thermocouple, the distance between the heater and the sensor is of 500 µm, this distance would be important at a later stage to determine the dissipation of the heat towards the sensor.

2.2.5. Sensor signal measurement before integration in microfluidic device

Once the sensor fabrication is achieved thanks to the lift-off process, it remains to observe whether a measurable signal is obtained and how it behaves with respect to temperature. Both types of sensors were characterized thanks to a multimeter using the 2-wire method for Pt (RTD sensor) and for Pt/PtRh (thermocouple) sensor a voltmeter (nanovoltmeter) with high sensitivity for small voltages (millivolts) was used. Both techniques will be explained, and results will be discussed.

To connect the sensor to the measurement circuit, contact pads were patterned on both ends of the sensor. Contact pads are used in microelectronics and microsystems to bridge the length-scale gap between on-chip microscale interconnects and macroscale devices. The measurement instrument is connected to the metal pattern *via* two spring loaded pogo-pins (Figure 45) placed on the contact pads. As the name suggests, a pogo pin is a linear spring-loaded pin that presses against a contact pad. Pogo pins are a low-cost and easy to execute alternative in comparison to micromanipulators or wire bonding.

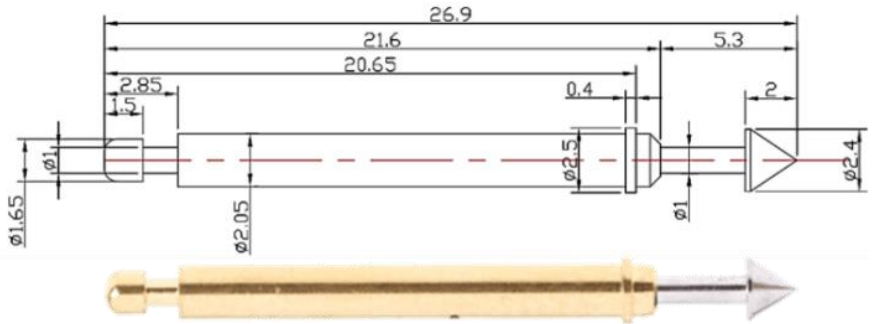

Figure 45: Pogo-pin RS Pro 20 with respective dimensions in mm, from ref. [234].

2.2.5.1. Resistance measurement for RTD type sensors

The main factor in determining thermal conductivity is the resistance of the microsensor [235]. The theory behind this type of sensor, called RTD, is that the resistance of a conductive material changes with temperature. In this study, the Pt spiral is considered an RTD and will be used for both sensing and heating.

Two-wire method

The most common method for resistance measurement is the two-wire method, imposing a current (by imposing a tension) and using a multimeter to measure the desired resistance. The resistance measured by the instrument is the sum of the wiring resistances (R_{wire}) and the unknown resistance (R_0), shown in Figure 46. When measuring resistances that are significantly higher than the resistance of the wires being used (greater than 10 Ω), the resistance of the wires has little effect on the measured value. Therefore, the measured value will be closed to the actual resistance value. This also applies to sensor measurement that have resistance values over a hundred of Ω.

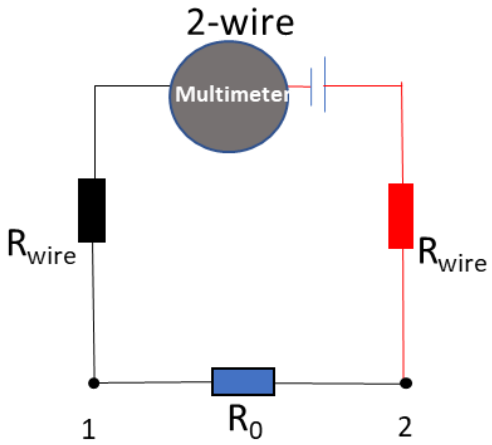

Figure 46: Schematic of the 2-wire method.

2.2.5.2. Thermocouple measurement

As already mentioned in Chapter I section 1.6.3.2, the Seebeck effect is used in thermocouples, which are made up of two different metal wires joined at two junctions. This effect occurs when a temperature difference between two different metals in contact generates a voltage. The thermocouple is usually connected to a voltmeter, which measures the electromotive force produced.

When the Seebeck voltage take places, it is usually nonlinear with respect to temperature. However, for small temperature variations, the voltage can be approximated by:

$$\Delta V \approx S\Delta T$$

where ΔV is the change in voltage (V), ΔT is the change in temperature (K) and S is the Seebeck coefficient (V/K).

To avoid undesirable thermocouple interactions coming from external metals, the connections to the instrument should be simple. Each association from wire terminal, to pad contacts can create a new junction. In the ideal case, the electrical interface (pogo pin) should have the same material that the sensor. Since the electrical interfaces connected to the voltmeter are made of the same material and at the same temperature, there is no creation of dissimilar metal junctions, and this does not impact the measurement.

2.2.5.3. Experimental set-up for both resistance and voltage measurement

A custom-made equipment was created to ensure consistent and replicable measurements. This equipment includes two 3D printed pieces (black) that holds and fix the pogo pins, an insulation platform, and a heating element. To reduce contact resistance, the pogo-pins are coated with silver conductive paste. Two thermocouples are used to measure and control the temperature, with one placed between the Pyrex substrate and heating element and the other as close as possible to the sensor. The resistance or voltage values as a function of temperature are recorded when both values stabilize (after 10 minutes). Consequently, the plot of resistance or voltage variation versus temperature is set. The illustration of the set-up is shown in Figure 47.

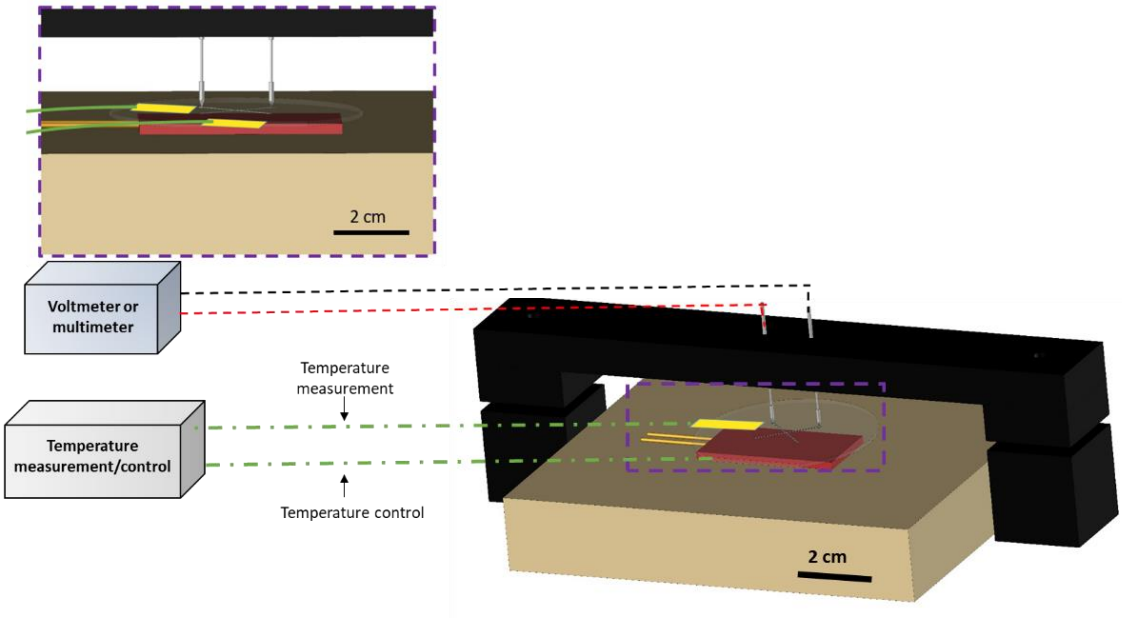

Figure 47: Illustration of the resistance and voltage set-up.

2.2.6. Experimental results

- **RTD sensor**

The electrical resistance of the Pt increases linearly with temperature. The relationship between temperature and resistance is called the temperature coefficient of resistance TCR or α (detailed in chapter I section 1.6.3.2), which is expressed K^{-1}. The sensor should be made of a metal possessing a high TCR to produce a measurable change in its resistance as in function of temperature. Pt is the metal of choice, with a TCR of approximately 0.0039 K^{-1} [236] is relatively high and stable, making it an ideal material for temperature detection. The measurement of α was performed and the results with respect to the different spiral dimensions will be discussed.

The Figure 48 shows two graphs of the platinum resistance increase with respect to temperature from two different spiral dimensions. The first graph 1) correspond to the higher dimension demonstrates a linear relationship between resistance and changes in temperature, both when it increases and decreases. On the other hand, the second graph 2) with the smallest dimensions (surface divided by two) shows a linear resistance behavior when the temperature increases but it exhibits a hysteresis when decreasing the temperature.

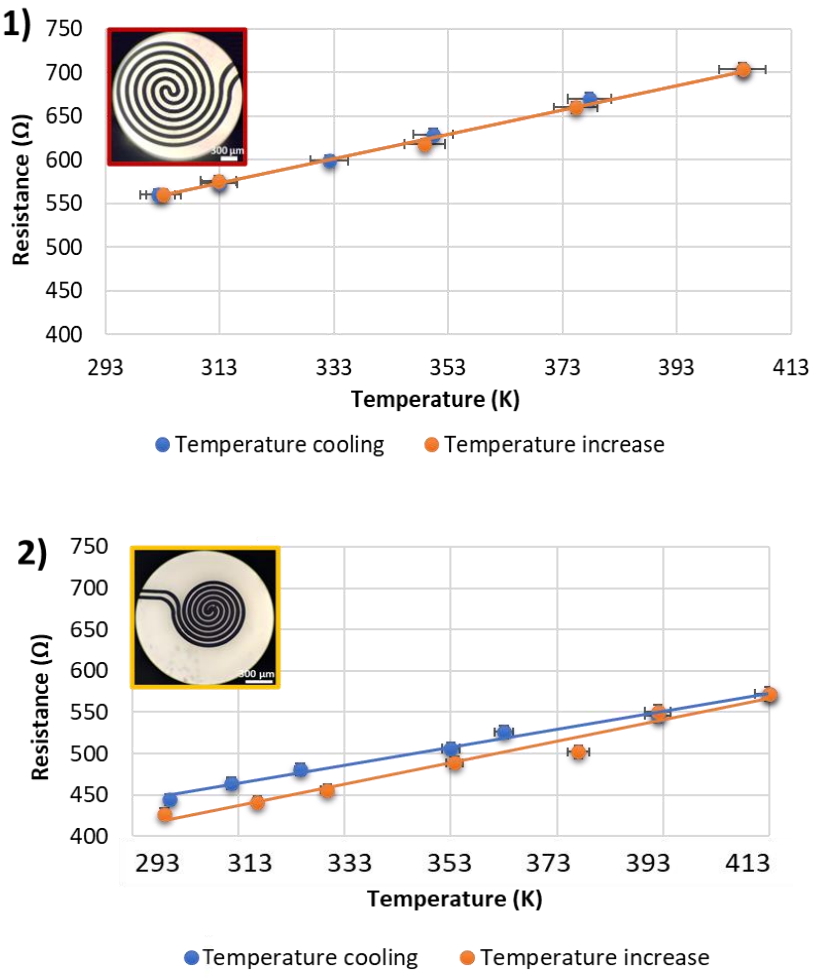

Figure 48: Measurement of resistance vs temperature of the two spirals geometries dimensions.

For both dimensions the temperature coefficient of resistance is calculated and shown in Table 8. The α calculated for sensor 1 is 0.0026 K^{-1} ± 0.0002 for the temperature increasement. This value is less than that for the Pt bulk found in the literature (0.0039 K^{-1}). Due to the size-limiting effect, some studies have shown that α Pt thin-film is typically lower than bulk [237,238]. Thin films have a reduced thickness, which limits the available space for electron movement in one direction, leading to a decrease in α. On the other hand, in bulk materials, electrons have the freedom to move in three dimensions, resulting in a larger number of potential electronic states and greater mobility. In addition, the surface area of the thin film is larger than in the bulk, which can lead to greater electron diffusion, also reducing α. Table 8 also shows the sensor 2 (having a reduced surface area than sensor 1), and its α values which are even lower with respect to the literature. Reducing the spacing between the concentric rings results in a more confined thermal environment. This restricts heat conduction pathways and increases thermal gradients within the spiral. As a result, the sensor's sensitivity is limited when it reaches a certain minimum size.

Table 8: Dimensions characteristics of each spiral sensor and α results.

Sensors dimensions	Spacing (mm)	Surface area (mm^2)	α increase (K^{-1})	α cooling (K^{-1})	Uncertainty
1	0.1	2.8	0.0026	0.0025	0.0002
2	0.06	1.3	0.0022	0.0018	0.0003

In the same way, Figure 49 shows the graph of the platinum linear resistance increases and decreases with respect to temperature for two distinct meander designs. In both cases, the resistance behavior of platinum remains consistently linear as the temperature is increased or decreased.

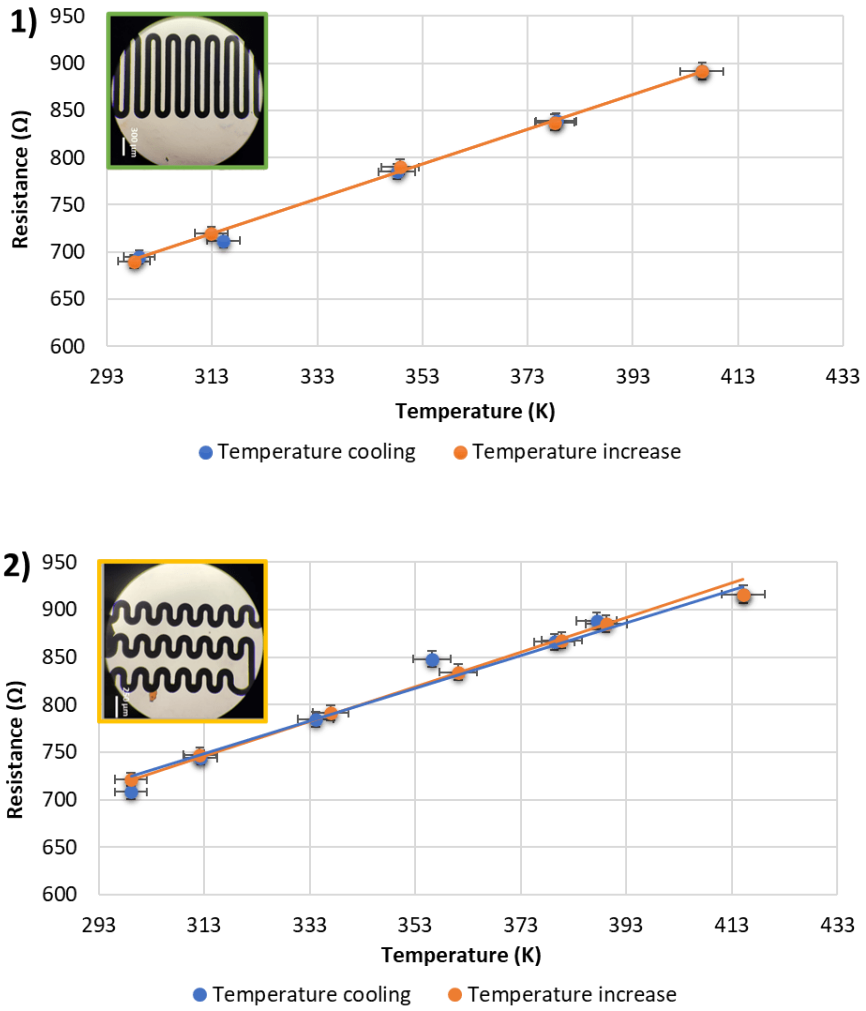

Figure 49: Measurement of resistance vs temperature of two spirals geometries dimensions.

For both dimensions the temperature coefficient of resistance is calculated and shown in Table 9. As well as from the spiral; the α calculated for sensor 1is 0.0026 K^{-1} ± 0.0002 for the temperature increasement. Sensor 2 the α calculated is 0.0024 K^{-1} ± 0.0004. In both cases, for spirals and meanders; higher surface areas induce higher α.

Table 9: Dimensions characteristics of each spiral sensor and α results.

Sensors dimensions	Surface area (mm^2)	α increase (K^{-1})	α cooling (K^{-1})	Uncertainty
1	2.75	0.0026	0.0024	0.0002
2	2.15	0.0024	0.0021	0.0004

- Thermocouple

We can observe the curve of the thermocouple EMF as a function of the temperature. As shown in Figure 10 from chapter I section Temperature sensing 1.6.3.2, the electrofemotive force (EFM) of the Pt/Pt-Rh (type R) reference is minimal at low temperatures, resulting in lower voltage across the junction for small temperature differences. This leads to higher measurement error compared to resistance temperature detectors (RTDs), with thermocouples having a 10% error and RTDs having a 2% error. This is significant because accurate temperature measurement is crucial when determining thermal conductivity. Also, it is observed that the change in EMF is negligible when heating the temperature from 293K to 333 K. Signal detection only becomes significant at 353K. We anticipated that the EMF would be improved in a microfluidic device, due to its confined environment. This can prevent issues with convection that could explain these significant errors.

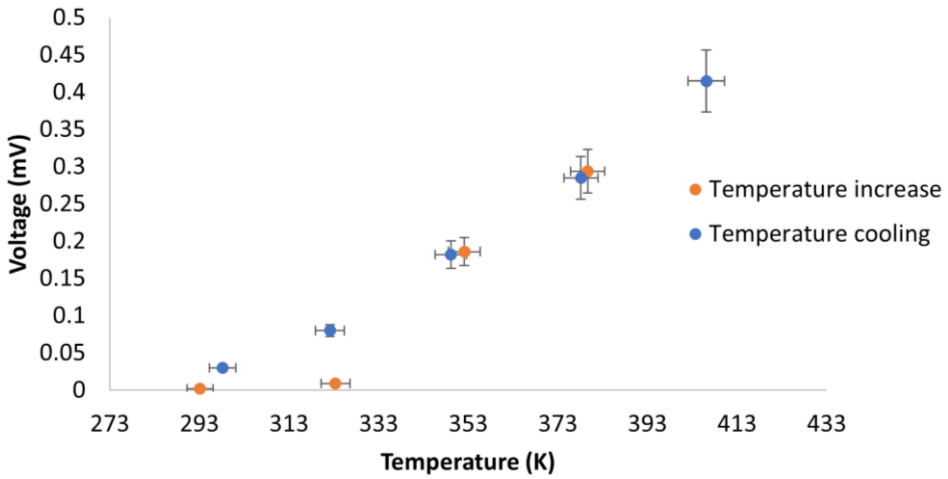

Figure 50 : Measurement of voltage vs temperature for the thermocouple configuration.

Once it was confirmed that both the RTD and thermocouple displayed a linear behavior change with temperature, the sealing between the fluidic part and the sensors can be implemented.

2.3. Microchannel fabrication

2.3.1. Choice of microchannel geometry

The microchannels were designed using the AutoCAD® software and then printed on flexible photomasks. As shown in Figure 51, for a) corresponding to the design of the one element approach, the measurement micropool has dimensions of 2 mm x 3 mm and for b) corresponding to the design of the two element approach, the micropool has dimensions of 1.5 mm x 3 mm and the main microchannel is 200 µm wide and 60 µm deep for both approaches. Two identical microchannels and sensors were created in order to have a larger number of units available for replication in experiments

and to provide a backup option in case one of the sides was damaged during the fabrication process or during the λ measurement. The size of the micropool was chosen and adapted based on the final sensor dimensions. The depth of the micropool was selected based on previous research that used volumes that were suitable for measuring thermal conductivity [30,42,134] . These volumes needed to be both small enough and large enough to detect a measurable signal (between 0.5µl and 4µl). This design enables the micropool to encompass the sensor, allowing the fluid to completely cover it.

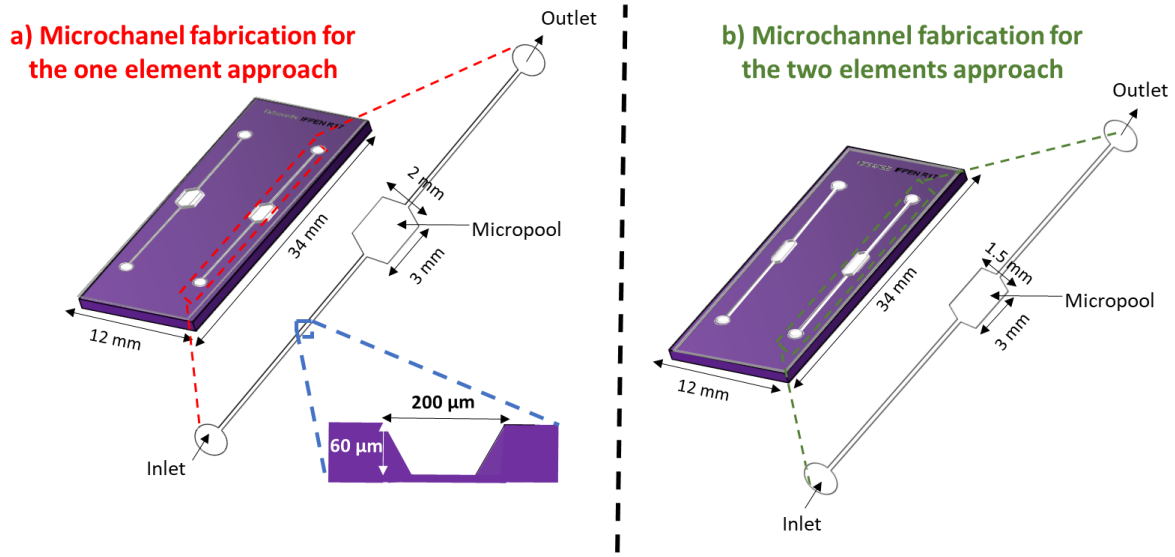

Figure 51: Illustration of the dimensions and geometries for methodology a) the one element approach and b) the two-element approach. The microchannel red and green dotted rectangles represent a zoom of the microchannel (micropool), blue dotted square represents the cross-section microchannel's trapezoidal geometry [1].

2.3.2. Photolithography

The desired patterns are drawn beforehand in silico using the AutoCAD® software. Once the mask geometry is established, it is printed at a resolution of 50000 dpi (dots per inch) on a flexible plastic substrate (photolithography mask or photomask).

The microchannel was etched on a silicon substrate surface following the standard photolithography and etching protocol, previously described and summarized hereafter [33]. The process starts with the use of a silicon wafer, covered with a 500 nm layer of SiO_2. The same steps with the same operating parameters mentioned in Section 2.2.4 are used to pattern the photoresist resin layer (spin coating, UV exposure, development…). At the end of this step, the design of the channels is reproduced on the resin in hallow. Figure 52 presents the steps followed during the photolithography process.

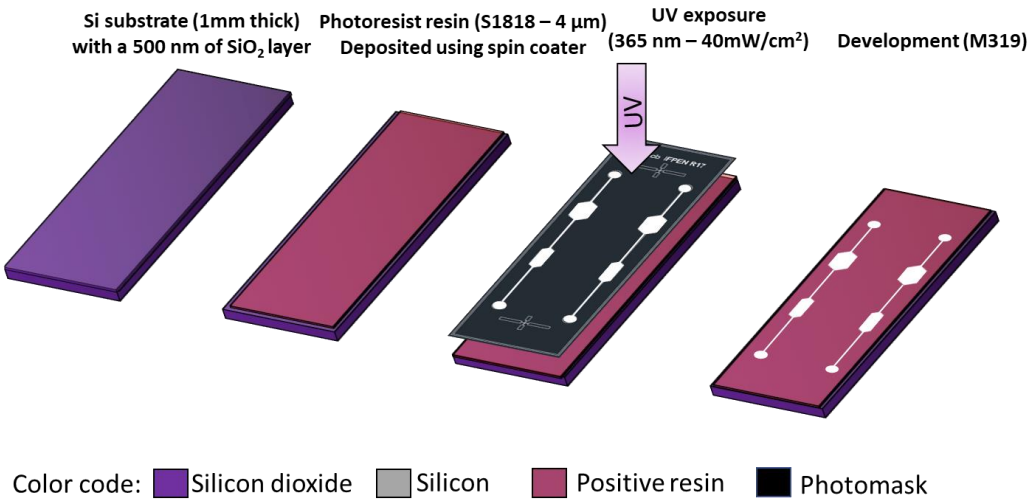

Figure 52: Illustration of photolithography steps used for microchannels fabrication.

2.3.3. Chemical etching

Once the mask is reproduced in negative on the wafer, two etching steps are necessary to create the microchannels: a first one to etch the sacrificial silicon oxide layer and the second one for the silicon itself.

Removal of the silicon oxide layer

The silicon wafers used have a 500 nm thick silicon oxide layer. The SiO_2 layer serves as a mask for the etching of the silicon.

The removal of the SiO_2 layer is carried out by an attack with a solution of buffered hydrofluoric acid (HF) (1% in water) according to the following equation.

$$SiO_2 + 4HF + 2NH_4F \rightarrow (NH_4)_2SiF_6 + 2H_2O \qquad (2\text{-}1)$$

When handling the HF solution, it is necessary to wear a gown and special gloves, over-gloves, and a face mask for protection. The solution is then deposited on the wafer. Therefore, the wafer is in contact with HF for at least 8 min to ensure that the entire targeted oxide layer (500 nm thick) is removed. The etching speed of the oxide layer is estimated at 100 nm per minute. It is then rinsed thoroughly with DI water to remove all traces of HF, and the resin is removed with acetone Figure 53.

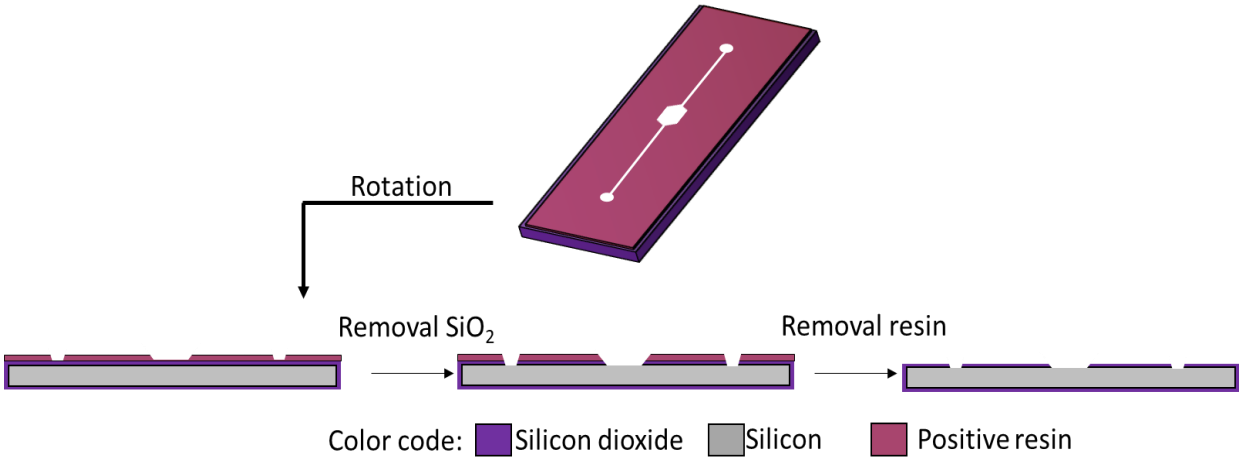

Figure 53: Removal of the silicon oxide layer using HF.

Chemical etching of Silicon

Once the silicon oxide layer is removed, the silicon etching can be done Figure 54. For this, an alkaline base is used, the Tetramethyl Ammonium Hydroxide (TMAH) at 25 wt% in water. The chemical reaction of the etching is as follows [239].

$$Si_{(s)} + 2OH^-_{(aq)} + 4H_2O_{(l)} \rightarrow Si(OH)^{2-}_{6(aq)} + 2H_{2(g)} \quad (2\text{-}2)$$

The silicon atoms are oxidized by OH- ions and then removed from the wafer. The etching rate of silicon, which is about 40 µm/h at 83°C, depends on the concentration of OH- ions (and the pH) near the substrate. Therefore, it is important to have sufficient agitation to supply the wafer surface with OH- ions and to pay particular attention to the evaporation of the solution during the etching process. A stirring is also important to eliminate the H_2 bubbles that form on the surface of the Silicon.

Figure 54: Chemical etching of Silicon.

The etching of Silicon is anisotropic [240,241]. Indeed, the etching rate is different according to the crystal planes. The etching rate for the <100> plane is about 25 times higher than that of the <111> planes [241]. This is due to the difference in density of the atoms in these two planes. The etching, therefore, has a trapezoidal shape, with an angle of θ = 54.7° Figure 55.

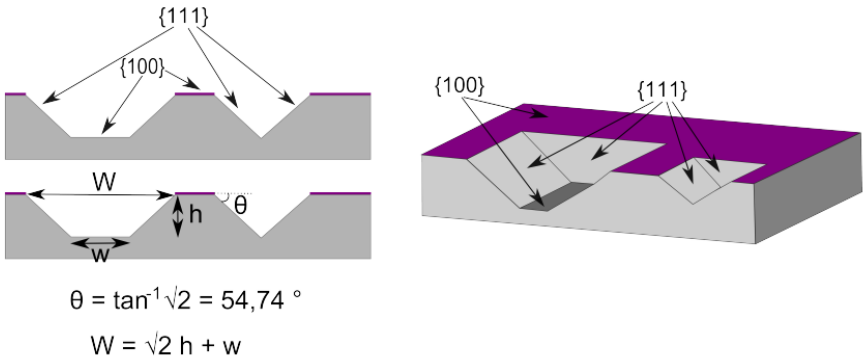

Figure 55: Scheme showing the anisotropy of the etching on silicon by a solution of TMAH at 25% in water [242].

Once the etching is done, the wafer is rinsed with water. The etching depth is measured with a mechanical profilometer Veeco DEKTAK 8. Fluid inlet holes are then drilled into the silicon wafer with a sandblaster.

2.3.4. Oxidation layer

The channel is etched in silicon, which is hydrophobic, while the Pyrex® that will close the system is hydrophilic. To make the wettability of all channel walls uniform, it is necessary to grow a layer of SiO_2 on the silicon surface. To create the oxidation layer, the silicon wafer, after being thoroughly cleaned with isopropanol and ethanol, is placed in an oven. A heat treatment at 1000 °C for two hours is applied in a "wet" atmosphere. To do this, water is injected inside the oven at a flow rate of 1 ml/h. The oxidation layer grows according to the following reaction:

$$Si_{(s)} + 2H_2O_{(g)} \rightarrow SiO_{2(s)} + 2H_{2(g)} \quad (2\text{-}3)$$

As shown in the Equation (2-3), the oxidation of the wafer leads to a consumption of silicon atoms. It is not a deposition (as possible with PECVD techniques) but a chemical transformation of the surface. The reaction will create a Si/SiO_2 interface that will grow to the inside of the substrate, and at the same time, the oxidation layer will also grow to the outside of the wafer.

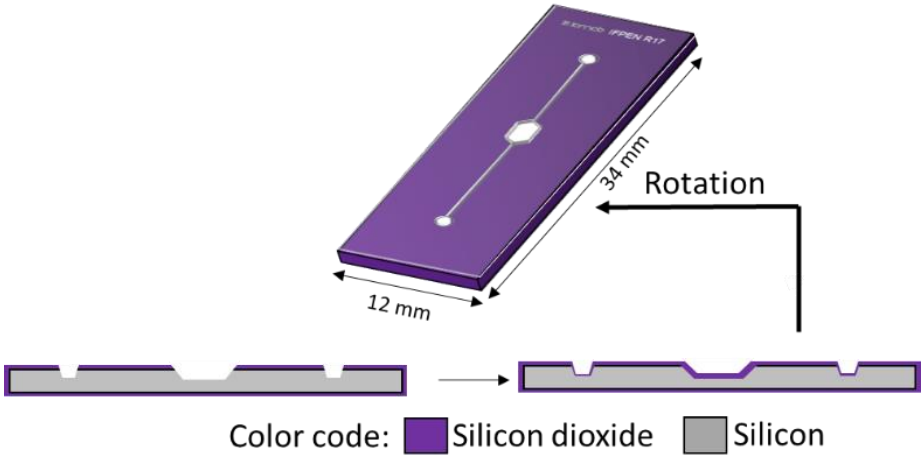

Figure 56: Schematic of oxidation layer formed after exposure at 1000°C in a wet atmosphere.

2.4. Challenges faced when sealing silicon and borosilicate glass substrates

So far, the conventional method to seal silicon and borosilicate glass is the anodic bonding [33]. However, this type of bonding involves the use of harmful acids (piranha solution), for cleaning the surfaces substrates, which can potentially harm the sensor. It also requires applying a high voltage (up to 1000V) and subsequently heat to annealing reaching temperatures of 450 °C. These temperature conditions were the highest tested during the metal selection process in Section 2.2, as we initially planned to use the anodic bonding. These two main steps were originally used during the sealing of the microfluidic devices are discussed hereafter.

Acid cleaning

Initially, during the anodic bonding procedure both wafers were cleaned with a piranha solution: each wafer was placed in a crystallizer containing 60 ml sulfuric acid (H_2SO_4) and 20 ml hydrogen peroxide (H_2O_2). The mixture creates the Caro's acid (H_2SO_5), which allows to eliminate any organic trace deposited on the substrates, leading to bonding defects. For saving time and practical matters, a thermocouple already designed in a "macro" size was used as test during the sealing optimization process. We can observe in Figure 57, an example of a Borofloat 33 substrate with the deposited Pt-PtRh thin film sensor before and after being exposed to the piranha solution. The thin film is seen to degrade after being exposed to the Piranha solution.

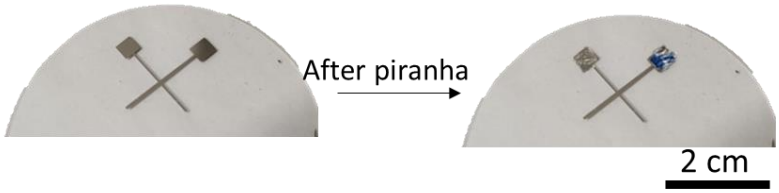

Figure 57: Image of the Pt sensor deposited on a Borofloat 33 substrate before and after the Piranha exposure.

Therefore, during the anodic bonding procedure the piranha cleaning could not be used. Instead, the substrates were cleaned using isopropanol and then following the original protocol, by being then raised with water before being brought into contact for pre-bonding. The cleaning step is crucial for anodic bonding and was therefore performed in a clean environment (clean room) to prevent any impurities from causing defects during the bonding process.

Anodic bonding

After the new adapted cleaning process, the procedure was then started by sandwiching both substrates between two conductive plates that were set up on a heating plate. As previously mentioned, the anodic bonding is initiated by applying high voltage and exposing the substrates to temperatures of 450 °C.

In Figure 58, the left image shows an example test conducted on the silicon and glass part that were sealed together using anodic bonding. The zoomed image of the sensor (on the right) inside the channel shows, iridescence, damage on the surface of the sensor, and the presence reaming water. However, although the iridescence is not visible outside the channel, violet lines around the sensor suggest that proper bonding was not achieved.

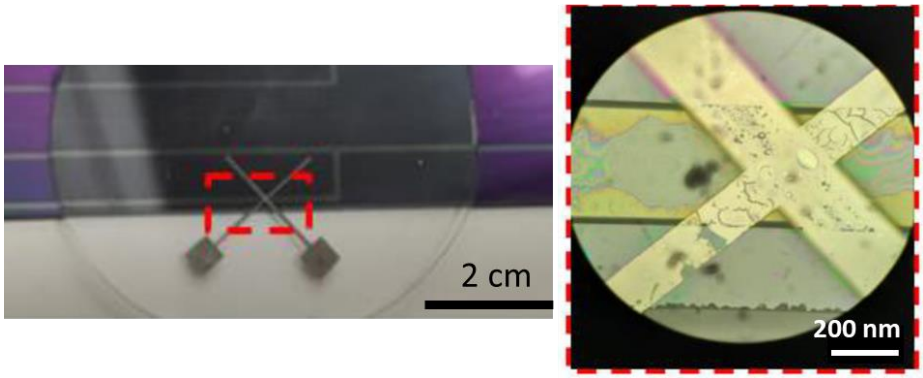

Figure 58: Result after anodic bonding first tests using "macro" size channel and sensor, red rectangle presents a zoom of the device.

Voltage measurements were however carried out after bonding are shown in Figure 59. As we can observe, the sensor faced issues with its voltage response to temperature as a result of complications during the sealing process. The voltage response was significantly different from the initial measurement before bonding, as shown in Figure 50.

In Figure 59, we can see an exponential relationship between temperature and voltage measurement, with negative values. The uncertainties in the measurements have increased significantly, ranging from 10 to 35% of the standard error. The changes observed may be a result of interactions between silicon, water, and other metals. It is also possible that Pt is diffusing into the Borofloat 33 material, causing a phenomenon called "poling," which is the alignment of molecules in a specific direction using an electric field.

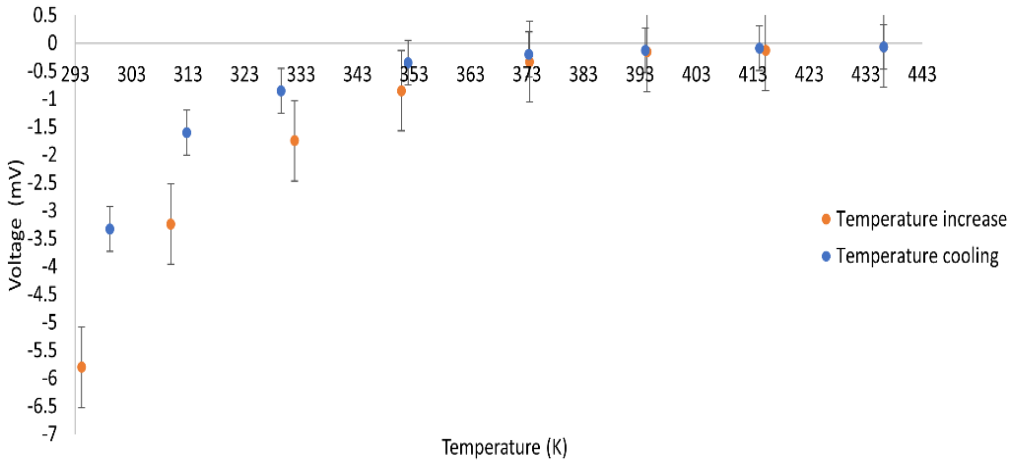

Figure 59 : Measurement of voltage versus temperature of thermocouple inside the channel. Experimental points when heating the thermocouple (red points), experimental points when cooling the thermocouple (blue points).

The complications caused by anodic bonding led to the exploration of an alternative method called fusion bonding. Fusion bonding does not rely on voltage for bonding, but rather requires cleanliness and heat.

2.5. Fusion bonding

Fusion bonding is a widely used technique in microfluidics to permanently bond two or more structures. It involves bringing two substrates into contact and applying heat and pressure to create a strong diffusion bond between them. The substrates are typically made of materials like glass, silicon, or polymers, which can be easily shaped and used into complex microfluidic systems. Fusion bonding has many advantages, including strong bonds, resistance to chemicals, and compatibility with different fluids. It allows for the creation of microfluidic channels without leaks and the integration of various functional elements into one device, such as electrodes, sensors, or filters [109,243].

2.5.1. Surface activation

The fusion bonding procedure started by cleaning the glass and silicon surfaces with isopropanol to avoid undesired contamination. Then, instead of using piranha cleaning both substrates were placed in an air plasma cleaner model PDC-002 at 1000 W and 1,2 Torr for 10 min. The surfaces of silicon dioxide and glass contain silanol groups. During plasma treatment, ions and reactive species are generated, which can cause chemical activation of the glass and silicon surfaces, leading to the formation of new Si-OH bonds. By increasing the bonding sites between glass and silicon, a higher density of silanol groups improves the adhesion and reduces the annealing temperature necessary to achieve a good bond strength. This step is illustrated in Figure 60.

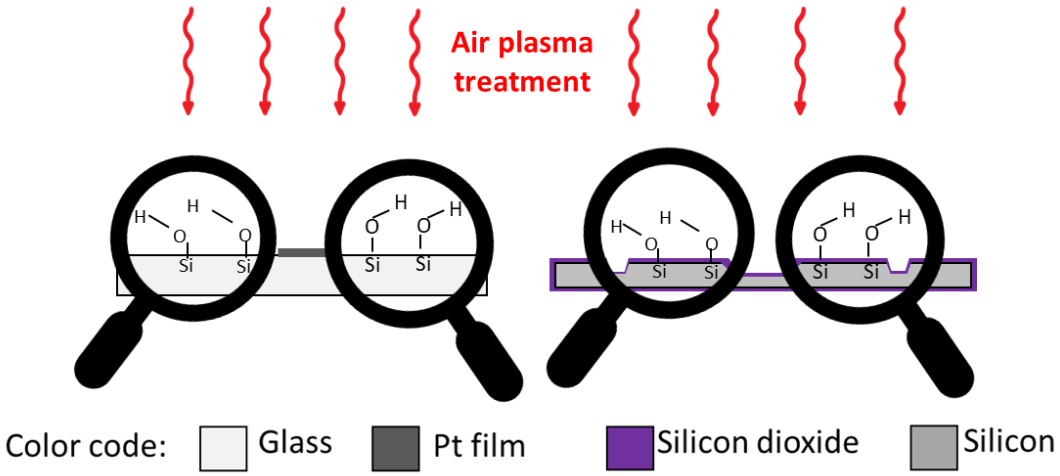

Figure 60: Illustration of surface activation using an air Plasma on glass and silicon substrate.

2.5.2. Diffusion layer at interface and siloxane bond formation

Before bonding, alignment of the substrates was performed with the help of an optical microscope by placing sensor on the top of the micropool and then pressing them together, thereby initiating a pre-bonding process. The pre-bonded substrates were placed in an oven between two graphite sheets that allow a proper and uniform heat conduction, while preventing glass bonding to other materials (glass does not wet graphite). All the elements are placed on a ceramic plate, a weight of about 1 Kg is placed to apply a constant pressure on the assembly.

The thermal treatment consists in reaching 700°C in 1 hour, followed by a 20-min plateau. This allows silicon dioxide and borosilicate surfaces to reach a partial melting point, allowing a thin layer on each surface to partially melt. Then, an aging step at 600 °C is maintained for 5h. When the molten surfaces

come into contact, the silanol groups in the silicon react with the hydroxyl groups in the borosilicate to form siloxane (Si-O-Si) bonds. These bonds are very strong and stable. Finally, a decreasing ramp at 5 °C/min down to 25 °C is performed. The molten surfaces cool and solidify, preserving the siloxane bond formed and creating a strong, durable bond between the two materials. Figure 61, presents the applied thermal treatment and the formation of siloxane bonds.

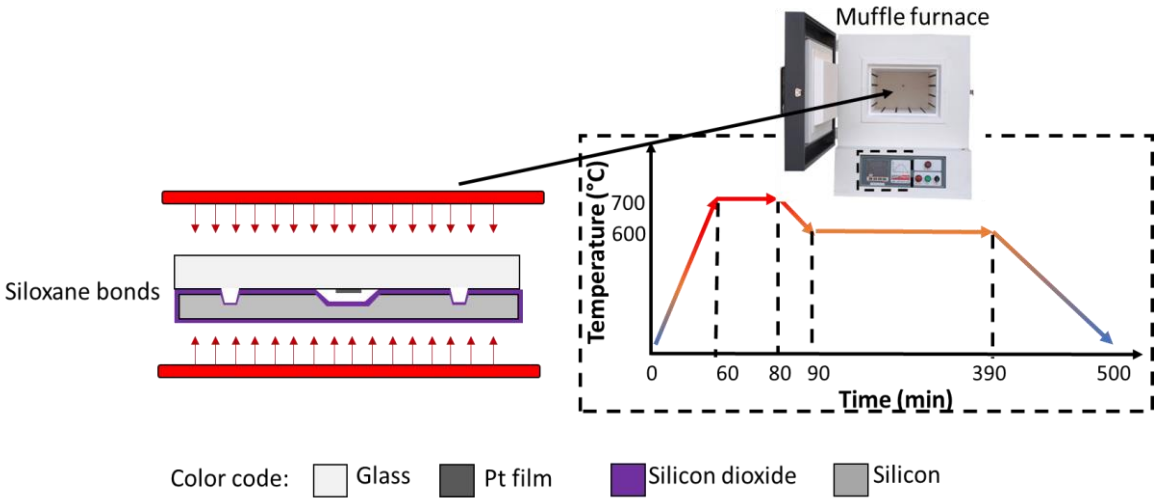

Figure 61: Illustration of the applied thermal treatment and the formation of siloxane bonds.

2.6. Final microfluidic device

Given the obtained information on devices fabrication, it has been chosen that the one element method will be used to measure the thermal conductivity in this thesis work. This choice was influenced by the observed signals and the additional requirements of the two-element method, such as fragility concerns, cost, and time. The microchip with the meander geometry was designed and fabricated, however, mainly due to time constraints, it was never used or tested for thermal conductivity measurements.

After reviewing the results of the one element approach, the spiral shape was selected for the sensor's final design because it offers a large surface contact area, uniform thermal distribution, and low power consumption [227]. The spiral shaped metal structure has a 2 mm diameter with 6 concentric rings, each having a width and spacing of 50 µm and 100 µm, respectively. Figure 62 illustrates the final microfluidic device for the RTD sensor type after fusion bonding.

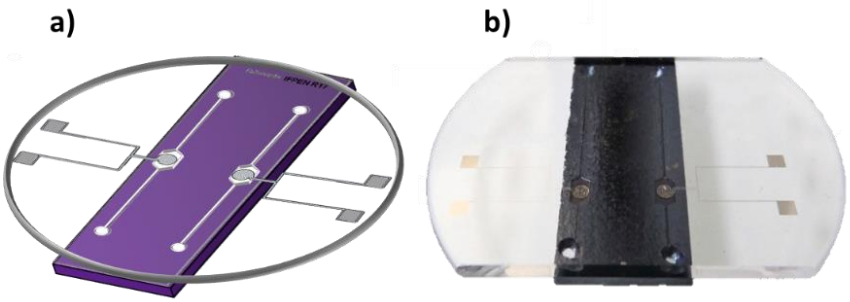

Figure 62: Final microfluidic device a) illustration and b) picture of the final microsystem.

2.7. Conclusion

A new microfluidic device has been designed for integrating MEMS technologies such as microsensors for measurements of thermal conductivity of liquids, in the holder setup at IFPEN. The microfluidics device, including a sensor integrated into a microchannel, was fabricated following a three-step procedure:

- Sensors created by depositing a thin metal film on the surface of a borosilicate glass substrate. A careful selection of metals, geometries, and measurement behaviors was made using setup of experiments and experimental techniques. The one element methodology used thin metal film made of Pt in a spiral shape for both sensing and heating. In contrast, the two elements methodology used a Pt/PtRh thermocouple for sensing and a separate spiral shaped metal thin film for heating.
- Microfluidic channels were etched on a silicon substrate using photolithography / wet etching techniques.
- The silicon and borosilicate glass substrates were assembled using a fusion bonding process.

Then, to observe how signal behaviors varied with temperature, electrical resistance (Pt thin film) or electromagnetic field (EMF) measurements were performed before the sealing of silicon and glass substrates. Until reaching a certain spiral dimension (2 mm diameter and 0.1 mm of spacing) the electrical resistance has a linear response with respect to temperature (from 293K to 413K). On the other hand, when the dimension and the space between the concentric ring is reduced (1 mm of diameter and 0.06 of spacing) the phenomenon of hysteresis was noticed. Consequently, the sensor's sensitivity is constrained once it reaches a certain minimum dimension.

The EMF thermocouple did not show a linear behavior for low temperatures (between 293 and 343K). As a result, it was decided not to pursue with the two-element approach due to various constraints and additional steps needed during the sensor fabrication process.

Furthermore, a spiral-shaped Pt thin film was used for the measurement using the one element approach. The following chapter explains how the microfluidic device is incorporated into a measuring system, allowing for the measurement of thermal conductivity in liquids.

Chapter III: Implementation of the microfluidic device to measure thermal conductivity of liquids

In the previous chapter, the development and conception of the microfluidic device to measure λ_L was reported. This chapter focuses on the integration of the microfluidic device into a scale-lab measuring system, which purpose is to test and validate the microfluidic approach for measuring λ. The system includes fluidic interfacing such as specialized tubing for microfluidics with outer and inner diameters in the mm range, pumps for controlling fluid flow inside the microreactor as well as electronic instrumentation and components adapted to the micro-size volume sample.

3.1. Introduction

The microfluidic device resulting from the fabrication detailed in the previous chapter, more precisely the micropool/cavity, is summarized in Figure 63. The bottom part of the device consists in a thermal/electrical insulator (borosilicate glass substrate) on which a Pt thin film spiral planar heating structure is deposited. The top of the microchannel is made of a thermal conductor top reference (silicon substrate). As reminder, the decision to use silicon was made in purpose because of its high thermal conductivity properties. This device is conceptually advantageous due to its chemical inertness, the ability to work at higher temperatures than other microfluidic materials and optical access for coupling to other *in situ* characterization.

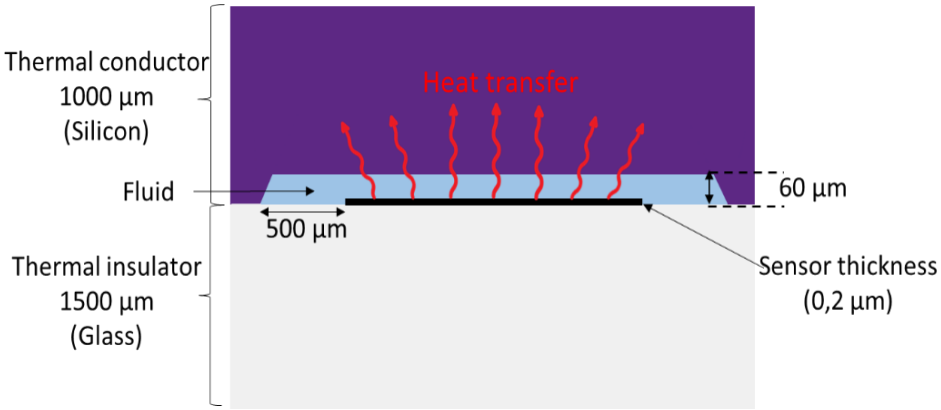

Figure 63: A generalized schematic longitudinal cross-section view of the microfluidic cavity designed for measurements of fluids thermal conductivity. Heat transfer generated by metallic spiral is represented by red arrows. Extracted from ref. [1].

Briefly, silicon is a useful heat sink because of its high thermal conductivity, which eliminates uncertainties related to thermal penetration depth, which are present in micro-scale systems [41,132,244]. A thermal pulse that goes beyond the limits of the liquid in the microchannel is applied. Because of the high thermal effusivity of silicon, the heat dissipated by the sensor structure is absorbed, leading to a constant temperature increase rates for all the measurements. The sensor is placed in a specific circuit so that a well-defined measurement setup can be used to measure the temperature changes generated by the sensor. Then, simple data analysis can be employed to determine the thermal conductivity of fluid samples. The strategy implemented, the overall measurement setup, the readout device used to measure fluid's thermal conductivity, and the measurement procedure will be detailed.

Then, the obtained results are discussed, including the microdevice calibration on microliter-sized samples of water/ethanol binary mixtures, the validation measurements performed on well-known

fluids (n-pentadecane and ethan-1,2-diol), and the acquisition of new experimental data for 2,5-dimethylfuran, which is one typical product issued from the conversion of biomass.

3.2. Microfluidic device's fluidic interface designed for the acquisition of λ.

In the previous chapter, the design and fabrication of the microfluidic device was described, with the aim of performing the acquisition of λ_L. This device was designed while considering several constraints:

- Geometric constraints related to the fluidic interfacing of the microfluidic device (maximum external dimensions of 1.5 cm x 4.5 cm).
- The characterization instrumentation to be used.
- The mechanical strength required (temperature).

A conventional experimental set-up for working with microsystems consists of pumps, tubing, connectors, and the microfluidic system. At IFPEN, the microfluidic bench (Figure 64) provides control over all operating conditions (temperature, pressure, flow rate). Briefly, the bench includes two pumps that provide fluids to the microsystem and can operate at high pressures of up to 500 bar. However, for safety reasons, its operating pressure is limited to 100 bar, and the temperature of the microsystem is limited to 350°C. The tubes connecting the different parts of the bench are made of a nickel-based alloy (Hastelloy), allowing for the use of a variety of liquids except strong acids. The microfluidic device is connected to the experimental environment using a compression piece called a "holder". As shown in Figure 64 on the left image with the red frame, the holder can be heated using three heating cartridges positioned inside it. A K-type thermocouple, with a probe diameter of 0.3 mm, is placed between the holder and the microfluidic device to monitor the temperature.

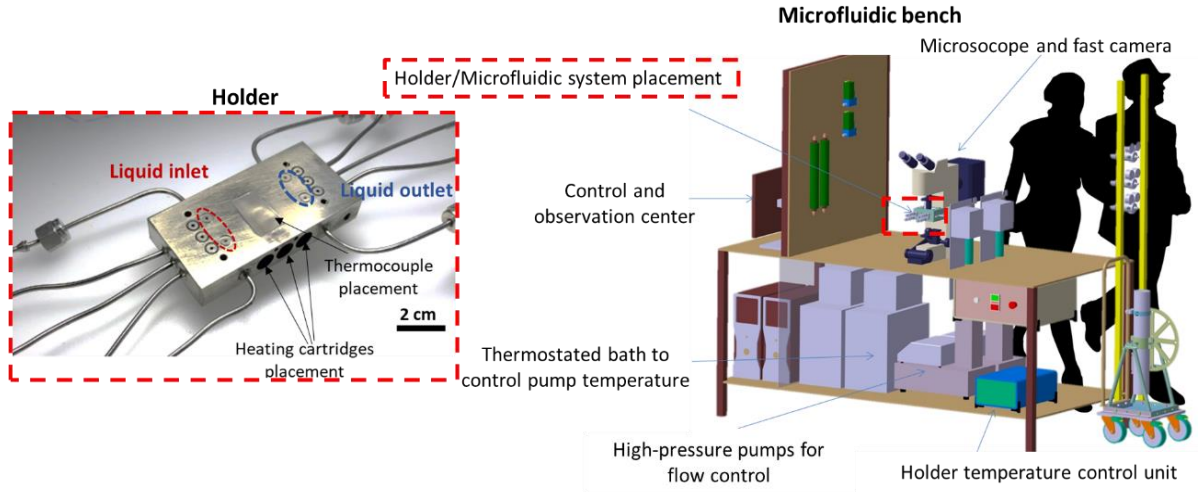

Figure 64 : Representation of the high-pressure – high-temperature microfluidic bench set up at IFPEN on the right taken from ref. [212]. View of the holder (zoom with red frame), the inlet and outlet channels are circled, and the arrow shows the thermocouple positioning, adapted from ref. [212].

The microfluidic bench was however not used in the development of the thermal conductivity measurement strategy due to the unsuitable temperature control provided by the heating cartridges. The system's attempting to stabilize the reference temperature led to fluctuations when measuring the sensor's temperature increase. As a result, only the holder was used for the measurements. The

following paragraph explains how the microfluidic device and measurement system were adjusted to fit with the holder.

The sensor used in the microfluidic device was designed to have a specific size and shape in order to meet certain requirements and fit properly into the holder. For instance, the electric interfaces are connected via square contact pads on both ends of the sensor, and it is important for these contact pads to be easily accessible. The pads and therefore the sensor, are connected to the electronic measuring device through two contact pins that are held in place by a 3D support piece. Additionally, the holder possesses an observation window in which the micropool is placed for possible observation with microscope. This can be seen in Figure 65.

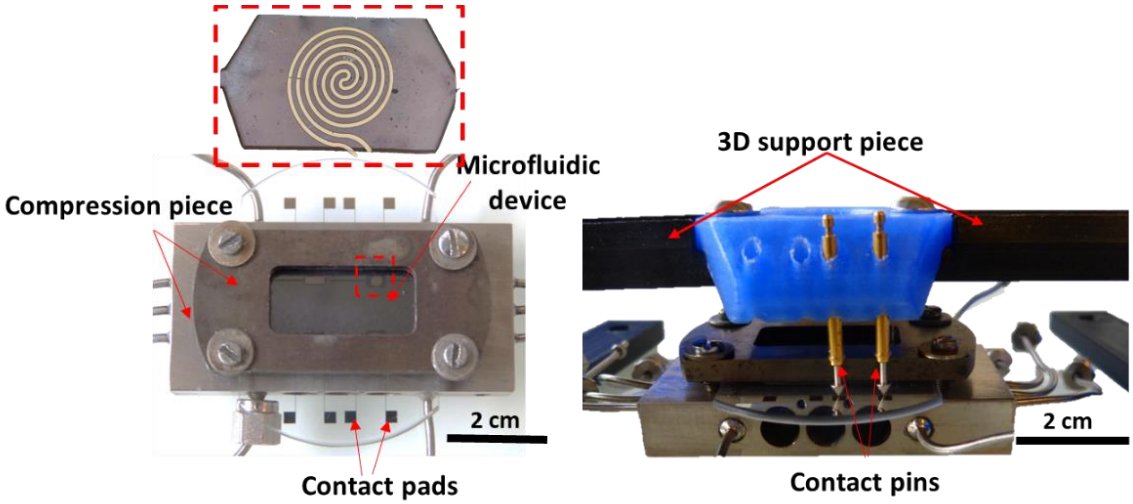

Figure 65: Photo of the microfluidic device positioned and fixed in the compression piece with an illustration of the sensor in the micropool (red frame). Photo of the support piece used to hold contact pins pressing against the contact pads.

The microfluidic device needs a localized heating through the sensor and the fluid of which thermal conductivity can be measured. With the aid of the sensor positioned inside the micropool (Figure 65), we have demonstrated in this work that the measurement can be achieved with just 0.5 µl [1].

As observed in Figure 66, the process of setting up the thermal conductivity measurement involves a) using a power supply to apply an electrical current that passes through b) a circuit called "Wheatstone bridge", within which the sensor structure is placed. The heat produced by the current induce a change in the sensor resistance. This resistance change is measured using the Wheatstone bridge principle. c) The recorded data is then, d) processed to convert the resistance into a temperature change. The temperature change of the sensor can be measured to determine the heat transfer that occurs due to the temperature difference between the sensor and the surrounding fluid. This data can be used to calculate the fluid's thermal conductivity. Each of these stages are explained in detail hereafter.

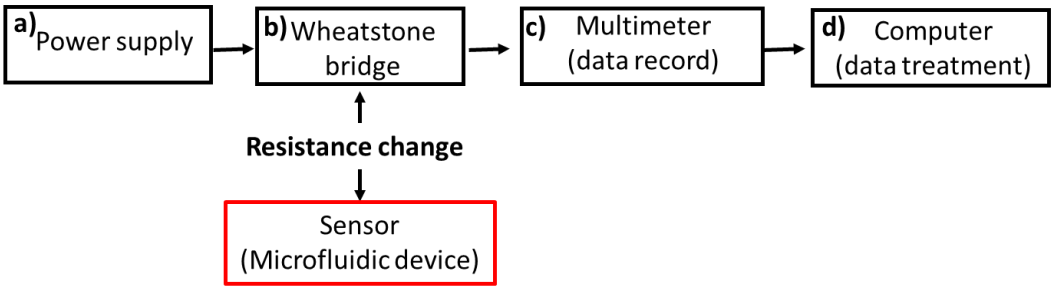

Figure 66: Schematic diagram of thermal conductivity measurement set up.

3.3. Wheatstone bridge to measure changes in electrical resistance

A Wheatstone bridge is a fundamental electrical circuit used to precisely measure changes in electrical resistance. Its principle and importance are explained hereafter.

The Wheatstone bridge is an electrical circuit that balances the two legs of a bridge circuit, one of which contains the unknown component, to measure an unknown electrical resistance. The circuit's ability to deliver highly accurate measurements is its main advantage.

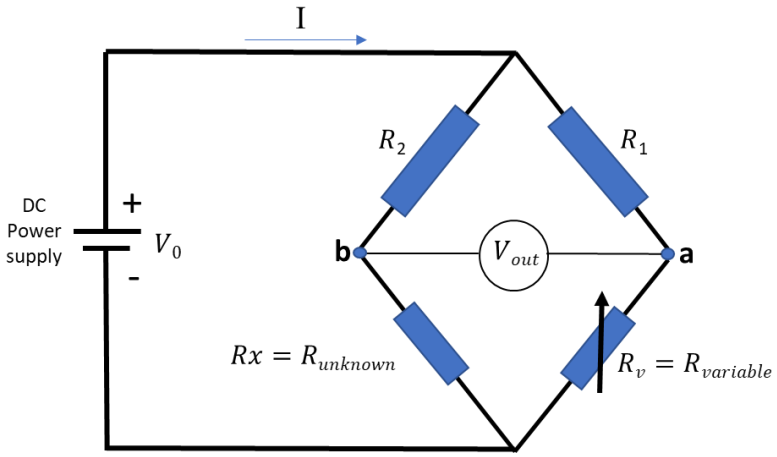

Figure 67: A Wheatstone bridge schematic.

The scientist and mathematician, Samuel Hunter Christie, developed the Wheatstone bridge circuit to measure unknown electrical resistances and first described it in 1833. Then, Charles Wheatstone, popularized it in 1843. The Wheatstone bridge is a circuit with four resistors arranged in a diamond shape, that is used to accurately measure unknown resistance values (see Figure 67). The circuit includes two resistors with known values (R_1 and R_2), one resistor with an unknown value (R_x), and one resistor with an adjustable value R_v. The resistance R_v is adjusted until the bridge is "balanced" and there is no current passing through "V_{out}" (Figure 67). When the bridge is balanced, the potential difference between the two midpoints b and a is zero. $\frac{R_v}{R_1}$ (ratio of the two resistances in the known leg) and $\frac{R_x}{R_2}$ (ratio of the two resistances in the unknown leg) are therefore equal. The direction of the current can indicate if R_v value is too high or too low when the bridge is unbalanced. At the point of balance, the equation is the following:

$$R_x = \frac{R_v}{R_1} \times R_2 \quad (3\text{-}1)$$

The Wheatstone Bridge is used in situations where sensors require the measurement of small changes in resistance, which can be related to changes in temperature. By incorporating a temperature-sensitive resistor into the bridge, such as a thermistor or RTD, the bridge can accurately measure temperature. When the temperature changes, the resistance of the temperature-sensitive resistor also changes, causing an imbalance in the bridge. This imbalance is then detected as a voltage difference, which is directly related to the temperature change. This allows for precise temperature measurements without requiring complicated circuits. Another benefit of using the Wheatstone Bridge in temperature sensing is that it can be easily calibrated. By setting the bridge to balance at a known temperature, the sensor's resistance can be calibrated against a reference temperature. This ensures accurate measurements over the entire temperature range. Therefore, the use of a Wheatstone bridge for the thermal conductivity measurement has been implemented in this work.

3.4. Experimental procedure for thermal conductivity measurement

The Wheatstone bridge has been already used in several occasions as thermal conductivity measurement system to monitor the electrical resistance variations [245–248]. These works, rely on the use of various instruments including, the power supply, the fixed and variables resistance in the Wheatstone bridge, and data acquisition/readout device. This experimental procedure is explained hereafter.

Power supply

The schematic measurement system (Figure 68) consists in a DC power with constant voltage supplied (V_0) by a generator RS Pro model RS6005P. The power supply has a line regulation, which refers to the ability of a device or system to maintain a constant current or voltage output even when there are variations in the input voltage or current, which are respectively current ($\leq$ 0.1% + 3 mA) and voltage ($\leq$0.01%+3 mV) supplied. To maintain a constant measurement, the current should be > to 3 mA and the voltage > 3 mV, respectively. If this level is not fulfilled, the measurements may be unstable. Increasing the power supply may be an obvious solution, but it is important to note that the sensors and liquid samples operate on a micro-scale and only require a small amount of current to detect temperature changes. Therefore, ff the power supplied is too high, it could potentially harm the sensor. The amount of current initially applied is controlled by the power supply but also by another multimeter model C.A 5233 with higher resolution than the generator (0.001 A) placed in between the relay to the Wheatstone bridge, as shown in Figure 68.

Fixed resistors (R_1 and R_2) in Wheatstone bridge

In order to maintain precise control over the current applied, two highly accurate and fixed resistors were selected being used in the Wheatstone bridge. These resistors with respective values of R_1 = R_2 = 465.8 Ω, have an accuracy of 0.01% at room temperature. The resistance value falls within the range of the initial resistance sensor value, indicating that the current that goes through the sensor corresponds approximately to half of the initial current applied by the power supply. This allows for easy calculation or estimation of the current being sent, and only a small amount of current is required to detect temperature changes without damaging the sensor or exceeding the device limits.

Sensor resistance (R_s) and variable resistance (R_v) in the Wheatstone bridge

The thin film sensor's electrical resistance (R_S) has an initial value (R_{init}) when the bridge is balanced at the selected temperature. R_v is a variable resistor consisting in a precision resistance decade box, which is a device used to measure and create a range of specific resistance values. The box typically has several switches, which can be used to add or remove resistors in a circuit to create a specific resistance value. The decade box is a Guildline Instruments model 9346/10kΩ that can be adjusted to provide a range of resistance values from 0.01 Ω to 10 kΩ, which is used to balance the bridge ($R_{v=}\ R_{init}$). A Voltcraft-655 BT multimeter with a sampling frequency of 64 Hz and a measuring range of 10 mV was used to acquire the unbalanced DC voltage ΔV (between V_a and V_b).

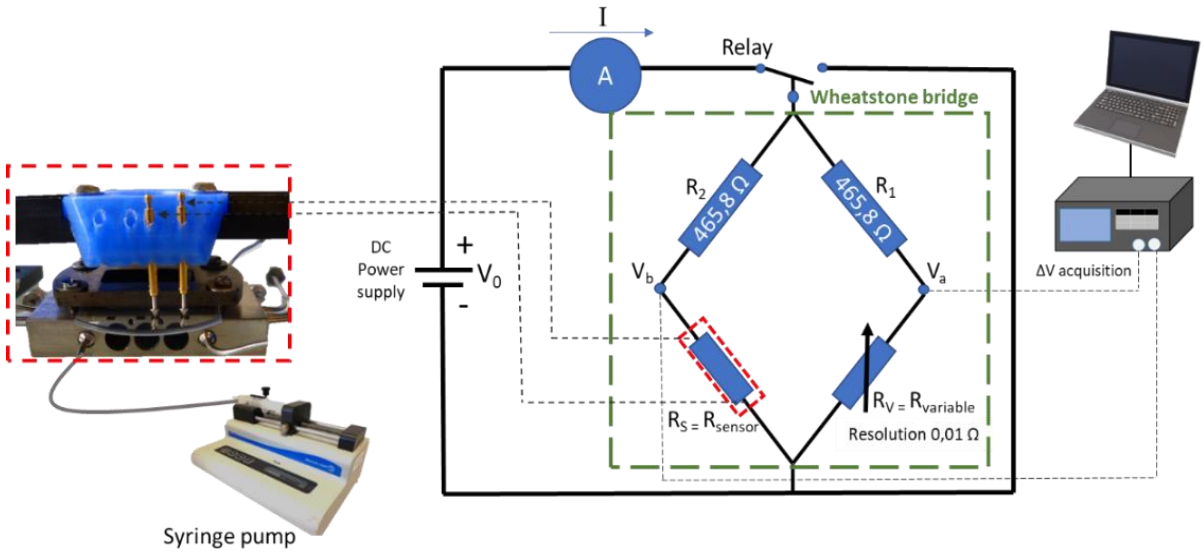

Figure 68: Schematic of the thermal conductivity measurement system.

The fabrication procedure presented in chapter II Section 2.2 and 2.3 was performed to generate 8 sensors with the spiral geometry, resulting in four microfluidic devices. However, during the implementation of the setup, 3 sensors were damaged. Therefore, 5 remaining sensors were tested. For each device, the initial electrical resistance of the sensor at room temperature was measured, and R_{init} values ranging from 480 Ω to 630 Ω were determined, roughly corresponding to the resistance of the thin Pt spirals, which are about 200 ± 20 nm thick. The different thickness values are shown in Table 10.

Table 10: Summarized results providing information about the thin film thickness and initial resistance values for each sensor.

Microfluidic device n°	Sensor	Thin film thickness (nm)	Initial resistance (Ω)
1	1	200 ± 5	602 ± 3
1	2	215 ± 5	564 ± 3
2	3	185 ± 2	637 ± 3
3	4	220 ± 5	516 ± 3
3	5	235 ± 10	489 ± 2
Average		211 ± 5	562 ± 3

The data from Table 10 is displayed in a graph showing the relationship between. We can observe in Figure 69 that the resistance of a thin film increases when its thickness decreases, this is due to the phenomenon known as quantum confinement effect [249,250] and the trend appears to follow a linear regression. When the film is thicker, there are more energy states for electrons to occupy, resulting in easier electron flow or lower resistance. However, as the film becomes thinner, electron motion is restricted and they experience more scattering, which interferes with their flow and increases resistance.

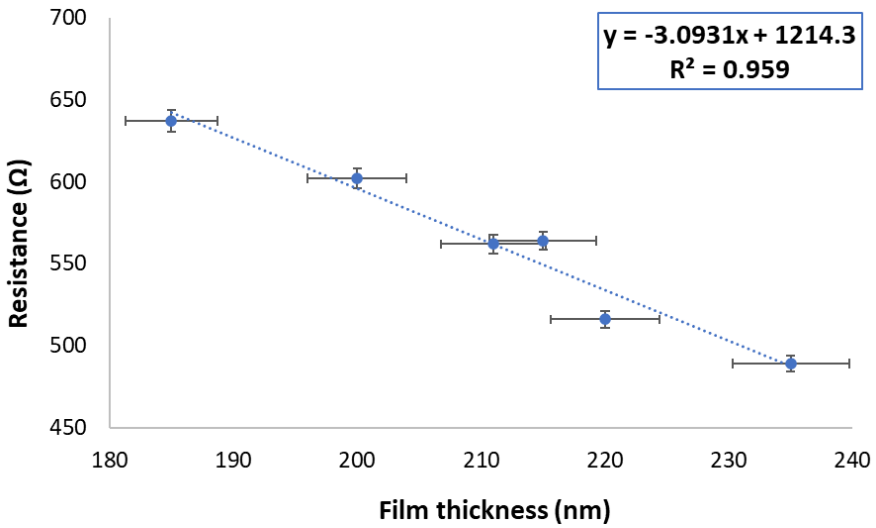

Figure 69: Evolution of initial sensor resistance as a function of the film thickness at room temperature.

Lead wire contribution in the Wheatstone bridge

In a Wheatstone bridge, lead wires can contribute to the overall resistance of the circuit. The use of long wires > 1 m, for example, can add extra resistance, causing measurement errors. To ensure accurate readings, it is crucial to minimize the resistance of the connecting wires by using wires that have low resistance and are short in length. We have chosen connection wires that are 10 cm long and 2 mm in diameter to minimize their impact on the circuit. Even though the impact of the lead wires and pogo pin on the resistance was small, it was considered in the calculations. The overall internal resistance was found to be 0.0015 Ω, and this value was subtracted from the resistance change caused by temperature in the sensor.

3.4.1. Measurement protocol

A syringe pump (Fisherbrand™ KDS100) is used to inject the fluid inside the microreactor. The liquids are delivered to the microdevice at a flowrate of 10 µL/s with steps of 200 µL injection per measurement. Apart from these flushes, the fluid in the micropool remains static inside the microdevice between injection steps. Once the fluid is loaded inside the microcpool, the relay is switched on, connecting the bridge to the DC power supply. The Wheatstone bridge is initially balanced under the lowest current deliverable by our device (< 1.0 mA). This small amount of current activates a transistor, which controls the flow of electric current in a power supply circuit. It also ensures that there is a minimum amount of current flowing through the bridge to avoid any sensor's heating: the voltage measured by the data acquisition system (DAQ) has to be maintained around zero, which corresponds to the R_{init} of the sensor. This is because when the bridge is balanced $R_{v=} R_{init}$.

3.4.1.1. Potential difference measurement and sensor resistance calculation

The thin Pt spiral is used as a Joule heating element. However, depending on the sensor's R_{init}, the voltage and current sent to the heating element must be slightly tuned to ensure that all applied pulses have the same power regardless of the sensors, allowing to compare each sensors response. The power equation (3- 2) is used to determine the amount of current (I, in A) needed to produce a desired power (P, in W).

$$I = \sqrt{\frac{P}{R_{init}}} \tag{3- 2}$$

Then, the desired DC power is applied to the sensor. The voltage produced at the bridge ends is measured, and the resistance of the sensor (R_S) can be deduced from equation (3- 3) [251].

$$\Delta V = \left(\frac{R_s}{R_2 + R_s} - \frac{R_v}{R_1 + R_v}\right) \times V_0 \tag{3- 3}$$

3.4.1.2. Thermal coefficient of resistance ($\boldsymbol{TCR} - \boldsymbol{\alpha}$)

As mentioned in chapter I section 1.6.3.2, the temperature coefficient of resistance ($\boldsymbol{\alpha}$) in $\boldsymbol{K^{-1}}$ for a resistor defines the change in the value of resistance when the temperature is changed by one kelvin. It is given by equation(1- 22) in chapter I as:

$$\alpha = \frac{1}{R_0}\frac{\Delta R}{\Delta T}$$

Figure 70 shows the example of the linear resistance behavior *vs* temperature curve plotted for sensor 2, using the calibration experiment of the protocol mentioned in chapter II in section 2.2.5. Thanks to the slope and initial resistance (R_0) of the sensor shown in the graph, the α was obtained.

The determination of α is necessary to convert resistance into temperature changes that allows to determine thermal conductivity values. The α value indicates how much the resistance of a material changes with a change in temperature**.** A higher TCR means that the resistance change is larger for the same temperature increase.

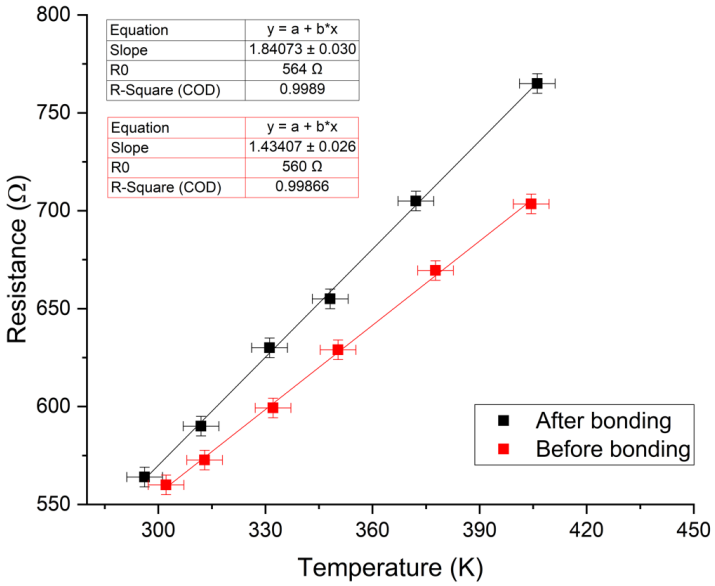

Figure 70 : Experimental curve illustrating the measurement of α before and after bonding variations of sensor resistance are linear as a function of temperature. The coefficient is calculated from the slope of the curve.

As we can observe in in Figure 70, the values from the red curve (before bonding) with an initial resistance of 564 Ω and the slope value of 1.43, respectively, led to a $\alpha_{\text{before bonding}} = 2.4 \times 10^{-3} \pm 0.2 \times 10^{-3}\, K^{-1}$. On the other hand, the black curve (after bonding) shows an increase of the slope value to 1.84, leading to a $\alpha_{\text{after bonding}} = 3.2 \times 10^{-3} \pm 0.3 \times 10^{-3}\, K^{-1}$. Several literature works have shown this type of behavior when exposing the thin film to high temperature [252,253]. Cheng *et al.* [218] suggested that if the thin film is exposed to high temperatures during annealing, it can eliminate impurities and flaws in the film's structure. This would make the film more uniform and crystalline, leading to less scattering of electrons [218]. As a result, the film would have increased conductivity and a higher α value. The summarized results of α before and after bonding for each sensor are shown in Table 11.

Table 11: Summarized results providing information about α before and after bonding for each sensor.

Microfluidic device n°	Sensor	Thin film thickness (nm)	Initial resistance (Ω)	$\alpha_{\text{before bonding}}$	$\alpha_{\text{after bonding}}$
1	1	200 ± 5	602 ± 3	$2.5 \times 10^{-3} \pm 0.2 \times 10^{-3}$	$3.1 \times 10^{-3} \pm 0.2 \times 10^{-3}$
1	2	215 ± 5	564 ± 3	$2.4 \times 10^{-3} \pm 0.2 \times 10^{-3}$	$3.2 \times 10^{-3} \pm 0.3 \times 10^{-3}$
2	3	185 ± 2	637 ± 3	$2.4 \times 10^{-3} \pm 0.2 \times 10^{-3}$	$3.2 \times 10^{-3} \pm 0.2 \times 10^{-3}$
3	4	220 ± 5	516 ± 3	$2.7 \times 10^{-3} \pm 0.2 \times 10^{-3}$	$3.3 \times 10^{-3} \pm 0.2 \times 10^{-3}$
3	5	235 ± 10	489 ± 2	$2.7 \times 10^{-3} \pm 0.2 \times 10^{-3}$	$3.4 \times 10^{-3} \pm 0.3 \times 10^{-3}$
Average		211 ± 5	562 ± 3	$2.5 \times 10^{-3} \pm 0.2 \times 10^{-3}$	$3.2 \times 10^{-3} \pm 0.2 \times 10^{-3}$

For each microfluidic device and sensor α determination the calibration was done later with the holder which has a more controlled temperature system thanks to three heating cartridges placed in its body. The value of α was validated to be $\alpha = 3.0 \times 10^{-3} \pm 0.2 \times 10^{-3}\, K^{-1}$, which is in agreement with the value previously found.

3.4.1.1. Conversion of resistance to temperature

Once $\boldsymbol{\alpha}$ is known, resistance conversion to temperature is straightforward using equation (3- 4) [254], which corresponds to relationship between temperature and sensor resistance:

$$R_s = R_{ref}\left[1 + \alpha\left(T - T_{ref}\right)\right] \tag{3- 4}$$

Where T is the temperature of the sensor, R_{ref} is the electrical resistance of the sensor at temperature T_{ref}.

3.4.1.2. Thermal conductivity calculation

The temperature change of the sensor structure due to the heating pulse can then be plotted as a function of time, more precisely $\sqrt{t}$. During the measurement, as already reported by Gustavsson *et al.* [67] and Harris *et al.* [255], a linear fit can be made once the value of ΔT reaches the equilibrium and where s is the slope of the curve, as shown in equation (3- 5):

$$\Delta T(t) = s\sqrt{t} \tag{3- 5}$$

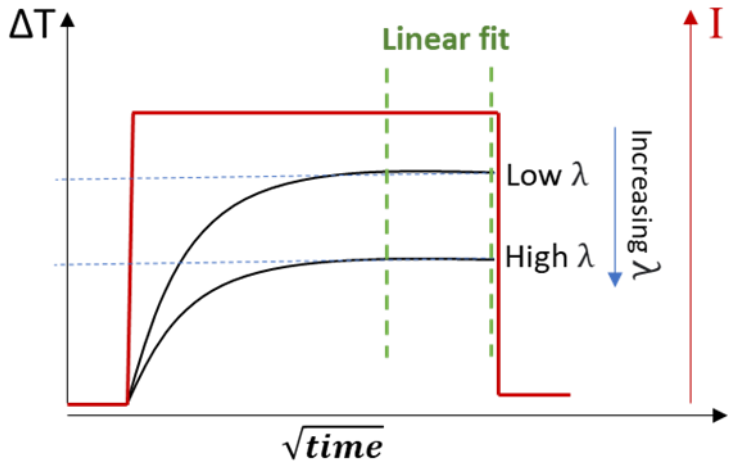

Figure 71: Simulated temperature response curves adapted from reference [256], showing that the offset of a linear regression at the end of a sensor response curve can be used to determine thermal conductivity of a static fluid inside the microchannel. The electrical current applied vs $\sqrt{\text{time}}$ is displayed in the parallel axis in red.

According to Figure 71, when the sensor is heated for a sufficient time, its temperature response should approach linearity when plotted versus the square root of time. The first non-linear portion at the beginning of the squared root trend curve, is attributed to the substrate effect, and is ignored in data processing [67]. In the linear part, the slope (s) is related to the silicon top reference acting as a heat sink. The silicon top material should be thicker than the microchannel depth, so that it acts as a semi-infinite medium during a heating step [65]. This implies that, regardless of the thermal properties of the fluid inside the micropool, the linear part of the curves - sensor temperature responses - are expected to be parallel. The constant value of the measured slopes at the end of each sensor response indicates that the thermal penetration depth is adequate [23]. Therefore, all uncertainties about probing depth are eliminated. The offset of the linear part at the end of the sensor's response curve can be used to determine λ.

However, other types of uncertainties need to be taken into consideration. A comprehensive measurement of uncertainty analysis has been performed to ensure accurate and reliable thermal conductivity measurements and this will be detailed in the next sub-section.

3.4.2. Uncertainty estimation

The reliability of every measurement is confirmed only when accompanied by a quantitative statement of its uncertainty. General rules for evaluating and expressing uncertainty in measurement, which can be followed at various levels of accuracy, have been established by the GUM method (Guide to the Expression of Uncertainty in Measurement) [257].

All measurements have errors that cause a difference between the measured value and the true value of the property being measured. The true value is an ideal concept that cannot be determined and is only estimated through multiple independent measurements. Formally, the output quantity about which information is required (Y), is often related to input quantities about which information is available (X_1,X_2, … X_n)), by a measurement model in the form of:

$$Y = f\ (X_1, X_2, \dots X_n) \tag{3-6}$$

The uncertainty of the result of a measurement generally consists of several components, which may be gathered into two categories according to the method used to estimate their numerical values: $Type\ A$ standard uncertainties, which are determined by analyzing a series of observations using statistical methods such as calculating the standard deviation of the mean or fitting a curve to the data in order to estimate the parameters of the curve and their standard deviations. This helps identify random effects in certain types of measurements.

When a set of several repeated readings has been recorded (for a $Type\ A$ estimate of uncertainty), the estimated standard deviation, s, can be calculated for the set. From these, the estimated standard uncertainty, u is calculated from:

$$u = \frac{s}{\sqrt{n}} \tag{3-7}$$

Where n is the number of measurements, when the number of measurements is small, which would correspond to the repeatability (typically less than 30). The Student t-distribution is considered to estimate and expanded uncertainty for a $Type\ A$ uncertainty. The equation is as follows:

$$U = t \times \frac{s}{\sqrt{n}} \tag{3-8}$$

Where t is the Student coverage factor based on the degrees of freedom n -1.

Then $Type\ B$ evaluations of standard uncertainty rely on scientific judgment and consider all relevant information, such as previous measurement data, knowledge of materials and instruments, manufacturer specifications, calibration reports, and reference data. All these factors contribute to the overall uncertainty of the measurement and should be combined.

The standard deviation of the estimated measurement result y, called combined standard uncertainty $u_c(y)$, is obtained by combining the individual standard uncertainties $u(X_i)$ from a $Type\ A$ or $Type\ B$, using the usual statistic method of combining standard deviations "root – sum – squares" according to the formula:

$$u_c{}^2(y) = \sum_{i=1}^{n} \left(\frac{\partial f}{\partial X_i}\right)^2 u^2\ (X_i) \tag{3- 9}$$

This equation is called the law Propagation of Uncertainty and the partial derivatives $\partial f/\ \partial X_i$ are referred to sensitivity coefficients. The sensitivity coefficient is calculated as the partial derivative of the function, with respect to input quantity, and describes how the estimate output quantity (y) would be influenced by small changes in the estimates input quantities (X).

Input sources of uncertainties are the relation of estimate standard deviation and the probability distribution. If it is a normal distribution, then the divisor value is equal 1. On the other hand, if the distribution is rectangular, then the divisor value is √3. In this case it is used when the data is equally likely to occur within a specific range.

$$u\ (X_i)\text{:}\ \frac{Value}{Divisor} \tag{3- 10}$$

The combined standard uncertainty (u_c) has a level of confidence of 68.27 %. If the purpose of the uncertainty statement is to provide coverage with a high level of confidence, then an expanded uncertainty (U) is obtained by equation (3- 11), where k is the coverage factor.

$$U(y) = k \times u\ (y) \tag{3- 11}$$

In this study, the value of the coverage factor is equal 2 and the expanded uncertainty is assumed to provide a level of confidence of 95%.

When the uncertainties of thermal conductivity were evaluated, the following input quantities were considered: temperature, sample preparation and instrumentation. The main input sources of uncertainty contributions in the thermal conductivity measurements are illustrated in Figure 72. The uncertainty contribution diagram provides information on the sources and magnitudes of uncertainties in the measurement. The temperature, instrumentation, and sample preparation all have known standard deviations, which means they follow a normal distribution. The uncertainty for λ is expanded due to these factors. Additionally, since the experimental λ measurement is less than 30, the population variance is unknown. As a result, the Student distribution is used.

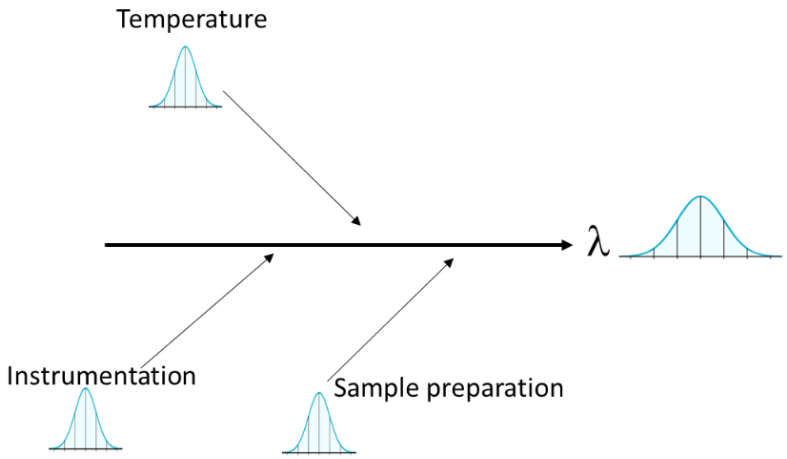

Figure 72: Uncertainty contribution diagram.

Temperature

When the λ measurement is carried out at different temperatures, the microfluidic device as well as the sample are subjected to selected temperature. The temperature was controlled by an oven (Memmert U15) and measured by a thermocouple K-type (probe diameter: 0.3 mm). The uncertainty source associated to the oven is the stability and for the thermocouple are the resolution, and repeatability evaluated by experiments and adopted from the equipment catalogue. The expanded uncertainty value for the thermocouple and oven combined was calculated as 1 K.

Sample preparation

A precision balance METTLER Toledo XPR204 was used to weight all the compounds involved in the sample preparation. The sample preparation uncertainty sources, such as resolution, calibration, linearity, and repeatability, are provided in the equipment catalogue. The expanded uncertainty value was calculated as 0.0002 wt.%

Instrumentation

For instrumentation, several uncertainty sources are involved. One of these contributors is the DC voltage generator. Then, the uncertainty sources associated with this are resolution and precision. Another contributor is the multimeter used to measure the Intensity. Then the acquisition system given by the multimeter to record the change in the resistance of the sensor. The uncertainty associated with the intensity and the resistance is given by the acquisition system and are resolution and repeatability. Finally, the combined expanded uncertainty for the power generation were 0.00063 W.

The calculation of the uncertainties for each factor used to measure thermal conductivity is explained in detail hereafter. More information can be found in Appendix E: Uncertainty $Type\ B$.

The other uncertainty factors such as the slope and the thermal conductivity of each liquid was experimentally determined for each microfluidic device using equation (3- 8).

3.5. Sensor calibration with ethanol/water mixtures

The calibration of microfluidic devices ensures accurate measurements and improves the repeatability of experiments. Calibration allows for error correction, optimizing parameters, and maintaining long-term stability, making these devices valuable for research purposes.

The calibration of each sensor was performed based on different water/ethanol mixtures for which thermal conductivity values are experimentally known. Indeed, the use of these two liquids in mixture, which are harmless and easily accessible, allows a wide range of liquid thermal conductivity values to be covered, from 0.180 to 0.603 W/(m.K). The considered volume fractions of ethanol in mixtures were as follows: 0% (pure water), 25%, 50%, 75%, and 100% (pure ethanol). For all these mixtures, reference thermal conductivity values were taken from the literature [136,258], and values are reported in Table 12.

Table 12: Experimental reference values of thermal conductivity at 293.15 K for the ethanol/water mixtures considered. The composition of mixtures is given in vol%.

Fluids	λ (W/(m.K))	Ref.
Ethanol	0.168	[258]
Ethanol/water 75:25	0.286	[136]
Ethanol/water 50:50	0.392	
Ethanol/water 25:75	0.497	
Water	0.603	[258]

Digital signal processing of the sensor response allows time changes in resistance to be expressed as temperature changes, and curve's offsets converted in thermal conductivity values. Several parameters inherent to the device may be set properly to improve the accuracy of λ values obtained during experimental measurements. Among them we investigated: (i) the electrical power applied during heating, (ii) the duration of the heating pulse, and (iii) the selection of the suitable time interval for the λ calculation.

3.5.1. Electrical power effect

To generate a desired temperature change, we have investigated the effect of the heating power values from 30mW to 90mW. To ensure that all sensors deliver the same heating power during the pulse, the electrical current is adapted by considering Equation (3- 12) along with the determined sensor R_{init} value. The amount of power going through the sensor in the unbalanced Wheatstone bridge is calculated and can be divided into three components in Figure 73:

- a) A simpler illustration of the actual Wheatstone bridge of which we can observe that the parallel resistance of R_1 and R_2 and the parallel resistance of R_s and R_v calculated using the following equations:

$$R_{1,2} = \left(\frac{1}{\frac{1}{R_1} + \frac{1}{R_2}} \right) and\ R_{s,v} = \left(\frac{1}{\frac{1}{R_s} + \frac{1}{R_v}} \right) \quad (3\text{- }12)$$

- b) both $R_{1,2}$ and $R_{s,v}$ are placed in series. Thus, the total resistance (R_{total}) can be calculated:

$$R_{total} = R_{1,2} + R_{s,v} \quad (3\text{-}13)$$

- c) the total current (I_{total}) can be therefore calculated:

$$I_{total} = R_{total} \times V_0 \quad (3\text{-}14)$$

This current is the same current that passes through $R_{1,2}$ and $R_{s,v}$ from which it is possible to deduce the parallel voltage in the sensor and the variable resistance ($V_{s,v}$) and therefore the current in the sensor (I_s):

$$V_{s,v} = R_{s,v} + I_{total} \; and \; I_s = \left(\frac{V_{s,v}}{R_s}\right) \quad (3\text{-}15)$$

Finally, the power in the sensor (P_s) in Watts is calculated:

$$P_s = V_{s,v} \times I_s \quad (3\text{-}16)$$

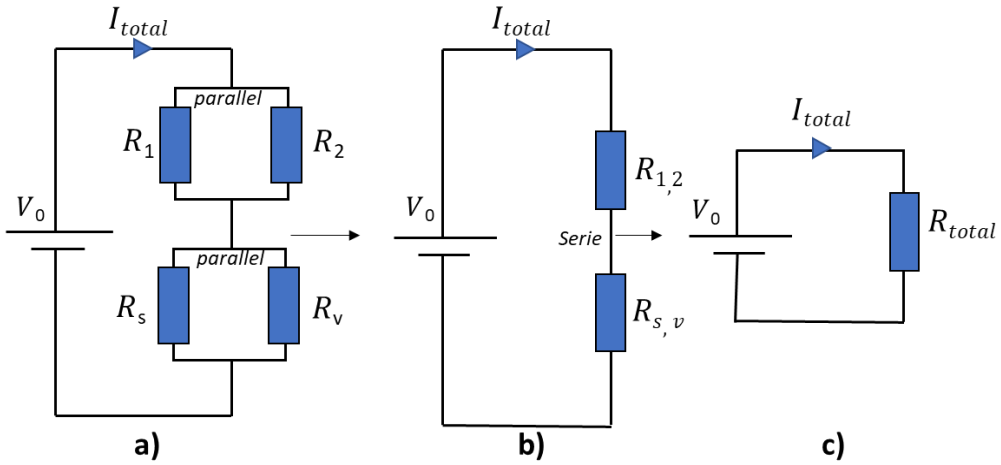

Figure 73: illustration of the Wheatstone bridge decomposed in three parts: a) illustration of simplified Wheatstone bridge (circuit in parallel), b) illustration of the circuit in series with respective calculated $R_{1,2}$ and $R_{s,v}$, c) illustration of the circuit with the respective calculated R_{total}.

In practice, we can consider that the accuracy of the sensor increases with the heating power. However, applying a too high heating power might result in disadvantages, such as local vaporization of the liquid and the formation of bubbles or even failure of the sensor.

For the temperature response curves, each curve corresponds to the average result of three acquisitions. Figure 74 shows the temperature response curves obtained for the considered water/ethanol mixtures applying a heating power of 30 mW. The amount of power used is not enough to differentiate between certain water/ethanol mixtures and does not result in consistent slopes for all of them, possibly because the heat flux is not reaching the maximum capacity of the microfluidic device.

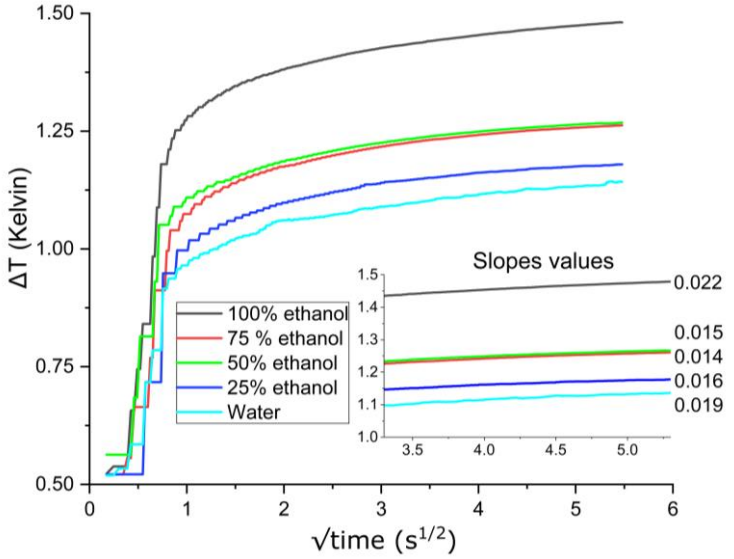

Figure 74: Time variations of the temperature in the microcavity filled with water/ethanol mixtures when a heat pulse (30 mW during 30 s) is applied to the heater/sensor. The observed slopes are shown from a time interval of [3.3 $s^{1/2}$; 5.3 $s^{1/2}$].

The behaviors observed in the two mixtures of ethanol, both 75% and 50%, are similar. This is also the case for the mixture of 25% ethanol and water, which have relatively similar transient curves. The hypothesis is that if the sensor does not receive enough power, the temperature difference between the sensor and the surrounding fluid is not large enough for the desired heat transfer rate. The heat flux could be also affected by external factors such as the density of the liquid. Heat transfer happens because of temperature differences, and a higher temperature difference leads to a faster rate of heat transfer. When fluids have similar densities, less temperature difference is formed for effective heat transfer.

Increasing the heating power to 40 mW led to different offsets for mixtures but still different slopes for all of them as observed in Figure 75. When applying a heating power of 50 mW (Figure 76), slopes became similar and useable for the λ calculation.

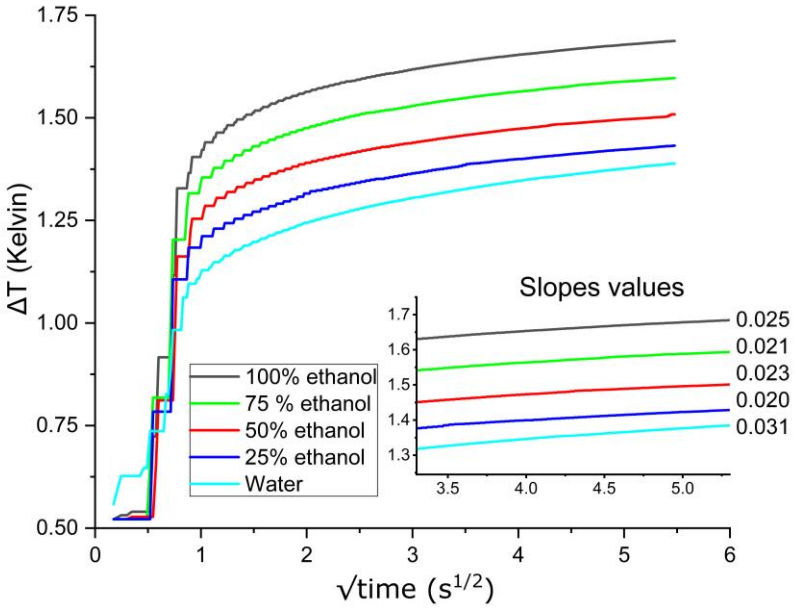

Figure 75: Time variations of the temperature in the microcavity filled with water/ethanol mixtures when a heat pulse (40 mW during 30 s) is applied to the heater/sensor. The observed slopes are shown from a time interval of [3.3 $s^{1/2}$; 5.3 $s^{1/2}$].

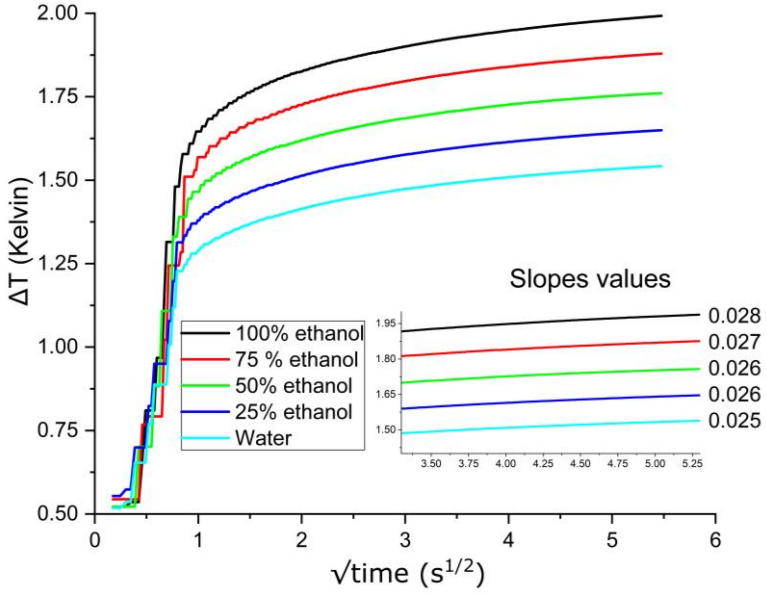

Figure 76: Time variations of the temperature in the microcavity filled with water/ethanol mixtures when a heat pulse (50 mW during 30 s) is applied to the heater/sensor. The observed slopes are shown from a time interval of [3.3 $s^{1/2}$; 5.3 $s^{1/2}$].

Figure 77 shows the comparison between slope values obtained for power ranging from 30 to 60 mW. This comparison was conducted using only two sensors. It has been studied whether the experimental results show any dependence on the intensity of the power used, which is equivalent to see if there is any systematic deviation. We present in Figure 77 values of the slopes obtained from 30 individuals heating with different power levels for two microfluidic devices. When using insufficient electrical power of 30 mW, there is an instability in the in the heat flux, resulting in inconsistent slope values for each individual heating. This instability decreases as the power is increased to 50 and 60 mW.

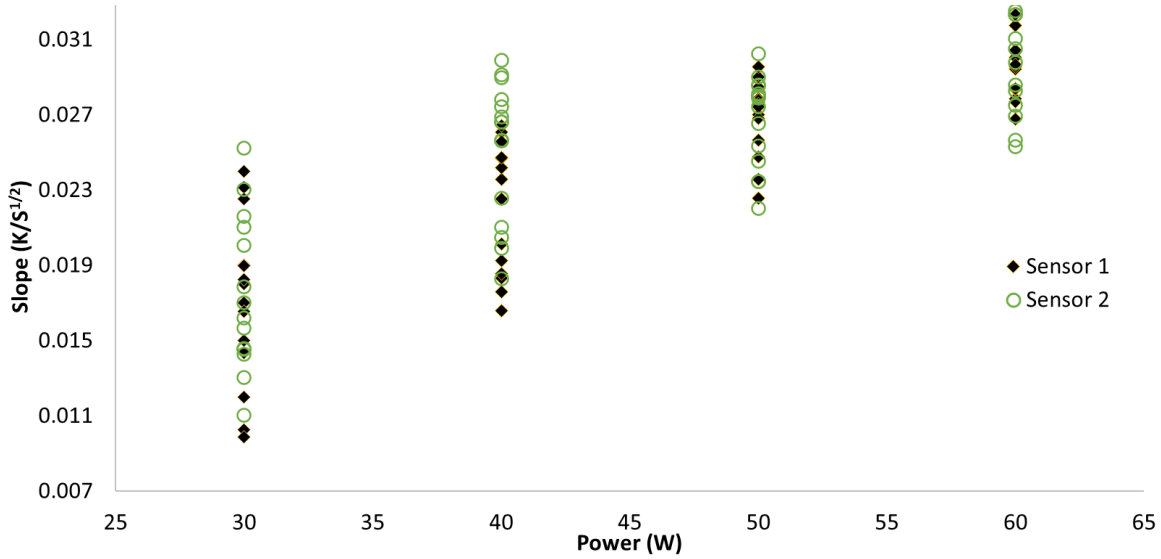

Figure 77: Slope values obtained at different individual heating as a function of the electrical power applied. The measurements correspond to the measurement of calibration fluids at 273K and show the results of 30 individual heating for each microfluidic device.

The coefficient of variation (CV) is a statistical measure that shows the relative variability of a dataset, particularly when the means of the datasets are different. It is calculated by dividing the standard deviation of the dataset by the mean of the dataset and multiplying the result by 100 and it is expressed percentage. A higher CV indicates a higher relative variability, while a lower CV indicates a lower relative variability. For each power applied the CV was calculated, to quantify this dispersion and compare the results between each sensor.

Table 13 : Comparative table of the variation coefficient for each sensor and power used

Microfluidic device	Number of heating	CV (%) P= 30 mW	CV (%) P=40 mW	CV (%) P=50 mW	CV (%) P=60 mW
Sensor 1	30	26.5	16.7	8.0	6.0
Sensor 2	30	24.6	15.6	9.6	9.5

As observed in Table 13, the CV for both sensors at 30 mW is between 25 and 27% while at 50 and 60 mW the CV is reduced to 6 and 10%. Sensor 2 shows the same level of variation for both 50mW and 60mW, suggesting that increasing the power at this level does not necessarily reduce the dispersion of the slopes data. After evaluating the potential deviation in heating power levels, we concluded that a heating power of 60 mW (60.03 ± 0.63 mW) is suitable for our microfluidic sensor device. 50 mW was not considered because of its proximity to the frontier where higher deviations may occur, such as at 40 or 45 mW.

3.5.2. Heat pulses duration

The duration of the heat pulses must be chosen to ensure that the thermal energy reaches the limits of the static fluid sample within the microcavity. This study was conducted using sensor 1 and sensor 2. In practice, it could be considered that the accuracy is improved with the pulse duration. However, after a certain period, the temperature of the fluid does not rise as much because the silicon top reference dissipates the heat, acting as heat sink. Thus, there is a compromise to find between

accuracy and time measurement. We investigated heating pulse durations from 15 s to 60 s. Figure 78 shows the temperature response curves for the water/ethanol mixtures applying a heating pulse of 60 s. Clearly, a heat pulse greater than 12 s (corresponding to 3.5 $s^{1/2}$ on Figure 78) appears mandatory, which means that for shorter measurement times, the heat flow has not covered the distance between the heater and the silicon substrate (59.8 µm). Also, we can observe the temperature difference calculation between certain zones of the curve. For the interval A, its ΔT is at 0.12 K, and for interval B and C the temperature stabilizes (0.031 K). We attempted to increase the duration of heat exposure and see if the temperature difference (ΔT) would stabilize at 0 K between intervals. However, we did not observe any difference, possibly because the environmental temperature is not controlled, which could explain why the ΔT does not stabilize to 0 K. Nevertheless, the observed temperature difference remains minimal and within acceptable limits, indicating that there is a stabilization due to the maximum heat flux reaching the boundary of the microfluidic device. This ΔT difference was also observed in previous experimental work of Oudebrouckx *et al*. [42]. In their study, there is a ΔT of 0.1 K at the selected interval. The same conclusions are observed for both sensor 1 and sensor 2. To have a sufficient integration period for data treatment with the proposed microfluidic device, we considered a heat pulse duration of 60 s was appropriate and this value will be used hereafter.

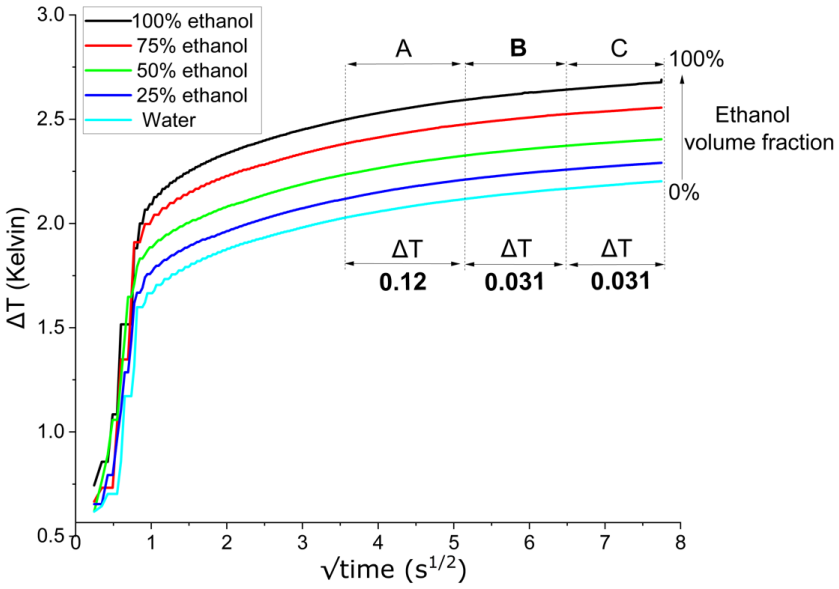

Figure 78: Time variations of the temperature in the microcavity filled with water/ethanol mixtures as detailed in Table 1, when a heat pulse (60 mW during 60 s) is applied to the heater/sensor. A, B, and C stand for three different intervals each having a 16 s duration .

3.5.3. Time interval selection for λ calculation

The time interval of the curve used to derive temperature variations, which are then related to λ values, must be carefully fixed. In practice, it can be assumed that the greater the time interval (close to the end of the curve), the greater the accuracy. However, the local slope of the curve decreases with time along with the ΔT values until reaching a stable value.

Linear regressions were performed on the obtained temperature response curves for the water/ethanol mixtures (Figure 79), over subsets of the time interval [3.5 $s^{1/2}$; 7.7 $s^{1/2}$], the time

interval was divided into three, each having a duration of 16 s, *i.e.*, A: [3.5 $s^{1/2}$; 5.3 $s^{1/2}$], B: [5.3 $s^{1/2}$; 6.6 $s^{1/2}$], and C: [6.6 $s^{1/2}$; 7.7 $s^{1/2}$]. This example was taken from the information data of sensor 2.

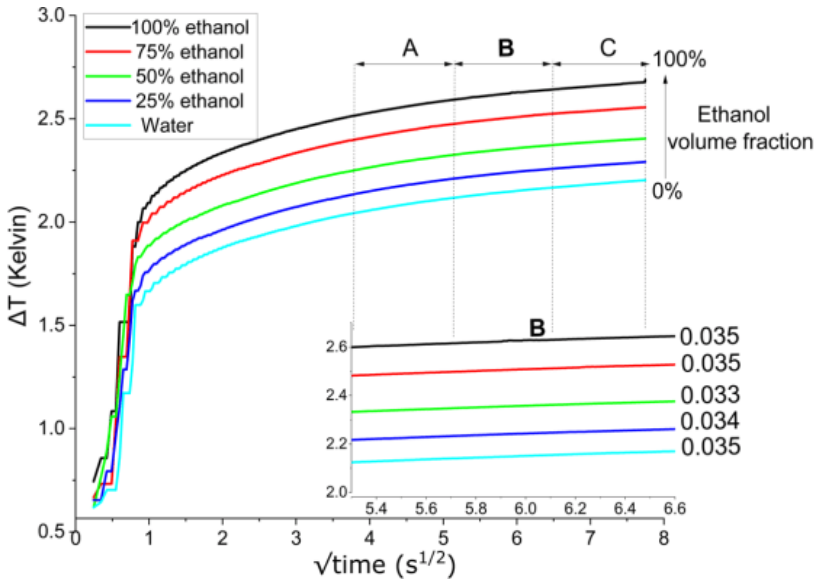

Figure 79: Time variations of the temperature in the microcavity of sensor 2 filled with water/ethanol mixtures, as detailed in Table 1, when a heat pulse (60mW during 60s) is applied to the heater/sensor. A, B, and C stand for three different intervals each having a 16s duration. Extracted from ref. [1].

As shown in Table 14, while the slopes obtained for interval A are similar across mixtures, these values are about twice as high as those derived for intervals B and C, which is also related to the fact that heat flux has not yet reached the liquid boundary. Also, in that can be noticed that uncertainties for interval C (longer heat duration) are greater than for the other two cases, which can be due to a beginning of heat dissipating by other directions in the microfluidic device.

Table 14: Slopes values for each time interval for sensor 2.

Fluid	Slope Interval A ($K/s^{1/2}$)	Slope Interval B ($K/s^{1/2}$)	Slope Interval C ($K/s^{1/2}$)
100% ethanol	0.058	0.035	0.028
75% ethanol	0.058	0.035	0.025
50% ethanol	0.057	0.033	0.026
25% ethanol	0.057	0.034	0.025
Water	0.056	0.035	0.029
Uncertainty	0.0014	0.0031	0.0051

Overall, based on these observations we found appropriate to use the following parameters: P = 60 mW, heating duration of 60 s and selection of time interval of B: [5.3 $s^{1/2}$; 6.6 $s^{1/2}$].

3.5.4. Optimized parameters for calibration curve

From the curves shown in Figure 80, the offset values resulting from linear regressions performed in the interval B [5.3$s^{1/2}$; 6.6$s^{1/2}$] were extracted and related to the thermal conductivity λ of the corresponding water/ethanol mixtures. Depending on the sensor (sensor 1, sensor 2 or sensor 3), the

slopes obtained from linear fits at [$5.3s^{1/2}$; $6.6s^{1/2}$] ranges from 0.025 to 0.035 at 60mW for three sensors.

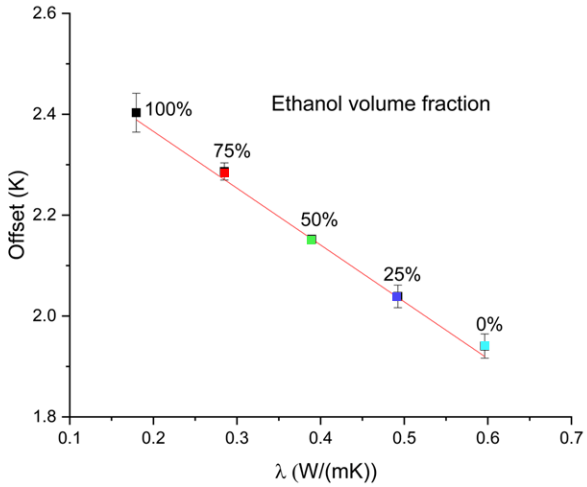

Figure 80: Illustration of a calibration curve plotting the offset values (ΔT) resulting from fittings as a function of reference λ values for corresponding water/ethanol mixtures.

Depending on the composition of the water/ethanol mixture, the ΔT values caused by a heat pulse as defined before, ranges from 1.9 K to 2.5 K (Figure 80). In the investigated time interval, the variation of the offset values with thermal conductivities can be assumed as a linear model (R^2 = 0.992) with offset = a. λ + b. The a and b values obtained for each sensor are reported in Table 15. The so-obtained expression stands for the calibration curve. Note that Oudebrouckx *et al.* suggested the use of an exponential relation between the temperature offset and λ. However, such fitting curves are not adapted to our microfluidic device and operating conditions. Moreover, the use of a linear relation between the offset and λ makes the uncertainty on the determination of λ constant over the whole range. Finally, it should be noticed that due to the variability of the parameters a and b among sensors, it is not possible to establish a universal curve applicable to all sensors.

Table 15: Values of the a and b parameters obtained for the calibration curve for each of the three sensors.

	a (K^2m/W)	b (K)
Sensor 1	-1.485 ± 0.078	2.819 ± 0.022
Sensor 2	-1.126 ± 0.061	2.591 ± 0.024
Sensor 3	-1.138 ± 0.056	2.596 ± 0.024

3.6. Sensor calibration with external validation

Two fluids with known experimental thermal conductivity behaviors were selected to perform the validation of the microfluidic methodology for λ measurement, *i.e.* fluids not used to set the calibration curve (Table 16). First an hydrocarbon, n-pentadecane having at 293.15 K a λ value of 0.137 W/(m.K), slightly outside of the calibration curve. The results obtained for this fluid should lead to conclusions about extrapolations from the calibration curve. Then, an oxygenated fluid, ethan-1,2-diol having at 293.15 K a λ value of 0.255 W/(m.K), which is within the calibration curve's range, but with a more pronounced non-linear trend in λ with temperature variations than other fluids [259].

Table 16: Experimental reference values of thermal conductivity at 293.15 K for the fluids considered for the external validation.

Fluids	λ (W/(m.K))	Ref.
n-pentadecane	0.137	[260]
ethane-1,2-diol	0.255	[261]

For each fluid, measurements were performed using the three sensors and then, the λ values were determined by applying the corresponding calibration curve. Table 17 presents the λ values measured for n-pentadecane and ethan-1,2-diol at 293.15 K. For n-pentadecane, the values obtained for λ range between 0.128 and 0.138 with a mean value of 0.134 W/(m.K). This latter is in good agreement with the reference experimental value of 0.137 W/(m.K) [260] This external validation point demonstrates that calibration curves can be extrapolated to lower values of λ – or higher offset values – than the range covered by water/ethanol mixtures. For ethan-1,2-diol, the λ measured values range between 0.290 and 0.316 with a mean value of 0.303 W/(m.K). The observed systematic deviation of about 20% from the reference experimental value of 0.255 W/(m.K) [261] is unsatisfactory and appear to be similar to data from the DIPPR database [262] that was not considered for correlations settings. Searching for artefacts inherent to our experiments, we investigated property correlations [176] and properties differences between ethan-1,2-diol and other fluids considered in this work. It highlighted dissimilarities, primarily in viscosity. Indeed, the value for ethan-1,2-diol (21 mPa.s) is about one order of magnitude higher than the value for water (1.0 mPa.s), ethanol (1.2 mPa.s), and n-pentadecane (2.5 mPa.s), at 293.15 K [176,262]. This would suggest that heat transfer by convection is not so negligible in microfluidics, and in our case, λ measurements are accurate for the range of viscosity values covered by fluids used during calibration.

Table 17: λ (W/(m.K)) values measured for the n-pentadecane and ethan-1,2-diol using the three sensors, at 293.15 K.

Sensor n°	Theorical value	n-pentadecane	ethan-1,2-diol
		0.137 ± 0.007	0.255 ± 0.008
Sensor 1	λ1	0.128 ± 0.010	0.290 ± 0.029
Sensor 2	λ2	0.138 ± 0.027	0.316 ± 0.015
Sensor 3	λ3	0.138 ± 0.004	0.300 ± 0.026
	< λ >	0.134 ± 0.019	0.303 ± 0.028

The variation of λ with the temperature was then investigated for n-pentadecane and ethan-1,2-diol. The obtained values are presented in Table 18, and Figure 81 compares the obtained values to those suggested by the literature [176,260–262]. For n-pentadecane, the good agreement observed with respect to reference λ values at 293.15 K are confirmed at 313.15 and 333.15 K, with a mean absolute relative deviation of about 8%. This validates the ability of our microfluidics device as well as our approach to be used to quantitatively predict the λ of liquids. Regarding ethan-1,2-diol, similarly to observations done at 293.15 K, our measured λ values overestimate reference values at 313.15 and 333.15 K. It can be noticed that the trend observed with temperature variations – ranging from 293.15 and 333.15 K – agrees with that of the reference values.

Table 18: Thermal conductivity (W/(m.K)) values measured for the n-pentadecane and ethan-1,2-diol using our microfluidic device, for temperature ranging from 293.15 to 333.15 K.

	n-pentadecane	ethan-1,2-diol
293.15 K	0.134 ± 0.019	0.303 ± 0.028
313.15 K	0.125± 0.024	0.303 ± 0.027
333.15 K	0.111 ± 0.026	0.305 ± 0.027

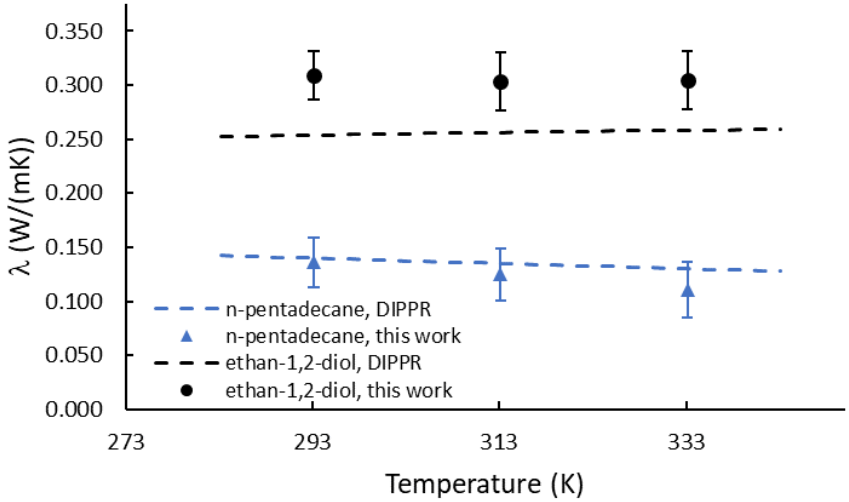

Figure 81: The evolution of λ value as a function of temperature for n-pentadecane (blue) and ethan-1,2-diol (black). Experimental values obtained in this work for n-pentadecane (triangles) and ethan-1,2-diol (circles) are compared to predictions using DIPPR's correlations (dashed lines). Extracted from ref. [1].

The calibration of the sensor was validated with the use of two well-known fluids. Now we proposed to use the microfluidic device to generate new experimental data of one typical product issued from the conversion of biomass. The results are detailed hereafter.

3.7. New experimental data for 2-5 dimethylfuran

The biomass can be seen as a raw material from which high-value products can be derived. For instance, cellulose present in lignocellulosic biomass can be converted into glucose or fructose, from which compounds with potential as biofuels can be derived, *e.g.* 2,5-dimethylfuran. To our knowledge, there is no experimental λ data for 2,5-dimethylfuran. Therefore, we used our microfluidic device to generate new data points, and each data point is the average result of 10 acquisitions. The λ values measured for 2,5-dimethylfuran at 293.15, 313.15 and 333.15 K are reported in Table 19. Indeed, its viscosity value of 0.4 mPa.s at 293.15 K [49,50] is similar to that of fluids used to during sensors calibrations.

Figure 82 shows a comparison between our data points and the predicted evolutions of the λ value as a function of temperature for 2,5-dimethylfuran using two models: one available from the DIPPR [262] and one proposed by Chung *et al.* [263]. It can be noticed that the two predictive models overestimate our experimental data, and that the trends observed with temperature – ranging from 293.15 to 333.15 K – reasonably agree. Based on our experimental data and temperature ranges, we can suggest

the use of the model parameters proposed by Jamieson [264] found in chapter I section 1.3.1, to estimate the thermal conductivity 2,5-dimethylfuran as a function of temperature, as follow:

$$\lambda = 0.046(\,1 + (-0.209)\,\times \tau^{\frac{1}{3}} + 1.242 \times \tau^{\frac{2}{3}} + 2.062 \times \tau) \qquad (3\text{-}17)$$

with $\tau = 1 - \frac{T}{T_c}$, where is T_c is the critical temperature of 2,5-dimethylfuran in this case.

Table 19: Thermal conductivity (W/(m.K)) values measured for 2,5-dimethylfuran at 293.15, 313.15 and 333.15 K.

< λ >	293.15 K	313.15 K	333.15 K
λ	0.120 ± 0.018	0.114 ± 0.015	0.103 ± 0.021

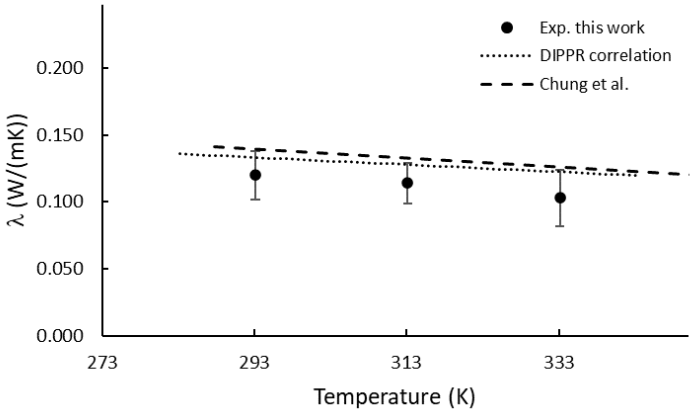

Figure 82: The evolution of λ as a function of temperature for 2,5-dimethylfuran. Experimental values from this work are compared to predictions using DIPPR's correlations (dashed line) and the model by Chung *et al.* [263] (dotted line). Extracted from ref.[1].

3.8. Conclusions

We investigated the use of silicon-borosilicate materials commonly employed for microfluidic reactors compatible with harsh processes conditions to develop a new microdevice for thermal conductivity measurements, with an operating principle based on the transient thermal offset approach. We discussed the different instruments required to measure thermal conductivity. This involves generating heat on a sensor by Joule effect, which causes the sensor's temperature to change, resulting in a change in its resistance.

A Wheatstone bridge-based experimental setup was created to enable the measurement of thermal conductivity with our microfluidic device. The uncertainties associated with the instruments used (such as power supply, current, and resistance) as well as the repeatability of the measurements (including slope, offset, and thermal conductivity values) were evaluated. Then, thermal conductivity measurements of different liquids were achieved. First, the sensor response was calibrated by fitting the thermal behaviors of well-known fluids mixtures containing water and ethanol. As a result of conclusions reached at this stage, we decided to set the heating power applied, the length of the heating pulse, and the time interval for the λ calculation to 60 mW, 60 s and [28 s ; 44 s], respectively. The microfluidics device and its settings were then externally validated on two fluids: n-pentadecane

and ethan-1,2-diol, for temperatures ranging from 293.15 K to 333.15 K. Finally, we proposed new experimental values for 2,5-dimethylfuran a biomass by-product for which there is a lack of thermal conductivity data information in the literature.

We demonstrated that it is feasible to miniaturize existing thermal conductivity measurement devices, for instance considering microfluidic procedures and using silicon as heat sink on one side/surface of the micro-chip. Also, besides the conception of the microfluidic device, the measurement set-up does not require expensive equipment in comparison to the other systems suggested in the literature [30,41,42] and it allows a straightforward data analysis to calculate the thermal conductivity of fluids sample.

We also extended the approach and design the micro-chip to investigate the temperature effect on thermal conductivity for both well-known fluids as well as new experimental values for 2,5-dimethylfuran. This study demonstrated that new experimental data can be generated by using this microfluidic approach. The following chapter discusses the inclusion of this new experimental data in a database to develop predictive models to determine thermal conductivity of hydrocarbons and oxygenated compounds.

Chapter IV: Predictive models for thermal conductivity

The last two chapters were dedicated to the fabrication and the use of a microfluidic device to measure the thermal conductivity of liquids at varying temperatures. Through this, we demonstrated that this method allows generating new experimental data, which were subsequently included in the process of the model development.

The combination of microfluidics and predictive modeling is a powerful approach enabling researchers to explore inaccessible experimental data, analyze complex data, and speed up scientific and technological discoveries, all while reducing costs and the number of reagents used.

This chapter presents the development of new models for the prediction of thermal conductivity of hydrocarbons and oxygenated compounds. The procedure covered in this chapter involves the collection and pre-processing of a database containing chemical structures and property values, the use of specific descriptors to represent the structural information of molecules, employing a modeling technique to train and fine-tune the model, optimizing hyperparameters, evaluating the model's performance using suitable metrics, and validating the model's ability to make accurate predictions.

4.1. Introduction

Models have been developed and used in some scenarios for the prediction of thermal conductivity of liquids. These models include Equation of State (EoS) models. However, these models have not been widely applied to polar substances such as alcohols, ketones, and organic acids, among others. Accurate prediction of EoS for specific compounds is still difficult due to the scarcity of experimental data on certain parameters required to compute the developed models.

There are also models obtained using cheminformatics, which is a more recent field of science that combines statistics, computer science, and chemistry to convert data into information and knowledge. One significant use of cheminformatics is the prediction of thermophysical properties through models like Quantitative Structure-Property Relationships (QSPR) [148,165,166,189,265]. These models rely on the correlation of molecular structure descriptors and property values to develop models for the property prediction. Some of the thermophysical properties that have been modelled using QSPR include boiling points, melting points, density, enthalpy of vaporization, heat capacity, solubility parameters and thermal conductivity. QSPR models have been successfully applied to a variety of compounds, ranging from simple organic molecules to complex polymers and pharmaceutical compounds. The group contribution method is one approach frequently employed in QSPR works for precisely describing the chemical structure of the chemical molecules. This method involves splitting the molecule into smaller fragments and calculating its properties by summing up the contributions of the chemical groups present. GCM methods are advantageous due to their simplicity and have also been used for predicting thermophysical properties [165,191].

QSPR methods have been used to predict the thermal conductivity of liquids, but only a few studies have considered the impact of temperature on this property. Hence, Liu *et al.* reported an improved QSPR model for predicting thermal conductivity of liquid aliphatic alcohols [148]. Their model was trained on 65 alcohols at different temperatures. A 4-descriptors linear model was developed, by using the stepwise regression and the best subset regression method. However, the authors did not use the same amount of data for each compound in the Training set, leading to compounds with more data having a greater impact on the model's predictions, potentially causing biases. Also, some compounds

are both in the Training and Test sets which avoid any conclusion regarding the accuracy of the model's predictions. Later, Lu *et al.* recently reported the development of a QSPR based model to predict the thermal conductivity of diverse organic compounds in liquid phase [147]. Their model was trained on a set of chemical compounds including chemical families such as alcohols, ethers, aldehydes, ketones, acids, and esters – similar to our target. A 6-descriptor linear model was developed, combining a genetic function approximation and a variety of molecular descriptors derived from geometries optimized using density functional theory. However, the model assumed that the temperature dependency of thermal conductivity is the same for all compounds, which experimental data do not seem to show. Moreover, it seems that the Training/Test sets splitting randomly performed led to compounds representation in both sets for different temperature values [147].

While QSPR provides powerful tools for property estimation, it is important to note that the accuracy of predictions depends on the quality and diversity (diverse compounds, diverse conditions…) of the available experimental data used for model development.

We focus on the development of a QSPR model for predicting thermal conductivity of liquids, using a group contribution method and machine learning algorithm, which offers a non-linear approach. The model was built using accurate reference data to obtain a coherent database and performing an appropriate Training/Test set splitting. After presenting the data collection and curation methods and the strategy followed to develop new QSPR based models, we expose the predictive performances of models and discuss their utilization for external data prediction, before concluding.

4.2. Strategy & methodology

4.2.1. Database

As previously stated, the accuracy of predictive ML models depends on the quality of the data used to develop/train them. Thus, one of the keystones of such a work success stands in the database itself. Data collection requires considerable time to collect and clean the data because the quality of the data may not be sufficient. Ensuring the reliability and accuracy of the collected data can be a time-consuming process due to various factors such as inconsistencies, missing values, errors, and duplicates etc. The final database corresponds to the data used for the considered predictive model.

4.2.1.1. Targeted chemical families

This works focuses on the hydrocarbons and oxygenated compounds that are found in liquid form during the conversion of biomass into biofuels. These compounds are mainly derived from vegetable oils and lignocellulosic biomass and can be transformed into bio-oils or ethanol through various processes such as transesterification, pyrolysis, and hydrolysis. For example, when vegetable oils are transesterified, they react with alcohols and a catalyst to produce biodiesel and glycerol. Pyrolysis produces fuels with mostly light hydrocarbons (from C1 to C14), cyclic alkanes, aldehydes, ketones, and carboxylic acids.

Lastly, catalytic hydrotreating of oils fully hydrogenates unsaturated fatty acid chains and carboxylic groups to form n-alkanes (C12-C18) and water. Therefore, the chemical families likely to be encountered from this feedstock transformation are:

- Hydrocarbons, alkenes, aromatics, branched molecules.
- Alcohols, polar molecules forming self-associations in competition with the cross association.
- Ketones and aldehydes (R-(C=O)-R'), polar molecules that can form a cross association with the OH group of the alcohols.
- Carboxylic acids(R–COOH), polar molecules forming self-associations and probably less cross-association.
- Esters (R-COO-R'), polar bodies that can form a cross association with OH.
- Ethers (R-O-R'), polar molecules forming cross-associations probably less marked.
- Cyclic ethers (epoxides, furans…)
- Polyfunctional molecules (phenols, benzenediols, triols, etc.).

4.2.1.2. Initial data collection

We have mentioned that creating a comprehensive database by collecting data from various sources is a tedious task that demands careful attention. Challenges such as data compatibility, heterogeneity, privacy issues, and large data volume can make this process difficult. Hence, it is a time-consuming and effort-intensive step.

The available experimental data on thermal conductivity were collected from existing databases, mainly the DETHERM [266] but also, NIST, DIPPR [176,262] and data from the literature [146–148] including data for 2,5-dimethylfuran recently measured using the microfluidic device developed in this work [1].

Existing databases contain information on thermal conductivity for various substances, including solid, gas, and liquid states. This type of information was filtered and organized on an excel table focusing on specific parameters such as name, reference, SMILES, chemical family group, state of matter (liquid), temperature etc. Then, the units were standardized according to the International Unit System. The use of Excel macros and Python scripts facilitated the automation of the data organization process. After these steps being executed, we collected about 760 hydrocarbons and oxygenated compounds, with thermal conductivities at different temperatures.

As seen in Figure 83 that the number of oxygenated compounds seems predominant with respect to hydrocarbons. However, if we go deeper into the quantity of data available, for only 27% of molecules (200 hydrocarbons) there is still 45% of data information (5800 data points) representing thermal conductivities from various references or at different temperature ranges. On the other hand, even if that database counts with more than 73% of oxygenated molecules (around 560 molecules), it represents only 55% of datapoints (4500 data points).

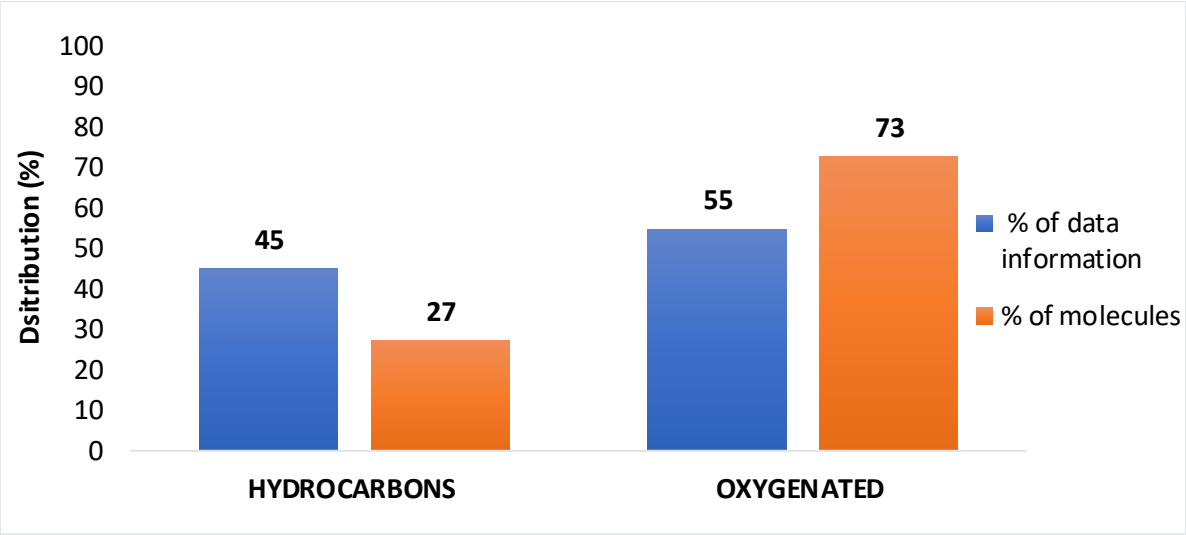

Figure 83 : Composition of the database in terms of percentage with respect to the number of molecules and the data information.

Outlier removal

At this point, the quality or reliability of data extracted is not yet determined. Therefore, it is essential to clean and curate the data. The initial step involved identifying any potential outliers in the database. An outlier refers to a data point that greatly differs from the rest of the data points in a dataset. It can be an exceptionally high or low value of thermal conductivity compared to the average. Outliers can occur due to measurement errors, fluctuations in the data, or unusual events.

The most common way for outlier detection is the use of statistical methods such as Z-Score (Standard Deviation Method). This method involves calculating the Z-score for each data point by subtracting the mean and dividing by the standard deviation. Any data point with a Z-score above a certain threshold (typically 2 or 3) is considered an outlier. However, there are three main issues when using the mean to indicate central tendency. Firstly, it assumes a normal distribution, including outliers. Secondly, outliers strongly affect the mean and standard deviation. Finally, it is unlikely to detect outliers in small samples [267].

An alternative method for detecting outliers is to use the median absolute deviation (MAD). The MAD is a robust measure of central tendency that is not affected by extreme values in the data set. By using MAD, the identification of outliers becomes more cautious and concentrates on most of the data rather than a few extreme values. This is especially beneficial when dealing with skewed or heavy-tailed datasets where outliers can have a substantial impact on the standard deviation.

$$MAD = b \times Median(|x_i - Median(x)|) \quad (4\text{-}1)$$

Where the x_i represents each individual point in the dataset (each thermal conductivity value), $Median(x)$ is the median of the dataset. The $Median$ is usually multiplied by b = 1.4826, a constant linked to the assumption of normality of the data, disregarding the abnormality induced by outliers [268].

It is therefore important to establish a criterion for rejecting a value. This criterion is subjective and depends on the researcher's decision. The researcher can choose a level of stringency, such as 3 (very conservative), 2.5 (moderately conservative), or 2 (poorly conservative), and justify their choice [15]. In this work, a threshold of 2.5 was chosen based on performed comparisons with different thresholds applied. The decision criterion becomes:

$$Median - 2.5 \times MAD < x_i < Median + 2.5 \times MAD \quad (4\text{- }2)$$

This formula was applied for each compound and by temperature.

After using equation (4- 1) and applying a threshold by equation (4- 2), 187 data points that were considered outliers were removed from the database. By doing this, we can see that the thermal conductivities now follow a more well-defined tendance of normal distribution, as shown in the histogram in Figure 84 b). Although the main outliers were removed, they only accounted for about 2% of the total data points, so it is important to confirm that all outliers were in fact removed. To ensure this, we conducted a residuals analysis.

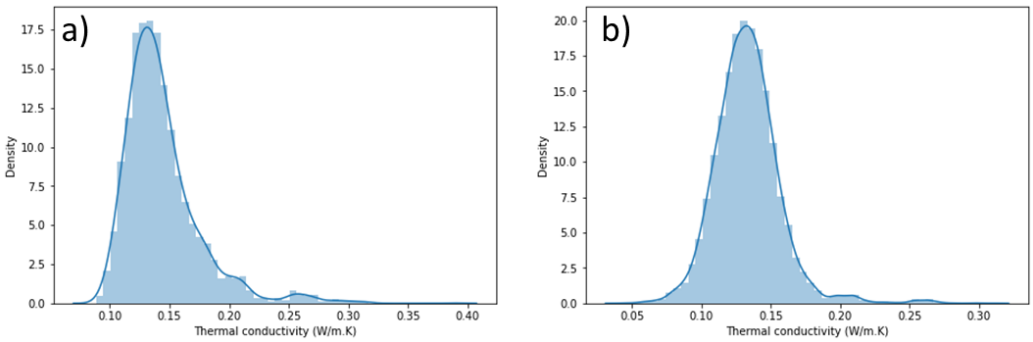

Figure 84: Histograms of thermal conductivities distribution a) before and b) after the outlier's removal.

Residuals analysis

According to the literature and equation (1- 9) in chapter I, thermal conductivities of most liquids decrease with temperature as a linear relationship. Many QSPR models used to predict thermal conductivity of liquids have assumed that the temperature dependency of thermal conductivity remains constant for all compounds [146,147,172]. This assumption was initially proposed and is supported by some collected values [146].

As shown in Figure 85, the process began by calculating the average thermal conductivity based on temperature and compounds. Then, a linear regression model was fitted for each compound using the average thermal conductivity as the dependent variable (Y-axis) and temperature as the independent variable (X-axis). The model parameters, A (slope) and B (intercept), were estimated for each compound. Residuals were then calculated for each data point, which represent the differences between the observed and predicted values of thermal conductivity. This is expressed in equation (4- 3):

$$r_i = y_i - \hat{y}_i \quad (4\text{- }3)$$

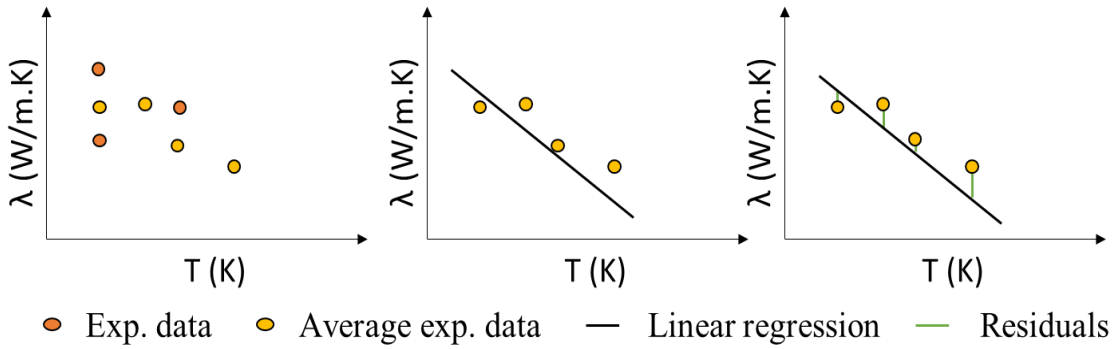

Figure 85: Steps for residuals analysis.

By performing a residuals analysis, we can identify any outliers that significantly deviate from the predicted thermal conductivity value. This analysis helps us to assess the suitability of the regression model accurately representing the actual data.

As observed in Figure 86, there are still some residuals that are significantly different from the predicted values and need to be eliminated. One approach would be to remove these residuals that are far from the predicted value. However, determining the maximum acceptable distance for these residuals would be necessary.

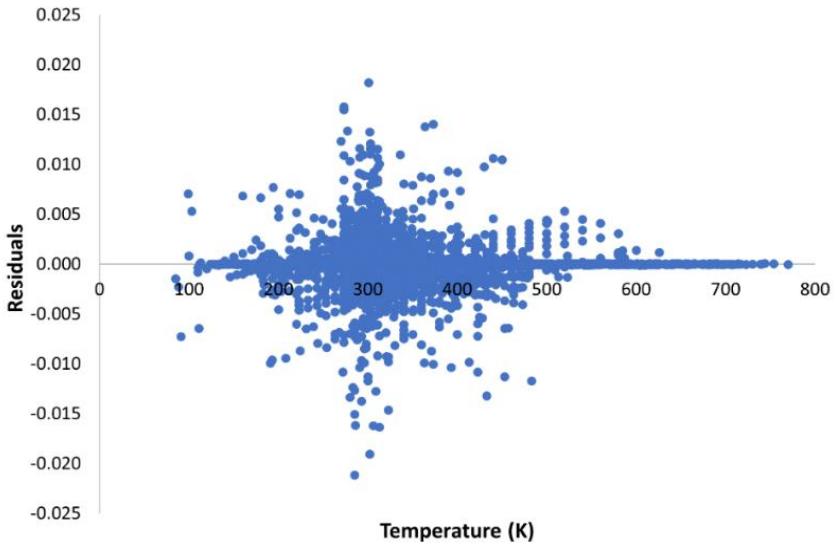

Figure 86: Residuals distribution after removal of outliers.

Hence, our attempt to eliminate the remaining residuals encountered a challenge. We faced a situation where the data extracted from external published sources in the literature were not consistently generated in the same manner. This meant that some thermal conductivity values included a mix of data originating from models or data fittings, as well as experimental data, with no possibility of dissociating them properly. As a result, we made the decision to discard this dataset entirely. Subsequently, we initiated a new data collection, adhering to specific criteria, to establish a new and reliable database.

4.2.1.3. New data collection

No data from models or data fittings were considered and the new data collection, which includes only experimental data. The values reported as 'Accepted' by the DIPPR staff reviewers were prioritized. The term 'Accepted' data in the DIPPR database refers to thermophysical property data that has been carefully examined and compiled by experts from different sources. This data has undergone a thorough review process to ensure its accuracy and reliability, making it the most trustworthy and recommended data for engineering and scientific applications.

For each compound, as many data points as possible were collected to account for the temperature dependence of λ. As compared to the first database, the number of compounds is much smaller and reduced to 178. Nevertheless, we can be confident in the accuracy of the data used to create the model as only experimental accepted data are considered. Figure 87 shows the distributions of the two classes of compounds in the database: hydrocarbons and oxygenated, as well as distributions of considered subfamilies. It shows that hydrocarbons and oxygenates represent roughly 40% and 60% of chemicals, respectively. Hydrocarbons may then be discretized in terms of alkanes, alkenes, and cyclic molecules such as naphthenics and aromatics. In the database, cyclic compounds represent about 31% of hydrocarbons and the remaining ones are for 61% saturated paraffins (n- and i-alkanes) and 8% alkenes. Concerning oxygenated compounds, the database includes, in decreasing order of occurrence: alcohols, esters, carboxylic acids, ethers, ketones, formats, aldehydes, and epoxides. It should be noted that 6 oxygenated are polyfunctionals, *i.e.* they are constituted of at least two of the latter chemical characteristics.

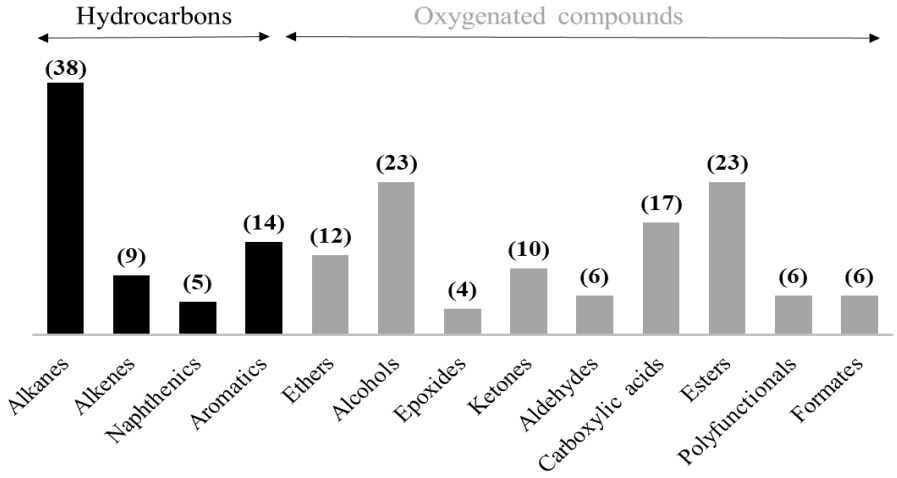

Figure 87: Distributions of hydrocarbons (black) and oxygenated compounds (dark grey) considered within the all database (178 compounds). The values in brackets above bars stand for the number of compounds of each chemical family

As shown in Figure 88 a), in some cases, experimental thermal conductivity values reported for one compound at a specific temperature can vary depending on the sources of data, and only one value has been retained for each molecule and temperature condition and when necessary, averages were taken (Figure 88 b)). Then, parameters of the expression proposed by Jamieson – equation (1- 11) from chapter I, were regressed using data points within the database (Figure 88 c)), with $\tau = 1 - {}^{T}/_{T_c}$ where T_c is the critical temperature in K [264]. The as-obtained A to D parameters were subsequently

used together with equation equation (1- 11) to generate, for each compound, 10 data points by varying the temperature from the lowest of collected data up to T_c (Figure 88 d)). These steps are summarized in Figure 88.

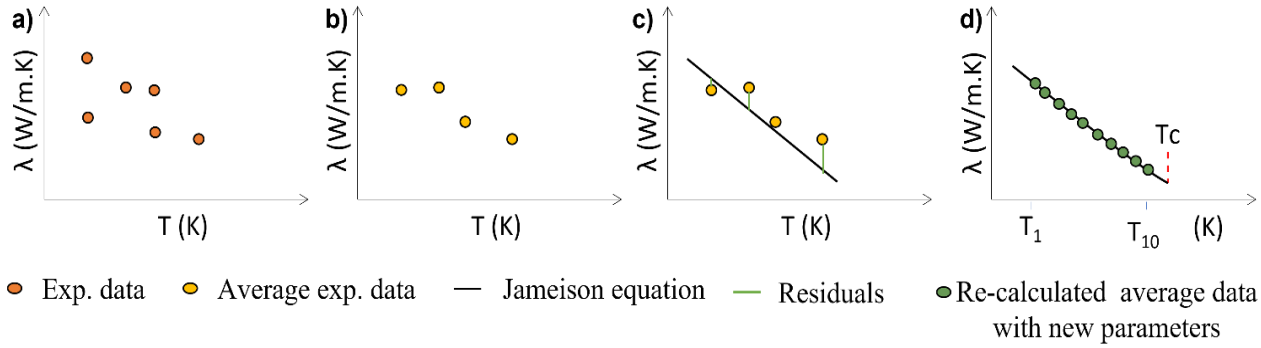

Figure 88: Steps during the creation of the database.

For certain chemical compounds, there was insufficient experimental data, often limited to just 1 or 2 data points, to derive the necessary parameters for the equation. In such cases, these compounds (a total of 23) were set aside and designated as a validation set and are discussed in section 4.3. Overall, parameters were successfully regressed for 155 compounds (1550 data points). The updated distribution of chemical families is illustrated in Figure 89. The list of the chemical molecules representing the 155 compounds can be found in the Supporting information from ref. [2].

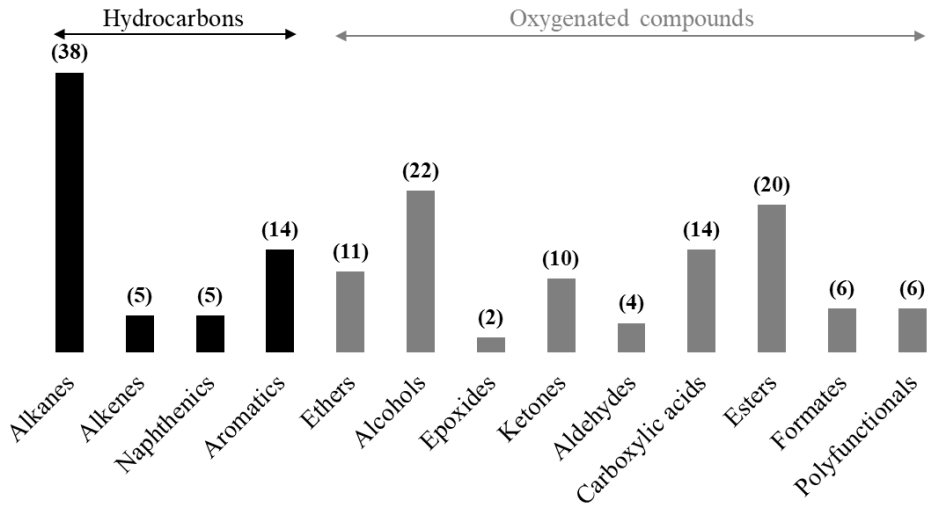

Figure 89. Distributions of hydrocarbons (black) and oxygenated compounds (dark grey) considered for the 155 compounds from the database. The values in brackets above bars stand for the number of compounds of each chemical family. Extracted from ref. [2]

4.2.1.4. Descriptors generation: 0D and 1D descriptors

Descriptors used in QSPR studies can be categorized into various types, including molecular constitutional descriptors, topological descriptors, geometric descriptors, electronic descriptors. Molecular constitutional descriptors only require atom and bond labels and usually represent counts

of different types of atoms, bonds, fragments or functional groups. There are also more complex descriptors such as geometric descriptors which require a 3D conformation (interatomic distances, molecular volume and surface areas) as input and therefore the computations time is longer.

There are several works that used the GCM approach to predict several properties of hydrocarbons and oxygenated compounds. Few examples can be mentioned, Saldana *et al*. [164] used Molecular Descriptors and Functional Group Count Descriptors (FGCD) to predict the cetane Number and flash Point on hydrocarbons and oxygenated compounds. This approach was later used for the prediction of density and kinematic density [151] and then for the prediction of melting point and net heat of combustion of hydrocarbons and oxygenated compounds [189].

Therefore, based on the conclusion of these studies, solely FGCD descriptors derived from the chemical and structural formulae were considered. In this latter, family of molecular descriptors are included counts of atoms and groups of atoms identified as relevant from chemical aspects. Such a simple representation of compounds has been shown to provide relevant descriptors usable in QSPR procedure [164]. FGCD initially considered in this study, were labelled from X1 to X44, are listed in Table 20. As an example, the FGCD labelled X3 denotes the number of CH_3 groups. The molar mass (MM) of neat compounds was also computed and used as an additional descriptor (labelled X44). Simplified molecular input line entry specification (SMILES) codes were assigned to each neat compound within the database. FGCD were automatically calculated using the RDKit [269] and SMILES arbitrary target specification (SMARTS) matching functionalities [270], which notation is an enhanced version of SMILES that is used to specify substructures in chemical structures. It includes special characters and symbols to enable more accurate and customizable substructure searching. SMARTS codes corresponding to considered FGCD are given in Table 20.

Table 20. Molecular descriptors initially considered for the development of models.

Label	SMARTS	Label	SMARTS
X1	[H]	**X23**	[CX4H3][OX2H0][#6]
X2	[C,c]	**X24**	[CX4H2][OX2H0][#6]
X3	[CX4H3]	**X25**	[CX4H1][OX2H0][#6]
X4	[CX4H2]	**X26**	[CX3H0](=[O])[OX2H1]
X5	[CX4H1]	**X27**	[CX3H1](=[O])[OX2H1]
X6	[CX4H0]	**X28**	[OX2H0][CX3H0](=[O])
X7	[CX3H2]=[CX3H1]	**X29**	[OX2H1][CX4H2][CX4H2][OX2H0][#6]
X8	[CX3H1]=[CX3H1]	**X30**	[OX2H0][CX4H1][OX2H0]
X9	[CX3H2]=[CX3H0]	**X31**	[cX3H0][O][cX3H0]
X10	[cH1]	**X32**	[#6][CX3H1](=O)
X11	[cH0]	**X33**	[#6][OX2H0][#6]
X12	[c][CX4H3]	**X34**	[#6][CX3H0](=[O])[#6]
X13	[c][CX4H2]	**X35**	[#6][CX4H2][OX2H1]
X14	[OX2H1]	**X36**	[#6][CX4H1]([#6])[OX2H1]
X15	[CX4H3][OX2H1]	**X37**	[CX4H3][CX3H0](=[O])[OX2H1]
X16	[c][OX2H1]	**X38**	[#6][OX2H0][CX3H0](=[O])[#6]
X17	[CX4H3][CX3H0](=[O])[#6]	**X39**	[#6][CX3H0](=[O])[#8]
X18	[CX4H2][CX3H0](=[O])[#6]	**X40**	[#6][OX2H0][CX4H3]

X19	[CX3H1](=[O])	**X41**	[O;R]
X20	[CX4H3][CX3H0](=[O])[OX2H0]	**X42**	[C;R]
X21	[CX4H2][CX3H0](=[O])[OX2H0]	**X43**	[c;R]
X22	[CX3H1](=[O])[OX2H0]	**X44**	molecular_weight

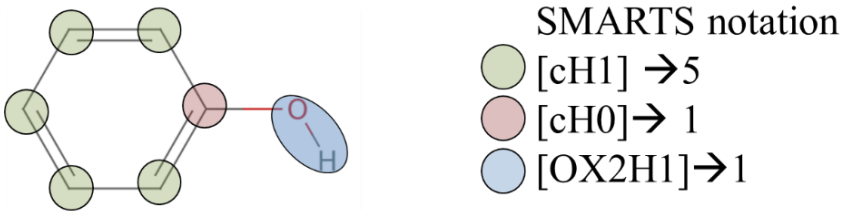

Figure 90: Different fragments found in the phenol molecule, using SMARTS notation.

For instance, the phenol molecule has 3 different FGCD which are labelled on Table 20 as X10, X11 and X14. These 3 FGCD are shown in Figure 90. Label X10 refers to the aromatic carbons with an additional hydrogen atom highlighted in green and is equal to 5 for phenol. X11 represents the aromatic carbon with no hydrogen atoms highlighted in red which is equal to 1 for phenol. X14 corresponds to the aliphatic oxygen with an additional hydrogen, or the hydroxyl group highlighted in blue, which is equal to 1 in the case of phenol. To ensure that all FGCD descriptors were considered for each molecule, an image was created showing all the molecules present in the database. Each descriptor was automatically highlighted by a red circle, as shown in Appendix F, noticing that all chemical families were considered.

The calculated descriptors were stored in a $\boldsymbol{X}\ matrix$ of $n \times p$, where n is the number of samples (equal to 155), and p, the number of molecular descriptors or variables (equal to 44), as shown in Figure 91.

$\boldsymbol{X}\ matrix =$

Descriptors → p = 44

n = 155 Individuals ↓

Compound	[cH1]	cH0]	[OX2H1]
Phenol	5	1	1
Benzene	6	0	0
Propanol	0	0	1

Figure 91: X matrix containing the calculated descriptors in the database.

Duplicates removal

Initially, from the calculated FGCD the study considered 44 different descriptors. However, using a heat map correlation using the $\boldsymbol{X}\ matrix$ table, it was discovered that some descriptors provided the same information and were therefore considered as "duplicate". A correlation heat map is a visual representation that displays the relationships between variables, with each variable represented by a row and column. The cells in the map display the correlation coefficient, which measures the strength and direction of the linear relationship between two variables and the cells show the correlation coefficient between them, ranging from -1 to +1. A positive correlation means that as one variable increases, the other is also likely to increase, while a negative correlation suggests that as one variable

increases, the other is likely to decrease. A correlation coefficient of zero means there is no correlation between the variables. The heat map uses different colors to indicate the strength of relationships, with dark colors, (black) representing negative correlation), neutral colors (purple) representing no or weak correlation, and warm colors (light orange) representing positive correlation. A value of +1 is represented by a yellowish or white color. Visualizing the correlation matrix as a heat map allows for easier identification of patterns and relationships between variables in extensive datasets.

In Figure 92, there are four cases where the correlation is +1. There is a correlation between the number of carbons in a molecule (X2) and its molar weight (X44), however this correlation is not considered as "duplicate" because it is known that as the number of carbons increases, the molar weight also tends to increase.

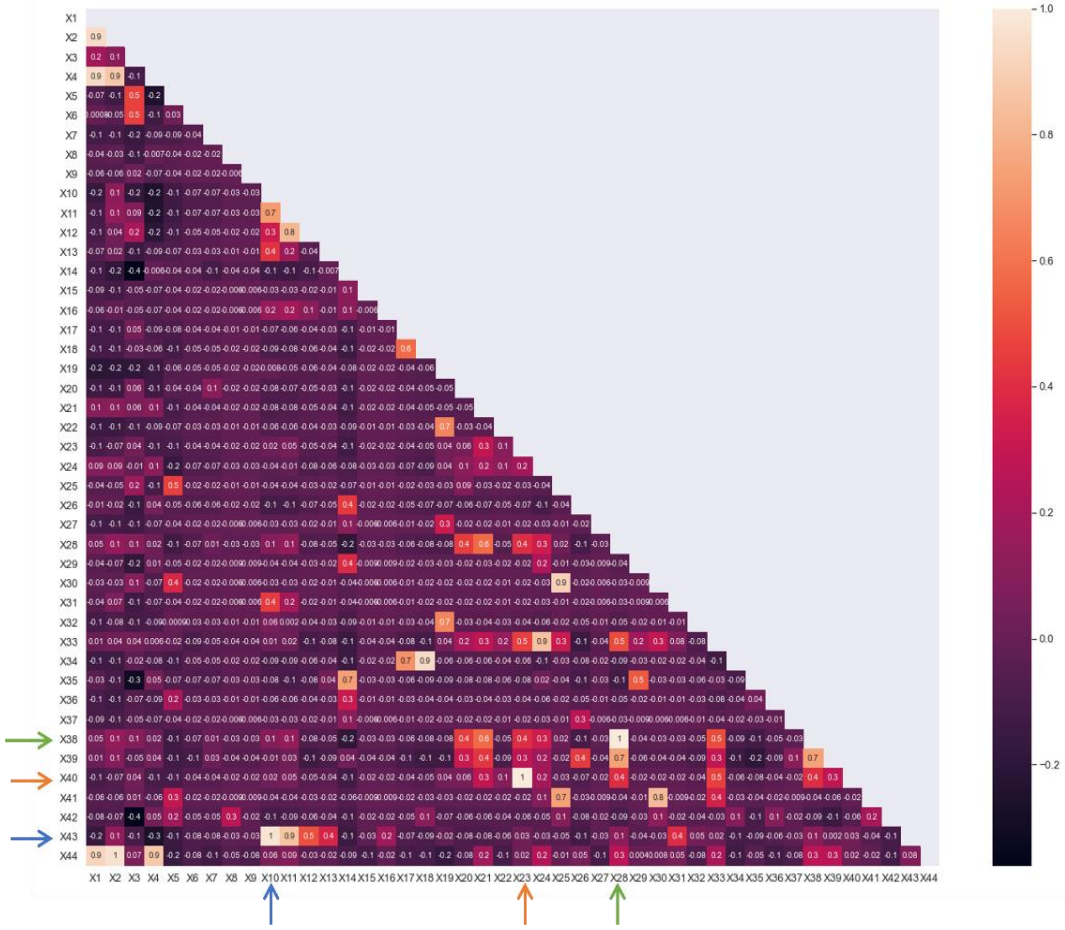

Figure 92: Heatmap correlation of the initial 44 variables.

On the other hand, correlation is observed between variables X10/43 (highlighted with blue arrows), X23 /X40 (highlighted with orange arrows), and X28/X38 (highlighted with green arrows). After comparison, this correlation indicates that these variables provide identical information to the database and can be considered duplicates of each other. These variables are shown in Table 21.

Table 21: pair of molecular descriptors that provides equal information.

SMARTS variables	Label	Duplicate
[cH1]	~~X10~~	~~1~~
[c;R]	X43	1

[OX2H0][CX3H0](=[O])	X28	2
[#6][OX2H0][CX3H0](=[O])[#6]	~~**X38**~~	~~**2**~~
[CX4H3][OX2H0][#6]	X23	3
[#6][OX2H0][CX4H3]	~~**X40**~~	~~**3**~~

After identifying these duplicates variables, the ones highlighted in red were eliminated from the initial descriptors list, resulting in a final set of the 42 descriptors shown in Table 22.

Table 22. Molecular descriptors selected for the development of models. Extracted from ref. [271].

Label	SMARTS	Label	SMARTS
X1	[H]	**X22**	[CX4H2][CX3H0](=[O])[OX2H0]
X2	[C,c]	**X23**	[CX3H1](=[O])[OX2H0]
X3	[O,o]	**X24**	[CX4H3][OX2H0][#6]
X4	[CX4H3]	**X25**	[CX4H2][OX2H0][#6]
X5	[CX4H2]	**X26**	[CX4H1][OX2H0][#6]
X6	[CX4H1]	**X27**	[CX3H0](=[O])[OX2H1]
X7	[CX4H0]	**X28**	[CX3H1](=[O])[OX2H1]
X8	[CX3H2]=[CX3H1]	**X29**	[OX2H0][CX3H0](=[O])
X9	[CX3H1]=[CX3H1]	**X30**	[OX2H1][CX4H2][CX4H2][OX2H0][#6]
X10	[CX3H2]=[CX3H0]	**X31**	[OX2H0][CX4H1][OX2H0]
X11	[cH1]	**X32**	[cX3H0][O][cX3H0]
X12	[cH0]	**X33**	[#6][CX3H1](=O)
X13	[c][CX4H3]	**X34**	[#6][OX2H0][#6]
X14	[c][CX4H2]	**X35**	[#6][CX3H0](=[O])[#6]
X15	[OX2H1]	**X36**	[#6][CX4H2][OX2H1]
X16	[CX4H3][OX2H1]	**X37**	[#6][CX4H1]([#6])[OX2H1]
X17	[c][OX2H1]	**X38**	[CX4H3][CX3H0](=[O])[OX2H1]
X18	[CX4H3][CX3H0](=[O])[#6]	**X39**	[#6][CX3H0](=[O])[#8]
X19	[CX4H2][CX3H0](=[O])[#6]	**X40**	[O,o;R]
X20	[CX3H1](=[O])	**X41**	[C;R]
X21	[CX4H3][CX3H0](=[O])[OX2H0]	**X42**	MM

Following this, the $\boldsymbol{X}\ matrix$ contains the molecules and their 42 respective descriptors in a high dimensional space, which can be difficult to interpret or exploit. To analyze this data effectively, we used a technique called Principal Component Analysis (PCA), which is described hereafter.

4.2.2. Chemical space representation

Nowadays, there are many experimental techniques that generate a large amount of data. However, analyzing this data is challenging because it has a high number of dimensions. To address this issue, various techniques have been created to reduce the dimensionality of the data, with PCA being the most used method.

The concept of PCA is mostly credited to Karl Pearson (1911) [272] and later to Harold Hotelling (1933) [273], which belongs to a group of multivariate statistical techniques, eminently descriptive. The principle of PCA is to obtain an approximate representation of the variables in a lower K-dimensional subspace, meaning by transforming the original set of p variables into another set of a smaller number of q decorrelated variables, called principal components (PCs).

PCA builds the PCs as linear combination of the original variables and successively have maximum variance. The selected principal components are those that maximize the distribution of points, preserving the original data as much as possible. The PCs are sorted according to the percentage of variance explained. The first component is considered the most significant as it explains the highest

percentage of variance. Consequently, the N principal components can be represented in the space by these axes, by an orthogonal projection of the N observation vectors onto the K PCs axes, as shown in Figure 93.

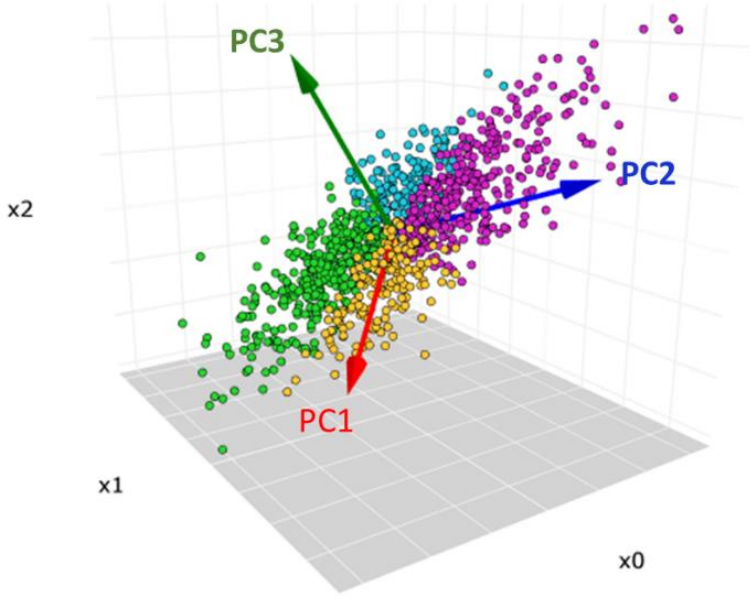

Figure 93: Al 3-dimensional data set space. The red, blue, green arrows are the direction of the first, second, and third principal components, respectively. Extracted from ref [274].

PCA is an unsupervised analysis and is useful for identifying fundamental variables, as well as groups of variables that are correlated with each other. Beyond its use in reducing the dimensionality while minimizing the loss of information, it is used to bring out the most characteristic information in a data set. Additionally, PCA can be used to visually group samples or highlight variables that are related or not significant. However, since it involves projecting the data, there are limitations as some information may be lost, leading to potentially incorrect interpretations.

The data from the $\boldsymbol{X}\ matrix$ was pre-processed by PCA on molecular descriptor values. The first three principal components resulting from the PCA were used as an approximated graphical representation of the chemical space for our database. Figure 94 represents the projections of compounds within this chemical space, which represents 30% of the explained variance. As seen, some molecules are isolated from all others, located at the borders of the domain, which is typically the case for molecules such as butyl octadecenoate, bis(2-ethylhexyl) benzene-1,2-dicarboxylate, Dihexyl hexanedioate, or even 2,4,6-Trimethyl-1,3,5-trioxane. These specific molecules and many others – 32 compounds in total –, were identified not only by analyzing the chemical space using the three main PCs but also by considering additional PCs. Their presence in external sets may induce violations of the applicability domain of models. These 32 molecules were therefore systematically used during the learning processes, as detailed hereafter.

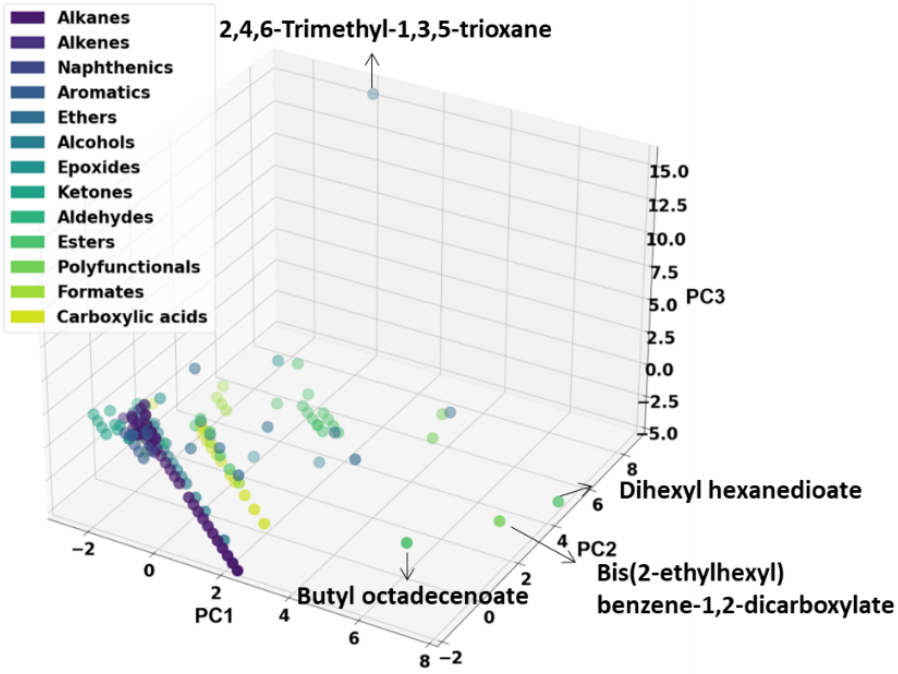

Figure 94: Projections of compounds into the space formed by PC1, PC2 and PC3, the three first principal components resulting from the PCA on descriptor values. Adapted from ref. [2]

4.2.3. Machine learning modeling

During last decades of QSPR model developments, the use of external validation has been shown necessary to ensure their ability to be applied to new fluids, *i.e.* not considered within the data set used to train the model [275]. Its popular version is the n-fold cross-validation (n-CV) in which the data set is randomly divided in approximately equal *n* portions. An aggregate of (*n-1*) portions forms a Training set – used to train models, and the remaining portion constitutes an external set or Test set – used to evaluate model's performances. We emphasize that no data point belonging to external sets was used to derived models. This procedure is repeated *n* times choosing for each a new portion of data as an external set. The subject of external validation for QSPR analysis has been addressed by Muratov *et al.* [276]. Considering our database content with ten temperatures – ten thermal conductivity values – for each molecule, a 'compound out' strategy was applied in this study, meaning that a molecule belongs to only one-fold. To avoid any strong violation of the applicability domain of models during the cross-validation procedure, we fixed 32 molecules in a specific fold always used to form Training sets. A 5-CV was applied to the 125 remaining molecules, and the Training and Test sets thus represent 84% and 16% of the database, respectively.

Historically, multilinear regression (MLR), principal component analysis (PCA) and partial least squares (PLS) have been the most widely used methods in the development of QSAR/QSPR models. However, one limitation is that these methods require assuming the form of the model to be linear beforehand.

It has been demonstrated in a number of previous works that the combination of molecular descriptors such as FGCD and Support Vector Machines (SVM) provides accurate solutions in terms of property modelling [164,189,277]. The Support Vector Regression (SVR) as implemented within the LibSVM library [278] was employed, with both linear and radial basis function kernels, and with an epsilon

insensitive zone [279]. According to this method, three parameter values need to be optimized: cost, epsilon, and gamma. We followed the approach previously proposed by Gantzer *et al*. [280] and the Sequential Quadratic Approximation (SQA) method implemented in our in-house program [281], was used to optimize the SVR parameter values within a 5-CV procedure. Finally, a model was developed using the set of optimized parameters and considering the 1570 data points of the database.

Models are evaluated according to their ability to predict reference thermal conductivity values. Predicted values are compared to reference pseudo-experimental data, and the performances of models are evaluated by means of metrics such as Mean Absolute Error (MAE, equation (4- 4)), Root Mean Squared Error (RMSE, equation (4- 5)), coefficient of determination (R^2, equation (4- 6)), or Concordance Correlation Coefficient (CCC, equation (4- 7)), defined respectively as:

$$\boldsymbol{MAE} = \frac{\mathbf{1}}{\boldsymbol{N}} \sum_{\mathbf{1}}^{\boldsymbol{N}} |\boldsymbol{y_i} - \boldsymbol{x_i}| \tag{4- 4}$$

$$\boldsymbol{RMSE} = \sqrt{\frac{\mathbf{1}}{\boldsymbol{N}} \sum_{\mathbf{1}}^{\boldsymbol{N}} (\boldsymbol{y_i} - \boldsymbol{x_i})^{\mathbf{2}}} \tag{4- 5}$$

$$\boldsymbol{R^2} = \mathbf{1} - \sum_{\mathbf{1}}^{\boldsymbol{N}} (\boldsymbol{y_i} - \overline{\boldsymbol{x}})^{\mathbf{2}} \Big/ \sum_{\mathbf{1}}^{\boldsymbol{N}} (\boldsymbol{x_i} - \overline{\boldsymbol{x}})^{\mathbf{2}} \tag{4- 6}$$

$$\boldsymbol{CCC} = \frac{\mathbf{2} \sum_{\mathbf{1}}^{\boldsymbol{N}} (\boldsymbol{x_i} - \overline{\boldsymbol{x}})(\boldsymbol{y_i} - \overline{\boldsymbol{y}})}{\sum_{\mathbf{1}}^{\boldsymbol{N}} (\boldsymbol{x_i} - \overline{\boldsymbol{x}})^{\mathbf{2}} + \sum_{\mathbf{1}}^{\boldsymbol{N}} (\boldsymbol{y_i} - \overline{\boldsymbol{y}})^{\mathbf{2}} + \boldsymbol{N} (\overline{\boldsymbol{x}} - \overline{\boldsymbol{y}})^{\mathbf{2}}} \tag{4- 7}$$

with y_i the predicted value, x_i the experimental value, $\bar{x}$ the average of experimental thermal conductivity values, $\bar{y}$ the average of predicted thermal conductivity values, and N is the number of data points in the considered set. Chirico *et al.* have shown that the use of CCC is advocated considering various scenarios such as location shifts, scale shifts, and location plus scale shifts [282,283] MAE and RMSE values have the unit of the property under consideration, while R^2 and CCC are unitless.

4.3. Results and discussions

The entire collection of experimental data, curated as detailed in the previous section, was used to derive predictive models. From the performed regressions of experimental data points using equation (1- 11) we generated a set of pseudo-experimental data subsequently used to train a machine learning algorithm.

Figure 95 a) presents evolutions of thermal conductivity values as a function of the temperature for alkan-1-ols. No clear trend appears for this subfamily of alcohols, with slope values in between -0.0002 to -0.0003 $W.m^{-1}.K^{-2}$, for pentan-1-ol and octan-1-ol, respectively. A similar study was carried out for n-alkanes and Figure 95 b) presents the evolution of thermal conductivity values as a function of temperature for this family of compounds. The figure clearly shows an evolution of slopes when moving from light linear alkanes to higher numbers of carbon atoms, from -0.0006 to -0.0002 $W.m^{-1}.K^{-2}$. It is interesting to note that this latter value is in line with that reported by Lu *et al.* in their model [147]. The observed variation in slopes from one compound to another justifies our decision to use an algorithm that establishes non-linear correlations between the descriptors and the reference thermal

conductivity values, such as SVM. Because of its obvious effect on thermal conductivity values – λ values are negatively correlated with T – the temperature (expressed in Kelvin) was considered as an additional descriptor. This approach is commonly employed for temperature dependent properties [151].

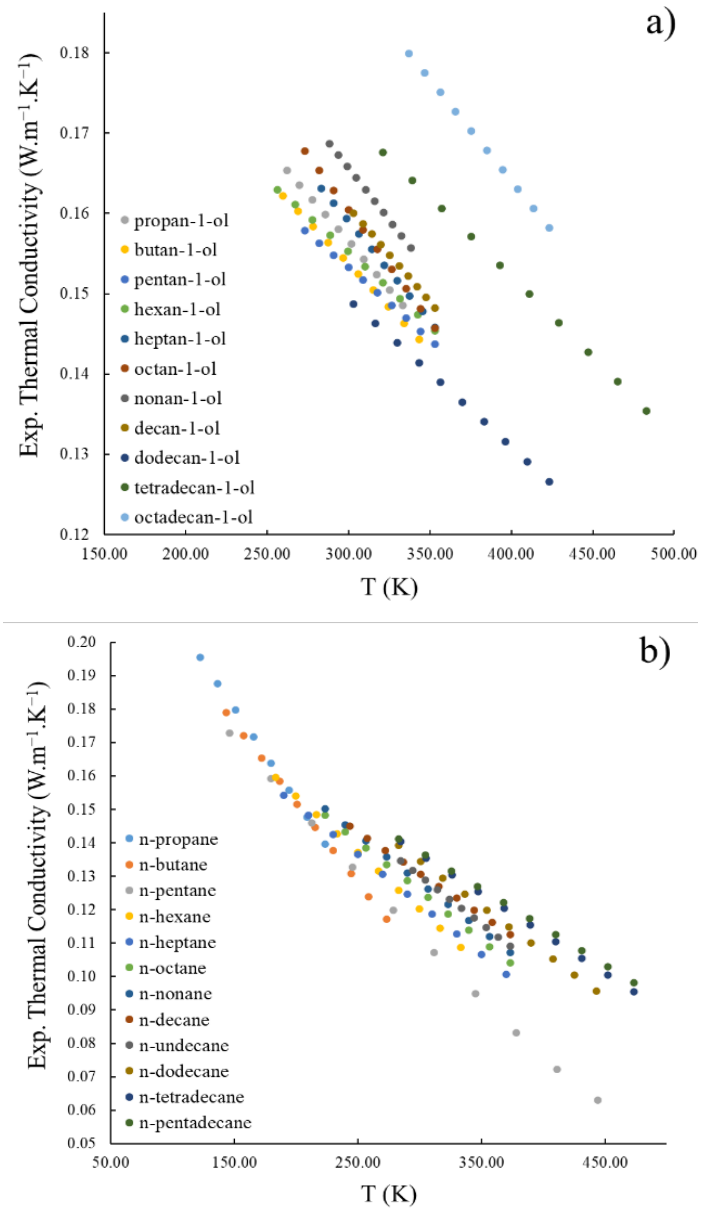

Figure 95: Thermal conductivity values as a function of temperature for a) alkan-1-ols and b) n-alkanes. Extracted from ref. [2]

A 5-CV was applied resulting in a splitting of the database into 5 folds, plus one additional containing the molecules fixed in training to avoid violation of the applicability domain. Note that for each compound, the dependency of λ on temperature is ensured by ten data points, which avoids any over-representation or unbalance effect of compounds within the database. The cost, epsilon, and gamma parameters of the SVR were optimized considering the six folds. A final model was then trained using the set of optimized parameters and considering all reference data within the Training set.

Performances of the obtained SVM-based model were evaluated using metrics such as MAE, RMSE, R^2, and CCC, which values are presented in Table 23.

Table 23. Performance characteristics (statistical metrics) of the SVR based model.

	Training	Validation
MAE ($W.m^{-1}.K^{-1}$)	0.0018	0.0060
RMSE ($W.m^{-1}.K^{-1}$)	0.0024	0.0080
R^2	0.992	0.836
CCC	0.996	0.920

When applied to Training data, metrics indicate that the developed model accurately reproduces reference data, with for instance a R^2 of 0.992. The good agreement between reference and predicted values using the SVR model is illustrated in Figure 96.

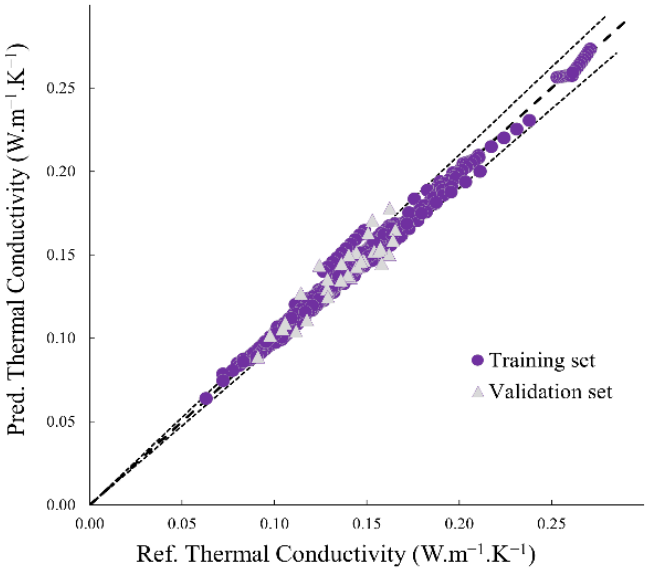

Figure 96. Scatterplots of pseudo-experimental *vs.* predicted thermal conductivity values using the SVM-based model. The dashed line stands for the bisector of the diagram. The dashed line stands for the bisector of the diagram surrounded by two dotted lines corresponding to a 5% uncertainty. Extracted from ref. [2]

Figure 96 presents the scatterplots of reference *vs.* predicted thermal conductivity values using the SVM-based model. All data points are not too scattered on both sides of the bisector, indicating that predicted values are in good agreement with reference data. However, several data points appear to have been overestimated by the model, more precisely, they correspond to the 10 data related to dodecan-1-ol for which absolute relative deviations of about 11% are observed with respect to pseudo-experimental data. Analysing the information contained in Figure 95 a), data points corresponding to dodecan-1-ol (represented by dark blue circles) seem to be abnormally low roughly considering the trend with the number of carbon atoms in alkan-1-ols, while emphasising that we have taken into account the values quoted as 'Accepted' by the DIPPR [176,262]. It should be noted that, in the database used by Lu *et al.* [147], reference thermal conductivity values for dodecan-1-ol range from 0.148 $W.m^{-1}.K^{-1}$ (at 440 K) to 0.166 (at 310 K) $W.m^{-1}.K^{-1}$, in reasonable agreement with our predicted

values (an absolute relative deviations of about 5%). For their 6-descriptor linear model, Lu *et al.* reported a R^2 value of 0.914 and a RMSE of 0.0067 $W.m^{-1}.K^{-1}$. However, authors did not perform the Training/Test splitting following a 'compound-out' approach, which represents a too favourable scenario and avoid any conclusion regarding predictive ability of the model.

During the data curation, many chemical compounds were discarded due to an insufficient number of experimental data to regress parameters of equation (1-11) (23 compounds in total). These data points were set aside to be considered as a Validation set. Our SVM-based model was applied to compounds and temperature conditions within the Validation set. Predictive performances of our SVR model were evaluated on the Validation set using metrics such as MAE, RMSE, R^2, and CCC, which values are presented in Table 23. Metrics suggested that the developed model has a good predictive ability and accurately reproduces reference data, with for instance a R^2 value of 0.836 and a RMSE of 0.0080 $W.m^{-1}.K^{-1}$. As for the Training set, the good agreement observed between reference and predicted values using the SVR model is illustrated in Figure 96.

For compounds belonging to the Validation set, the SVR model was used to predict thermal conductivity values for temperatures up to critical temperatures. A to D parameters of equation (1-11) were then regressed on the basis of predicted values. The as-obtained parameter values are reported in Appendix G. As an example, Figure 97 presents the evolution of thermal conductivity values as a function of temperature for diethyl oxalate – with SMILES formula CCOC(=O)C(=O)OCC –, and proposes a comparison between predictions using the SVR model and equation (1-11) fed with regressed parameters displayed in Appendix G, and the experimental data reported by Riedel [284]. It shows the good agreement between the three sources of data at 293.15 K. Figure 97 illustrates the possible use of our SVR model: the prediction of thermal conductivity values for temperatures and/or compounds that are not covered experimentally in the literature.

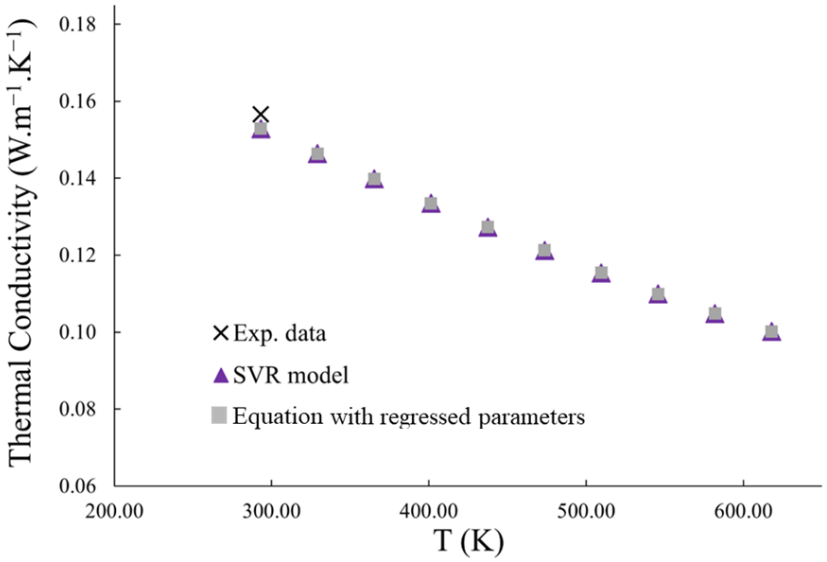

Figure 97. Evolution of thermal conductivity values as a function of temperature for CCOC(=O)C(=O)OCC (diethyl oxalate), predicted using the SVR model (triangle) and equation (1-11) fed with regressed parameters in Appendix G (square), and compared with available experimental data (cross) [284]. Extracted from ref. [2].

4.4. Conclusions

We have proposed here the application of Chemoinformatics methodologies to investigate the thermal conductivity prediction for hydrocarbons and oxygenated compounds in liquid phase. A compilation of experimental data and then a careful data curation, including filtering, converting units, recalculating parameters, and creating consistent data points with equal importance to create a database of reference values. Then, FGCD descriptors were carefully identified and selected based on the structural information of molecules contained in the database. A dimensional reduction on the $\boldsymbol{X}\ matrix$ containing the molecules and their respective descriptors was performed and projected in a 3D chemical space. This projection allowed to identify the molecules located at the borders of the domain, allowing for their inclusion in the training process. A pre-processing of the data has demonstrated that the use of algorithm leading to linear models would be a too strong approximation in terms of modelling for predicting the effects of temperature. Thus, a SVM algorithm was applied to the database to generate predictive models, within a 5-CV procedure and we emphasize the 'compound out' strategy followed for the splitting of data into Training and Test sets. Comparisons performed with respect to reference data have demonstrated that our SVR model has good predictive reliability and robustness, with a MAE of 0.0018 $W.m^{-1}.K^{-1}$ calculated on the entire database.

The SVR model has been used to predict the evolution of the thermal conductivity as a function of the temperature for a series of compounds, for which there were too few experimental data in the literature to be included in the learning process. Performed comparisons showed the good agreement between predicted values and available experimental data. This confirms that our SVR model can be used for the prediction of thermal conductivity values for temperatures and/or compounds that are not covered experimentally in the literature.

General conclusion

In this manuscript, we have discussed the issue of the existing lack of thermal conductivity data for certain oxygenated compounds under various temperature conditions. These data can be crucial for several industries. For instance, alcohols and ketones are used in chemical engineering and pharmaceutical manufacturing as solvents and reactants. It is crucial to understand the thermal conductivity of these compounds for processes like crystallization and distillation. These oxygenated compounds are also used in food processing for refrigeration and freezing, and understanding their thermal conductivity helps improve safety and shelf life.

The context of this thesis work focuses on new alternatives to produce cleaner energy and emphasizes the importance of thermal conductivity in oxygenated compounds. This knowledge is crucial for developing an efficient biomass conversion process for biofuel production, which can help limit greenhouse gas emissions and promote environmentally sustainable energy solutions. We also highlighted the limitations of conventional methods in generating new data for this property due to the large amount of product needed and errors caused by heat transfer phenomena. Therefore, a new microfluidic device was proposed made of specific materials that can withstand harsh conditions and measure the thermal conductivity of liquids, especially those used in the production of biofuels from biomass.

Although microfluidics is a useful method for generating data, it is also important to use modeling in conjunction with experimental data. In this study, ML based models have been developed to determine thermal conductivity of liquids. The strategy and results obtained for both microfluidics and modeling are summarized hereafter.

Microfluidics

Microfluidics is a rapidly expanding area within the fields of chemical engineering and fluid dynamics that focuses on controlling and manipulating small volume (microliter) of fluid in microchannels. It involves the control and manipulation of small volumes of fluid in microchannels, usually on the order of microliters or nanoliters. This technology offers numerous advantages over conventional macroscale fluid handling systems, including enhanced mixing and reaction control, reduced sample and reagent consumption, high-throughput analysis, low operating time, *in situ* analysis, heat improvement, mass transfers etc.

The combination of microfluidics along with MEMS technologies led to the development of a microsensor integrated into a microfluidic device allowing the measurement of λ of liquids. The device has two parts - a bottom part made of borosilicate glass acting as an insulator, and a top part made of silicon acting as a conductor. Silicon was chosen specifically because it exhibits a high λ, which makes it an effective heat sink and reduces uncertainties in micro-scale systems. First, microchannels were etched the silicon substrate using photolithography and wet etching techniques. Then, the bi-layer photolithography was used to fabricate a sensor by depositing a thin metal film on the surface of a borosilicate glass substrate. A careful selection of metals, geometries, and measurement behaviors was made using a setup of experiments. In the end, a spiral-shaped Pt microsensor was chosen as the most suitable option for heating and sensing purposes. This device is advantageous because it is chemically inert, can work at higher temperatures than other materials used in microfluidics fabrication, and allows for optical access, allowing the coupling with other *in situ* characterizations techniques.

Then, we investigated the integration of the microfluidic device into a larger measuring system, with the goal of testing and validating the microfluidic approach for measuring λ. The measurement involved the use of the Joule effect to generate heat on the sensor, which simultaneously leads to a change in its temperature and subsequently its resistance. A Wheatstone bridge-based experimental setup was built to detect changes in the sensor's electrical resistance. The uncertainties linked with the considered instruments, and the repeatability of the measurements were assessed. The sensor response was calibrated by fitting the thermal conductivity behaviors of well-known binary mixtures containing water and ethanol. Parameters such as heating power, heating pulse length, and time interval were optimized to calibrate the sensor, and were set to 60 mW, 60 seconds, and a time range of 28 to 44 seconds, respectively. The microfluidics device and its settings were used to measure λ values for two different fluids, n-pentadecane and ethan-1,2-diol, at temperatures ranging from 293.15 K to 333.15 K. The mean absolute deviations provided for n-pentadecane and ethan-1,2-diol were of 8% and 20%, respectively. It was suggested that the higher error in λ for ethan-1,2-diol may be due to its higher viscosity compared to other fluids. However, the λ measurements are still accurate for the range of viscosities covered by the fluids used for calibration. Finally, we proposed new experimental values for 2,5-dimethylfuran a biomass by-product for which there is a lack of thermal conductivity data information in the literature. However, the study pointed out certain limitations, such as the fragility of the sensor due to its direct contact with the fluid, which decreases its expected lifetime at high temperature (*i.e* 200 °C). Additionally, the study focused solely on temperature as a physical parameter, and it remains limited in temperature ranges conditions (up to 60°C) for thermal conductivity measurement.

Modeling

In parallel to microfluidics experimental measurements of λ, we proposed the application of Chemoinformatics methodologies to investigate the λ prediction for hydrocarbons and oxygenated compounds in liquid phase. Artificial intelligence (AI) has revolutionized various industries, and its application in predictive modeling, particularly in a field as Quantitative Structure-Property. Relationships (QSPR) has yielded significant advancements. QSPR uses mathematical models to predict the properties of chemical compounds based on their molecular structure. By employing AI techniques such as ML, existing datasets can be analyzed to identify patterns and relationships between molecular structures and corresponding properties. By continuously learning from new data, AI-powered predictive models can adapt and improve their predictions over time.

The development of QSPR-based models involved the collection and curation of experimental data. During this stage, we have seen that creating consistent and equally important data points is crucial in developing QSPR models, as compounds with more data can have a greater influence on the model's predictions. A database containing reference thermal conductivity values was created gathering data from both published literature and our new measurements. Molecular structures were encoded using FGCD (descriptors) to feed ML algorithms. The chosen algorithm was Support Vector Machine (SVM) to create models for predictions. This algorithm has the capability to find the non-linear correlations between the descriptors and the targeted property, thermal conductivity. The data was split into Training and Test using a 5-CV procedure and we emphasize that a 'compound out' strategy was applied. The obtained SVR models showed good predictive accuracy and stability when compared to reference data. The mean absolute error (MAE) for the entire database was calculated to be 0.0018 $W.m^{-1}.K^{-1}$. Then, the SVR model was used to predict the λ of compounds with limited experimental

data. The results demonstrated that the model is proficient in both interpolating and extrapolating, particularly in temperature ranges that have not been yet covered.

Experiments in microfluidics and modeling

Modeling and experiments complement each other to observe how the thermophysical properties of fluid systems behave. Experiments provide controlled conditions for scientists to observe and collect data, while modeling uses mathematical or computational tools to simulate experiments that may be difficult or impractical to perform.

To enhance de predictive power of models, the use of more experimental data is essential. This is why the combination of microfluidic techniques and modeling is significant in developing automated methods for measuring thermophysical properties with efficient and fast results.

At this point, we have successfully fabricated a microfluidic device capable of measuring λ at different temperature conditions of two different types of chemicals families: hydrocarbons and oxygenated compounds. The database was initially created with a limited amount of experimental data and specific temperature conditions for certain types of oxygenated compounds like epoxides or aldehydes. Because of this, it is necessary for the microfluidic device to produce new experimental data to increase the variety of chemicals in the database and enhance the applicability domain of the models. Furthermore, the inclusion of new experimental data can also help identify any limitations or deficiencies in the original database.

To summarize, the majority of the three-year PhD work was focused on developing the microfluidic device, as illustrated in Figure 98. This development process took approximately 22 months to reach the final version of the device, which accounted for 70% of the overall time (represented by the dark blue section in Figure 98). An additional 5 months were dedicated to optimizing parameters and conducting thermal conductivity measurements at different temperatures, constituting around 15% of the time (shown in light blue in Figure 98). Manuscript writing took approximately 4 months (not depicted in the figure), leaving the remaining time to be utilized for developing predictive models (indicated by the green section in Figure 98). Consequently, there are still opportunities for further improvements and perspectives that can be explored.

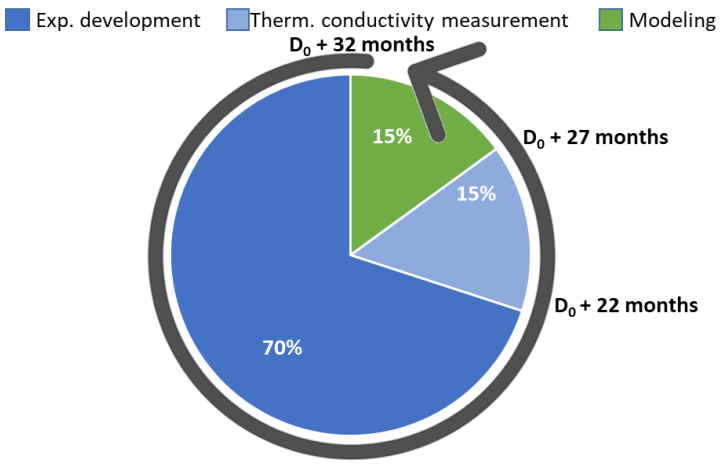

Figure 98: PhD workload time allocation

Perspectives

The extended and intensive use of new chemistries, along with varying temperature and pressure conditions, creates opportunities for future research in measuring thermal conductivity through microfluidics.

An important limitation that needs to be addressed is the fragility of the sensor. One potential solution is to deposit a thin protective film on the top of the sensors (of few hundreds of nm) made of materials such as borosilicate, which have good transparency and acceptable λ. This could open ways to extend this approach to more aggressive chemicals, since in the proposed design, the sensor is directly in contact with the fluid. Some investigations and experiments regarding the deposition of SiO_2 on the top of the sensor have been carried out. However, further development and optimization are required to establish an effective irreversible seal between the silicon and borosilicate glass. Additionally, given that the silicon/borosilicate technology can be used in a large range of pressure and temperature conditions, future works will include the investigations of pressure effects on the λ of liquid. Considering that these effects are generally negligible for pressures below about 50 bar [285], the microdevice – and more specifically the measurement micro-cavity – will have to be redesigned to withstand pressures well above this limit.

This study showed that the amount of power and time of heating can affect how heat is transferred in the sensor through the liquid in the microfluidic device. To support experimental data obtained, simulations can be used to further investigate this heat transfer behavior and other parameters that could be optimized. For instance, Ouderbrouckx *et al*. [42] proposed the use of 2D simulations, specifically using the numerical model of COMSOL. This model simulated a 2D cross section of a resistive meander structure, with dimensions and materials chosen to comply the experimental setup. The simulations allowed for investigating how thermal pulses from the sensor structure were affected by the thermal properties of the fluid sample in the microchannel. The model also proved to be useful in evaluating different sensor designs, such as varying microchannel heights and finding that decreasing the microchannel height reduces the offset of the thermal pulses. We have also demonstrated that we can replicate various sensor geometries in practice, but due to time constraints, we were unable to test additional geometries, such as meanders. It would be interesting to compare various geometries and see whether the λ measurement would have any effect based on the geometry used thanks to simulations.

Furthermore, we noticed that during the measurement, the temperature difference of the sensor's transient curve did not reach absolute zero because of fluctuations in the surrounding temperature. To improve temperature control when measuring λ, it could be recommended to use a convective liquid bath to effectively regulate both room temperature and other desired temperatures.

New experimental data from a range of temperature conditions must be added to the database in order to improve the modeling process. We have demonstrated that there are noticeable gaps in the database's inclusion of chemical species when approaching the boundaries. We have observed that polyfunctional compounds (*e.g.,* bis(2-ethylhexyl) benzene-1,2-dicarboxylate) and molecules containing a specific chemical family multiple times (e.g., 2,4,6-trimethyl-1,3,5-trioxane) are frequently located near the boundary of the applicability domain. As a result, the selection of additional compounds to optimally complete this space is necessary. Additionally, more data must be produced for chemical families with limited availability, such as epoxides, aldehydes, or even other hydrocarbon

families like naphthenic or alkenes. For instance, Furan derivatives like DMF and 5-hydroxymethylfurfural (HMF), show great potential as alternative fuels. HMF, in particular, is an interesting compound to add to the database due to its polyfunctionality. It would also be beneficial to include the other parameters influencing λ such as pressures above 50 bar, and different types of molecule compositions, such as mixtures, into the database. Finally, to improve the quality and relevance of a database, it is necessary to conduct a Design of Experiments (DOE) to reduce experimental errors, evaluate variable interactions, and generalize the results.

References

[1] R. Moreno Jimenez, B. Creton, C. Marliere, L. Teule-Gay, O. Nguyen, S. Marre, A microfluidic strategy for accessing the thermal conductivity of liquids at different temperatures, Microchemical Journal 193 (2023) 109030. https://doi.org/10.1016/j.microc.2023.109030.

[2] R. Moreno Jimenez, B. Creton, S. Marre, Machine learning-based models for accessing thermal conductivity of liquids at different temperature conditions, SAR and QSAR in Environmental Research (2023) 1–13. https://doi.org/10.1080/1062936X.2023.2244410.

[3] J. Woodcock, D. Banister, P. Edwards, A.M. Prentice, I. Roberts, Energy and transport, Lancet 370 (2007) 1078–1088. https://doi.org/10.1016/S0140-6736(07)61254-9.

[4] Z. Zhang, T. Wang, M.J. Blunt, E.J. Anthony, A.-H.A. Park, R.W. Hughes, P.A. Webley, J. Yan, Advances in carbon capture, utilization and storage, Applied Energy 278 (2020) 115627. https://doi.org/10.1016/j.apenergy.2020.115627.

[5] H. Naims, Economics of carbon dioxide capture and utilization-a supply and demand perspective, Environ Sci Pollut Res 23 (2016) 22226–22241. https://doi.org/10.1007/s11356-016-6810-2.

[6] D. Sutter, M. van der Spek, M. Mazzotti, 110th Anniversary Evaluation of CO 2 -Based and CO 2 -Free Synthetic Fuel Systems Using a Net-Zero-CO 2 -Emission Framework, Ind. Eng. Chem. Res. 58 (2019) 19958–19972. https://doi.org/10.1021/acs.iecr.9b00880.

[7] P.H. Raven, L.R. Berg, D.M. Hassenzahl, Environment, eighthth ed., Wiley, Hoboken NJ, 2012.

[8] T. Abbasi, S.A. Abbasi, Biomass energy and the environmental impacts associated with its production and utilization, Renewable and Sustainable Energy Reviews 14 (2010) 919–937. https://doi.org/10.1016/j.rser.2009.11.006.

[9] A. Garba, Biomass Conversion Technologies for Bioenergy Generation: An Introduction, in: T. Peixoto Basso, T. Olitta Basso, L. Carlos Basso (Eds.), Biotechnological Applications of Biomass, InTech, 2021.

[10] K.J. Ptasinski, Efficiency of biomass energy: An exergy approach to biofuels, power, and biorefineries, Wiley, Hoboken New Jersey, 2016.

[11] K. Biernat, Biofuels - Status and Perspective. page 380, IntechOpen, [S.l.], 2015.

[12] Z.-H. Zhang, R. Balasubramanian, Influence of butanol addition to diesel–biodiesel blend on engine performance and particulate emissions of a stationary diesel engine, Applied Energy 119 (2014) 530–536. https://doi.org/10.1016/j.apenergy.2014.01.043.

[13] C.-S. Lim, J.-H. Lim, J.-S. Cha, J.-Y. Lim, Comparative effects of oxygenates-gasoline blended fuels on the exhaust emissions in gasoline-powered vehicles, J. Environ. Manage. 239 (2019) 103–113. https://doi.org/10.1016/j.jenvman.2019.03.039.

[14] A. Demirbas, Combustion Efficiency Impacts of Biofuels, Energy Sources, Part A: Recovery, Utilization, and Environmental Effects 31 (2009) 602–609. https://doi.org/10.1080/15567030701743718.

[15] H. Chen, Lignocellulose biorefinery conversion engineering, in: Lignocellulose Biorefinery Engineering, Elsevier, 2015, pp. 87–124.

[16] A. Mittal, A. Saxena, B. Mohapatra, Oxygen Enrichment Technology—An Innovation for Improved Solid Fuel Combustion and Sustainable Environment, in: K.S. Sangwan, C. Herrmann (Eds.), Enhancing Future Skills and Entrepreneurship, Springer Nature, Cham, 2020, pp. 13–19.

[17] S.C. Bhatia, Biodiesel, in: Advanced Renewable Energy Systems, Elsevier, 2014, pp. 573–626.

[18] C.A. Cardona, O.J. Sánchez, Fuel ethanol production: process design trends and integration opportunities, Bioresour. Technol. 98 (2007) 2415–2457. https://doi.org/10.1016/j.biortech.2007.01.002.
[19] P.S. Veloo, Y.L. Wang, F.N. Egolfopoulos, C.K. Westbrook, A comparative experimental and computational study of methanol, ethanol, and n-butanol flames, Combustion and Flame 157 (2010) 1989–2004. https://doi.org/10.1016/j.combustflame.2010.04.001.
[20] S. Namysl, M. Pelucchi, O. Herbinet, A. Frassoldati, T. Faravelli, F. Battin-Leclerc, A first evaluation of butanoic and pentanoic acid oxidation kinetics, Chemical Engineering Journal 373 (2019) 973–984. https://doi.org/10.1016/j.cej.2019.05.090.
[21] M. Eldeeb, B. Akih-Kumgeh, Recent Trends in the Production, Combustion and Modeling of Furan-Based Fuels, Energies 11 (2018) 512. https://doi.org/10.3390/en11030512.
[22] G. Anitescu, T.J. Bruno, Liquid Biofuels: Fluid Properties to Optimize Feedstock Selection, Processing, Refining/Blending, Storage/Transportation, and Combustion, Energy Fuels 26 (2012) 324–348. https://doi.org/10.1021/ef201392s.
[23] K Midttoemme., Thermal conductivity of sedimentary rocks-selected methodological, mineralogical and textural studies, 1997.
[24] X. Xu, J. Chen, J. Zhou, B. Li, Thermal Conductivity of Polymers and Their Nanocomposites, Adv. Mater. 30 (2018) e1705544. https://doi.org/10.1002/adma.201705544.
[25] J. Yang, Z.-H. Wang, K.E. Kaloush, H. Dylla, Effect of pavement thermal properties on mitigating urban heat islands: A multi-scale modeling case study in Phoenix, Building and Environment 108 (2016) 110–121. https://doi.org/10.1016/j.buildenv.2016.08.021.
[26] N.B. Vargaftik, L.P. Filippov, A.A. Tarzimanov, E.E. Totskii, Handbook of Thermal Conductivity of Liquids and Gases, 1978.
[27] Y.C. Lim, A.Z. Kouzani, W. Duan, Lab-on-a-chip: a component view, Microsyst Technol 16 (2010) 1995–2015. https://doi.org/10.1007/s00542-010-1141-6.
[28] N. Srivastava, M.A. Burns, Electronic drop sensing in microfluidic devices: automated operation of a nanoliter viscometer, Lab Chip 6 (2006) 744–751. https://doi.org/10.1039/b516317j.
[29] Z. Wang, L. Tan, X. Pan, G. Liu, Y. He, W. Jin, M. Li, Y. Hu, H. Gu, Self-Powered Viscosity and Pressure Sensing in Microfluidic Systems Based on the Piezoelectric Energy Harvesting of Flowing Droplets, ACS Appl. Mater. Interfaces 9 (2017) 28586–28595. https://doi.org/10.1021/acsami.7b08541.
[30] S.R. Choi, J. Kim, D. Kim, 3omega method to measure thermal properties of electrically conducting small-volume liquid, Review of Scientific Instruments 78 (2007) 84902. https://doi.org/10.1063/1.2777162.
[31] L. Binda, M. Bolado, A. D'Onofrio, V.M. Freytes, Analysis of a microfluidic device for diffusion coefficient determination of high molecular weight solutes detectable in the visible spectrum, Eur. Phys. J. E Soft Matter 45 (2022) 56. https://doi.org/10.1140/epje/s10189-022-00211-4.
[32] H. Fadaei, J.M. Shaw, D. Sinton, Bitumen–Toluene Mutual Diffusion Coefficients Using Microfluidics, Energy Fuels 27 (2013) 2042–2048. https://doi.org/10.1021/ef400027t.
[33] S. Marre, A. Adamo, S. Basak, C. Aymonier, K.F. Jensen, Design and Packaging of Microreactors for High Pressure and High Temperature Applications, Ind. Eng. Chem. Res. 49 (2010) 11310–11320. https://doi.org/10.1021/ie101346u.
[34] S. Marre, J. Park, J. Rempel, J. Guan, M.G. Bawendi, K.F. Jensen, Supercritical Continuous-Microflow Synthesis of Narrow Size Distribution Quantum Dots, Adv. Mater. 20 (2008) 4830–4834. https://doi.org/10.1002/adma.200801579.

[35] S. Marre, Y. Roig, C. Aymonier, Supercritical microfluidics: Opportunities in flow-through chemistry and materials science, The Journal of Supercritical Fluids 66 (2012) 251–264. https://doi.org/10.1016/j.supflu.2011.11.029.
[36] B. Pinho, S. Girardon, F. Bazer-Bachi, G. Bergeot, S. Marre, C. Aymonier, Simultaneous measurement of fluids density and viscosity using HP/HT capillary devices, The Journal of Supercritical Fluids 105 (2015) 186–192. https://doi.org/10.1016/j.supflu.2015.04.016.
[37] S. Morais, A. Cario, N. Liu, D. Bernard, C. Lecoutre, Y. Garrabos, A. Ranchou-Peyruse, S. Dupraz, M. Azaroual, R.L. Hartman, S. Marre, Studying key processes related to CO 2 underground storage at the pore scale using high pressure micromodels, React. Chem. Eng. 5 (2020) 1156–1185. https://doi.org/10.1039/D0RE00023J.
[38] T. Gavoille, N. Pannacci, G. Bergeot, C. Marliere, S. Marre, Microfluidic approaches for accessing thermophysical properties of fluid systems, React. Chem. Eng. 4 (2019) 1721–1739. https://doi.org/10.1039/C9RE00130A.
[39] B. Pinho, S. Girardon, F. Bazer-Bachi, G. Bergeot, S. Marre, C. Aymonier, A microfluidic approach for investigating multicomponent system thermodynamics at high pressures and temperatures, Lab Chip 14 (2014) 3843–3849. https://doi.org/10.1039/c4lc00505h.
[40] S.R. Choi, D. Kim, Measurement of thermal properties of microfluidic samples using laser point heating thermometry, Thermochimica Acta 455 (2007) 11–15. https://doi.org/10.1016/j.tca.2006.11.035.
[41] S.R. Choi, D. Kim, Real-time thermal characterization of 12 nl fluid samples in a microchannel, Review of Scientific Instruments 79 (2008) 64901. https://doi.org/10.1063/1.2937180.
[42] G. Oudebrouckx, T. Vandenryt, S. Bormans, P.H. Wagner, R. Thoelen, Measuring Thermal Conductivity in a Microfluidic Device With the Transient Thermal Offset (TTO) Method, IEEE Sensors J. 21 (2021) 7298–7307. https://doi.org/10.1109/JSEN.2020.3047475.
[43] L.M. Jiji, Heat Conduction: Third Edition, Springer Berlin Heidelberg, Berlin, Heidelberg, 2009.
[44] J.-B.-J. Fourier, The analytical theory of heat, Cosimo Classics, New York, 2007.
[45] F. Kreith, R.M. Manglik, M. Bohn, Principles of heat transfer, seventhth ed., Cengage Learning, Australia, Canada, Mexico etc., 2011.
[46] F.P. Incropera, Fundamentals of heat and mass transfer, sixthth ed., John Wiley, Hoboken NJ, 2007.
[47] C.A. Meyer, ASME steam tables: Thermodynamic and transport properties of steam comprising tables and charts for steam and water, calculated using the 1967 IFC formulation for industrial use, in conformity with the 1963 international skeleton tables, as adopted by the Sixth International Conference on the Properties of Steam, sixthth ed., American Society of Mechanical Engineers, New York, 1993.
[48] R. DiGuilio, A.S. Teja, Thermal conductivity of poly(ethylene glycols) and their binary mixtures, J. Chem. Eng. Data 35 (1990) 117–121. https://doi.org/10.1021/JE00060A005.
[49] S. Sastri, K.K. Rao, A new temperature–thermal conductivity relationship for predicting saturated liquid thermal conductivity, Chemical Engineering Journal 74 (1999) 161–169. https://doi.org/10.1016/S1385-8947(99)00046-7.
[50] R.B. Bird, W.E. Stewart, E.N. Lightfoot, Transport phenomena, Revised secondnd edition, John Wiley & Sons Inc, New York etc., 2007.
[51] Reid, R C, Prausnitz, J M, and Poling, B E, The properties of gases and liquids., United States, 1987.
[52] A.K. Rahalkar, D.S. Viswanath, N.R. Kuloor, Prediction of thermal conductivity of organic liquids – a corresponding states approach, Ind. J. Technol., 7 (3) (1969), pp. 67-74.

[53] C. CHRISTIANSEN, Einige Versuche über die Wärmeleitung: Ann. der Physik und Chemie, t. XIV, p. 23; (1881).
[54] The thermal conductivities of certain liquids, Proc. R. Soc. Lond. A 117 (1928) 459–470. https://doi.org/10.1098/rspa.1928.0010.
[55] P.K. Das, A review based on the effect and mechanism of thermal conductivity of normal nanofluids and hybrid nanofluids, Journal of Molecular Liquids 240 (2017) 420–446. https://doi.org/10.1016/j.molliq.2017.05.071.
[56] A. R. Challoner and R. W. Powell, Thermal conductivities of liquids: new determinations for seven liquids and appraisal of existing values, Proc. R. Soc. Lond. A 238 (1956) 90–106. https://doi.org/10.1098/rspa.1956.0205.
[57] U. Hammerschmidt, Thermal conductivity of a wide range of alternative refrigerants measured with an improved guarded hot-plate apparatus, Int J Thermophys 16 (1995) 1203–1211. https://doi.org/10.1007/BF02081288.
[58] J.V. Sengers, W.T. Bolk, C.J. Stigter, The thermal conductivity of neon between 25°C and 75°C at pressures up to 2600 atmospheres, Physica 30 (1964) 1018–1026. https://doi.org/10.1016/0031-8914(64)90233-2.
[59] M.H. Rausch, K. Krzeminski, A. Leipertz, A.P. Fröba, A new guarded parallel-plate instrument for the measurement of the thermal conductivity of fluids and solids, Int. J. Heat Mass Transf. 58 (2013) 610–618. https://doi.org/10.1016/j.ijheatmasstransfer.2012.11.069.
[60] N. Yüksel, The Review of Some Commonly Used Methods and Techniques to Measure the Thermal Conductivity of Insulation Materials, in: A. Almusaed, A. Almssad (Eds.), Insulation materials in context of sustainability, InTech, Rijeka, 2016.
[61] M.J. Assael, K.D. Antoniadis, W.A. Wakeham, Historical Evolution of the Transient Hot-Wire Technique, Int J Thermophys 31 (2010) 1051–1072. https://doi.org/10.1007/s10765-010-0814-9.
[62] J. K. Horrocks, E. Mclaughlin, Non-steady-state measurements of the thermal conductivities of liquid polyphenyls, Proc. R. Soc. Lond. A 273 (1963) 259–274. https://doi.org/10.1098/rspa.1963.0087.
[63] J. Kestin, W.A. Wakeham, A contribution to the theory of the transient hot-wire technique for thermal conductivity measurements, Physica A: Statistical Mechanics and its Applications 92 (1978) 102–116. https://doi.org/10.1016/0378-4371(78)90023-7.
[64] Y. Nagasaka, A. Nagashima, Absolute measurement of the thermal conductivity of electrically conducting liquids by the transient hot-wire method, J. Phys. E: Sci. Instrum. 14 (1981) 1435–1440. https://doi.org/10.1088/0022-3735/14/12/020.
[65] S.E. Gustafsson, E. Karawacki, M.N. Khan, Transient hot-strip method for simultaneously measuring thermal conductivity and thermal diffusivity of solids and fluids, J. Phys. D: Appl. Phys. 12 (1979) 1411–1421. https://doi.org/10.1088/0022-3727/12/9/003.
[66] S.E. Gustafsson, Transient plane source techniques for thermal conductivity and thermal diffusivity measurements of solid materials, Review of Scientific Instruments 62 (1991) 797–804. https://doi.org/10.1063/1.1142087.
[67] M. Gustavsson, E. Karawacki, S.E. Gustafsson, Thermal conductivity, thermal diffusivity, and specific heat of thin samples from transient measurements with hot disk sensors, Review of Scientific Instruments 65 (1994) 3856–3859. https://doi.org/10.1063/1.1145178.
[68] Tec-Science (2021) Transient-hot-wire method method for determining thermal conductivity (THW) - TEC-science, tec., Available at: https://www.tec-

science.com/thermodynamics/heat/transient-hot-wire-method-method-for-determining-thermal-conductivity-thw/ (Accessed: 18 August 2023).
[69] A. Franco, An apparatus for the routine measurement of thermal conductivity of materials for building application based on a transient hot-wire method, Applied Thermal Engineering 27 (2007) 2495–2504. https://doi.org/10.1016/j.applthermaleng.2007.02.008.
[70] C. Gobbé, S. Iserna, B. Ladevie, Hot strip method: application to thermal characterisation of orthotropic media, International Journal of Thermal Sciences 43 (2004) 951–958. https://doi.org/10.1016/j.ijthermalsci.2004.02.002.
[71] H. Czichos, T. Saito, L.R. Smith (Eds.), Springer handbook of materials measurement methods, Springer, Berlin, 2006.
[72] S. E. Gustafsson, International Patent Application No. PCT/SE89/00137.
[73] Silas E Gustafssonf, Ernest Karawackif and M Nazim Khan, Transient hot-strip method for simultaneously measuring thermal conductivity and thermal diffusivity of solids and fluids, Journal of Applied Physics (1979).
[74] D.G. Cahill, Thermal conductivity measurement from 30 to 750 K: the 3ω method, Review of Scientific Instruments 61 (1990) 802–808. https://doi.org/10.1063/1.1141498.
[75] Y. Shi, L. Sun, F. Tian, J.E.S. Venart, R.C. Prasad, Fluid radiation effects in the transient hot-wire technique, J Therm Anal Calorim 90 (2007) 693–698. https://doi.org/10.1007/s10973-007-8524-7.
[76] A.L. Pope, B. Zawilski, T.M. Tritt, Description of removable sample mount apparatus for rapid thermal conductivity measurements, Cryogenics 41 (2001) 725–731. https://doi.org/10.1016/S0011-2275(01)00140-0.
[77] T.M. Tritt, D. Weston, Measurement Techniques and Considerations for Determining Thermal Conductivity of Bulk Materials, in: T.M. Tritt (Ed.), Thermal conductivity: Theory, properties, and applications, Springer, New York, 2004, pp. 187–203.
[78] J.J. Atherton, M.C. Rosamond, S. Johnstone, D.A. Zeze, Thermal characterisation of µL volumes using a thin film thermocouple based sensor, Sensors and Actuators A: Physical 166 (2011) 34–39. https://doi.org/10.1016/j.sna.2011.01.001.
[79] H. Takamatsu, H. Wang, T. Fukunaga, K. Kurata, Measurement of fluid thermal conductivity using a micro-beam MEMS sensor, Int. J. Heat Mass Transf. 117 (2018) 30–35. https://doi.org/10.1016/j.ijheatmasstransfer.2017.09.117.
[80] Z. Wu, Y. Zhang, Q. Wang, K.-H. Kim, S.-H. Kwon, The Thermal Resistance Performance of WTi Alloy-Thin-Film Temperature Sensors Prepared by Magnetron Sputtering, Applied Sciences 13 (2023) 4747. https://doi.org/10.3390/app13084747.
[81] N. Maluf, K. Williams, An introduction to microelectromechanical systems engineering, secondnd ed., Artech House, Boston, 2004.
[82] N.S. Kale, Introduction to MEMS; their applications as sensors for chemical & bio sensing, in: 2015 19th International Symposium on VLSI Design and Test, Ahmedabad, India, IEEE, 26/06/2015 - 29/06/2015, pp. 1–2.
[83] S. Bhansali, A. Vasudev, MEMS for biomedical applications, Woodhead Pub, Oxford, 2012.
[84] E.B. Chancellor, J.P. Wikswo, F. Baudenbacher, M. Radparvar, D. Osterman, Heat conduction calorimeter for massively parallel high throughput measurements with picoliter sample volumes, Appl. Phys. Lett. 85 (2004) 2408–2410. https://doi.org/10.1063/1.1790075.

[85] E.A. Olson, M.Y. Efremov, A.T. Kwan, S. Lai, V. Petrova, F. Schiettekatte, J.T. Warren, M. Zhang, L.H. Allen, Scanning calorimeter for nanoliter-scale liquid samples, Appl. Phys. Lett. 77 (2000) 2671–2673. https://doi.org/10.1063/1.1319506.

[86] P. Camilleri, Capillary electrophoresis: Theory and practice, secondnd edition, CRC Press, Boca Raton (Fla.), Boston (Mass.), New York etc., 1998.

[87] K. Mullis, F. Faloona, S. Scharf, R. Saiki, G. Horn, H. Erlich, Specific enzymatic amplification of DNA in vitro: the polymerase chain reaction, Cold Spring Harb. Symp. Quant. Biol. 51 Pt 1 (1986) 263–273. https://doi.org/10.1101/sqb.1986.051.01.032.

[88] Y. Xia, G.M. Whitesides, Soft Lithography, Angewandte Chemie International Edition 37 (1998) 550–575. https://doi.org/10.1002/(SICI)1521-3773(19980316)37:5<550:AID-ANIE550>3.0.CO;2-G.

[89] R.B. Fair, A. Khlystov, T.D. Tailor, V. Ivanov, R.D. Evans, V. Srinivasan, V.K. Pamula, M.G. Pollack, P.B. Griffin, J. Zhou, Chemical and Biological Applications of Digital-Microfluidic Devices, IEEE Des. Test. Comput. 24 (2007) 10–24. https://doi.org/10.1109/MDT.2007.8.

[90] F. Olivier, A.A. Maurice, D. Meyer, J.-C.P. Gabriel, Liquid–liquid extraction: thermodynamics–kinetics driven processes explored by microfluidics, Comptes Rendus. Chimie 25 (2022) 137–148. https://doi.org/10.5802/crchim.172.

[91] V. Narayanamurthy, Z.E. Jeroish, K.S. Bhuvaneshwari, P. Bayat, R. Premkumar, F. Samsuri, M.M. Yusoff, Advances in passively driven microfluidics and lab-on-chip devices: a comprehensive literature review and patent analysis, RSC Advances 10 (2020) 11652–11680. https://doi.org/10.1039/D0RA00263A.

[92] J.M.K. Ng, I. Gitlin, A.D. Stroock, G.M. Whitesides, Components for integrated poly(dimethylsiloxane) microfluidic systems, ELECTROPHORESIS 23 (2002) 3461–3473. https://doi.org/10.1002/1522-2683(200210)23:20<3461:AID-ELPS3461>3.0.CO;2-8.

[93] G.M. Whitesides, A.D. Stroock, Flexible Methods for Microfluidics, Physics Today 54 (2001) 42–48. https://doi.org/10.1063/1.1387591.

[94] C. Iliescu, B. Chen, J. Miao, On the wet etching of Pyrex glass, Sensors and Actuators A: Physical 143 (2008) 154–161. https://doi.org/10.1016/j.sna.2007.11.022.

[95] R.M. Tiggelaar, F. Benito-López, D.C. Hermes, H. Rathgen, R.J. Egberink, F.G. Mugele, D.N. Reinhoudt, A. van den Berg, W. Verboom, H.J. Gardeniers, Fabrication, mechanical testing and application of high-pressure glass microreactor chips, Chemical Engineering Journal 131 (2007) 163–170. https://doi.org/10.1016/j.cej.2006.12.036.

[96] C.-Y. Lee, C.-L. Chang, Y.-N. Wang, L.-M. Fu, Microfluidic mixing: a review, International Journal of Molecular Sciences 12 (2011) 3263–3287. https://doi.org/10.3390/ijms12053263.

[97] V. Hessel, H. Löwe, F. Schönfeld, Micromixers—a review on passive and active mixing principles, Chemical Engineering Science 60 (2005) 2479–2501. https://doi.org/10.1016/j.ces.2004.11.033.

[98] J. Green, A. Holdø, A. Khan, A review of passive and active mixing systems in microfluidic devices, The International Journal of Multiphysics 1 (2007) 1–32. https://doi.org/10.1260/175095407780130544.

[99] C.N. Baroud, F. Gallaire, R. Dangla, Dynamics of microfluidic droplets, Lab Chip 10 (2010) 2032–2045. https://doi.org/10.1039/C001191F.

[100] C. Liu, C. Zhu, T. Fu, Y. Ma, H.Z. Li, Interfacial dynamics of the core-annular flow for glycerol–water solution / ionic liquid ([BMIM][PF6]) two-phase flow in a microfluidic flow-focusing junction, Journal of the Taiwan Institute of Chemical Engineers 98 (2019) 45–52. https://doi.org/10.1016/j.jtice.2018.04.033.

[101] Li Dai, X. Zhao, J. Guo, S. Feng, Y. Fu, Y. Kang, J. Guo, Microfluidics-based microwave sensor, Sensors and Actuators A: Physical 309 (2020) 111910. https://doi.org/10.1016/j.sna.2020.111910.

[102] J. Wu, M. Gu, Microfluidic sensing: state of the art fabrication and detection techniques, J. Biomed. Opt. 16 (2011) 80901. https://doi.org/10.1117/1.3607430.

[103] G. Maltezos, M. Johnston, A. Scherer, Thermal management in microfluidics using micro-Peltier junctions, Appl. Phys. Lett. 87 (2005) 154105. https://doi.org/10.1063/1.2089174.

[104] H. Mao, T. Yang, P.S. Cremer, A microfluidic device with a linear temperature gradient for parallel and combinatorial measurements, J. Am. Chem. Soc. 124 (2002) 4432–4435. https://doi.org/10.1021/ja017625x.

[105] B. Selva, J. Marchalot, M.-C. Jullien, An optimized resistor pattern for temperature gradient control in microfluidics, J. Micromech. Microeng. 19 (2009) 65002. https://doi.org/10.1088/0960-1317/19/6/065002.

[106] D. Vigolo, R. Rusconi, R. Piazza, H.A. Stone, A portable device for temperature control along microchannels, Lab Chip 10 (2010) 795–798. https://doi.org/10.1039/b919146a.

[107] A.I. Lao, T.M. Lee, I.-M. Hsing, N.Y. Ip, Precise temperature control of microfluidic chamber for gas and liquid phase reactions, Sensors and Actuators A: Physical 84 (2000) 11–17. https://doi.org/10.1016/S0924-4247(99)00356-8.

[108] B. Selva, P. Mary, M.-C. Jullien, Integration of a uniform and rapid heating source into microfluidic systems, Microfluid Nanofluid 8 (2010) 755–765. https://doi.org/10.1007/s10404-009-0505-7.

[109] M. Andersson, J. Ek, L. Hedman, F. Johansson, V. Sehlstedt, J. Stocklassa, P. Snögren, V. Pettersson, J. Larsson, O. Vizuete, K. Hjort, L. Klintberg, Thin film metal sensors in fusion bonded glass chips for high-pressure microfluidics, J. Micromech. Microeng. 27 (2017) 15018. https://doi.org/10.1088/0960-1317/27/1/015018.

[110] G. Yaralioglu, Ultrasonic heating and temperature measurement in microfluidic channels, Sensors and Actuators A: Physical 170 (2011) 1–7. https://doi.org/10.1016/j.sna.2011.05.012.

[111] J.J. Shah, S.G. Sundaresan, J. Geist, D.R. Reyes, J.C. Booth, M.V. Rao, M. Gaitan, Microwave dielectric heating of fluids in an integrated microfluidic device, J. Micromech. Microeng. 17 (2007) 2224–2230. https://doi.org/10.1088/0960-1317/17/11/008.

[112] D. Issadore, K.J. Humphry, K.A. Brown, L. Sandberg, D.A. Weitz, R.M. Westervelt, Microwave dielectric heating of drops in microfluidic devices, Lab Chip 9 (2009) 1701–1706. https://doi.org/10.1039/b822357b.

[113] J. Wu, W. Cao, W. Wen, D.C. Chang, P. Sheng, Polydimethylsiloxane microfluidic chip with integrated microheater and thermal sensor, Biomicrofluidics 3 (2009) 12005. https://doi.org/10.1063/1.3058587.

[114] M. Robert de Saint Vincent, R. Wunenburger, J.-P. Delville, Laser switching and sorting for high speed digital microfluidics, Appl. Phys. Lett. 92 (2008) 154105. https://doi.org/10.1063/1.2911913.

[115] H. Kim, S. Vishniakou, G.W. Faris, Petri dish PCR: laser-heated reactions in nanoliter droplet arrays, Lab Chip 9 (2009) 1230–1235. https://doi.org/10.1039/B817288A.

[116] T.J. Seebeck, Ueber den Magnetismus der galvanischen Kette, 1822.

[117] G.W. Burns, M.G. Scroger, The Calibration of Thermocouples and Thermocouple Materials, U.S. Department of Commerce, National Institute of Standards and Technology, 1989.

[118] C.D. Miller, A Potentiometer Arrangement for the Measurement of emf Over a Wide Range, J. Opt. Soc. Am. 15 (1927) 238. https://doi.org/10.1364/JOSA.15.000238.
[119] OMEGA Engineering in, Thermocouple vs RTDs. https://www.omega.com/en-us/resources/rtd-vs-thermocouple.
[120] D. Bucci, Analog electronics for measuring systems, ISTE; Wiley, Londres, Hoboken, NJ, 2017.
[121] J.F. Creemer, S. Helveg, P.J. Kooyman, A.M. Molenbroek, H.W. Zandbergen, P.M. Sarro, A MEMS Reactor for Atomic-Scale Microscopy of Nanomaterials Under Industrially Relevant Conditions, J. Microelectromech. Syst. 19 (2010) 254–264. https://doi.org/10.1109/jmems.2010.2041190.
[122] G. Guenther, E. Aulbach, H. Hahn, O. Guillon, High-temperature chip calorimeter with atmosphere control, Thermochimica Acta 522 (2011) 77–85. https://doi.org/10.1016/j.tca.2011.03.013.
[123] V. Hoang, G. Kaigala, C. Backhouse, Optimization of thin film heater/sensor design for miniature devices using finite element analysis, COMSOL Multiphysics User's conference, Boston., 2005.
[124] J. Courbat, D. Briand, N.F. de Rooij, Reliability improvement of suspended platinum-based micro-heating elements, Sensors and Actuators A: Physical 142 (2008) 284–291. https://doi.org/10.1016/j.sna.2007.04.006.
[125] U. Hammerschmidt, W. Sabuga, ransient Hot Wire (THW) Method: Uncertainty Assessment, Int J Thermophys 21 (2000) 1255–1278. https://doi.org/10.1023/A:1006649209044.
[126] R.J. Warzoha, A.S. Fleischer, Determining the thermal conductivity of liquids using the transient hot disk method. Part II: Establishing an accurate and repeatable experimental methodology, Int. J. Heat Mass Transf. 71 (2014) 790–807. https://doi.org/10.1016/j.ijheatmasstransfer.2013.10.062.
[127] S.-M. Lee, D.G. Cahill, Heat transport in thin dielectric films, Journal of Applied Physics 81 (1997) 2590–2595. https://doi.org/10.1063/1.363923.
[128] J.H. Kim, A. Feldman, D. Novotny, Application of the three omega thermal conductivity measurement method to a film on a substrate of finite thickness, Journal of Applied Physics 86 (1999) 3959–3963. https://doi.org/10.1063/1.371314.
[129] Y. Zhang, S. Tadigadapa, Thermal characterization of liquids and polymer thin films using a microcalorimeter, Appl. Phys. Lett. 86 (2005) 34101. https://doi.org/10.1063/1.1850186.
[130] D. Kuvshinov, M.R. Bown, J.M. MacInnes, R.W.K. Allen, R. Ge, L. Aldous, C. Hardacre, N. Doy, M.I. Newton, G. McHale, Thermal conductivity measurement of liquids in a microfluidic device, Microfluid Nanofluid 10 (2011) 123–132. https://doi.org/10.1007/s10404-010-0652-x.
[131] M. Gustavsson, H. Nagai, T. Okutani, Thermal effusivity measurements of insulating liquids using microsized hot strip probes, Review of Scientific Instruments 74 (2003) 4542–4548. https://doi.org/10.1063/1.1606537.
[132] G. Velve Casquillas, M. Le Berre, C. Peroz, Y. Chen, J.J. Greffet, Microlitre hot strip devices for thermal characterization of nanofluids, Microelectronic Engineering 84 (2007) 1194–1197. https://doi.org/10.1016/j.mee.2007.01.187.
[133] R. Karthik, N. Harish Nagarajan, B. Raja, P. Damodharan, Measurement of thermal conductivity of fluids using 3-ω method in a suspended micro wire, J. Engin. Thermophys. 21 (2012) 60–68. https://doi.org/10.1134/S1810232812010067.

[134] S. Roy-Panzer, T. Kodama, S. Lingamneni, M.A. Panzer, M. Asheghi, K.E. Goodson, Thermal characterization and analysis of microliter liquid volumes using the three-omega method, Rev. Sci. Instrum. 86 (2015) 24901. https://doi.org/10.1063/1.4907353.

[135] S.E. Gustafsson, Transient plane source techniques for thermal conductivity and thermal diffusivity measurements of solid materials, Review of Scientific Instruments 62 (1991) 797–804. https://doi.org/10.1063/1.1142087.

[136] A.O. Guimarães, F.A.L. Machado, E.C. da Silva, A.M. Mansanares, Thermal Effusivity and Thermal Conductivity of Biodiesel/Diesel and Alcohol/Water Mixtures, Int J Thermophys 33 (2012) 1842–1847. https://doi.org/10.1007/s10765-012-1280-3.

[137] M.H. Ahmadi, M. Sadeghzadeh, A.H. Raffiee, K. Chau, Applying GMDH neural network to estimate the thermal resistance and thermal conductivity of pulsating heat pipes, Engineering Applications of Computational Fluid Mechanics 13 (2019) 327–336. https://doi.org/10.1080/19942060.2019.1582109.

[138] B. Sohn, J. Wi, S. Park, J. Lim, H. Choi, Evaluation of Conventional Prediction Models for Soil Thermal Conductivity to Design Horizontal Ground Heat Exchangers, Journal of the Korean Geotechnical Society 29 (2013) 5–14. https://doi.org/10.7843/kgs.2013.29.2.5.

[139] S. Khosharay, K. Khosharay, G. Di Nicola, M. Pierantozzi, Modelling investigation on the thermal conductivity of pure liquid, vapour, and supercritical refrigerants and their mixtures by using Heyen EOS, Physics and Chemistry of Liquids 56 (2018) 124–140. https://doi.org/10.1080/00319104.2017.1306859.

[140] X.-Q. Guo, C.-Y. Sun, S.-X. Rong, G.-J. Chen, T.-M. Guo, Equation of state analog correlations for the viscosity and thermal conductivity of hydrocarbons and reservoir fluids, Journal of Petroleum Science and Engineering 30 (2001) 15–27. https://doi.org/10.1016/S0920-4105(01)00098-5.

[141] Van der Waals, Over de Continuiteit van den Gas-en Vloeistoftoestand (On the Continuity of the Gas and Liquid State). Ph.D. Thesis, University of Leiden, Leiden., 1873.

[142] O. REDLICH, J.N.S. KWONG, On the thermodynamics of solutions; an equation of state; fugacities of gaseous solutions, Chem. Rev. 44 (1949) 233–244. https://doi.org/10.1021/cr60137a013.

[143] D.-Y. Peng, D.B. Robinson, A New Two-Constant Equation of State, Ind. Eng. Chem. Fund. 15 (1976) 59–64. https://doi.org/10.1021/i160057a011.

[144] T. Heckenberger, K. Stephan, Cubic equations of state for transport properties: An equation for the thermal conductivity of oxygen, Int J Thermophys 11 (1990) 1011–1023. https://doi.org/10.1007/BF00500556.

[145] L.F. Cardona, L.A. Forero, J.A. Velásquez, Correlation and Prediction of Thermal Conductivity Using the Redlich–Kwong Cubic Equation of State and the Geometric Similitude Concept for Pure Substances and Mixtures, Ind. Eng. Chem. Res. 58 (2019) 23417–23437. https://doi.org/10.1021/acs.iecr.9b04974.

[146] F. Gharagheizi, P. Ilani-Kashkouli, M. Sattari, A.H. Mohammadi, D. Ramjugernath, D. Richon, Development of a quantitative structure–liquid thermal conductivity relationship for pure chemical compounds, Fluid Phase Equilibria 355 (2013) 52–80. https://doi.org/10.1016/j.fluid.2013.06.043.

[147] H. Lu, W. Liu, F. Yang, H. Zhou, F. Liu, H. Yuan, G. Chen, Y. Jiao, Thermal Conductivity Estimation of Diverse Liquid Aliphatic Oxygen-Containing Organic Compounds Using the Quantitative Structure-Property Relationship Method, ACS Omega 5 (2020) 8534–8542. https://doi.org/10.1021/acsomega.9b04190.

[148] Wanqiang Liu, aixia Lu, Chenzhong Cao, Yinchun Jiao, and Guanfan Chen, An Improved Quantitative Structure Property Relationship Model for Predicting Thermal Conductivity of Liquid Aliphatic Alcohols, Chemical & Engineering data (2018). https://doi.org/10.1021/acs.jced.8b00764.

[149] M. Pirashvili, L. Steinberg, F. Belchi Guillamon, M. Niranjan, J.G. Frey, J. Brodzki, Improved understanding of aqueous solubility modeling through topological data analysis, J Cheminform 10 (2018) 54. https://doi.org/10.1186/s13321-018-0308-5.

[150] C. Nieto-Draghi, G. Fayet, B. Creton, X. Rozanska, P. Rotureau, J.-C. de Hemptinne, P. Ungerer, B. Rousseau, C. Adamo, A General Guidebook for the Theoretical Prediction of Physicochemical Properties of Chemicals for Regulatory Purposes, Chem. Rev. 115 (2015) 13093–13164. https://doi.org/10.1021/acs.chemrev.5b00215.

[151] D.A. Saldana, L. Starck, P. Mougin, B. Rousseau, N. Ferrando, B. Creton, Prediction of Density and Viscosity of Biofuel Compounds Using Machine Learning Methods, Energy Fuels 26 (2012) 2416–2426. https://doi.org/10.1021/ef3001339.

[152] H. Gao, T.J. Struble, C.W. Coley, Y. Wang, W.H. Green, K.F. Jensen, Using Machine Learning To Predict Suitable Conditions for Organic Reactions, ACS Central Science 4 (2018) 1465–1476. https://doi.org/10.1021/acscentsci.8b00357.

[153] F.K. Brown, Chemoinformatics: What is it and How does it Impact Drug Discovery, in: Elsevier, 1998, pp. 375–384.

[154] D.S. Wishart, Introduction to cheminformatics, Curr. Protoc. Bioinformatics Chapter 14 (2007) Unit 14.1. https://doi.org/10.1002/0471250953.bi1401s18.

[155] B. Zdrazil, R. Guha, Diversifying cheminformatics, J Cheminform 14 (2022) 25. https://doi.org/10.1186/s13321-022-00597-5.

[156] A.C. Brown, T.R. Fraser, On the Connection between Chemical Constitution and Physiological Action; with special reference to the Physiological Action of the Salts of the Ammonium Bases derived from Strychnia, Brucia, Thebaia, Codeia, Morphia, and Nicotia, J. Anat. Physiol. 2 (1868) 224–242.

[157] C. Richet, On the relationship between the toxicity and the physical properties of substances: Comptes Rendus des Seances de la Societe de Biologie et de ses Filiales, 1893.

[158] H. Meyer, Zur Theorie der Alkoholnarkose, Archiv f. experiment. Pathol. u. Pharmakol 42 (1899) 109–118. https://doi.org/10.1007/BF01834479.

[159] J Ferguson, The use of chemical potentials as indices of toxicity, Proc. R. Soc. Lond. B 127 (1939) 387–404. https://doi.org/10.1098/rspb.1939.0030.

[160] L.P. Hammett, Some Relations between Reaction Rates and Equilibrium Constants, Chem. Rev. 17 (1935) 125–136. https://doi.org/10.1021/cr60056a010.

[161] RW Taft Jr, Polar and Steric Substituent Constants for Aliphatic and o-Benzoate Groups from Rates of Esterification and Hydrolysis of Esters1, Journal of the American Chemical Society, 1952.

[162] C. Hansch, T. Fujita, p -σ-π Analysis. A Method for the Correlation of Biological Activity and Chemical Structure, J. Am. Chem. Soc. 86 (1964) 1616–1626. https://doi.org/10.1021/ja01062a035.

[163] A. Cherkasov, E.N. Muratov, D. Fourches, A. Varnek, I.I. Baskin, M. Cronin, J. Dearden, P. Gramatica, Y.C. Martin, R. Todeschini, V. Consonni, V.E. Kuz'min, R. Cramer, R. Benigni, C. Yang, J. Rathman, L. Terfloth, J. Gasteiger, A. Richard, A. Tropsha, QSAR modeling: where have you been? Where are you going to?, J. Med. Chem. 57 (2014) 4977–5010. https://doi.org/10.1021/jm4004285.

[164] D.A. Saldana, L. Starck, P. Mougin, B. Rousseau, L. Pidol, N. Jeuland, B. Creton, Flash Point and Cetane Number Predictions for Fuel Compounds Using Quantitative Structure Property Relationship (QSPR) Methods, Energy Fuels 25 (2011) 3900–3908. https://doi.org/10.1021/ef200795j.

[165] D. Sola, A. Ferri, M. Banchero, L. Manna, S. Sicardi, QSPR prediction of N-boiling point and critical properties of organic compounds and comparison with a group-contribution method, Fluid Phase Equilibria 263 (2008) 33–42. https://doi.org/10.1016/j.fluid.2007.09.022.

[166] M. Roubehie Fissa, Y. Lahiouel, L. Khaouane, S. Hanini, QSPR estimation models of normal boiling point and relative liquid density of pure hydrocarbons using MLR and MLP-ANN methods, J. Mol. Graph. Model. 87 (2019) 109–120. https://doi.org/10.1016/j.jmgm.2018.11.013.

[167] S. Trohalaki, R. Pachter, Prediction of Melting Points for Ionic Liquids, QSAR Comb. Sci. 24 (2005) 485–490. https://doi.org/10.1002/qsar.200430927.

[168] O. Ivanciuc, T. Ivanciuc, P.A. Filip, D. Cabrol-Bass, Estimation of the Liquid Viscosity of Organic Compounds with a Quantitative Structure−Property Model, J. Chem. Inf. Comput. Sci. 39 (1999) 515–524. https://doi.org/10.1021/ci980117v.

[169] K. Tochigi, H. Yamamoto, Estimation of Ionic Conductivity and Viscosity of Ionic Liquids Using a QSPR Model, J. Phys. Chem. C 111 (2007) 15989–15994. https://doi.org/10.1021/jp073839a.

[170] B. Sepehri, A review on created QSPR models for predicting ionic liquids properties and their reliability from chemometric point of view, Journal of Molecular Liquids 297 (2020) 112013. https://doi.org/10.1016/j.molliq.2019.112013.

[171] A.P. Fröba, M.H. Rausch, K. Krzeminski, D. Assenbaum, P. Wasserscheid, A. Leipertz, Thermal Conductivity of Ionic Liquids: Measurement and Prediction, Int J Thermophys 31 (2010) 2059–2077. https://doi.org/10.1007/s10765-010-0889-3.

[172] A. Khajeh, H. Modarress, Quantitative structure–property relationship prediction of liquid thermal conductivity for some alcohols, Struct Chem 22 (2011) 1315–1323. https://doi.org/10.1007/s11224-011-9828-6.

[173] J.S. Torrecilla, J. Palomar, J. Lemus, F. Rodríguez, A quantum-chemical-based guide to analyze/quantify the cytotoxicity of ionic liquids, Green Chem 12 (2010) 123–134. https://doi.org/10.1039/B919806G.

[174] A.R. Katritzky, M. Kuanar, S. Slavov, C.D. Hall, M. Karelson, I. Kahn, D.A. Dobchev, Quantitative correlation of physical and chemical properties with chemical structure: utility for prediction, Chem. Rev. 110 (2010) 5714–5789. https://doi.org/10.1021/cr900238d.

[175] CrowdFlower 2016, https://visit.figure-eight.com/rs/416-ZBE-142/images/CrowdFlower_DataScienceReport_2016.pdf.

[176] J.C. Bloxham, M.E. Redd, N.F. Giles, T.A. Knotts, W.V. Wilding, Proper Use of the DIPPR 801 Database for Creation of Models, Methods, and Processes, J. Chem. Eng. Data 66 (2021) 3–10. https://doi.org/10.1021/acs.jced.0c00641.

[177] D. Weininger, SMILES, a chemical language and information system. 1. Introduction to methodology and encoding rules, J. Chem. Inf. Comput. Sci. 28 (1988) 31–36. https://doi.org/10.1021/ci00057a005.

[178] US. Environmental Protection Agency, SMILES Tutorial, 2016. https://archive.epa.gov/med/med_archive_03/web/html/smiles.html.

[179] R. Todeschini, V. Consonni, Handbook of molecular descriptors, Wiley-VCH, Weinheim, New York, 2011.

[180] R. Todeschini, P. Gramatica, The Whim Theory: New 3D Molecular Descriptors for Qsar in Environmental Modelling, SAR and QSAR in Environmental Research 7 (1997) 89–115. https://doi.org/10.1080/10629369708039126.

[181] V. Consonni, R. Todeschini, M. Pavan, Structure/response correlations and similarity/diversity analysis by GETAWAY descriptors. 1. Theory of the novel 3D molecular descriptors, J. Chem. Inf. Comput. Sci. 42 (2002) 682–692. https://doi.org/10.1021/ci015504a.

[182] Danishuddin, A.U. Khan, Descriptors and their selection methods in QSAR analysis: paradigm for drug design, Drug Discov. Today 21 (2016) 1291–1302. https://doi.org/10.1016/j.drudis.2016.06.013.

[183] M. Nagvekar, T.E. Daubert, A group contribution method for liquid thermal conductivity, Ind. Eng. Chem. Res. 26 (1987) 1362–1365. https://doi.org/10.1021/ie00067a017.

[184] K.G. JOBACK, R.C. REID, ESTIMATION OF PURE-COMPONENT PROPERTIES FROM GROUP-CONTRIBUTIONS, CHEMICAL ENGINEERING COMMUNICATIONS 57 (1987) 233–243. https://doi.org/10.1080/00986448708960487.

[185] L. Constantinou, R. Gani, New group contribution method for estimating properties of pure compounds, AIChE J. 40 (1994) 1697–1710. https://doi.org/10.1002/aic.690401011.

[186] J. Marrero, R. Gani, Group-contribution based estimation of pure component properties, Fluid Phase Equilibria 183-184 (2001) 183–208. https://doi.org/10.1016/S0378-3812(01)00431-9.

[187] F. Alves de Lima Ribeiro, M.M.C. Ferreira, QSPR models of boiling point, octanol–water partition coefficient and retention time index of polycyclic aromatic hydrocarbons, Journal of Molecular Structure: THEOCHEM 663 (2003) 109–126. https://doi.org/10.1016/j.theochem.2003.08.107.

[188] P.R. Duchowicz, E.A. Castro, F.M. Fernández, M.P. Gonzalez, A new search algorithm for QSPR/QSAR theories: Normal boiling points of some organic molecules, Chemical Physics Letters 412 (2005) 376–380. https://doi.org/10.1016/j.cplett.2005.07.016.

[189] D.A. Saldana, L. Starck, P. Mougin, B. Rousseau, B. Creton, On the rational formulation of alternative fuels: melting point and net heat of combustion predictions for fuel compounds using machine learning methods, SAR and QSAR in Environmental Research 24 (2013) 259–277. https://doi.org/10.1080/1062936X.2013.766634.

[190] F. Gharagheizi, S.A. Mirkhani, A.-R. Tofangchi Mahyari, Prediction of Standard Enthalpy of Combustion of Pure Compounds Using a Very Accurate Group-Contribution-Based Method, Energy Fuels 25 (2011) 2651–2654. https://doi.org/10.1021/ef200081a.

[191] L.F. Cardona, L.A. Forero, J.A. Velásquez, A group contribution method to model the thermal conductivity of pure substances, Fluid Phase Equilibria 564 (2023) 113592. https://doi.org/10.1016/j.fluid.2022.113592.

[192] G.K. Uyanık, N. Güler, A Study on Multiple Linear Regression Analysis, Procedia - Social and Behavioral Sciences 106 (2013) 234–240. https://doi.org/10.1016/j.sbspro.2013.12.027.

[193] S. Agatonovic-Kustrin, R. Beresford, Basic concepts of artificial neural network (ANN) modeling and its application in pharmaceutical research, J. Pharm. Biomed. Anal. 22 (2000) 717–727. https://doi.org/10.1016/S0731-7085(99)00272-1.

[194] J. Cervantes, F. Garcia-Lamont, L. Rodríguez-Mazahua, A. Lopez, A comprehensive survey on support vector machine classification: Applications, challenges and trends, Neurocomputing 408 (2020) 189–215. https://doi.org/10.1016/j.neucom.2019.10.118.

[195] H.R. Baghaee, D. Mlakic, S. Nikolovski, T. Dragicevic, Support Vector Machine-Based Islanding and Grid Fault Detection in Active Distribution Networks, IEEE J. Emerg. Sel. Topics Power Electron. 8 (2020) 2385–2403. https://doi.org/10.1109/jestpe.2019.2916621.

[196] K. Roy, R.N. Das, P. Ambure, R.B. Aher, Be aware of error measures. Further studies on validation of predictive QSAR models, Chemometrics and Intelligent Laboratory Systems 152 (2016) 18–33. https://doi.org/10.1016/j.chemolab.2016.01.008.

[197] M. Taraji, P.R. Haddad, R.I.J. Amos, M. Talebi, R. Szucs, J.W. Dolan, C.A. Pohl, Error measures in quantitative structure-retention relationships studies, J. Chromatogr. A 1524 (2017) 298–302. https://doi.org/10.1016/j.chroma.2017.09.050.

[198] G.W. Kauffman, P.C. Jurs, Prediction of surface tension, viscosity, and thermal conductivity for common organic solvents using quantitative structure-property relationships, J. Chem. Inf. Comput. Sci. 41 (2001) 408–418. https://doi.org/10.1021/ci000139t.

[199] Y. Marcus, The properties of solvents, Wiley, Chichester, New York, 1998.

[200] S. Albawi, T.A. Mohammed, S. Al-Zawi, Understanding of a convolutional neural network, in: 2017 International Conference on Engineering and Technology (ICET), IEEE, 2017.

[201] Yaws" Handbook of thermodynamic and physical properties of chemical compounds, 2003.

[202] S.H. Jing-Jie, C. Li-Ping, C. Wang-Hua, S.H. Ning, Y. Hui, X.U. Wei, Prediction of the Thermal Conductivity of Organic Compounds Using Heuristic and Support Vector Machine Methods, Acta Physico-Chimica Sinica 28 (2012) 2790–2796. https://doi.org/10.3866/PKU.WHXB201209273.

[203] Data Manual for the Physical Property of Organic Compounds, 2006.

[204] G. Latini, G. Di Nicola, M. Pierantozzi, G. Coccia, S. Tomassetti, Artificial Neural Network Modeling of Liquid Thermal Conductivity for alkanes, ketones and silanes, J. Phys.: Conf. Ser. 923 (2017) 12054. https://doi.org/10.1088/1742-6596/923/1/012054.

[205] M. Pierantozzi, G. Di Nicola, G. Latini, G. Coccia, Artificial neural network modelling of liquid thermal conductivity for alcohols, Physics and Chemistry of Liquids 56 (2018) 363–380. https://doi.org/10.1080/00319104.2017.1341980.

[206] N.B. Vargaftik, Handbook of thermal conductivity of liquids and gases, CRC Press, Boca Raton (Fla.), 1994.

[207] C.M. Rodenbush, D.S. Viswanath, F. Hsieh, A Group Contribution Method for the Prediction of Thermal Conductivity of Liquids and Its Application to the Prandtl Number for Vegetable Oils, Ind. Eng. Chem. Res. 38 (1999) 4513–4519. https://doi.org/10.1021/ie990320v.

[208] K.R. S.R.S. Sastri, A new temperature±thermal conductivity relationship for predicting saturated liquid thermal conductivity, Chemical Engineering Journal (1999 74:161–169.).

[209] W. Su, Li Zhao, S. Deng, Group contribution methods in thermodynamic cycles: Physical properties estimation of pure working fluids, Renewable and Sustainable Energy Reviews 79 (2017) 984–1001. https://doi.org/10.1016/j.rser.2017.05.164.

[210] G. Oudebrouckx, T. Vandenryt, S. Bormans, P. Wagner, R. Thoelen, Measuring Thermal Conductivity in a Microfluidic Device with the Transient Thermal Offset (TTO) Method, in: 2020 IEEE SENSORS, Rotterdam, Netherlands, IEEE, 25/10/2020 - 28/10/2020, pp. 1–4.

[211] E.R. Murphy, T. Inoue, H.R. Sahoo, N. Zaborenko, K.F. Jensen, Solder-based chip-to-tube and chip-to-chip packaging for microfluidic devices, Lab Chip 7 (2007) 1309–1314. https://doi.org/10.1039/b704804a.

[212] Theo Gavoille, Methodologies pour la caracterisation de propriétés thermodynamiques dans des systèmes microfluidiques. Thèse de doctorat, Université de Bordeaux, 2019.

[213] H. Darrell, Evaluating Thin Film RTD Stability, Sensors-the Journal of Applied Sensing Technology 14, no. 10, 1997.

[214] W.A. Clayton, Thin-film platinum for appliance temperature control, IEEE Trans. on Ind. Applicat. 24 (1988) 332–336. https://doi.org/10.1109/28.2875.

[215] A. Ehrlich, U. Weiß, W. Hoyer, T. Geßner, Microstructural changes of Pt/Ti bilayer during annealing in different atmospheres — an XRD study, Thin Solid Films 300 (1997) 122–130. https://doi.org/10.1016/S0040-6090(96)09452-7.

[216] J.O. Olowolafe, R.E. Jones, A.C. Campbell, R.I. Hegde, C.J. Mogab, R.B. Gregory, Effects of anneal ambients and Pt thickness on Pt/Ti and Pt/Ti/TiN interfacial reactions, Journal of Applied Physics 73 (1993) 1764–1772. https://doi.org/10.1063/1.353212.

[217] A. Scorzoni, D. Caputo, G. Petrucci, P. Placidi, S. Zampolli, G. de Cesare, M. Tavernelli, A. Nascetti, Design and experimental characterization of thin film heaters on glass substrate for Lab-on-Chip applications, Sensors and Actuators A: Physical 229 (2015) 203–210. https://doi.org/10.1016/j.sna.2015.03.011.

[218] J. Han, P. Cheng, H. Wang, C. Zhang, J. Zhang, Y. Wang, Li Duan, G. Ding, MEMS-based Pt film temperature sensor on an alumina substrate, Materials Letters 125 (2014) 224–226. https://doi.org/10.1016/j.matlet.2014.03.170.

[219] F. Samaeifar, H. Hajghassem, A. Afifi, H. Abdollahi, Implementation of high-performance MEMS platinum micro-hotplate, Sensor Review 35 (2015) 116–124. https://doi.org/10.1108/SR-05-2014-654.

[220] V. Guarnieri, L. Biazi, R. Marchiori, A. Lago, Platinum metallization for MEMS application. Focus on coating adhesion for biomedical applications, Biomatter 4 (2014). https://doi.org/10.4161/biom.28822.

[221] E. Guk, M. Ranaweera, V. Venkatesan, J.-S. Kim, Performance and Durability of Thin Film Thermocouple Array on a Porous Electrode, Sensors (Basel) 16 (2016). https://doi.org/10.3390/s16091329.

[222] High Temperature Oxidation of Thin Chromel-Alumel Thermocouples.

[223] C.J. Elliott, A. Greenen, D. Lowe, J.V. Pearce, G. Machin, High temperature exposure of in-situ thermocouple fixed-point cells: stability with up to three months of continuous use, Metrologia 52 (2015) 267–271. https://doi.org/10.1088/0026-1394/52/2/267.

[224] Rita Kriūkienė, Sigitas Tamulevičius, High Temperature Oxidation of Thin Chromel-Alumel Thermocouples, 2004.

[225] R. Marshall, L. Atlas, T. Putner, The preparation and performance of thin film thermocouples, J. Sci. Instrum. 43 (1966) 144–149. https://doi.org/10.1088/0950-7671/43/3/305.

[226] J.S. Acken, Some physical properties of platinum-rhodium alloys, BUR. STAN. J. RES. 12 (1934) 249. https://doi.org/10.6028/jres.012.023.

[227] Z.E. Jeroish, K.S. Bhuvaneshwari, F. Samsuri, V. Narayanamurthy, Microheater: material, design, fabrication, temperature control, and applications-a role in COVID-19, Biomed. Microdevices 24 (2021) 3. https://doi.org/10.1007/s10544-021-00595-8.

[228] V. P., V. Juliet A., S. Jebakumar J., J. R, Design and Fabrication of Temperature Sensor for Weather Monitoring System using MEMS Technology, Orient. J. Chem 34 (2018) 2510–2516. https://doi.org/10.13005/ojc/340537.

[229] S.J. Bharathi, S.H. Thilagar, Heat transfer analysis on platinum-based thin-film temperature sensor element for liquid temperature measurement applications, HTR 52 (2021) 35–60. https://doi.org/10.1615/HeatTransRes.2021037906.

[230] M. Hatzakis, B.J. Canavello, J.M. Shaw, Single-Step Optical Lift-Off Process, IBM J. Res. & Dev. 24 (1980) 452–460. https://doi.org/10.1147/rd.244.0452.

[231] J. Liang, F. Kohsaka, T. Matsuo, X. Li, T. Ueda, Improved bi-layer lift-off process for MEMS applications, Microelectronic Engineering 85 (2008) 1000–1003. https://doi.org/10.1016/j.mee.2008.01.104.

[232] Y. Chen, A lift-off process for high resolution patterns using PMMA/LOR resist stack, Microelectronic Engineering 73-74 (2004) 278–281. https://doi.org/10.1016/j.mee.2004.02.053.

[233] J Golden, H Miller, D Nawrocki, J Ross, Optimization of bi-layer lift-off resist process, 2009.

[234] RS components, Datasheet Point Spring- loaded test terminal.

[235] J.J. Healy, J.J. de Groot, J. Kestin, The theory of the transient hot-wire method for measuring thermal conductivity, Physica B+C 82 (1976) 392–408. https://doi.org/10.1016/0378-4363(76)90203-5.

[236] E.G. PRICE, B. TAYLOR, Temperature Coefficient of Electrical Resistance of High-Purity Rhodium, Nature 195 (1962) 272–273. https://doi.org/10.1038/195272a0.

[237] H.J.K. Kim, K.E. Kaplan, P. Schindler, S. Xu, M.M. Winterkorn, D.B. Heinz, T.S. English, J. Provine, F.B. Prinz, T.W. Kenny, Electrical Properties of Ultrathin Platinum Films by Plasma-Enhanced Atomic Layer Deposition, ACS Appl. Mater. Interfaces 11 (2019) 9594–9599. https://doi.org/10.1021/acsami.8b21054.

[238] Y. Zhai, C. Cai, J. Huang, H. Liu, S. Zhou, W. Liu, Study on the Resistance Characteristic of Pt Thin Film, Physics Procedia 32 (2012) 772–778. https://doi.org/10.1016/j.phpro.2012.03.634.

[239] H. Seidel, L. Csepregi, A. Heuberger, H. Baumgärtel, Anisotropic Etching of Crystalline Silicon in Alkaline Solutions: I Orientation Dependence and Behavior of Passivation Layers, J. Electrochem. Soc. 137 (1990) 3612–3626. https://doi.org/10.1149/1.2086277.

[240] M. Shikida, K. Sato, K. Tokoro, D. Uchikawa, Comparison of anisotropic etching properties between KOH and TMAH solutions, in: MEMS '99 Twelfth IEEE International Conference on Micro Electro Mechanical Systems, Orlando, FL, USA, IEEE, Piscataway NJ, 1999, pp. 315–320.

[241] O. Tabata, R. Asahi, H. Funabashi, K. Shimaoka, S. Sugiyama, Anisotropic etching of silicon in TMAH solutions, Sensors and Actuators A: Physical 34 (1992) 51–57. https://doi.org/10.1016/0924-4247(92)80139-T.

[242] Sandy Morais, Applications des laboratoires géologiques sur puce pour les problématiques du stockage du CO2: Thèse de doctorat, 2017.

[243] L.I. Segerink, A.J. Sprenkels, P.M. ter Braak, I. Vermes, A. van den Berg, On-chip determination of spermatozoa concentration using electrical impedance measurements, Lab Chip 10 (2010) 1018–1024. https://doi.org/10.1039/b923970g.

[244] M. Gustavsson, H. Nagai, T. Okutani, Thermal effusivity measurements of insulating liquids using microsized hot strip probes, Review of Scientific Instruments 74 (2003) 4542–4548. https://doi.org/10.1063/1.1606537.

[245] W. Guo, G. Li, Y. Zheng, C. Dong, Measurement of the thermal conductivity of SiO 2 nanofluids with an optimized transient hot wire method, Thermochimica Acta 661 (2018) 84–97. https://doi.org/10.1016/j.tca.2018.01.008.

[246] G.-Y. Jeong, S.P. Jang, H.-Y. Lee, J.-C. Lee, S. Choi, S.-H. Lee, Magnetic-Thermal-Fluidic Analysis for Cooling Performance of Magnetic Nanofluids Comparing With Transformer Oil and Air by Using Fully Coupled Finite Element Method, IEEE Trans. Magn. 49 (2013) 1865–1868. https://doi.org/10.1109/TMAG.2013.2245411.

[247] D.-W. Oh, Thermal Conductivity Measurement of Liquids by Using a Suspended Microheater, Int J Thermophys 38 (2017). https://doi.org/10.1007/s10765-017-2278-7.

[248] J. Maroofi, S.H. Hashemabadi, Experimental and numerical investigation of parameters influencing anisotropic thermal conductivity of magnetorheological fluids, Heat Mass Transfer 55 (2019) 2751–2767. https://doi.org/10.1007/s00231-019-02618-w.

[249] F. Lacy, Developing a theoretical relationship between electrical resistivity, temperature, and film thickness for conductors, Nanoscale Res. Lett. 6 (2011) 636. https://doi.org/10.1186/1556-276X-6-636.

[250] S. Dutta, K. Sankaran, K. Moors, G. Pourtois, S. van Elshocht, J. Bömmels, W. Vandervorst, Z. Tőkei, C. Adelmann, Thickness dependence of the resistivity of platinum-group metal thin films, Journal of Applied Physics 122 (2017) 25107. https://doi.org/10.1063/1.4992089.

[251] K. Hoffmann, Applying the Wheatstone Bridge Circuit, HBM S1569–11 en, HBM, Darmstadt, Ger., 2001.

[252] 2016 11th International Conference on Advanced Semiconductor Devices & Microsystems (ASDAM), IEEE, 2016 - 2016.

[253] M. Kandpal, V. Shirhatti, J. Singh, B.A. Sontakke, A. Jejusaria, S.P.S. Arora, S. Singh, Experimental study of chromium oxide thin films as an intermediate layer for Pt-based temperature sensor applications, J Mater Sci: Mater Electron (2022). https://doi.org/10.1007/s10854-022-08915-1.

[254] J. Whitfield, Electrical craft principles 1, fourth. ed., Stevenage, Herts, 1995.

[255] A. Harris, S. Kazachenko, R. Bateman, J. Nickerson, M. Emanuel, Measuring the thermal conductivity of heat transfer fluids via the modified transient plane source (MTPS), J Therm Anal Calorim 116 (2014) 1309–1314. https://doi.org/10.1007/s10973-014-3811-6.

[256] G. Oudebrouckx, D. Nieder, T. Vandenryt, S. Bormans, H. Möbius, R. Thoelen, Single element thermal sensor for measuring thermal conductivity and flow rate inside a microchannel, Sensors and Actuators A: Physical 331 (2021) 112906. https://doi.org/10.1016/j.sna.2021.112906.

[257] E. Arri, F. Cabiati, S. D'Emilio, L. Gonella, On the application of the guide to the expression of uncertainty in measurement to measuring instruments, Measurement 16 (1995) 51–57. https://doi.org/10.1016/0263-2241(95)00017-F.

[258] D. R. Lide, CRC handbook of chemistry and physics, 81st ed. (CRC, New York 2000).

[259] M. Mebelli, D. Velliadou, M.J. Assael, K.D. Antoniadis, M.L. Huber, Reference Correlation for the Thermal Conductivity of Ethane-1,2-diol (Ethylene Glycol) from the Triple Point to 475 K and Pressures up to 100 MPa, Int J Thermophys 42 (2021). https://doi.org/10.1007/s10765-021-02904-y.

[260] G.F. Bogatov, Y.L. Rastorguev, B.A. Grigor'ev, Thermal conductivity of normal hydrocarbons at high pressures and temperatures, Chem Technol Fuels Oils 5 (1969) 651–653. https://doi.org/10.1007/BF00729686.

[261] L. Riedel, Forsch. Geb. Ing. Wes., 11, 6, 340 (1940).

[262] R.L. Rowley, W.V. Wilding, A. Congote, N.F. Giles, The Use of Database Influence Factors to Maintain Currency in an Evaluated Chemical Database, Int J Thermophys 31 (2010) 860–874. https://doi.org/10.1007/s10765-010-0706-z.

[263] T.H. Chung, M. Ajlan, L.L. Lee, K.E. Starling, Generalized multiparameter correlation for nonpolar and polar fluid transport properties, Ind. Eng. Chem. Res. 27 (1988) 671–679. https://doi.org/10.1021/ie00076a024.

[264] D.T. Jamieson, Thermal conductivity of liquids, J. Chem. Eng. Data 24 (1979) 244–246. https://doi.org/10.1021/je60082a037.
[265] C.X. Xue, R.S. Zhang, H.X. Liu, M.C. Liu, Z.D. Hu, B.T. Fan, Support vector machines-based quantitative structure-property relationship for the prediction of heat capacity, J. Chem. Inf. Comput. Sci. 44 (2004) 1267–1274. https://doi.org/10.1021/ci049934n.
[266] D.F. Ilten, DETHERM: Thermophysical property data for the optimization of heat-transfer equipment, J. Chem. Inf. Comput. Sci. 31 (1991) 160–167. https://doi.org/10.1021/ci00001a029.
[267] D. Cousineau, S. Chartier, Outliers detection and treatment: a review, Int. j. psychol. res. 3 (2010) 58–67. https://doi.org/10.21500/20112084.844.
[268] C.C. PJ Rousseeuw, Alternatives to the Median Absolute Deviation, Journal of the American Statistical Association Volume 88 (1993).
[269] RDKit: Open-Source Cheminformatics Software, Accessed in 2023. URL: http://www.rdkit.org/.
[270] SMARTS - a language for describing molecular patterns; daylight chemical information systems inc.: Laguna niguel, ca, Accessed in 2023. URL: http://www.daylight.com/dayhtml/doc/theory/theory.smarts.html.
[271] Rosa Moreno Jimenez, Benoit Creton, Samuel Marre, Machine learning based models for accessing thermal conductivity of liquids at different temperature conditions, SAR and QSAR in Environmental Research (2023). https://doi.org/10.1080/1062936X.2023.2244410.
[272] K. Pearson, LIII. On lines and planes of closest fit to systems of points in space, The London, Edinburgh, and Dublin Philosophical Magazine and Journal of Science 2 (1901) 559–572. https://doi.org/10.1080/14786440109462720.
[273] H. Hotelling, Analysis of a complex of statistical variables into principal components, Journal of Educational Psychology 24 (1933) 417–441. https://doi.org/10.1037/h0071325.
[274] Casey Cheng, Principal Component Analysis (PCA) Explained Visually with Zero Math, 2022. https://towardsdatascience.com/principal-component-analysis-pca-explained-visually-with-zero-math-1cbf392b9e7d.
[275] P. Gramatica, Principles of QSAR models validation: internal and external, QSAR Comb. Sci. 26 (2007) 694–701. https://doi.org/10.1002/qsar.200610151.
[276] E.N. Muratov, E.V. Varlamova, A.G. Artemenko, P.G. Polishchuk, V.E. Kuz'min, Existing and Developing Approaches for QSAR Analysis of Mixtures, Mol. Inform. 31 (2012) 202–221. https://doi.org/10.1002/minf.201100129.
[277] B. Creton, B. Veyrat, M.-H. Klopffer, Fuel sorption into polymers: Experimental and machine learning studies, Fluid Phase Equilibria 556 (2022) 113403. https://doi.org/10.1016/j.fluid.2022.113403.
[278] C.-C. Chang, C.-J. Lin, LIBSVM, ACM Trans. Intell. Syst. Technol. 2 (2011) 1–27. https://doi.org/10.1145/1961189.1961199.
[279] L.M. Hiot, Y.S. Ong, Y. Tenne, C.-K. Goh, Computational Intelligence in Expensive Optimization Problems, Springer Berlin Heidelberg, Berlin, Heidelberg, 2010.
[280] P. Gantzer, B. Creton, C. Nieto-Draghi, Comparisons of Molecular Structure Generation Methods Based on Fragment Assemblies and Genetic Graphs, Journal of Chemical Information and Modeling 61 (2021) 4245–4258. https://doi.org/10.1021/acs.jcim.1c00803.
[281] H. Langouët, F. Delbos, D. Sinoquet, S. Da Veiga, A Derivative Free Optimization Method for Reservoir Characterization Inverse Problem, ECMOR XII - 12th European Conference on the Mathematics of Oil Recovery (2010) cp-163-00073. https://doi.org/10.3997/2214-4609.20144992.

[282] L.I.-K. Lin, A Concordance Correlation Coefficient to Evaluate Reproducibility, Biometrics 45 (1989) 255. https://doi.org/10.2307/2532051.

[283] N. Chirico, P. Gramatica, Real external predictivity of QSAR models: how to evaluate it? Comparison of different validation criteria and proposal of using the concordance correlation coefficient, Journal of Chemical Information and Modeling 51 (2011) 2320–2335. https://doi.org/10.1021/ci200211n.

[284] L. Riedel, Thermal Conductivity of Liquids (in German). Mitt. Kaltetech. Inst. Karlsruhe 2 (1948).

[285] G. Latini, Thermophysical properties of fluids: dynamic viscosity and thermal conductivity, J. Phys.: Conf. Ser. 923 (2017) 12001. https://doi.org/10.1088/1742-6596/923/1/012001.

[286] R. Mannhold, H. Kubinyi, G. Folkers, Methods and principles in medicinal chemistry. Wily-VCH: Verlag GmbH & Co. KGaA: (2007.).

[287] J. Gálvez, R. García-Domenech, J.V. de Julián-Ortiz, R. Soler, Topological approach to drug design, J. Chem. Inf. Comput. Sci. 35 (1995) 272–284. https://doi.org/10.1021/ci00024a017.

APPENDIX

Appendix A - Descriptors used in literature works to predict thermal conductivity

Kauffman, G. W. & Jurs, P. C. Prediction of surface tension, viscosity, and thermal conductivity for common organic solvents using quantitative structure-property relationships[198].	• *The CPSA FPSA-3 and FNSA-3 descriptors: encode information about the positively charged and negatively charged surface areas, respectively, using a weighted atomic charge* • *The RPCS-1 and RNCS-1 CPSA descriptors : contain information about the charged surface area relative to the most positively charged and negatively charged atoms.* • KAPA-2: *is the second-order path κ shape index* • *KAPA-2 MDE-14 : topological descriptors measure the degree of branching and provide information about the shape of the molecules.* • *1SP3-1 : number of sp3 carbons attached to only one other carbon atom*
Khajeh, A. & Modarress, H. Quantitative structure–property relationship prediction of liquid thermal conductivity for some alcohols[172].	• ATS2m: Broto–Moreau autocorrelation of a topological structure—lag 2/weighted by atomic masses. • GATS1m: Geary autocorrelation—lag 1/weighted by atomic masses, • G1s: 1st component symmetry directional WHIM index/weighted by atomic electrotopological states. • HATS2p: Leverage-weighted autocorrelation of lag 2/weighted by atomic polarizabilities, Hy: Hydrophilic factor.
Jing-Jie, S. H. *et al.* Prediction of the Thermal Conductivity of Organic Compounds Using Heuristic and Support Vector Machine Methods [202].	• X_1 ; HA dependent HDSA-1/TMSA represents solvent-accessible surface area of H-bonding donor H atoms which is affected by the size of the hydrogen bonding interaction. • X_3; FPSA3 = PPSA3/TMSA, PPSA3 indicates total charge weighted partial positively charged molecular surface area, TMSA refers to total molecular surface area. FPSA3 fractional atomic charge weighted partial positive surface area. • (X_4) Relative molecular weight.

	• (X_5) Relative number of C atom. (X_2) of the model is minimum (Min> 0.1) bond order of an F atom
Wanqiang Liu, Haixia Lu, Chenzhong Cao, Yinchun Jiao & and Guanfan Chen. An Improved Quantitative Structure Property Relationship Model for Predicting Thermal Conductivity of Liquid Aliphatic Alcohols [148].	• JGT: global topological charge index • temperature (T), • (Psi_i_1s)[286],: intrinsic state pseudo connectivity index-type 1s • (Eig06_AEA(Ed))[286]: sixth eigenvalue from augmented edge adjacency mat. weighted by edge degree • (JGT)[286,287] : global topological charge index
Lu, H. *et al.* Thermal Conductivity Estimation of Diverse Liquid Aliphatic Oxygen-Containing Organic Compounds Using the Quantitative Structure-Property Relationship Method[147]	• $\mathrm{SM2_{B(s)}}$: spectral moment of order 2 from the Burden matrix weighted by I-state, • $SIC0$:structural information content index (neighborhood symmetry of 0- order), • $IC1$:information content index (neighborhood symmetry of 1-order), • T : temperature. • Eta_F : eta functionality index, $MATS2m$: Moran autocorrelation of lag 2 weighted by mass
Latini, G., Di Nicola, G., Pierantozzi, M., Coccia, G. & Tomassetti, S. Artificial Neural Network Modeling of Liquid Thermal Conductivity for alkanes, ketones and silanes[204].	• $T_{r:}$ Reduced temperature • *MW :* Molecular weight ω : Acentric factor
Pierantozzi, M., Di Nicola, G., Latini, G. & Coccia, G. Artificial neural network modelling of liquid thermal conductivity for alcohols[205].	• $T_{r:}$ Reduced temperature • P_c :critical pressure*)*,and the melting point • $T_{mp:}$ melting point

Appendix B - Resistance measurement: 4-wire method

The 4-wire method is used to measure the resistance of a material or device accurately. It involves using four wires - two for passing current and two for measuring voltage. The goal is to eliminate the resistance of the measurement leads from affecting the measurement of the material/device's resistance. This is done by using separate measurement leads.

The principle involves injecting a current between the two outer metal pins (1 and 4) and measuring the voltage generated between the two inner pins (2 and 3).

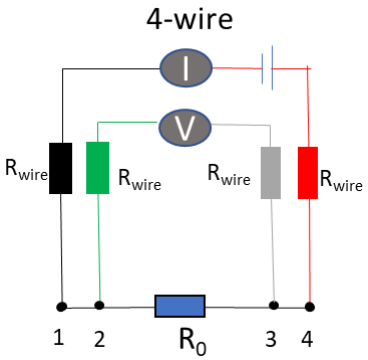

Figure A- 1: Schematic of the 4-wire method

Finally, the resistance R_0 can be calculated by applying the Ohm's law:

$$R_0 = \frac{V}{I} \tag{0-1}$$

Where *I* is the current supplied by the multimeter and *V* is the voltage measured across the resistance R_0.

This characterization method can be used was used thin films deposited on a glass substrate and it was implemented to observe if there were small changes in resistance to understand the effect on electron transfer due to surface degradation or the thickness of the adhesion layer.

Appendix C - Hazardous and physical properties of substances

Product name	Formula	Hazardous substance label			Physical properties			
		 Flammable	 Harmful	 Health hazard	State of matter. (20°C)	T_{eb} 1 atm (°C)	T flash point (°C)	T autoignition (°C)
Ethanol	C_2H_6O	x	x		liquid	78	13	365
Water	H_2O				liquid	271	-	
N-pentadecane	$C_{15}H_{32}$			x	liquid	92	-1	
Ethane-1,2-diol	$C_2H_6O_2$		x		liquid	100		
2,5-dimethylfuran	C_6H_8O	x	x		liquid	197	11	> 398

Appendix D - Metal deposition samples

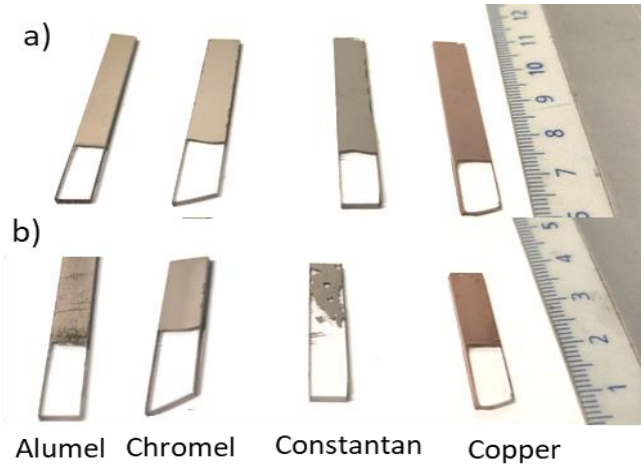

Figure A- 2: Metal deposition samples before(a) and after (b) 3 cycles of oxygenated and temperature resistance protocol using ethanol

Appendix E - Uncertainty type B

Type B

Balance Mettler Toledo					
Specifications	Units	Value	Divisor	Sensitivity coefficient	u^2
Resolution	g	1.00E-04	3.46	1	8.33E-10
Linearitiy	g	2.00E-04	1	1	4.00E-08
repetability	g	4.00E-05	1	1	1.60E-09
u(g)					2.06E-04
U(g)				K=2	4.12E-04

U15 memmert oven					
Specifications	Units	Value	Divisor	Sensitivity coefficient	u^2
Homogeneity	K	5.00E-02	1.00E+00	1.00E+00	2.50E-03
Stability	K	1.00E-01	1.00E+00	1.00E+00	1.00E-02
u(T)					1.12E-01
U(T)				K=2	2.24E-01

Type K thermocouple					
Specifications	Units	Value	Divisor	Sensitivity coefficient	u^2
Repetability	K	4.00E-01	1.00E+00	1.00E+00	1.60E-01
u(T)					4.00E-01
U(T)				K=2	8.00E-01

RS DC voltage					
Specifications	Units	Value	Divisor	Sensitivity coefficient	u^2
Resolution	V	1.00E-02	1.73E+00	1.00E+00	3.34E-05
Precision	V	5.00E-02	1.73E+00	1.00E+00	8.35E-04
u(V)					2.95E-02
U(V)				K=2	5.89E-02

Multimeter (I)					
Specifications	Units	Value	Divisor	Sensitivity coefficient	u^2

Resolution	A	1.00E-03	1.73E+00	1.00E+00	3.34E-07
Precision	A	2.00E-03	1.73E+00	1.00E+00	1.34E-06
u(I)					5.78E-04
U(I)				K=2	1.16E-03

Resistance (R)					
Specifications	Units	Value	Divisor	Sensitivity coefficient	u^2
Voltage	V	2.95E-02	1.00E+00	1.00E+01	8.69E-02
Intensity	A	5.78E-04	1.00E+00	-1.12E+02	4.19E-03
Temperature	1/K	3.00E-03	1.00E+00	1.84E+00	3.05E-05
u(R)					3.02E-01
U(R)				K=2	6.04E-01

Heat generation (P)					
Specifications	Units	Value	Divisor	Sensitivity coefficient	u^2
Intensity	A	3.05E-05	1.00E+00	8.00E+00	5.95E-08
Resistance	Ω	3.02E-01	1.00E+00	8.00E-03	5.83E-06
u(P)					2.43E-03
U(P)				K=2	4.85E-03

Appendix F - List of molecules present in the database

Appendix G - Values of the parameters regressed on predictions using the SVR model

IUPAC name	A	B	C	D	Tc (K)
octan-2-one	0.076	0.386	-1.790	3.050	632.7
pentan-2-one	0.088	0.207	-0.987	2.203	561.1
prop-2-en-1-ol	0.097	0.191	-0.921	2.093	545.1
octanoic acid	0.086	0.116	-0.639	1.764	693.0
1-propoxypropane	0.059	0.333	-1.625	4.243	530.6
2-methylpropanal	0.066	0.504	-2.419	4.684	544.0
4-methylphenol	0.108	0.286	-1.265	1.802	704.6
octadec-9-enoic acid	0.114	0.017	-0.231	0.943	781.0
diethyl oxalate	0.100	0.118	-0.599	1.562	618.0
dibenzofuran	0.103	0.376	-1.665	2.019	824.0
bis(2-ethylhexyl) hexanedioate	0.100	0.312	-1.486	2.088	845.0
prop-2-enoic acid	0.106	0.123	-0.605	1.466	615.0
1,3-diacetyloxypropan-2-yl acetate	0.163	0.007	-0.034	0.049	701.4
dec-1-ene	0.063	0.461	-2.169	4.284	617.0
2,2,5-trimethylhexane	0.046	0.442	-2.208	4.601	569.8
2-methylbutane	0.054	-0.103	-0.062	3.023	460.4
butyl propanoate	0.060	0.359	-1.733	3.999	594.5
methyl benzoate	0.065	0.652	-2.988	4.758	702.0
propanal	0.104	0.208	-1.030	2.696	505.0
1,2-bis(2-methoxyethoxy)ethane	0.101	0.176	-0.868	1.885	651.0
1-methyl-2-propan-2-ylbenzene	0.056	0.687	-3.118	4.913	657.0